COSMIC-DANCE : A comprehensive census of nearby star forming regions

Núria Miret Roig

UNIVERSITÉ DE BORDEAUX
LABORATOIRE D'ASTROPHYSIQUE DE BORDEAUX
École Doctorale Sciences Physiques et de l'Ingénieur
Doctorat en Astrophysique, Plasmas, nucléaire

COSMIC DANCE: A comprehensive census of nearby star forming regions

Dissertation presented by
Núria Miret Roig
for the degree of
Doctor in Astrophysics by the Unversity of Bordeaux

Thesis supervisor: Dr. Hervé Bouy
Thesis advisor: Dr. Javier Olivares Romero

Jury members:

Dr. João Alves	University of Vienna	Referee
Dr. Christine Ducourant	University of Bordeaux	Examiner
Dr. Francesca Figueras Siñol	University of Barcelona	Examiner
Dr. Koraljka Mužić	University of Lisboa	Referee
Dr. Sofia Randich	NAF-Osservatorio Astrofisico di Arcetri	Examiner
Dr. Caroline Soubiran	University of Bordeaux	Jury president

Bordeaux, December 2020

Thèse présentée pour obtenir le grade de
docteur de l'Université de Bordeaux

École Doctorale Sciences Physiques et de l'Ingénieur

Par **Núria Miret Roig**

COSMIC DANCE: Un recensement complet des régions de formation stellaire proches

Sous la direction de : **M. Hervé Bouy**
Co-encadrant : **M. Javier Olivares Romero**

Soutenue le 17 décembre 2020

Membres du jury :

M. João Alves	Université de Vienna	Rapporteur
Mme. Christine Ducourant	Université de Bordeaux	Examinatrice
Mme. Francesca Figueras Siñol	Université de Barcelone	Examinatrice
Mme. Koraljka Mužić	Université de Lisboa	Rapporteur
Mme. Sofia Randich	NAF-Osservatorio Astrofisico di Arcetri	Examinatrice
Mme. Caroline Soubiran	Université de Bordeaux	Président du jury

COSMIC DANCE: A COMPREHENSIVE CENSUS OF NEARBY STAR FORMING REGIONS

NÚRIA MIRET ROIG

SUPERVISOR: Hervé Bouy
ADVISOR: Dr. Javier Olivares Romero

Laboratoire d'Astrophysique de Bordeaux
Université de Bordeaux

If I have seen further
it is by standing on the shoulders of giants.

— Sir Isaac Newton

ACKNOWLEDGMENTS

Són moltes les persones que han contribuït a que aquesta tesi sigui possible, tant des del món acadèmic com personal. A totes elles els dedico aquesta tesi i els estic enormement agraïda.

En primer lloc vull agrair als meus pares, Magda i Xavier, per haver-me educat i fet créixer convertint-me en la persona que sóc ara. Ells ho han donat tot perquè jo pogués tirar endavant els meus estudis amb les mínimes preocupacions possibles. Moltes gràcies per haver estat sempre al meu costat celebrant els millors moments i acompanyant-me en les decisions més difícils. Agraeixo especialment al meu pare haver-me iniciat en el món de l'astronomia *amateur* ja des de petita, que s'ha acabat convertint en la meva passió i professió. També vull agrair al Pau, el meu germà, tots els bons moments que hem passat junts i el seu optimisme crític amb que sempre m'ha aconsellat. Recordo amb especial carinyo les bones rebudes que m'has fet cada vegada que he tornat a casa i sé que sempre puc comptar amb tu.

A l'Aleix li agreixo el seu suport incondicional al llarg d'aquests tres anys, haver-me animat a iniciar, seguir i acabar aquesta tesi malgrat que això signifiques la distància (i molts viatgets a França). Tu m'has descobert *lo Burgà*, un lloc on el temps es para, on no hi ha preocupacions, on desconnecto de veritat. Aquest lloc ha estat un salvavides per moments en que m'he sentit totalment desbordada. Sense la teva alegria, coratge i força per tirar endavant, aquesta tesi hauria estat molt més difícil. També agraeixo a la família Benaiges-Lliberia haver-me acollit amb els braços oberts des del primer dia.

A la resta de la família els agraeixo l'escalf i amor que sempre m'han donat i l'alegria que els caracteritza. Al meu avi, la persona més alegre que conec, gràcies per regalar-me un somriure cada vegada que ens veiem, per totes les paraules amables i l'hospitalitat que sempre tens pels que et venen a veure. A tu et dedico un dels planetes trobats en aquesta tesi. A la iaia, gràcies per fer-me sentir sempre tant especial i estimada. Gràcies per rebre'm amb els braços oberts cada vegada que torno a casa i per preguntar-me sempre "i quan tornaràs?". A les meves tietes i oncle, Núria, Pep, Montse, Imma, Anna, Jose, Jordi i Salva els agraeixo que m'hagin ensenyat que la família és gent amb la que pots confiar i compartir, per estar sempre disposats a les celebracions o a fer pinya en els moments més baixos. Als meus cosins, Mireia, Raúl, Berta, Aina, Clàudia i Gael els agraeixo tots els bons moments.

L'altre gran pilar que m'ha mantingut alegre i feliç durant la tesi ha estat l'amistat. Judit i Laura gràcies per haver estat al meu costat tot aquest temps. Valoro especialment que haguem estat capaces de reinventar la nostra amistat malgrat la distància. Gràcies per estimar-me i valorar-me tal com sóc i per escolar-me sempre, perquè després de parlar amb volatres els problemes són menys greus i les alegries més grans. També vull agrair a la resta de la colla: Arnau, Berta, Erik, Ester, Guille, Joan, Sonia, Vera les vostres visites a Bordeus, les bones rebudes a Ribes i totes les festes que hem passat junts. Laia i Anna, us estic molt agaïda per la vostra amistat.

A Bordeus, més enllà de mantenir les amistats que ja tenia n'he descobert de noves. Laia, per molt que ja ens coneguéssim a Barcelona, viure experiències semblants a l'estranger m'ha apropat molt a tu. Ser companyes de feina (i de despatx!), compartir tants viatges Burdeus-Barcelona, Barcelona-Bordeus, les classes d'Ukelele, de ioga, les tardes al *gym*... són innumerables els bons records amb tu! T'estic molt agraïda per l'amistat que m'has regalat tot aquest temps així com els consells i suport en l'àmbit professional. Recordo amb molt d'escalf els caps de setmana i viatges que hem fet amb tu, l'Alfred i l'Aleix.

També agraeixo el suport de bons amics del Grau i Màster que m'han acompanyat la resta del temps. Guillem, ets un gran amic des de que ens vam conèixer. T'agraeixo tantes hores en biblioteques i aules d'estudi i per aportar calma i seny sempre que m'estresso. A la resta de companys del Grau i Màster Pol, Núria, Adrià, Bruno, Borja, Cate, Clara, Gemma, Glòria, Manel i tants altres els agraeixo tot el camí que hem fet junts, tant les hores de classe i estudi, com viatges i quedades que han reforçat la nostra amistat.

I would also like to thank Cristina, Giuliano, Laia, May and Silvia because with you I felt I was home. I remember with special affection all the dinners and trips as well as our endless conversations on how to deal with bureaucracy in France. I'm also extremely thankful to you for your help in moving, I can't imagine how I would have done it without you. Grazie mille a tutti!

This thesis would not have been possible without Hervé Bouy, my PhD supervisor. Thank you for giving me the great chance to join your team and pursue this thesis. I am very grateful for all the opportunities you gave me of visiting the most amazing telescopes in the world. I have a warm memory of the nights we spent at the CTIO and in la Palma, those were certainly the best moments of this thesis. I acknowledge you for the freedom you gave me during these three years of thesis and for the variety of topics in which you encouraged me to explore and which remarkably enriched this thesis. I thank Javier Olivares, co-advisor of this thesis, for his patience and kindness while teaching me statistics. I am especially grateful for your wise advise and because you have never had a no for an answer whenever I needed you. I

am extremely grateful to all the COSMIC DANCe team: Hervé, Ángel, David, Javier, Luisma, Maxime, Nuria, Phillip. Each of you has contributed to improve this thesis and I have learned a lot being by your side. I thank Nuria Hélamo for guiding me in the study of discs; Jorge Lillo-Box, David Barrado and Sean Raymond for introducing me in the amazing world of exoplanets; Phillip Galli for his contribution in providing the radial velocities analysed in this thesis; Francesca Figueras for her critical and constructive comments which significantly improved the study on the dynamical ages; Luis Sarro for his wise and kind advise in statistics and *Gaia*; Wolfgang Brander for helping me obtain the essential spectroscopic observations in FEROS; and Nicolas Lodieu and Koraljka Mužić for their help in the reduction and interpretation of spectra of ultracool dwarfs. I am grateful to Ingo Thies for sharing with me his models of the Initial Mass Function, to France Allard and Isabelle Barraffe for providing me with the latest version of the BT-Settl and BHAC15 models and to Ferran Torra for his advice in the proper use of *Gaia* DR2 data. I wish to thank the referees of this thesis João Alves and Koraljka Mužić for their constructive reports which contributed to improve this manuscript, and to all the members of the jury for the time devoted to this thesis.

Je veux remercier les doctorants et post-docs du LAB Audrey, Baptiste, César, Eugenia, Jordan, Lars, Maxime, Mélisse, Sacha, Tiziano, William, Yassin, Yoann pour tous les bons moments pause-cafe, after-labs qui ont rendu mon passage au LAB plus agréable. Je tiens à remercier la direction et l'administration pour leur accueil ansi que l'équipe M2A et sa directrice Caroline Soubiran.

M'agradaria dedicar les últimes paraules d'aquests agraïments a mestres o professos que més enllà d'haver-me educat, han marcat una diferència en mi i m'han fet despertar o aprofundir el meu amor per la ciència i, especialment, per l'astronomia. A nivell de l'institut, tinc un gran record de les classes de mates de l'Eugeni Perez: la seva energia incansable i determinació perquè cadascú aprengués tant com pogués. Malgrat que mai he estat una apassionada de la Química, el "Coro" (Josep Coromines) va aconseguir que gaudis aquelles classes com cap altre gràcies a la seva apassionant manera de transmetre i deixar-nos experimentar. Més endavant, a la universitat, vaig tornar a trobar grans professors que em van seguir inspirant. Del primer any de carrera recordo especialment les classes d'equacions diferencials de la Cesca (Francesca Figueras) pel seu entusiasme i il·lusió per ensenyar. Al final de la carrera vaig tenir la oportunitat de treballar amb ella i el seu equip gràcies a una beca d'estiu. Nomes puc tenir paraules d'agraïment per la Cesca, la Teresa Antoja i la Mercè Romero per la seva guia, dedicació i esforç durant els treballs de Grau i de Màster i perquè sempre que ho he necessitat han estat disposades a aconsellar-me. Moltes gràcies a elles i a tota la resta de l'equip de *Gaia* de

Barcelona, Alfred, Carme, Laia, Lola, Pau, Roger, Xavi i tants altres ja que sempre he pogut comptar amb vosaltres.

This research has received funding from the European Research Council (ERC) under the European Union's Horizon 2020 research and innovation programme (grant agreement No 682903, P.I. H. Bouy), and from the French State in the framework of the "Investments for the future" Program, IdEx Bordeaux, reference ANR-10-IDEX-03-02 . Based on observations collected at the European Southern Observatory under ESO programmes 60.A-9120(A), 60.A-9121(A), 60.A-9122(A), 68.C-0311(A), 69.A-9014(A), 69.C-0034(A), 69.C-0260(A), 69.C-0398(B), 69.C-0426(C), 69.D-0582(A), 60.A-9038(A),0103.A-9009, 088.A-9007, 089.A-9007, 089.A-9013, 089.D-0709, 090.A-9010, 090.C-0200, 090.C-0815, 091.A-9012, 091.A-9013, 091.C-0216, 091.C-0595, 092.A-9002, 092.A-9009, 093.A-9006, 093.A-9029, 094.A-9002, 094.A-9012, 095.A-9029, 099.A-9005, 099.A-9029. Based in part on observations made at Observatoire de Haute Provence (CNRS), France. Based on observations collected at the Centro Astronómico Hispano-Alemán (CAHA) at Calar Alto, operated jointly by Junta de Andalucía and Consejo Superior de Investigaciones Científicas (IAA-CSIC). This research draws upon data distributed by the NOAO Science Archive. NOAO is operated by the Association of Universities for Research in Astronomy (AURA) under cooperative agreement with the National Science Foundation. This work has made use of data from the European Space Agency (ESA) mission *Gaia* (http://www.cosmos.esa.int/gaia), processed by the *Gaia* Data Processing and Analysis Consortium (DPAC, http://www.cosmos.esa.int/web/gaia/dpac/consortium). Funding for the DPAC has been provided by national institutions, in particular the institutions participating in the *Gaia* Multilateral Agreement. This work is based [in part] on observations made with the Spitzer Space Telescope, which is operated by the Jet Propulsion Laboratory, California Institute of Technology under a contract with NASA. This publication makes use of data products from the Two Micron All Sky Survey, which is a joint project of the University of Massachusetts and the Infrared Processing and Analysis Center/California Institute of Technology, funded by the National Aeronautics and Space Administration and the National Science Foundation. This publication makes use of data products from the Wide-field Infrared Survey Explorer, which is a joint project of the University of California, Los Angeles, and the Jet Propulsion Laboratory/California Institute of Technology, funded by the National Aeronautics and Space Administration. This research has made use of the NASA/ IPAC Infrared Science Archive, which is operated by the Jet Propulsion Laboratory, California Institute of Technology, under contract with the National Aeronautics and Space Administration. This publication makes use of VOSA, developed under the Spanish Virtual Observatory project supported by the Spanish MINECO through grant AyA2017-84089. This research has made use of the VizieR and Aladin images and catalogue access tools and of the SIMBAD

database, operated at the CDS, Strasbourg, France. This publication makes use of data products from the Wide-field Infrared Survey Explorer, which is a joint project of the University of California, Los Angeles, and the Jet Propulsion Laboratory/California Institute of Technology, funded by the National Aeronautics and Space Administration. This research has made use of GNU Parallel (Tange 2011), Astropy (Astropy Collaboration et al. 2013), Topcat (Taylor 2005), STILTS (Taylor 2006).

ABSTRACT

Understanding how stars form is one of the fundamental questions which astronomy aims to answer. Currently, it is well accepted that the majority of stars form in groups and that their predominant mechanism of formation is the core-collapse. However, several mechanisms have been suggested to explain the formation of substellar objects, and their contribution is still under debate.

The main goal of this thesis is to determine the initial mass function, the mass distribution of stars at birth time, in different associations and star-forming regions. The mass function constitutes a fundamental observational parameter to constrain stellar and substellar formation theories since different formation mechanisms predict different fraction of stellar and substellar objects.

We used the *Gaia* Data Release 2 catalogue together with ground-based observations from the COSMIC-DANCe project to look for high probability members via a probabilistic model of the distribution of the observable quantities in both the cluster and background populations. We applied this method to the 30 Myr open cluster IC 4665 and the $1 - 10$ Myr star-forming region Upper Scorpius (USC) and ρ Ophiuchi (ρ Oph). We found very rich populations of substellar objects which largely exceed the numbers predicted by core-collapse models. In USC, where our sensitivity is best, we found a large number of free-floating planets and we suggest that ejection from planetary systems must have a similar contribution than core-collapse in their formation.

The age is a fundamental parameter to study the formation and evolution of stars and is essential to accurately convert luminosities to masses. For that, we also presented a strategy to study the dynamical traceback age of young local associations through an orbital traceback analysis. We applied this method to determine the age of the β Pictoris moving group and in the future, we plan to apply it to other regions such as USC.

The members we identified with the membership analysis are excellent targets for follow-up studies such as a search for discs, exoplanets, characterisation of brown dwarfs and free-floating planets. I this thesis, we presented a search for discs hosted by members of IC 4665 and we found six excellent candidates to be imaged with ALMA or the JWST. The tools we developed, are ready to be used in other regions such as USC and ρ Oph, where we expect to find a larger number of disc-host stars.

Keywords: star, brown dwarf, and planet formation – luminosity and mass function – kinematics and dynamics – stellar ages – solar neighbourhood – open clusters and associations: individual: Upper Scorpius, ρ Ophiuchus, IC 4665, β Pictoris moving group

---

Research unit
Laboratoire d'Astrophysique de Bordeaux
Université de Bordeaux & CNRS (UMR 5804)
Univ. Bordeaux – Bât. B18N, allée Geoffroy Saint-Hilaire, CS 50023, 33615
Pessac Cedex, France

RÉSUMÉ

Comprendre comment se forment les étoiles est l'une des questions fondamentales auxquelles l'astronomie entend répondre. Malheureusement, nous ne pouvons pas étudier la formation stellaire en temps réel et différentes méthodes indirectes doivent être utilisées pour faire la lumière sur ce sujet. L'objectif principal de cette thèse est de déterminer la fonction de masse initiale, la distribution de masse des étoiles à leur naissance, dans différentes associations et régions de formation d'étoiles. La fonction de masse est le produit direct de la formation stellaire et constitue donc un paramètre d'observation fondamental pour contraindre les théories de formation stellaire et sous-estellaire. Nous nous sommes concentrés sur l'amas ouvert de 30 Ma IC 4665 et la région de formation d'étoiles de $1 - 10$ Ma de Upper Scorpius (USC) et ρ Ophiuchi (ρ Oph). Nous avons combiné l'astrométrie et la photométrie de *Gaia* Data Release 2 avec nos observations au sol pour préparer un catalogue profond et étendu de chaque région. Ensuite, nous avons calculé les probabilités d'appartenance en utilisant toute l'astrométrie et la photométrie disponibles et identifié les membres à haute probabilité. Nous avons utilisé la liste finale des membres pour estimer la distribution de magnitude, et les fonctions de luminosité et masse de ces associations. Alors que la première a l'avantage d'être indépendante des modèles d'évolution, tandis que les fonctions de luminosité et de masse peuvent être utilisées pour contraindre les mécanismes de formation d'étoiles. L'étude d'IC 4556 nous a permis d'identifier des objets sous-stellaires, sans pour autant pouvoir fournir un recensement complet dans ce domaine de masse. Dans USC et ρ Oph, nous avons identifié une population très riche d'objets sous-stellaires, significativement plus nombreux que les prédictions des modèles de formation par effondrement de cœurs moléculaires, suggérant que la formation de naines brunes et d'objets de masses planétaires isolés par des phénomènes d'éjection dans des systèmes planétaires a une contribution importante et du même ordre que l'effondrement des cœurs moléculaires à la population finale d'objets dans un amas. L'âge est un paramètre fondamental pour étudier la formation et l'évolution des étoiles pour plusieurs raisons: premièrement puisqu'il établit une échelle de temps sur laquelle placer les observations. Deuxièmement car il est essentiel pour convertir les luminosités en masses, avec l'aide de modèles d'évolution stellaire. Les incertitudes sur l'age de USC et ρ Oph se traduisant en erreurs importantes dans notre estimation de la fonction de masse, j'ai développé une stratégie d'étude de "l'âge dynamique" au moyen d'une analyse

orbitale de traçage des mouvements des membres d'associations jeunes. J'ai ainsi mis au point une stratégie incluant i) les observations et la recherche de données dans les archives publiques, ii) la réduction et l'analyse des spectres échelles obtenus; iii) et l'analyse dynamique, pour déterminer l'âge d'une association. La méthodologie, développée avec l'association β Pictoris (β Pic), est prête à être appliquée à d'autres régions et en particulier à USC et ρ Oph. Les membres que nous avons identifiés sont par ailleurs d'excellentes cibles pour des études complémentaires telles que la recherche de disques (produit également fondamental de la formation stellaire), d'exoplanètes, de système multiples, mais aussi pour la caractérisation des atmosphères et propriétés physiques des naines brunes et des planètes errantes. Dans cet esprit, j'ai mené au cours de cette thèse la recherche de disques de débris autour des membres de IC 4665 qui a mené à la découverte de six excellents candidats. Ces objets seront des cibles idéales pour un futur suivi avec ALMA ou JWST. Les outils que j'ai développés pour IC 4665 sont directement applicables à d'autres régions et en particulier à USC et ρ Oph, où nous nous attendons à trouver un grand nombre de disques protoplanétaires.

Keywords: formation d'étoiles, de naines brunes et de planètes - luminosité et fonction de masse - cinématique et dynamique - âges stellaires - voisinage solaire - amas ouverts et associations: individu: Scorpion supérieur, ρ Ophiuchus, IC 4665, β Pictoris

---

Unité de recherche
Laboratoire d'Astrophysique de Bordeaux
Université de Bordeaux & CNRS (UMR 5804)
Univ. Bordeaux – Bât. B18N, allée Geoffroy Saint-Hilaire,
CS 50023, 33615 Pessac Cedex, France

LIST OF PUBLICATIONS

This thesis is based on the following refereed publications:

– **IC 4665 DANCe. I. Members, empirical isochrones, magnitude distributions, present-day system mass function, and spatial distribution**
Miret-Roig, N.; Bouy, H.; Olivares, J. et al. 2019, A&A 631, A57.

– **Searching for debris discs in the 30 Myr open cluster IC 4665**
Miret-Roig, N.; Huélamo, N.; Bouy, H. 2020, A&A 641, A156.

– **Dynamical traceback age of the β Pictoris moving group**
Miret-Roig, N.; Galli, P. A. B.; Brandner, W. et al. 2020, A&A 642, A179.

CONTENTS

ACRONYMS

2MASS	Two Micron All Sky Survey
4MOST	4-metre Multi-Object Spectroscopic Telescope
β Pic	β Pictoris
ρ Oph	ρ Ophiuchi
Gaia DR1	*Gaia* Data Release 1
Gaia DR2	*Gaia* Data Release 2
Gaia eDR3	early *Gaia* Data Release 3
ALMA	Atacama Large Millimeter/submillimeter Array
APOGEE	Apache Point Observatory Galactic Evolution Experiment
BCD	Basic Calibrated Data
BD	brown dwarfs
BIC	Bayesian information criterion
CADC	Canadian Astronomy Data Centre
CAFE	Calar Alto Fiber-fed Echelle spectrograph
CBCD	Corrected Basic Calibrated Data
CDS	Centre de Données astronomiques de Strasbourg
CFHT	Canada-France-Hawaii Telescope
CMD	color-magnitude diagram
CMF	core mass function
CTIO	Cerro Tololo Inter-American Observatory
DANCe	Dynamical Analysis of Nearby ClustErs
DECam	Dark Energy Camera
E-ELT	European Extremely Large Telescope
ESA	European Space Agency
ESO	European Southern Observatory
FEROS	Fiber-fed Extended Range Optical Spectrograph
FFP	free-floating planets
FIES	Fibre-fed Echelle Spectrograph
FWHM	full width at half maximum
GCRS	Geocentric Celestial Reference System
GMM	Gaussian mixture model

GMT	Giant Magellan Telescope
GTC	Gran Telescopio Canarias
HR diagram	Hertzsprung–Russell diagram
HSC	Hyper Suprime-Cam
IAU	International Astronomical Union
IMF	initial mass function
ING	Isaac Newton Group
INT	Isaac Newton Telescope
IPAC	Infrared Processing and Analysis Center
IR	infrared
IRAS	Infrared Astronomical Satellite
IRSA	Infrared Science Archive
IUE	International Ultraviolet Explorer
JWST	James Webb Space Telescope
KDE	kernel density estimation
KPNO	Kitt Peak National Observatory
KS	Kolmogorov-Smirnov
LCC	Lower Centaurus-Crux
LCO	Las Cumbres Observatory
LSST	Large Synoptic Survey Telescope
MOONS	Multi Object Optical and Near-infrared Spectrograph
NAOJ	National Astronomical Observatory of Japan
NOAO	National Optical Astronomy Observatory
NOT	Nordic Optical Telescope
NRES	Network of Robotic Echelle Spectrographs
OHP	Observatoire de Haute-Provence
Pan-STARRS	Panoramic Survey Telescope and Rapid Response System
PDMF	present-day mass function
PDSMF	present-day system mass function
PMS	pre-main-sequence
PSF	point spread function
PTF	Palomar Transient Factory
RUWE	renormalised unit weighted error
Sco-Cen	Scorpius-Centaurus
SED	spectral energy distribution
SES	STELLA échelle spectrograph

SMOKA	Subaru-Mitaka-Okayama-Kiso-Archive
SNR	signal-to-noise ratio
SVO	Spanish Virtual Observatory
TMT	Thirty Meter Telescope
UCL	Upper Centaurus-Lupus
UHS	UKIRT Hemisphere Survey
UKIDSS	UKIRT Infrared Deep Sky Survey
UKIRT	United Kingdom Infra-Red Telescope
USC	Upper Scorpius
UV	ultraviolet
VISTA	Visible and Infrared Survey Telescope for Astronomy
VLT	Very Large Telescope
VOSA	VO SED analyser
WEAVE	WHT Enhanced Area Velocity Explorer
WFC	Wide Field Camera
WFCAM	Wide Field Camera
WFI	Wide Field Imager
WHT	William Herschel Telescope
WIRCam	Wide-field InfraRed Camera
WSA	WFCAM Science Archive
ZAMS	Zero Age Main Sequences

Part I

INTRODUCTION

1

INTRODUCTION

Astronomy is one of the oldest sciences and, since antiquity, it has aroused the interest of the most advanced civilisations. In its origins, it was tightly related to religion and mythology and it was not until the Copernican Revolution in the 16^{th} century when it became a science completely separated from mystical beliefs. Unlike most natural sciences, in astronomy we cannot touch or experiment with the objects of our interest (i.e. celestial bodies), all we can do is observe them. It is by gathering the light they emit that we have learnt all we know about the Universe.

In 1609, Galileo Galilei performed the first documented observations with a telescope. He made important discoveries of solar system objects yet, probably, his greatest contribution was observing for the first time that the luminous band that crosses the sky, the Milky Way, was a collection of stars. Around 50 years later, in 1687, Isaac Newton published his *Philosophiæ naturalis principia mathematica* where he presented the universal law of gravitation, a framework still used nowadays to describe the motion of stars. With these discoveries, the modern astronomy began and since then innumerable advances have succeeded. Each time the instruments to observe the sky have improved, unexpected discoveries have been made. One example is the revolution in the construction of large telescopes (larger than 1 m) of the last century. In 1929, Edwin Hubble used the 2.5 m Hooker telescope at Mount Wilson to provide the observations which confirmed the expansion of the universe (Hubble 1929), however, Hubble himself was sceptical about this interpretation. Additionally, when astronomers started to observe in wavelengths other than the optical, new phenomena were revealed. For example, in 1983, the Infrared Astronomical Satellite (IRAS) was launched becoming the first infrared (IR) telescope in space (Beichman et al. 1988). Among many other sources, it observed the Vega star, a bright bluish star which can be seen in the northern sky, during summer, with the naked eye. IRAS detected an IR excess emission in Vega, meaning that it is emitting more light in the IR than expected (Aumann et al. 1984). Such IR excess is explained by the presence of a circumstellar disc.

In this introductory chapter, we present general concepts that are going to be used throughout this thesis. In Section 1.1 we review the main mechanisms to form stars and substellar objects. In Section 1.2 we introduce the *Gaia* mission and the COSMIC-DANCe project, two astrometric and photometric surveys

fundamental for the research developed in this thesis. Finally, we present the motivations and goals of the thesis in Section 1.3 and the thesis outline in Section 1.4.

1.1 STAR FORMATION IN THE SOLAR NEIGHBOURHOOD

Stars are huge spheres of gas held together by gravity that produce energy through thermonuclear fusion reactions, mainly of hydrogen. They represent the most fundamental building blocks of galaxies and, in consequence, the study of their formation, evolution and death is of uttermost importance in astronomy. Understanding how stars form is one of the fundamental questions which astronomy aims to answer. It is key to understand where does the matter that constitutes human beings come from and to predict the evolution of the Universe.

Currently, it is widely accepted that the majority of stars form in groups rather than in isolation. However, many details of the formation process remain unknown. How does star formation begin and propagate through the parent giant molecular cloud? What is the role of the local environment? Which is the efficiency of the star formation process? What is the origin of stellar masses? Which fraction of stars population ends up in gravitationally-bound structures? These are only some of the questions that star formation theories intend to answer and are still under debate.

The main observational challenge that hinders the study of the star formation process is that it happens on a much larger time-scale than the life of human beings and therefore it can not be studied in real-time. In this section and throughout this thesis, we discuss several indirect methods, using products of the star formation process, which help us to understand the global picture. Some of them are the study of the mass function, the dynamics, and the identification of stars hosting discs. All these parameters are strongly age-dependent and it is for this reason that it is essential to measure stellar ages precisely.

Aside from this intrinsic adversity, there are other difficulties related to the observation of recently formed stars. First, stars form in the densest regions of molecular clouds and most of the light they emit is blocked by dust and gas. In this sense, the beginnings of the IR astronomy were a milestone in the study of stellar formation. While newly born stars appear embedded in the optical wavelength range, in the IR we can see through dust and gas and detect the youngest objects. In Figure 1.1 we show an example of the impact of the extinction produced by a dark cloud at different wavelengths. It is remarkable the large number of stars which appear embedded at optical wavelengths (top panels) and which are detected in the IR (bottom panels). A

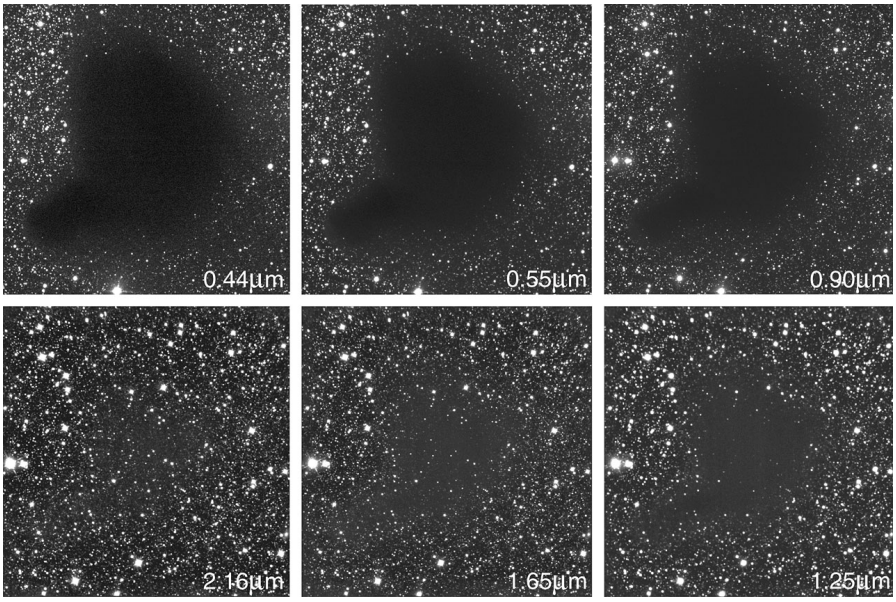

Figure 1.1. The Barnard 68 dark cloud imaged in six different wavebands, clockwise from the blue (optical) to the near-infrared spectral region. The extinction caused by the cloud diminishes dramatically with increasing wavelength. Since the outer regions of the cloud are less dense than the inner ones, the apparent size of the cloud also decreases, as more background stars shine through the outer parts. Credit: ESO & J. Alves

second observational limitation is related to the difficulty of observing an entire population of recently formed stars. Massive stars are rare and they evolve and die very quickly, making them even less numerous. On the other hand, low-mass stars are faint and hard to be observed at large distances.

Studying the star formation process in the solar vicinity has numerous advantages. First, the short distances allow us to observe the least massive objects which are also the faintest. Additionally, the solar neighbourhood is where the data is most precise, least biased, and least affected by other observational constraints such as crowding or unresolved binaries. For these reasons, several authors have mapped the star formation sites in the solar neighbourhood each time an improved instrument has surveyed the skies (de Zeeuw et al. 1999; Bouy et al. 2015; Zari et al. 2018).

Recently, astronomers have begun to analyse large portions of the sky thanks to modern all-sky surveys which provide immense amounts of data with unprecedented accuracy combined with improved computational capabilities. This revealed that the formation of stars is a process that happens at the scale of hundreds of pc or even kpc (Alves et al. 2020; Großschedl, Alves and Meingast 2020; Beccari, Boffin and Jerabkova 2020). These results encourage future studies to focus on larger and larger areas of the sky.

This section is structured as follows. In Section 1.1.1 we review the main theories to explain the formation of a star. In Section 1.1.2 we enumerate the mechanisms of formation that have been proposed to explain the existence and fraction of brown dwarfs and free-floating planets. Finally, in Section 1.1.3 we present the initial mass function (IMF) as a proxy for star formation processes.

1.1.1 *The star formation process*

Giant molecular clouds are vast clumps of gas and dust where stars form and for that they are often referred to as stellar nurseries. They represent the coldest ($T \sim 10$ K) and densest ($n \gtrsim 100$ cm^{-3}) regions of the interstellar medium with masses of $\sim 10^5$ M$_\odot$ and sizes of ~ 50 pc (Mac Low and Klessen 2004). These structures remain isothermal (i.e. at constant temperature) as long as their heating and cooling processes are balanced. The *Herschel* spatial mission has uncovered the substructure of molecular clouds which is heterogeneous, fractal and made by a network of filaments and clumps. It is at the intersection between filaments, in the densest regions, where stars form (see André et al. 2014, Molinari et al. 2014, and references therein). The most nearby, well studied giant molecular clouds are in the regions of Taurus, Ophiuchus, and Orion.

The formation of stars is a multi-scale process which involves large structures such as the molecular clouds (tens of pc) down to the final stellar bodies (sub-AU scales). Figure 1.2 illustrates the multi-scale structure of a molecular cloud by successive zooms. At each scale, different physical processes (gravity, turbulence, magnetic fields, radiation pressure) intervene with different importance. To understand the complexity of star formation it is essential to combine multi-wavelengths observations (from radio to optical) with recent theories and numerical simulations. In this section, we review the main theories and observations related to the formation of stars. First, we introduce the early studies which set the conditions necessary for a cloud to undergo gravitational collapse. Then, we describe modern theories in which turbulence and gravity are the main forces that drive the star formation process and finally, we describe the stages from the formation of a protostar to a main-sequence star.

Conditions for gravitational collapse

In 1902, James Jeans investigated for the first time the conditions for a spherical cloud to collapse under hydrostatic equilibrium (Jeans 1902). Although he made several simplifying assumptions such as neglecting the effect of turbulence, rotation, and magnetic fields, his results are a good approximation to explain the formation of protostars. He considered small deviations from hy-

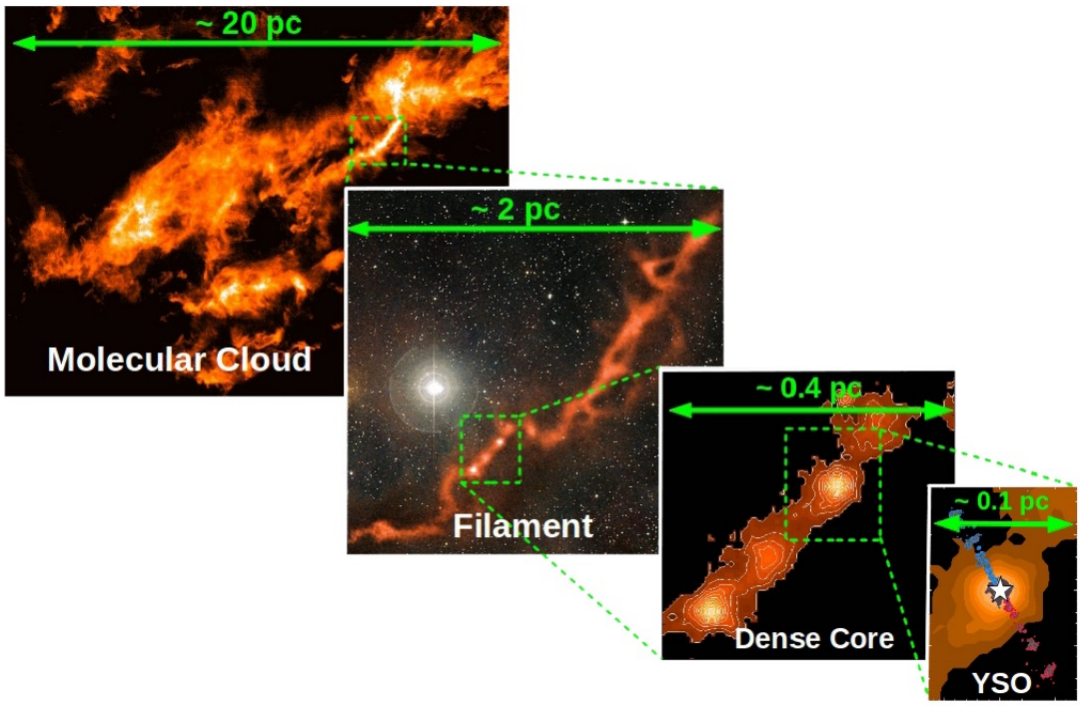

Figure 1.2. Illustration of the (sub-)structure of the star formation process in molecular clouds. From top left to bottom right: Image of the Taurus molecular cloud (Goldsmith et al. 2008); Filamentary structure of the molecular cloud (Hacar, Tafalla and Pierce-Price 2012); Fragmentation and formation of a dense core inside the filament (Hacar et al. 2013); Formation of a young stellar object through gravitational collapse of the core (Hacar et al. 2013). Adapted from Hacar (2013).

drostatic equilibrium and established the minimum mass of a core necessary to start a spontaneous collapse. This is the so-called Jeans criterion and is usually expressed as $M_c > M_{Jeans}$, where M_c is the mass of a cloud that collapses under its self-gravity and M_{Jeans} is the Jeans mass which depends on the temperature (T) and density (ρ_0) of the cloud.

$$M_{Jeans} \simeq \left(\frac{5kT}{G\mu m_H}\right)^{3/2} \left(\frac{3}{4\pi\rho_0}\right)^{1/2} \tag{1.1}$$

In this equation, k is Boltzmann's constant, G is the gravitational constant, μ is the mean molecular weight, and m_H is the mass of a hydrogen atom. One can find slightly different pre-factors on the expression of M_{Jeans} depending on the treatment of the perturbation problem, here we have considered the approach of Carroll and Ostlie (2007). A typical value of the Jeans mass in the solar neighbourhood is 1.1 $M_\odot$ (Kippenhahn, Weigert and Weiss 2012).

When we consider the pressure (P_0) on the core due to the surrounding interstellar medium (i.e. the giant molecular cloud in which the core is embedded) we arrive at an analogous critical mass known as the Bonnor-Ebert mass.

$$M_{BE} = \frac{1.18}{P_0^{1/2} G^{3/2}} \left(\frac{kT}{\mu m_H} \right)^2 \tag{1.2}$$

We note that the Jeans mass and the Bonnor-Ebert mass report similar critical masses in the solar neighbourhood.

Turbulent fragmentation and gravitational collapse

Starless cores are high-density regions placed at the intersections between filaments with no signs of collapse. Some of them are gravitationally unbound and eventually disperse. Others, are gravitationally bound and are likely to become unstable and collapse. These are the protostellar cores which are characterised by a central luminous source (Fig. 1.2 middle right illustrates an example of a protostellar core). In 1969, Larson and Penston led two independent and pioneering works to analytically describe the collapse of a core (Larson 1969; Penston 1969) which they found to be highly non-homogeneous. Initially, the central region collapses much faster than the outskirts and then, the protostar continues to contract at a lower rate. The main limitations of this theory are that the authors neglected the angular momentum and the magnetic field, two important ingredients according to observations. Later, Shu proposed another theory known as the *Standard theory* where the magnetic field was the dominant force to balance gravity (Shu 1977). However, this theory had a large number of observational problems, for example, the magnetic fields observed are significantly weaker than those assumed in the theory. We refer to the review of Mac Low and Klessen (2004) for a detailed discussion of the limitations of this theory.

Recent theories of star formation stress the importance of turbulence to explain the physics of molecular clouds. While at large scales turbulence increases the kinetic energy acting against gravitational collapse, locally, it compresses the gas fragmenting the original cloud into filaments and clumps. This process is known as gravoturbulent fragmentation (Mac Low and Klessen 2004; McKee and Ostriker 2007) and it can be a long process for massive clumps, with several fragmentation episodes. While the clump is contracting under constant temperature, the density increases allowing the clump to split (during isothermal contraction the Jeans mass becomes smaller, see Equation 1.1). The typical timescale of isothermal collapse is the free-fall time ($\sim 10^5$ yr, Carroll and Ostlie 2007).

The fragmentation process ends when the cloud becomes opaque (i.e. optically thick) and the heat generated due to the gravitational collapse can no longer efficiently cool by radiation. In consequence, this theory imposes a limit in the mass of the forming stars known as the opacity limit. For present star formation in the solar vicinity, the minimum mass formation due to gravitation fragmentation and collapse is 0.003 $M_\odot$ or $\sim$ 3 M_J[1] (Whitworth 2018) however, this limit has not been confirmed with observations. In this thesis, we make a huge effort to detect the lightest and coolest isolated objects in nearby star-forming regions to investigate this limit with observations.

From cores to stars

Once a stellar core is formed, it grows from the infall of envelope material. The protostar becomes a pre-main-sequence (PMS) star when it reaches a state of quasistatic contraction. Then, it continues to contract but at a much lower rate (the Kelvin-Helmholtz time). For instance, the PMS phase of a 1 $M_\odot$ star lasts around 40 Myr (Carroll and Ostlie 2007). During this phase, the main source of luminosity is the gravitational energy produced due to the gravitational contraction. The evolution of a PMS star is constrained by the physics of its interior which results in well-defined tracks in the Hertzsprung–Russell diagram (HR diagram) known as PMS evolutionary tracks.

During the first phases of quasistatic contraction, the PMS star has a convective envelope which can extend until the centre. This convective envelope prevents the radiation to escape efficiently and therefore, the PMS star suffers a decrease in its luminosity while it slowly increases its temperature. This behaviour describes an almost vertical line in the HR diagram known as the Hayashi track. With the increasing temperature, the star develops a radiative core that expands up to the surface of the star, allowing radiation to escape and increasing the luminosity. This is the end of the Hayashi track. Afterwards, the PMS star continues to increase its temperature due to the contraction until the temperature is high enough to trigger the first nuclear reactions at the centre. During this stage, the luminosity slightly rises as the PMS describes a roughly horizontal path in the HR diagram known as the Henyey track. The increase in luminosity is tightly related to the mass of the star, being nearly inexistent for massive stars and more important for low-mass stars. Eventually, the rate of nuclear reactions is so high that expands the central core. This effect is seen in the stellar atmosphere where the total luminosity and effective temperature decreases. When the central temperature is high enough to maintain the

1 Throughout this thesis we use the approximation that one Jupiter mass corresponds to 1 000 solar masses.

thermonuclear reaction of hydrogen at a sufficient rate to stop the gravitational collapse, the star is said to reach the Zero Age Main Sequences (ZAMS).

The evolution from the formation of a protostar to a main-sequence star is often divided into four evolutionary phases (see e.g. Lada 1987; Mac Low and Klessen 2004; Rosen et al. 2020, , and references therein), illustrated in Figure 1.3. While the PMS star evolves to the ZAMS, its temperature increases at the same time its configuration changes. In consequence, different evolutionary stages are best visible in certain regions of the electromagnetic spectrum as we describe in the following paragraphs. The spectral energy distribution (SED), i.e. the energy distribution as a function of wavelength, is an extremely useful parameter to characterise the evolutionary stage of young stellar objects and to detect the presence of discs.

- *Class* 0. At this stage, the protostar is fully embedded in its envelope. Due to the conservation of angular momentum, the envelope material starts to fall onto a disc which transports the material inwards where it is accreted by the protostar. The main source of luminosity comes from accretion and these objects are best observed at sub-millimetre and IR wavelengths.

- *Class I*. At this stage, the protostar starts to heat the surrounding dust. This phase is characterised by the formation of outflows in the direction of rotation (i.e. perpendicular to the plane of the disc) which dissipate the envelope. Class I objects are best observed in the IR. The protostar can also be seen in the optical but only in the direction of the outflows.

- *Class II* also known as *classical T Tauri*. At this stage, the envelope has either been accreted by the protostar or dissipated by outflows. The protostar crosses the so-called *birth line* and becomes a PMS star surrounded by a circumstellar disc. The spectrum of Class II objects is best described by a black body in the optical and shows an IR excess due to the presence of the disc.

- *Class III* also known as *weak-lined T Tauri*. At this stage, the PMS star is no longer accreting and the majority of circumstellar disc dissipates. The spectrum of the star is close to a black body and the PMS star is very close to the ZAMS.

Hitherto, we have described a simplified process in which a molecular cloud collapses to form a single star. In nature, stars form in groups where they are affected by the interactions with their neighbours and compete to accrete material (Bonnell et al. 2001). However, the impact of competitive accretion is still under debate (Krumholz, McKee and Klein 2005).

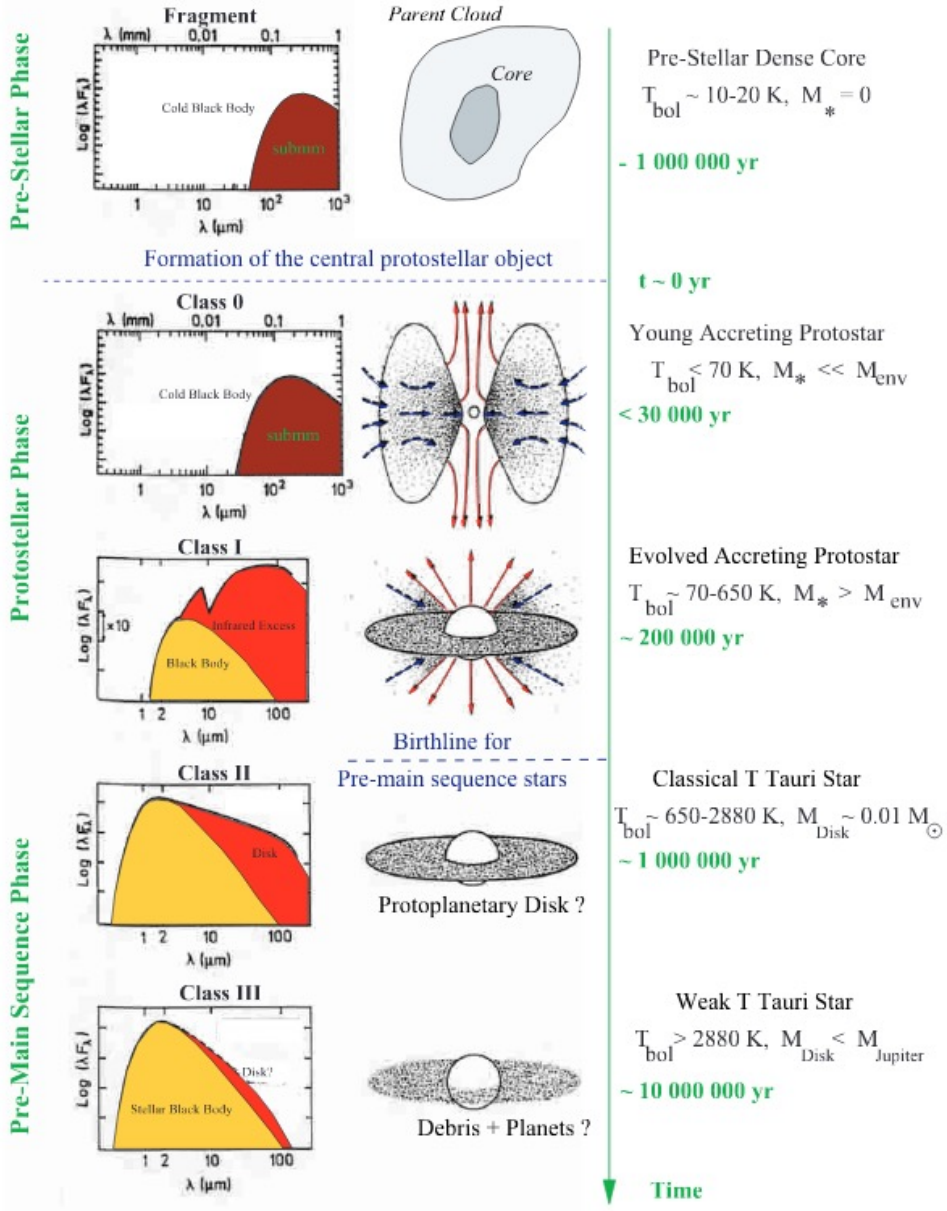

Figure 1.3. Schematic illustration of the evolution of a young stellar object from prestellar cloud core to a Class III object (middle column). The left column illustrates the evolution of the SED and on the right is indicated the bolometric temperature, the mass of the circumstellar material and the estimated age of each stage. From André (2002).

1.1.2 *Formation of substellar objects*

The existence of brown dwarfs (BD) was predicted in the 60s when Kumar (1962) and Hayashi and Nakano (1963) realised that there was a mass threshold below which a self-gravitating object cannot stably fuse hydrogen because the electron degeneracy pressure stops the gravitational collapse before the interior temperatures are high enough. These objects were initially named *black dwarfs* and it was later that the term *brown dwarf* was introduced by Jill Tarter in her PhD thesis (Tarter 1975). The first observational confirmation that such objects indeed exist came with the discovery of Gliese 229B, a brown dwarf orbiting an M dwarf (Oppenheimer et al. 1995). In the same year, a second brown dwarf was discovered, Teide 1, this time an isolated member of the Pleiades cluster (Rebolo, Zapatero Osorio and Martín 1995). The first brown dwarf spectroscopic binary was discovered soon after PPl 15 (Basri and Martín 1999). Since then, thousands of brown dwarfs have been detected composing a large sample to study and characterise these objects.

Despite the enormous progress achieved in the last decades on the understanding of the physics of brown dwarfs, there is still a large number of open questions. Among them, an accurate definition of the term brown dwarf. Nowadays, the boundary between stars and brown dwarfs is well established by the hydrogen-burning limit which, according to the models, occurs around 75 M_J. Objects above this threshold are massive enough to hold thermonuclear reactions on its interior and once they finish their hydrogen reservoir they become red giant stars and end their lives as a planetary nebula, expanding their outer shells. On the contrary, brown dwarfs never reach a temperature high enough to initiate the hydrogen burning in their interiors and spend their whole existence slowly contracting and cooling. Nonetheless, they can have partial or temporal nuclear reactions such as the deuterium burn. The boundary between brown dwarfs and planets is less clear. The Working Group on Extrasolar Planets of the International Astronomical Union (IAU) established the deuterium burning limit ($\sim$ 13 M_J) as a mass threshold to distinguish brown dwarfs from planetary-mass objects (Boss et al. 2007). At the same time, they recommended keeping the word *planet* for objects below the deuterium burning limit, with no thermonuclear reactions, and which orbit stars or stellar remnants. There is still debate on how to name objects lighter than 13 M_J which are isolated. Some of the names used in the literature are *sub-brown dwarfs*, *isolated planetary-mass objects*, *free-floating planets* (FFP) and through this thesis, we use the latter. Some authors have argued that the deuterium burning limit has little impact on the evolution of the source and suggested another division based on the formation mechanism (Chabrier 2005; Chabrier et al. 2014; Spiegel,

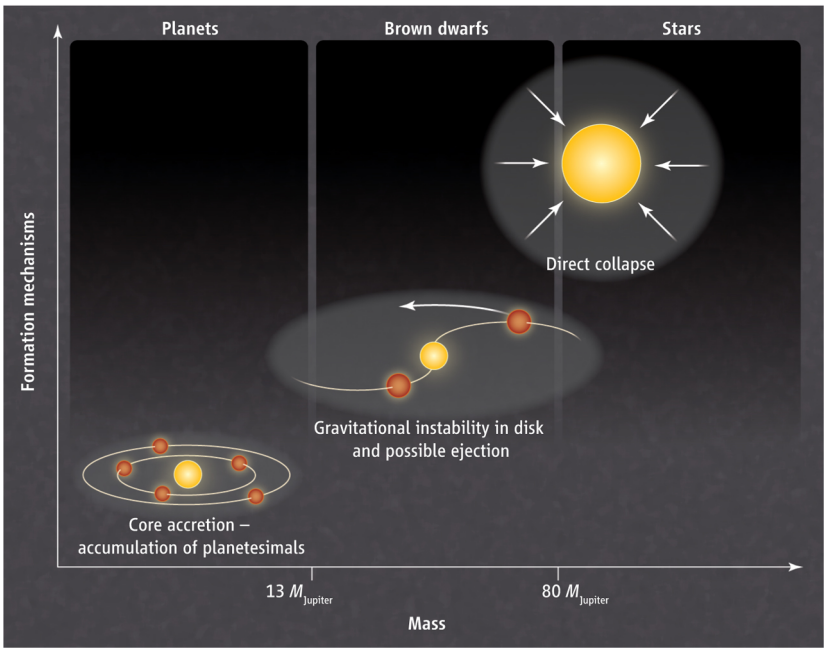

Figure 1.4. This figure illustrates the boundaries between stars, brown dwarfs, and planets. The mass criterion recommended by the IAU imposes a clear separation between these three categories (see text). However, a criterion based on the formation mechanism results in a blurred picture since several mechanisms are probably at work in each mass-defined category. From Basu (2012).

Burrows and Milsom 2011). In this perspective, brown dwarfs are substellar objects that form from a gravitational collapse like low-mass stars. This imposes a different low-mass limit for these objects, known as the opacity limit (> 3 M_J). In contrast, planets form in a bottom-up process by accretion of planetesimals and are always orbiting a more massive object. This second criterion to classify brown dwarf and planets implies a mass overlap between the two categories (see Fig. 1.4). Moreover, it is difficult to apply in practice because in general, we do not know the mechanism by which substellar objects are formed: some free-floating planets might indeed have formed around a star and have been dynamically ejected. For this reason, in this thesis, we follow the guidelines of the IAU and consider brown dwarfs all the objects with masses in the range $13 - 75$ M_J and free-floating planets the objects with masses < 13 M_J.

There is a puzzle that accompanies the understanding of brown dwarf formation: they are numerous (almost as much as stars) but have masses two orders of magnitude smaller than the average Jeans mass in star-forming clouds. To obtain lower Jeans masses, the densities of prestellar cores, parents of brown dwarfs, must be high (see Equation 1.1). Either or both, the accretion of material

has to stop before the prestellar core becomes a low-mass star. Several mechanisms have been proposed in the literature to explain the formation of low-mass stars and brown dwarfs (see e.g. Whitworth 2018). However, the feasibility and contribution of each of them are still under debate.

- *Turbulent fragmentation*. In this scenario, a prestellar core forms when the collision between turbulent flows creates a condensation unstable under the Jeans criterion. This is the main mechanism to form stars which we introduced in Section 1.1.1. André, Ward-Thompson and Greaves (2012) identified a prestellar core with a mass below the hydrogen-burning limit, indicating that brown dwarfs can form through gravoturbulent collapse. Still, it is unlikely that most brown dwarfs form by this mechanism (Lomax, Whitworth and Hubber 2016).

- *Disc fragmentation*. This mechanism occurs when the circumstellar disc surrounding a primary body (star or brown dwarf) fragments, becomes unstable and collapses. These fragments accrete material while they interact with the primary body to which they are bound and other fragments which may have formed in the same disc. Eventually, these interactions may end with the ejection of the lowest mass member. If the ejected body has enough material to resume accretion and sustain hydrogen nuclear reactions it becomes a low-mass star. Otherwise, it becomes a brown dwarf or a free-floating planet, depending on the final mass. According to Bate, Bonnell and Bromm (2002) this is the most common mechanism of brown dwarf formation.

- *Dynamical ejection*. Dynamical interactions among cores which are competing to accrete material from the same parent cloud may end with the ejection of the smallest bodies. If the accretion process stops before the cores are massive enough to begin the hydrogen-burning, they become a brown dwarfs (Reipurth and Clarke 2001). This mechanism predicts brown dwarfs with truncated discs, a small fraction of binaries, and peculiar kinematics resultant from the ejection.

- *Photo-erosion*. In this scenario, brown dwarfs form in the vicinity of an O-type star which radiation is strong enough to ionize and evaporate part of the outer layers of the core. At the same time, it adds pressure to the core so that the central part collapses to form a compact body (Whitworth and Zinnecker 2004). This mechanism can only explain the presence of brown dwarfs in the vicinity of O-type stars and thus cannot be the dominant channel.

The identification and characterisation of brown dwarfs and free-floating planets are fundamental to test the theories of star formation. The study of these objects will determine which is the minimum mass for star formation, the occurrence of different mechanisms to form objects of different masses, and the influence of the environment in the star formation process. Each formation mechanism predicts a different mass distribution therefore, the study of the IMF is an excellent way to test and quantify the contribution of these scenarios to the final population. Additionally, comparing the IMFs of different regions is important to evaluate the influence of the initial conditions on the final output.

1.1.3 *The initial mass function as a proxy for star formation*

The IMF is the mass distribution of stars arising from a star formation event, i.e. the mass distribution of a group of stars which formed together. It is an output of the star formation process and therefore helps to constrain the theories of star formation. In this section, we first introduce the different formulations of the IMF and describe its parameters. Then, we review the process to determine the IMF from observations, and finally, we discuss its origin.

Formulation of the IMF

The IMF was first introduced by Salpeter (1955) in the form of a power-law function.

$$\xi(\log m) \equiv dn/d\log m \propto m^{-\Gamma}, \tag{1.3}$$

where m is the mass of a star and n is the number of stars in a logarithmic mass bin between $\log m$ and $\log m + d\log m$. The mass function can also be defined in a linear mass scale,

$$\chi(m) \equiv dn/dm \propto m^{-\alpha}, \tag{1.4}$$

and the two exponents relate as $\alpha = \Gamma + 1$. Hereafter, we will use the logarithmic formulation. Integrating and normalising Equation 1.3, one can obtain the number of stars within a logarithmic mass range. In his work, Salpeter (1955) measured an exponent of $\Gamma \sim 1.35$, the so-called *Salpeter slope*, in the logarithmic mass range $\log m = [-0.4, 1]$ which corresponds to masses between 0.4 $M_\odot$ and 10 $M_\odot$.

Afterwards, Miller and Scalo (1979) proposed a different description of the IMF as a log-normal function.

$$\xi(\log m) = \frac{A}{\sqrt{2\pi\sigma}} \exp\left[-\frac{(\log m - \log m_c)^2}{2\sigma^2}\right] \tag{1.5}$$

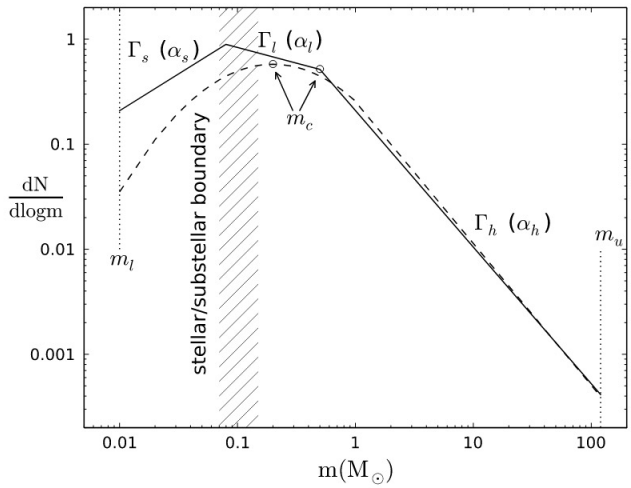

Figure 1.5. Illustration of the key aspects of the IMF parameterised as a piecewise series of power-law segments (solid line, e.g. Kroupa 2001) or a log-normal at low masses with a power-law tail at high masses (dashed line, e.g. Chabrier 2003). From Hopkins (2018).

Where m_c corresponds to the mean mass and $\sigma^2 = \left\langle (\log m - \langle \log m \rangle)^2 \right\rangle$ to the variance in $\log m$. This new formalism solved the divergence of the Salpeter function in the low-mass regime however, it under-represents the massive star population. More modern forms adopt a log-normal distribution at low-masses and a power-law above a solar mass (Chabrier 2003, 2005) or a series of power-law segments (Kroupa 2001, 2002). These two latter forms lead to similar results (see Fig. 1.5) and the main difference comes from the physical interpretation.

A power-law relationship between two quantities implies that a relative change in one of them results in a proportional change in the other, no matter their initial size. In consequence, a power-law IMF suggests that the star formation process is controlled by a scale-free process such as the turbulence (McKee and Ostriker 2007; Padoan et al. 2019). When several independent mechanisms (e.g. competitive accretion, sub-fragmentation of the cores, multiplicity) regulate the star formation process, the central limit theorem establishes that the IMF adopts the shape of a log-normal function. Chabrier (2003) proposed that the formation of massive stars is mainly dominated by turbulence (power-law IMF) and at lower masses, other mechanisms become relevant (log-normal IMF).

The IMF is characterised by the following parameters, illustrated in Figure 1.5.

– m_l is the low-mass limit. In the observational determinations of the IMF this parameter depends on the magnitude limit of the survey and the proximity of the region. Recent studies determined the IMF down to $m_l \sim 0.01$ M$_\odot$, well in the substellar regime (see Fig. 1.6).

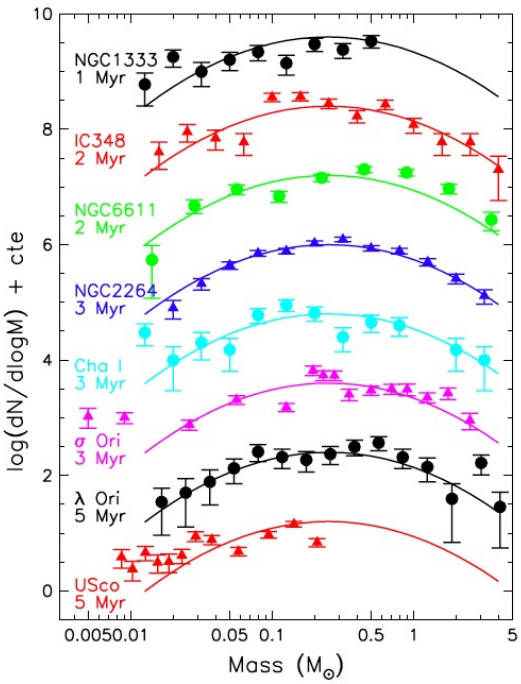

Figure 1.6. Recent IMF estimates for eight star-forming regions: NGC 1333 (Scholz et al. 2012a), IC 348 (Alves de Oliveira et al. 2013), NGC 6611 (Oliveira, Jeffries and van Loon 2009), NGC 2264 (Sung and Bessell 2010), Cha I (Luhman 2007), σ Ori, (Peña Ramírez et al. 2012), λ Ori (Bayo et al. 2011), USC (Lodieu 2013). The error bars represent the Poisson error for each data point. The solid lines are not a fit to the data but the log-normal form proposed by (Chabrier 2005) for the IMF, normalised to best follow the data. From Offner et al. (2014).

- m_u is the high mass limit. Typical values for this parameter in the solar neighbourhood are $m_u \sim 5$ M$_\odot$.
- m_c is the characteristic mass which corresponds to the peak of the log-normal form or to the turn over mass where the slope of the power-law changes. Common values for the m_c are of ~ 0.08 M$_\odot$ for single star IMFs and of $0.2 - 0.3$ M$_\odot$ in multiple system IMFs (Chabrier 2003).
- In the case of a power-law IMF, $\alpha_s, \alpha_l, \alpha_h$ are the slopes in the substellar, low-mass, and high mass regimes, respectively.

Observational determination of the IMF

The IMF is not a directly measurable quantity since the star formation process occurs on different timescales depending on the mass of the star. While massive stars form and evolve very quickly ($\lesssim 1$ Myr), low-mass stars take tens of

million years to reach the main-sequence. Additionally, these later are sensible to the dynamical evolution and may eventually be ejected through dynamical processes. Then, to study the IMF it is important to consider young systems where the most massive stars have not yet died and the least massive have not yet been evaporated (by dynamical interactions). Eventually, we never reach to measure the IMF but the present-day mass function (PDMF) i.e. the mass function observed in the present which is the result of the IMF plus the first stages of the stellar and dynamical evolution. Additionally, since in general, we do not resolve multiple stars, what we measure is the present-day system mass function (PDSMF).

There are two common approaches to determine the mass function from observations namely, using a sample of field stars or using a sample of cluster members. The first has the advantage that field stars are much more numerous than members in a cluster. However, the members of a cluster were born in the same starburst and thus, they share the same age and distance. These two parameters are best constrained for a group of coeval stars rather than for individual isolated stars. Knowing the age and distance with precision is fundamental to transform the observed magnitudes to masses. In this thesis, we chose the latter approach and considered different young clusters and star-forming regions to determine the mass function.

The determination of the mass function from observations is a multi-step process affected by the uncertainties of observations and models. In the following paragraphs, we enumerate the steps needed to obtain the IMF from a cluster population making a special emphasis on the major difficulties and limitations.

1. *Sample selection*.

   This is a crucial step which often is overlooked. If the sample of members is highly contaminated by field stars, incomplete, or affected by observational or membership selection biases then, it no longer represents the population which was formed together in the same starburst. For example, if the cluster is mass segregated it is important to make a census encompassing the outskirts of the cluster (Bastian, Covey and Meyer 2010; Jeffries 2012; Offner et al. 2014). Besides, nearby clusters have sometimes large apparent sizes, resulting in projection effects that can complicate the membership analysis. We are interested in studying young clusters so that the dynamical evolution has not yet erased all memory of the IMF shape and that the PDMF is still fairly close to the IMF. In practice, this means that we are dealing with regions of a few million years which are often still highly embedded and hence hard to observe. Other observational

limitations we face during the sample selection are that bright stars hide the faintest stars around them and the difficulty to separate close binaries.

2. *Magnitude distribution*.

   The magnitude distribution is the direct observable that we obtain once we have selected a list of members. Since it does only depend on the census, it is valid as long as the membership is not biased.

3. *Luminosity function*.

   The total luminosity of a star is not a direct observable but a function of the apparent magnitude, the distance, and the bolometric correction. The *Gaia* mission has provided parallaxes for a large sample of sources making it possible to obtain precise distances. For sources beyond the *Gaia* detection limit, the simplest approximation is to use the mean distance of the cluster and its depth as the corresponding uncertainty, which can be fairly large in some cases. The bolometric correction depends on stellar evolutionary models which at young ages are still uncertain (Baraffe et al. 2002).

4. *Present-day system mass function*.

   The only way to measure the mass of a star with precision is in binary systems for which the orbital parameters are known. In practice, this is only possible in very few cases and the alternative is to use mass-luminosity relationships which are strongly age-dependent and still uncertain and uncalibrated at young ages and for ultracool objects. The age is another difficult parameter to establish unless there is a group of coeval stars which is the case of open clusters. However, large star-forming regions might show important age spreads complicating, even more, the analysis. The majority of stellar systems are unresolved in the images and we are counting one massive star instead of several less massive stars. This effect can significantly alter the shape of the mass function (Kroupa 2001; Chabrier 2003) and only when it is corrected, one can obtain the single-star PDMF. This last step is out of the scope of our work and the final product of our analysis is the PDSMF.

5. *Initial mass function*.

   The mass distribution just after the stellar burst (i.e. the IMF) only resembles the PDMF for very young systems. Otherwise, the massive stars evolve and die quickly and the low-mass stars are ejected through dynamical interactions. Therefore, one can choose to study the mass function in young clusters or correct for the early cluster evolution. Such a correction

requires a fine knowledge of the early evolution of the cluster, which is in general poorly known.

Over the last decade, many studies have been devoted to measuring the mass function in different clusters and associations, making a strong effort to reach low-mass objects. Figure 1.6 illustrates some of the most representative studies. We see that the majority have a low-mass limit at $0.01 - 0.02$ $M_{\odot}$, hardly reaching the planetary-mass objects. Many authors report Poissonian or Gehrels (Gehrels 1986) errors in their luminosity and mass functions. These latter are more suitable for small number statistics although any of them include the (often many) observational uncertainties or the membership selection errors (contamination and incompleteness). Providing representative uncertainties of the mass function is as important as the function itself to compare with other studies and see if there are statistically significant differences. A robust study of the contamination is especially important for purely photometric studies which are often severely contaminated (typically 30% or more) in the ultracool regime. In this thesis, we address all these drawbacks to produce continuous mass functions over the widest possible mass range including the substellar and planetary mass regimes, with the most rigorous and realistic uncertainties possible.

Origin of the IMF

One of the most fundamental and controversial questions in astrophysics is understanding which is the origin of stellar masses (Offner et al. 2014). There is not yet a consensual answer to this question and the ideas proposed can be divided into two main groups. While some studies suggest that the origin of stellar masses is a deterministic process which depends only on the mass of the local reservoirs (Padoan and Nordlund 2002; Hennebelle and Chabrier 2008; Hopkins 2012), others argue that stellar masses are stochastic and depend on the dynamical interactions and competitive accretion (Zinnecker 1982; Bonnell et al. 2001; Bate, Bonnell and Bromm 2003; Clark, Klessen and Bonnell 2007). In other words, theories supporting a deterministic IMF defend the idea that the final mass of a star is mainly determined in the gaseous phase where turbulence plays a major role and other processes such as stellar winds, the division into binary and multiple systems, and accretion are second-order effects. If the mass of a star is indeed determined by the amount of gas on its parent reservoir, then, an important part of understanding the IMF comes from the understanding of the core mass function (CMF), i.e. the distribution of prestellar cores. Several authors determined from observations the CMF of different regions and found a distribution with a similar shape to the IMF but shifted towards higher masses.

This offset is interpreted as a star formation efficiency in which $\sim 30\%$ of the core mass ends forming the star (Motte, Andre and Neri 1998; Alves, Lombardi and Lada 2007; André et al. 2010; Di Francesco et al. 2020). While at higher masses the similarity between the CMF and the IMF seems well established it has not yet been proved how the CMF can explain the change in slope at lower masses and the characteristic mass of the IMF.

1.2 ASTROMETRIC AND PHOTOMETRIC SURVEYS

Astronomical observations are a key tool in our understanding of the Universe. The study of the electromagnetic radiation emitted by astronomical bodies gives us precious information on the characteristics of these bodies (e.g. luminosity, temperature, kinematics, composition). In practice, there is no instrument capable to detect the radiation over the entire electromagnetic spectrum simultaneously and different instruments are devoted to the study of different wavelength ranges. At the same time, astrophysical processes are best observed in a spectral window set by their temperature and the amount of energy associated with the phenomena. For instance, the most violent events in the Universe are seen as Gamma rays. Observations in the visible are the oldest and simplest but still in the present are used for pioneering science of Galactic archaeology among many others. Star-forming regions are best observed in the IR where the radiation can travel through the surrounding clouds of gas and dust. This thesis is focused on the study of star-forming regions and young clusters and for that, the observations used are in the optical and in the near-IR wavelength range.

Astronomical observations can also be distinguished according to the technique used to collect and measure the light. Those which precisely measure the positions and motions of celestial bodies are called astrometric observations. Photometric observations measure the flux or intensity of light of the radiation. These observations make use of a filter which limits the light received to a range of wavelengths. Spectroscopic observations make use of a device which disperses the light according to its wavelength. Spectra are very rich since they can reveal many properties of stars such as their chemical composition, temperature, density, mass, distance, luminosity, and relative radial motion using the Doppler shift. The major drawback of spectroscopy is that it is very time demanding. It can only be obtained for small samples and is often not possible for very faint objects. In this thesis, we combine astrometric, photometric, and spectroscopic observations to gather the largest amount of information possible.

In this section, we present the two main surveys used in this thesis namely, the *Gaia* mission and the COSMIC DANCe project. The first is a space mission with

the great advantage of not being affected by the atmosphere. The latter is based on images obtained at ground-based observatories and therefore suffers from the atmospheric turbulence but reaches greater sensitivities. In the following, we describe the content, completeness, and limitations of these two surveys.

1.2.1 *The Gaia mission*

Gaia is a space mission launched by European Space Agency (ESA) on 19$^{\text{th}}$ December 2013. After six months of commissioning period, the satellite started the nominal mission initially planned to last five years[2]. Since then, it has been scanning the skies to produce a 3D map of the Milky Way of more than one billion stars, approximately 1% of the Galactic stellar population. The ultimate objective of the mission is to study the structure, origin, and evolution of the Milky Way. Additionally, it aims at providing detailed information on star formation and evolution in our Galaxy, stellar multiplicity, substellar objects and exoplanets. Beyond these primary targets, *Gaia* also observes many solar system objects, extragalactic sources and quasars (Gaia Collaboration et al. 2016).

The *Gaia* catalogue is released in incremental stages, each new release including a longer time baseline improving the precision and increasing the contents. The most recent catalogue at the time of writing this thesis is the *Gaia* Data Release 2 (*Gaia* DR2), released on the 25$^{\text{th}}$ April 2018 and based on 22 months of observations (Gaia Collaboration et al. 2018c). The most important product of the *Gaia* catalogue for the present work is the five-parameter astrometric solution (2D positions on the sky, parallaxes, and proper motions) for more than one billion sources with a limiting magnitude of $G < 21$ mag and a bright limit of $G \sim 3$ mag. The *Gaia* DR2 astrometric uncertainties are strongly dependent on the magnitude, and some typical values are < 0.7 mas in parallaxes and $\lesssim 1$ mas yr^{-1} in proper motions. *Gaia* observes in the optical ($300 - 1\,100$ nm) and provides the photometry in the the *Gaia* DR2 photometric system, i.e. G, G_{BP}, G_{RP} (Jordi et al. 2010; Evans et al. 2018). Additionally, the *Gaia* DR2 catalogue includes the median radial velocities for more than 7.2 million stars with a magnitude $4 < G < 13$ mag and an estimate of their effective temperature (between $3\,550 < T_{\text{eff}} < 6\,900$ K). Depending on the brightness and effective temperature of the source, the median precision in the radial velocity varies between $0.2 - 2.5$ km s^{-1}. For a limited amount of sources, the catalogue also includes additional information such as the effective temperature, the line-of-sight extinction A_G, the reddening E(BP-RP), the luminosity and radius. Among the

2 In 2018 the mission was extended to 2020, with an additional indicative extension until 2022 (https://sci.esa.int/web/director-desk/-/60943-extended-life-for-esas-science-missions).

advantages of spatial missions are better accuracy, sensitivity, and sky coverage. This is the largest and most homogeneous sample available to date.

1.2.2 *The COSMIC-DANCe project*

The COSMIC DANCe project[3] (DANCe standing for Dynamical Analysis of Nearby ClustErs) started as a survey to map nearby (< 500 pc), young (< 500 Myr) associations and open clusters (Bouy et al. 2013). With wide-field, ground-based images we can detect objects several orders of magnitude deeper than *Gaia* and study the least massive objects down to a few Jupiter masses. Additionally, the stars in the youngest star-forming regions are still embedded in the molecular cloud where the extinction is high and *Gaia*, which operates in the visible, is mostly blind. On the contrary, the DANCe survey combines images in the visible and the IR. These latter are especially suited for regions with a significant amount of extinction. Figure 1.7 shows a composite image of the central part of IC 4665 where a large number of faint sources escape the *Gaia* detection limit but are clearly detected in the DANCe survey.

The DANCe survey analyses a massive amount of wide-field ground-based images (several thousands, depending on the region) in the optical and IR to provide catalogues of proper motions and multi-filter photometry for millions of sources. The coverage of the DANCe survey is far from uniform with a spatially uneven pattern which also depends on the photometric filter (see e.g. Fig. 4.1 and Fig. 1 from Bouy et al. 2013). In consequence, the magnitude limit and completeness in each band strongly depend on the region under study and the amount of data available. Something similar happens with the proper motions and, in this case, it is of uttermost importance to have images with a long time baseline to have good precision. In both cases (photometry and proper motions) the selection function is very complex and we did not attempt to characterise it. The typical uncertainties in proper motions in DANCe are of $\lesssim 1$ mas yr^{-1}.

The main goal of the DANCe project is to study the mass function down to the least massive objects. Besides the observational challenges related to the detection of the faintest objects, the membership classification is a major difficulty and is a classical example of a causality dilemma where we need to find at the same time the members that define a cluster and the cluster properties. A first attempt to solve this issue was presented by Sarro et al. (2014). Combining this new algorithm with the DANCe catalogue for the Pleiades the authors increased the number of known members by a 40% and multiplied

3 http://www.project-dance.com/

Figure 1.7. Composite image of the centre of IC 4665. The red circles indicate *Gaia* detections. The COSMIC-DANCe image goes well beyond the *Gaia* sensitivity and detects many faint sources.

by five the number of substellar members (Bouy et al. 2015). However, this algorithm presented two major drawbacks. First, the sources with missing data (i.e. sources which are not observed in all the photometric bands) could not be used to model the cluster although a final membership probability was eventually computed for them. This can introduce biases in the model since typically the missing data are not randomly distributed but are more frequent among the faint sources. Second, the desired degree of completeness or contamination is a free parameter which has to be set at the beginning by the user. Nevertheless, Sarro et al. (2014) showed that the results obtained were not significantly affected by that parameter. To overcome these difficulties, Olivares et al. (2018) developed a method based on Hierarchical models. In this framework, the observations in terms of uncertainties, correlations, and missing data are better modelled. Besides, it is a fully Bayesian model which provides posterior distributions for the parameters of the model (e.g. the luminosity function) and no longer needs to fix the completeness/contamination rate. With this new algorithm, also applied to the same observations of the Pleiades, the

authors found 10% of new members. The main drawback is that this method is significantly more computationally expensive.

1.3 MOTIVATION AND GOALS OF THE THESIS

In this introductory chapter, we stated some of the open questions regarding the stellar and substellar formation theories and have introduced the IMF as a fundamental observational parameter to constrain these theories. However, determining the mass function with precision over a wide mass range is extremely challenging, especially in the low-mass regime. To date, very few studies have attempted to determine the mass function of substellar objects and usually, the uncertainties are simplistically estimated, probably underestimating the effects of incompleteness and missing data. In this thesis, we took advantage of the DANCe project which has acquired deep, wide-field images over a large time span and complemented it with observations that were obtained during the thesis. With these data, we built a precise astrometric and photometric catalogue of different young clusters and star-forming regions. We analysed it with modern Bayesian statistical tools to provide a comprehensive list of candidate members with which we determined the mass function. Our Bayesian statistical framework allowed us to propagate the observational uncertainties throughout the full analysis until the mass function.

The age of some young associations and star-forming regions is not yet well constrained and, in some cases, there is possibly a significant age gradient among the members. That introduces large uncertainties in the mass determinations since the mass-luminosity relationship is strongly age-dependent. Among the methods existent to determine stellar ages, the kinematic or dynamic ages have the great advantage of being independent of evolutionary models, which are known to be less reliable at young ages. For that, we improved and extended a dynamical traceback age method I developed during my Master's degree.

The candidate members of the associations we obtained are also very useful for many other studies. Our samples contain tens or hundreds of substellar objects which are fundamental to constrain the evolutionary models at these young ages. Since our samples are young, many objects are still surrounded by discs which can help to constrain the planetary formation and early evolution theories. Because they include the least massive objects, which are the most sensitive to dynamical interactions, our samples are particularly useful for follow-up studies of the spatial distribution, mass segregation, and kinematics. These diagnostics are key to constrain the formation theories and, in particular, to distinguish or quantify the effects of the initial conditions and the early evolution of the final population.

1.4 THESIS OUTLINE

This thesis is organised in two main parts. The first one is devoted to obtaining the mass function of different regions. In Chapter 2, we present the observations we made in the context of the DANCe project, the astrometric and photometric catalogues we obtained and the statistical tools used to select members. We also present our strategy to convert our observed magnitude distributions to luminosity and mass functions, and how we propagated the observational uncertainties. In Chapter 3 we show the results obtained in the 30 Myr open cluster IC 4665 and in Chapter 4 we present the results of the USC association and the ρ Oph star-forming region which have an age between $1 - 10$ Myr. In the second part, we present a series of complementary studies related to the stellar formation and early evolution. In Chapter 5 we study the dynamical age of the young local association β Pic and in Chapter 6 we search for debris discs in the IC 4665 open cluster using the sample we determined in Chapter 3. Finally, in Chapter 7 we summarise the main results obtained in this thesis, present our conclusions, and future perspectives. In the end, we include an Appendix complementing the results presented in Chapter 5 (App. A), another with the queries used to download the data (App. B), another with additional tables (App. C), and a french summary of the thesis (App.D).

Part II

ORIGIN OF THE INITIAL MASS FUNCTION

This part is devoted to the study of the mass function as a parameter to constrain the stellar and substellar formation process. The strengths of our work compared to previous studies are:

- We compiled a large dataset of deep, wide-field images with a long time span (up to 20 years). This allowed us to compute multi-wavelength photometry (in the optical and IR) and proper motions for millions of objects with a magnitude limit up to ~ 5 magnitudes deeper than *Gaia*.
- We use a robust statistical method to compute membership probabilities combining all the information available, i.e. astrometry, photometry, and the corresponding uncertainties.
- Our methodology propagates consistently the observational uncertainties from the membership algorithm to the magnitude distribution and mass function and deals properly with censored data.

The IMFs we determine constitute a robust observational diagnostic to quantify the importance of different mechanisms of star formation. This is especially important in the substellar regime where several mechanisms are under debate and where little observational data is available to date.

> ***The first part of this thesis is divided into three chapters. In Chapter 2, we describe our methods to obtain the compilation of an observational catalogue, the membership analysis, and the determination of absolute magnitudes and masses to finally, derive the mass and luminosity functions. The methodology is then applied successively to an open cluster and a star-forming region in the following chapters. In Chapter 3, we study the 30 Myr open cluster IC 4665 which is located at a distance of 350 pc. At this age, the gas and dust from the parent molecular cloud have been dispersed and the extinction is low. This facilitates the detection of the stars and the analysis of their membership. In Chapter 4, we analyse the USC association and the ρ Oph star-forming region located at 140 pc and 120 pc respectively and which have an age between 1–10 Myr. Their proximity and youth facilitate the observation of the least massive members, well beyond the detection limit achieved in IC 4665. However, this region has a large apparent size in the sky ($17^\circ \times 13^\circ$) which adds complexity to our analysis. Additionally, the area of ρ Oph is still embedded in the parent molecular cloud, hindering the detection of all the most extinct members.***

2 STRATEGY

In this chapter we describe the methodology used in the first part of this thesis to i) build an astro-photometric catalogue of nearby star-forming regions and open clusters (Sect. 2.1), ii) identify the members among the vast number of Galactic and extragalactic sources (Sect. 2.2), iii) infer individual distances and masses which in turn allow us to estimate the luminosity and mass functions (Sect. 2.3).

2.1 THE DANCE CATALOGUE

The strategy used to prepare the DANCe catalogue was first introduced in Bouy et al. (2013) to survey the Pleiades cluster. Later, it was successfully applied to other regions with some improvements (Olivares et al. 2019; Miret-Roig et al. 2019). In short, this method consists of first gathering the largest amount of raw astronomical images covering the area of the sky of interest. Then, this vast amount of data has to be processed and finally, the position, proper motion, and photometry of each source can be measured in all the filters available.

2.1.1 *Compilation of wide-field images*

We did an effort to compile the most complete dataset in each of the regions we study. We aimed to have a large spatial coverage so that we can study also the outskirts of the association and a large time coverage to have the best precision possible in proper motions. For that, we combined our own observations with all the images found in various public in archives.

New wide-field images

The DANCe project started in 2011 (Bouy et al. 2011) and since then observational proposals have been successfully accepted in several observatories:

– The Dark Energy Camera (DECam) mounted on the 4 m telescope Blanco in Cerro Tololo Inter-American Observatory (CTIO)

- The Wide Field Camera (WFC) mounted on the Isaac Newton Telescope (INT)
- The MegaCam from the Canada-France-Hawaii Telescope (CFHT)
- The Wide-field InfraRed Camera (WIRCam) from the CFHT
- The Newfirm mounted on the 4 m telescope Mayall in Kitt Peak National Observatory (KPNO). This telescope is a twin of the Blanco telescope.
- The SuprimeCam from Subaru
- The Hyper Suprime-Cam (HSC) from Subaru

All the observations were carried in dithering mode with sequences of overlapping exposures at slightly shifted positions in the sky. This technique facilitates the elimination of cosmic rays and other random sources of noise present in the images. It is also fundamental to derive an accurate distortion map for the instrument, using the overlapping plate method described in (Bouy et al. 2013). I personally participated to or led the observations at the telescope during the nights of 28–30 December 2017 with DECam at CTIO, 15–20 June 2019 and 5–11 November 2019 with the WFC at the INT.

Archival data

To complement our own observations, we searched for wide-field images of the regions of interest in the optical and IR in public archives. The raw and calibration images were downloaded and processed together with our observations. Here we list the public archives that we queried.

- The European Southern Observatory (ESO) archive for the Paranal and La Silla telescopes
- The National Optical Astronomy Observatory (NOAO) archive for the CTIO and KPNO telescopes
- The Palomar Transient Factory (PTF) archive hosted at the NASA/IPAC Infrared Science Archive (IRSA)
- The Canadian Astronomy Data Centre (CADC) archive for the CFHT telescope
- The Isaac Newton Group (ING) archive for the INT telescope
- The WFCAM Science Archive (WSA) for the United Kingdom Infra-Red Telescope (UKIRT) telescope

– The Subaru-Mitaka-Okayama-Kiso-Archive (SMOKA) science archive for the Subaru telescope at the National Astronomical Observatory of Japan (NAOJ)

Image processing

In all cases except for MegaCam, WIRCam, PTF, DECam, HSC, and the Wide Field Camera (WFCAM) images, the raw data and associated calibration frames were downloaded and processed using standard procedures with an updated version of *Alambic* (Vandame 2002), a software suite developed and optimised for the processing of large multi-CCD images. The MegaCam images, processed and calibrated with the *Elixir* pipeline, were retrieved from the CADC archive (Magnier and Cuillandre 2004). The WIRCam images, processed with the official *'I'iwi* pipeline, were retrieved from the CADC archive. In the case of DECam, the images processed with the community pipeline (Valdes, Gruendl and DES Project 2014) were retrieved from the NOAO public archive. The pipeline-processed PTF images were downloaded from the Infrared Processing and Analysis Center (IPAC) archive. UKIRT images from the UKIRT Infrared Deep Sky Survey (UKIDSS) and UKIRT Hemisphere Survey (UHS) surveys (Dye et al. 2018) processed by the Cambridge Astronomical Survey Unit were retrieved from the WSA. Finally, the HSC raw images were processed using the official HSC pipeline (Bosch et al. 2018).

2.1.2 *Astrometric solution*

We performed the astrometric calibration as described in Bouy et al. (2013) with the updates listed in Olivares et al. (2019). Here we briefly review the main steps and refer to these articles for further details.

1. First of all, we standardised all the images providing the appropriate keywords in the headers. These include the detector gains, saturation levels, the approximate position and scale of the pixel grids on the sky, the dates and times of observation, exposure times, and airmass.

2. The images in the red optical bands (typically i, z and Y) often display fringing patterns which difficult the source detection. To correct these patterns we used fringing maps obtained by median-combining several images pointing to different regions of the sky with the same instrument and filter. This way, the stars are removed from the fringing map, only the fringes remain and can be subtracted from the scientific images.

3. We used the MaxiMask software (Paillassa, Bertin and Bouy 2020) to detect problematic pixels (cosmic rays, dead/hot pixels, satellite trails, saturated stars and associated blooming artefacts, diffraction spikes) and problematic astronomical images (e.g. tracking lost). We applied this tool only in the observational dataset described in Chapter 4 since our analysis in Chapter 3 was done before the publication of MaxiMask.

4. We computed the point spread function (PSF) with PSFex (Bertin 2013) for each image individually using the point sources with high signal-to-noise ratio (SNR). PSFex can model smooth variations of the PSF along the focal plane.

5. We extracted all the sources which occupy more than three pixels and which deviate from 1.5σ from the local background with SExtractor (Bertin and Arnouts 1996). SExtractor produces a catalogue of the flux and position of each source using the empirical PSF computed with PSFex. The uncertainties for photon-noise dominated sources were taken directly as the SExtractor's 1σ fitting uncertainties. For bright sources, the uncertainties are dominated by the relative variations in position caused by the atmospheric turbulence and they were estimated as described in (Bouy et al. 2013). The deblending of nearby sources is difficult to estimate individually and we added a 0.1 pixel error in quadrature to all the sources flagged as "blended" by SExtractor.

6. We computed the global astrometric solution with SCAMP (Bertin 2006). This tool uses the overlapping region of pairs of catalogues to minimise the quadratic sum of the differences in position between detections of the same source. SCAMP then computes and corrects the distortions of each instrument. Between different runs, detectors are usually unmounted from the telescope and this process modifies the distortion patterns. For this reason, we defined an instrument as a unique combination of detector, filter, and observing run. Once we had the final astrometric solution, we computed the differences between the positions in the *Gaia* DR2 catalogue and the ones we obtained. Depending on the instrument, the average 3σ residuals in individual epochs are of the order of $12 \sim 25$ mas for high signal-to-noise (photon noise limited) sources. This value is indicative of the precision of our measurements.

7. We computed the proper motions of all the sources with at least two detections with SCAMP. This software computes a linear fit of the source position as a function of the observation date. We neglected the effect of the parallax because the images were taken over a short time of the year (when

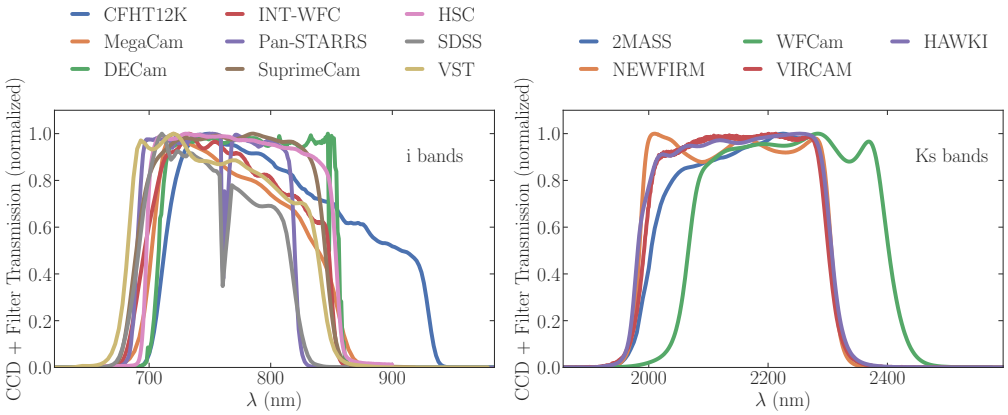

Figure 2.1. Transmission curves of the *i* and *Ks* filters used in the DANCe catalogue of USC.

the region under study is best visible). SCAMP can detect and filter outliers during the fitting process and the goodness of the fit is assessed with the χ^2 estimator. The proper motions we obtained with this procedure are relative and display an offset respect to the Geocentric Celestial Reference System (GCRS). We estimated the offset by computing the median offset between our values and the *Gaia* DR2 proper motion measurements after rejecting outliers using the modified Z-score (Iglewicz and Hoaglin 1993). We found offsets of $(\Delta\mu_\alpha \cos\delta, \Delta\mu_\delta) = (1.70, 4.48)$ mas yr^{-1}. We estimated the uncertainty on this offset using a bootstrap and we found it was negligible (< 0.003 mas yr^{-1}). Given the superiority and robustness of the *Gaia* measurements compared to our ground-based measurements, the *Gaia* DR2 proper motion measurements were always preferred when available.

2.1.3 *Photometric solution*

We computed the photometric solution for each photometric instrument with SCAMP. Here we defined a photometric instrument as a combination of detector and filter. To maximise the photometric coverage of our survey we combined the measurements obtained with filters from different instruments. This comes at the cost of photometric precision since the different camera filters often have slightly different transmission curves (see Fig. 2.1) which increase the errors in the photometry due to colour-terms. We estimated that these errors are of the order of $10 - 15\%$ at most. As we will see, the membership analysis is sensitive to missing photometric measurements, and the gain in photometric

completeness largely compensates this extra level of photometric uncertainty. These photometric errors are also mitigated since we compute the average of all photometric measurements obtained with all the cameras, hence averaging over all the filters. The photometric solution was computed by minimising the quadratic sum of the differences in overlapping areas from pairs of images with the same photometric instrument and exposure time. In this process, colour terms were ignored and the only free parameters were the magnitude zero-points. These were computed by direct comparison of the instrumental `MAG_AUTO` magnitudes from SExtractor with an external catalogue:

- J, H, Ks images were tied to the Two Micron All Sky Survey (2MASS) catalogue
- g, r, i, z, y images were tied to the Panoramic Survey Telescope and Rapid Response System (Pan-STARRS) PS1 first release

We median-combined all the images obtained with the same camera and in the same filter to build a deep stack and extracted the corresponding photometry. This allowed us to significantly improve the sensitivity in all filters and to recover or improve the photometry of faint sources obtained in the individual images.

In the case of USC, we decided to perform the astrometric analysis on the stacked images as well. We, therefore, stacked the individual images corresponding to a single epoch (usually on a nightly basis), producing intermediate stacked images significantly deeper than the individual images. The astrometric precision in these images is, in general, not as good as in the individual images, since the PSF can become more complex. But we find that it is nevertheless good enough for our purpose. The gain in sensitivity is indeed significant and allows us to detect and measure the proper motion and photometry of sources far fainter than in the individual images. As expected the proper motion precision is worse, with typical uncertainties of the order or $1 \sim 3$ mas yr^{-1} (compared to < 1 mas yr^{-1} for individual images) depending on the magnitude and coverage, but are more than enough for our purpose given the relatively large motion of USC (over 30 mas yr^{-1}).

As in Bouy et al. (2013), we complemented the photometry extracted from the images with that of external catalogues: *Gaia* DR2 ($GG_{BP}G_{RP}$), Pan-STARRS (*grizy*), 2MASS (*JHKs*), and ALLWISE (all four bands) to improve the spatial and wavelength coverage of the final dataset. Either the corresponding photometric measurements were added to our catalogue when no measurement was available in our data, or the weighted average of all measurements (our values and from external catalogues) was computed after rejecting outliers using the modified Z-score criterion.

Recent variability studies of young clusters found typical amplitudes of 0.03 mag (e.g. Rebull et al. 2016, 2018). To account for this source of uncertainty and the differences in transmission curves of filters, we added quadratically 0.05 mag to all the photometric measurement uncertainties in our catalogue. The final mean uncertainties in photometry depend on the photometric band and are of the order of 0.07 mag.

2.2 MEMBERSHIP ANALYSIS

To identify candidate members we used the methodology originally developed by Sarro et al. 2014. This algorithm was initially designed to find members in the Pleiades cluster with the DANCe catalogue and I participated in the generalisation of the code to other clusters and catalogues (for instance, the *Gaia* catalogue including the parallaxes). These upgrades are presented in Olivares et al. 2019 and mainly concern:

- the inclusion of the parallax in both the cluster[1] and field models
- the uncertainties and the correlations between the astrometric parameters

My contribution to these upgrades was the validation of these implementations.

This algorithm uses the Bayes theorem to infer posterior membership probabilities for all the sources in a region given their observations (astrometry and photometry). This theorem relates the posterior probability that a given source belongs to the cluster class, $p(C_{cluster}|D)$, to the likelihood that the data D is compatible with the cluster model $p(D|C_{cluster})$, a prior membership probability $p(C_{cluster})$, and a normalising constant.

$$p(C_{cluster}|D) = \frac{p(D|C_{cluster}) \cdot p(C_{cluster})}{p(D|C_{cluster}) \cdot p(C_{cluster}) + p(D|C_{field}) \cdot p(C_{field})} \tag{2.1}$$

The two prior membership probabilities $p(C_{cluster})$ and $p(C_{field})$ are defined as the proportion of cluster members and field stars in the data. The cluster and field models of the likelihood are described in the following subsections.

We computed membership probabilities for all the sources in the input catalogue, even if they had some missing values in the photometry. In this case, we used the final field and cluster models and marginalised over the missing values (see Sarro et al. 2014 for more details). Unfortunately, the current version of the algorithm does not use the sources with missing values for the construction of the model (neither the field nor the cluster). Typically, these sources

1 In the context of the membership analysis, we use the term cluster to refer to open clusters but also to associations and star-forming regions.

are concentrated in the faintest objects since they are the most challenging to observe, and this introduces more uncertainties in this part of the model. To minimise the impact of missing sources in the model, an adequate selection of the representation space, i.e. the set of astrometric and photometric variables used for the membership analysis, is essential. In this sense, we always avoided the bands with a large number of missing observations and looked for the combination of magnitudes and colours which separated best the cluster and field populations.

2.2.1 *Field model*

We modelled the field population with a Gaussian mixture model (GMM)[2] in the astrometric+photometric space. We explored GMMs with different numbers of components and chose the one that minimises the Bayesian information criterion (BIC). The field model was computed once at the beginning and fixed thereafter under the assumption that the new members discovered over the iterations (a few hundred) do not significantly affect the field population model (millions of sources). This approximation allowed us to tremendously reduce the computational time.

2.2.2 *Cluster model*

We represented the cluster population with a product of two independent models, one for the astrometry and another for the photometry. The astrometric model is a GMM with the number of components that optimises the BIC. The photometric model is defined by a principal curve representing the cluster sequence as described in (Sarro et al. 2014).

We computed the cluster model iteratively using an expectation-maximisation[3] algorithm, starting from an initial list of members. This initial list can be slightly contaminated and incomplete and serves only to define the cluster locus in the multi-dimensional space in the first iteration. Since we are especially interested in identifying the faintest members, we often have to explore a region of the representation space where no or little members in the literature are known and

2 A GMM is a probabilistic model that represents the distribution of a population with a finite number of Gaussians.

3 The expectation-maximisation algorithm is an iterative method to find (local) maximum likelihood estimates of parameters in a statistical model. The method is divided between an expectation step, where each source in the catalogue is assigned to the field or cluster population, and a maximisation step, where the parameters of the cluster model are updated. In principle, we should update the parameters of both the cluster and field models but we decided to maintain the field model fixed to reduce the computational time (see the description of the Field model). We refer to Sarro et al. (2014) for more details.

thus, where the cluster photometric locus (and hence the model) is not defined. For this reason, the algorithm extends the initial principal curve by progressively and iteratively extrapolating the photometric sequence to explore fainter regions. We considered small extensions of the curve and the new candidate members were added and used in subsequent iterations to better define (or correct if necessary) the extrapolation. The extrapolation of the photometric curve is guided by the astrometry, which does not change with magnitude. This extrapolation of the principal curve is further explained in Sarro et al. (2014) and ensures that the results are robust and converge to a proper solution.

At each iteration, we evaluated the likelihood of the astrometric and photometric models, and we assigned Bayesian membership probabilities to all the sources with complete measurements using Equation 2.1. These probabilities, together with a probability threshold, p_{in}, were used to reclassify the complete sources between members and non-members. The p_{in} is a free parameter of the model that defines the degree of completeness and contamination desired for the training set (and as a consequence, for the final list of members). We refer the interested reader to Sarro et al. (2014) and Olivares et al. (2019) for a more detailed description of this parameter. Eventually, the cluster model was recomputed based on the new list of members, and this process was repeated until convergence. We defined the convergence when the logarithm of the cluster likelihood of two consecutive iterations had a relative difference smaller than a tolerance (Olivares et al. 2019). This tolerance has been chosen in such a way that consecutive iterations do not include new members or remove the existing ones.

2.2.3 *Probability threshold from synthetic data*

Once the model converged, all the sources in the input catalogue have a membership probability. To select members and estimate the mass function, we thus need to define a membership probability threshold. The intuitive threshold at 50% could be highly non-optimal in terms of contamination and completeness. To better assess the completeness and contamination rate as a function of membership probability, we generated a synthetic dataset from the model learnt with observed data. Therefore, it has similar properties to the observed data (e.g. missing values, frequency of members, uncertainties). As a consequence, the results derived from the synthetic dataset are only valid for the used representation space and learnt model. We refer to Olivares et al. (2019) for the details on how this synthetic dataset is generated.

We used this synthetic dataset to analyse the goodness of our classification and to choose the optimum probability threshold, p_{opt}, used for the final

classification based on the contamination and completeness rates. The optimum threshold of course depends on the scientific goal behind the membership analysis. In our case and in order to study the mass function, we are interested in reaching a compromise between the contamination and the completeness. To this end, we chose as p_{opt} the value that minimises the distance to the perfect classifier (DST). This distance is defined in terms of the contamination rate (CR) and the true positive rate (TPR), which in turn depend on the confusion matrix: true positives (TPs), false positives (FPs), false negatives (FNs), and true negatives (TNs). These indices are defined as follows:

$$\begin{aligned} CR &= \frac{FP}{FP+TP}\,; \\ TPR &= \frac{TP}{TP+FN}\,; \\ DST &= \sqrt{(CR-0)^2+(TPR-1)^2}\,. \end{aligned} \tag{2.2}$$

As we mentioned, the estimations that can be obtained with this synthetic dataset are restricted to the same conditions as the observations and to the assumption that the model correctly represents the observed data. Thus, the measured CR and TPR can be underestimated and overestimated, respectively, compared to those obtained with better quality data and more realistic models.

2.3 TOWARDS THE MASS FUNCTION

In this section, we describe our strategy to obtain the mass function from the observables. First, we obtained absolute magnitudes from the apparent magnitudes and a distance estimate. Then, we inferred the luminosity and mass from evolutionary models. Finally, we used individual masses to derive the mass distribution of the region.

2.3.1 *From apparent to absolute magnitudes*

The conversion from apparent (m) to absolute (M) magnitudes involves the distance (d) and extinction (A_m) towards each source:

$$M = m - 5 \cdot \log_{10}(d[\mathrm{pc}]) + 5 + A_m \tag{2.3}$$

The term $\mu = 5 \cdot \log_{10}(d[\mathrm{pc}]) - 5$ is referred as the distance modulus and accounts for the differences in brightness (measured in units of magnitude) caused by the distance of the source. Since individual measurements of the extinction are not available for all the sources, we included it as a free parameter

in the next step where we use the absolute magnitudes to infer the luminosity and mass of each source.

Individual parallax measurements are now available for many stars thanks to *Gaia*. In theory, the distance can be derived in a very straightforward way by simply inverting the parallax. However, in practice, this can lead to important biases when the uncertainties in the parallax are large (typically when greater than $\sim 10\%$). Following the recommendations of Luri et al. (2018) we used a Bayesian approach to convert parallaxes to distances. We used the *Kalkayotl*[4] code (Olivares et al. 2020), which performs a Bayesian probabilistic inference to compute posterior probability distributions for the distance of each member. I participated in the validation of this code.

To compute the absolute magnitude of each source and properly estimate the corresponding uncertainties, we sampled the apparent magnitude with a Gaussian centred at the observed magnitude and a standard deviation equal to the uncertainty. Then, each sample was converted to absolute magnitude by sampling the posterior distance distribution obtained with *Kalkayotl* and applying it to Equation 2.3. For the sources in the DANCe catalogue, beyond the limit of sensitivity of *Gaia* and without parallax measurement, we sampled the distance from the cluster distance distribution obtained with all the *Gaia* members.

2.3.2 *From absolute magnitudes to luminosity and mass*

Once absolute luminosities were available, we compared them to theoretical evolutionary models to infer the bolometric luminosity and mass of each source. The comparison was done with *Sakam*[5] (Olivares et al. 2019), a software based on an algorithm that infers the posterior distribution of the luminosity and mass together with the A_V extinction, given the absolute photometry (and the corresponding uncertainties) of each source in various filters and a theoretical evolutionary model. *Sakam* ignores any possible source of uncertainty related to the theoretical evolutionary model chosen by the user. The model does not include effects on the variability of the source due to binarity, activity, or other factors. These effects eventually end up included in the extinction estimate, enlarging its uncertainties. My extensive use of *Sakam* over the course of my thesis contributed greatly to its validation.

There is no single set of models covering the entire mass range of our members and we were forced to use different models for the high and low-mass regimes.

4 https://github.com/olivares-j/kalkayotl
5 https://github.com/olivares-j/Sakam

For the high mass stars, we used the PARSEC-COLIBRI[6] models (Marigo et al. 2017). In the low-mass regime, we used a different set of models depending on the age of the region and choosing the model that best fitted our data in each case. We used the BT-Settl[7] models (Allard 2014) at 30 Myr and the BHAC15[8] models (Baraffe et al. 2015) at $3 - 8$ Myr.

2.3.3 *From individual masses to a mass distribution*

To obtain the mass distributions we sampled the individual mass of each source with a Gaussian centred at the mass inferred by *Sakam* and a standard deviation equal to the uncertainty. Then, we defined a grid between the least and most massive object in our sample and added the contribution of all the sources to each mass bin. We convoluted this distribution with a Gaussian kernel density estimation (KDE) with a bandwidth chosen according to Scott's rule (Scott 1992) and Silverman's rule (Silverman 1986). We estimated the uncertainties in the mass function with a bootstrap of 100 repetitions and reported the 1σ and 3σ confidence levels. The magnitude and luminosity distributions were obtained analogously.

6 http://stev.oapd.inaf.it/cgi-bin/cmd
7 http://perso.ens-lyon.fr/france.allard/
8 http://perso.ens-lyon.fr/isabelle.baraffe/

3

IMF AT 30 MYR: IC 4665

3.1 CONTEXT

IC 4665 is one of the few well-known, nearby (< 500 pc), pre-main sequence open clusters in the age interval $10 - 50$ Myr. It is located in the Ophiuchus constellation and it was first reported by Philippe Loys de Chéseaux in 1745. Its age was estimated to be $27.7^{+4.2}_{-3.5}$ Myr using the lithium depletion boundary (Manzi et al. 2008). A similar value of 36 ± 9 Myr was obtained from pre-main sequence isochrone fitting and 42 ± 12 Myr with upper-main sequence turn-off fitting (Cargile and James 2010). At 30 Myr, all the gas and dust from the parent molecular cloud has already vanished leaving a low degree of extinction which facilitates the observations and the identification of members. Its age makes of IC 4665 an excellent candidate were to study the mass function since dynamical interactions have not completely erased the memory of its IMF. Additionally, it is also a very interesting age to look for young planetary systems and study their early evolution.

The first study of the mass function of IC 4665 was carried out by de Wit et al. (2006). They selected members from photometric observations in the optical obtained at the CFHT. They estimated a high contamination rate by foreground and background stars of up to 85% using control fields, which can be explained by its low galactic latitude. They reported a mass function best described by a power-law with an exponent of -0.6 for the low-mass objects down to ~ 0.1 $M_\odot$. Later, Lodieu et al. (2011) performed a similar analysis adding near-infrared photometry from the UKIDSS (Lawrence et al. 2007) to the previous observations of de Wit et al. (2006). They revised the members of previous studies and proposed new candidate members as well. They reported a mass function best represented by a log-normal function with a peak at $0.25 - 0.16$ $M_\odot$. The differences between the mass functions obtained with these two studies can be mainly attributed to the high contamination rate by field stars, as we shall see later.

After the *Gaia* DR2, two different studies published a census of IC 4665. First, the demonstration paper of Gaia Collaboration et al. (2018b) studied the fine structures of the HR diagram in the field and open and globular clusters. IC 4665 was among their targets and they provided a list of 174 high-probability members up to magnitude $G < 18$. Soon after, Cantat-Gaudin et al. (2018)

presented another study of open clusters using *Gaia* DR2 data. They derived another membership list (with the same magnitude limit) made of 175 high-probability members, 146 of which are in common with Gaia Collaboration et al. (2018b). Both studies used only the *Gaia* data, applied strict and very conservative filtering and discarded sources fainter than $G = 18$ mag, thus delivering a clean yet incomplete sample.

In this chapter, we aim to study the mass distribution of IC 4665 and for that, we first revisited the membership analysis of this cluster. This chapter is based on the work published in Miret-Roig et al. (2019) and is structured as follows. In Section 3.2, we describe the data we used in this chapter. In Section 3.3, we describe the parameters of the membership algorithm we used to select members of the IC 4665 open cluster among a large number of foreground and background sources. We also include some validation tests and compare our members to previous studies. In Section 3.4, we analyse our sample of members: we compare the empirical isochrone of the cluster to theoretical evolutionary models, we determine the magnitude distribution and the mass function of the cluster and compare it with theoretical models. Additionally, we compute the median distance of the cluster and study the spatial distribution. Finally, in Section 3.5, we present our conclusions regarding this study.

3.2 DATA

In this work, we used two different catalogues with different origins and properties to look for members in the IC 4665 open cluster. In this section, we describe how we obtained each of them and their properties.

3.2.1 *The Gaia catalogue*

We queried a circular area of 3° radius around the centre of the cluster (RA = 266.6°, Dec = 5.7°), from the *Gaia* DR2 catalogue (see Appendix B.1) and we kept only those sources with a full five-parameter solution available. Several quality checks have been suggested in the literature. The filtering recommended by the *Gaia* team is based on the renormalised unit weighted error (RUWE) and is described in detail in a publicly available technical note[1]. The RUWE criterion is a quality indicator which can be used when the aim is to have only the most precise, reliable, and consistent astrometric solutions. However, it also leads to a higher degree of incompleteness. For instance, since the *Gaia* DR2 catalogue does not deal with binaries, their astrometric

1 https://www.cosmos.esa.int/web/gaia/dr2-known-issues

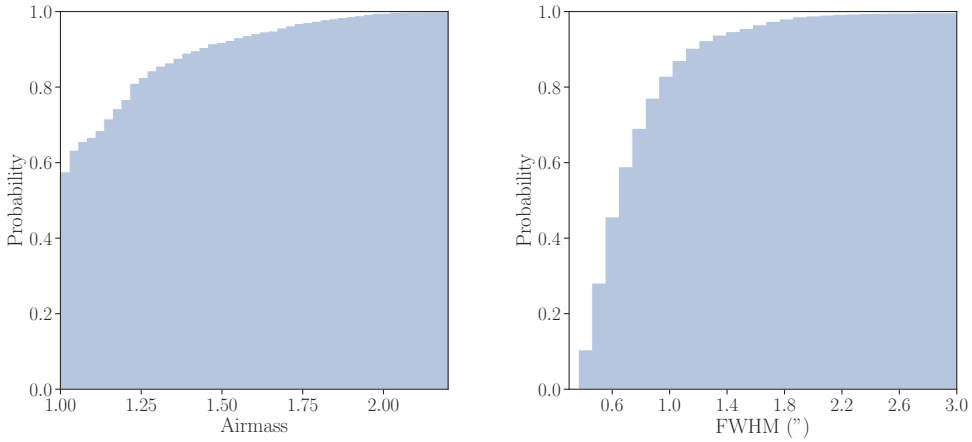

Figure 3.1. Left: Cumulative distribution of airmass for the observations. Right: Cumulative distribution of average FWHM for the images.

solution is likely to be 'inconsistent', and thus the RUWE filter will remove most of the binaries, already a low number, included in *Gaia* DR2. Since we aim to have a sample the most complete possible, we have no strong scientific argument for cutting our data by this or any other kind of filtering. Besides, the sources with problematic astrometric solutions can be rejected later on based on complementary observations and/or subsequent *Gaia* DRs.

This sample contains positions, proper motions, parallaxes, and G, G_{BP}, G_{RP} photometry for 1 217 725 sources. The mean errors of this catalogue are ~ 0.5 mas for parallaxes, ~ 1 mas yr^{-1} for proper motions, and < 0.1 mag for the photometry. According to Gaia Collaboration et al. (2018c), the catalogue is mostly complete down to $G = 7$ mag. On the faint side, Lindegren et al. 2018a reported that the five-parameter solution is 94.5% complete up to $G = 19$ mag (see their Table B.1). Then, we assume that the *Gaia* catalogue is complete between $7 < G < 19$ mag.

3.2.2 *The DANCe catalogue*

We searched in the public archives described in Section 2.1.1 for wide-field images within a circular region of 3° radius, centred on IC 4665. The data found in these public archives was complemented with our own observations using the Las Campanas Swope telescope and its Direct CCD camera, the DECam mounted on the Blanco telescope at the CTIO, the NEWFIRM camera mounted

Table 3.1. Instruments used in the Dynamical Analysis of Nearby ClustErs (DANCe) catalogue of IC 4665.

Telescope	Instrument	Filters	Platescale [pixel^{-1}]	Field of view	Epoch Min./Max.	Ref.
CTIO (Blanco)	DECam	g, r, i, z, y	$0''.27$	1.1° radius	2014–2018	(1)
KPNO (Mayall)	NEWFIRM	J, H, Ks	$0''.4$	$28' \times 28'$	2015	(2)
CFHT	MegaCam	r, i	$0''.18$	$1^\circ \times 1^\circ$	2005–2015	(3)
CFHT	WIRCam	y, J, H, Ks	$0''.3$	$20' \times 20'$	2007–2008	(4)
CFHT	CFH12K	I, z	$0''.21$	$42' \times 28'$	1999–2002	(5)
INT	WFC	u, v, b, β, y (Strömgren), U, B, V, Z, g, r, i[a]	$0''.33$	$34' \times 34'$	2000–2015	(6)
UKIRT	WFCAM	J, Ks	$0''.4$	$40' \times 40'$[b]	2006-2012	(7)
LCO Swope	Direct CCD	i	$0''.43$	$15' \times 14'$	2013	(8)
VST	OmegaCam	r	$0''.21$	$1^\circ \times 1^\circ$	2014	(9)
ESO (2.2 m)	WFI	R, I[a]	$0''.24$	$34' \times 33'$	2002	(10)
Subaru	HSC	y	$0''.17$	1.8° radius	2015	(11)
Palomar 48″	PTF	g, r	$1''.0$	$3.3^\circ \times 2.2^\circ$[c]	2010–2012	(12)
OMM (1.6 m)	CPAPIR	I, J, H	$0''.89$	$30' \times 30'$	2012–2015	(13)

[a] as well as various narrow and medium bands

[b] the chip layout has large gaps between detectors, and the coverage of the focal plane is only partial

[c] one of the 12 detectors is dead

References. (1) Flaugher et al. (2010); (2) Autry et al. (2003); (3) Boulade et al. (2003); (4) Thibault et al. (2003); (5) Cuillandre et al. (2000); (6) Ives (1998); (7) Casali et al. (2007); (8) Rheault et al. (2014); (9) Kuijken et al. (2002); (10) Baade et al. (1999); (11) Miyazaki et al. (2018); (12) Rahmer et al. (2008); (13) Thibault et al. (2002)

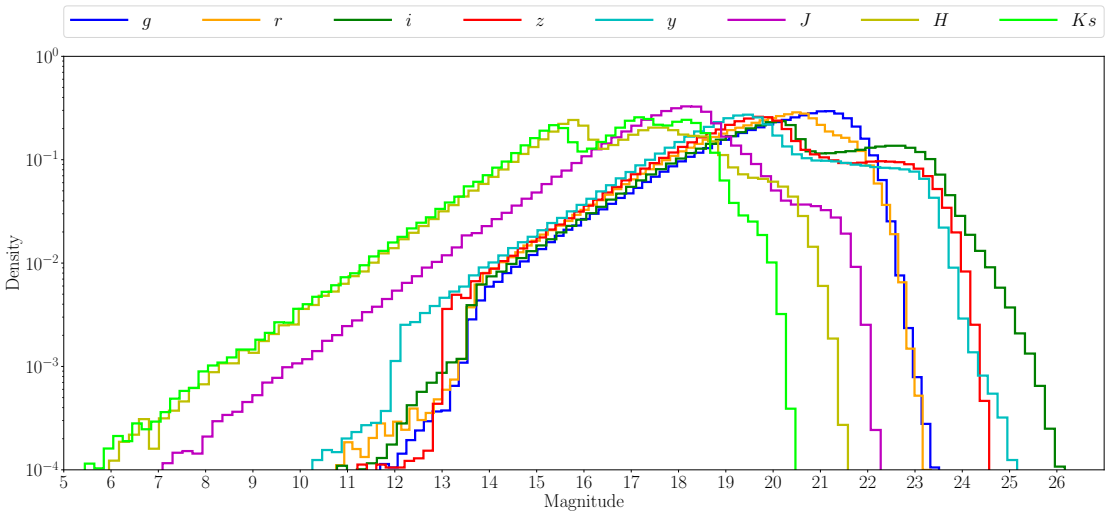

Figure 3.2. Density of sources as a function of magnitude for members of the DANCe catalogue of IC 4665.

on the 4 m telescope at the KPNO, the HSC mounted on the Subaru telescope at the NAOJ, and the WFC mounted on the INT. Several observations found in the archives were discarded after a visual inspection because of their poor quality, limited sensitivity, or acquisition problems (mostly due to loss of guiding, tracking, or electronics problems). The dataset included 6 774 individual images originating from 13 instruments. The total amount of data (scientific images, associated calibrations, and intermediate products) was almost 20 TB. Table 3.1 gives an overview of the various cameras used for this study.

The airmass and the full width at half maximum (FWHM) measured in the images using point-like sources are two important parameters influencing the achievable astrometric accuracy. About 90% of the observations were obtained at airmass ≤ 1.5 (see Fig. 3.1, left), ensuring that the chromatic diffraction due to the atmosphere is low. IC 4665 is located at a declination of $\delta \sim 5°$ and we gathered data from both hemispheres. About 82% of the images have FWHM $\leq 1''$, and 90% have FWHM $\leq 1''.2$ (see Fig. 3.1, right).

The astrometric solution was obtained as described in Section 2.1.2. We found that about 1.3% of the sources ($\sim$ 60 000) were duplicated in the final catalogue. A visual inspection showed that almost all of them had a very low SNR and that the SExtractor deblending algorithm resolved them as two sources instead of one, in one (or a few) images. These resolved sources later fooled the cross-identification algorithm and ultimately resulted in two independent sources instead of one. There is no straightforward solution to this problem for now,

Table 3.2. Number of measurements and completeness for each photometric band in the DANCe catalogue of IC 4665.

	g	r	i	z	y	J	H	Ks
No.	1 284 683	1 570 253	2 295 949	2 096 267	2 019 385	1 717 645	888 020	869 769
Pct.	54%	67%	97%	89%	86%	73%	38%	37%
BL	13.8	13.8	13.8	13.0	12.0	8.1	6.0	6.0
FL	21.2	20.6	20.3	19.8	19.6	18.5	17.7	18.0

Notes. The total number of sources is 2 358 937. The completeness is given in terms of the bright limit (BL) and faint limit (FL).

but given their very small number, we treated them as regular sources in the rest of the analysis and simply looked for duplicated entries in the final list of members.

The photometric calibration was performed only for the g, r, i, z, y and J, H, Ks filters as described in section 2.1.3. It was not attempted for the INT images obtained in any other filter, the ESO 2.2 m Wide Field Imager (WFI) images, the PTF images (because the camera has a significantly coarser pixel scale and the images reach a depth shallower than Pan-STARRS), and the CPAPIR I-band images.

Given the low extinction in that area of the sky, the maximum of the magnitude distributions (Fig. 3.2) gives an estimate of the completeness limit of the survey. It is nevertheless important to remember that the spatial coverage of the various instruments is not homogeneous and the depth of the survey varies spatially. The limits of sensitivity of the external catalogues merged with our data (2MASS and Pan-STARRS) are sometimes visible as secondary maxima. In Table 3.2 we give, for each photometric band, the number and percentage of measurements as well as the completeness limits we used in this study. This final catalogue includes 2 358 937 sources.

3.3 MEMBERSHIP ANALYSIS

In this section we apply the membership algorithm described in Section 2.2 to the catalogues described in the previous section. Due to the different observational parameters and completeness of the two catalogues analysed in this work, we did an independent membership analysis for each of them. In Section 3.3.1 we describe the parameters of the algorithm. In Section 3.3.2 we

compare the two lists of members obtained with the *Gaia* and DANCe catalogue. In Section 3.3.3 we compare our final list of members with other studies.

3.3.1 *Parameters of the membership algorithm*

The membership algorithm is described in Section 2.2. In this section, we discuss the parameters of the model used for the analysis of the IC 4665 open cluster.

Initial members

Two studies published members of IC 4665 using *Gaia* data before our work. Gaia Collaboration et al. 2018b published a list of 174 members, and the work of Cantat-Gaudin et al. 2018 published a list of 175 members. Both studies have a magnitude limit of $G = 18$ mag and most of the sources are in common. We combined their results and obtained a list of 203 members, which we used as the initial list for our membership analysis with the *Gaia* catalogue.

To start the membership algorithm for the DANCe catalogue, we used the members we obtained with the *Gaia* catalogue that have a counterpart in DANCe. In this case, the initial list does not cover the full magnitude range of the catalogue because DANCe goes fainter than the initial list of *Gaia* members. However, our algorithm is capable of exploring fainter regions as we explained in Section 2.2.

Representation space

We used all the astrometric observable present in the catalogue. To choose the photometric variables, we used a random forest algorithm, as in Olivares et al. (2019) and we avoided those bands with a large number of missing values. For the analysis with the *Gaia* catalogue, the representation space we used is `pmra`, `pmdec`, `parallax`, G_{RP}, $G_{BP} - G$, $G - G_{RP}$. With this representation space, 1 184 922 sources have complete data, 97% of the catalogue. For the analysis with the DANCe catalogue, the representation space we used is `pmra`, `pmdec`, J, $i - z$, $i - y$, $i - J$. With this representation space, 1 627 593 sources have observations in all the photometric bands, which represents a 69% of the catalogue. We decided not to include the g, r, H, and Ks bands in the representation space because of the large number of sources with missing photometry (see Table 3.2).

Table 3.3. Performance of the membership analysis obtained with different internal probability thresholds (p_{in}) for the two catalogues considered, namely *Gaia*, and DANCe.

	Gaia				DANCe			
p_{in}	p_{opt}	Memb	CR (%)	TPR (%)	p_{opt}	Memb	CR (%)	TPR (%)
0.5	0.86	539	14	87	0.86	716	12	86
0.6	0.78	567	15	90	0.87	669	10	90
0.7	0.77	434	10	89	0.87	647	10	89
0.8	0.76	405	11	86	0.83	644	10	91
0.9	0.68	383	11	86	0.80	582	9	90

Notes. For each internal probability threshold (p_{in}) we show the corresponding optimum probability threshold (p_{opt}), number of members (Memb), contamination rate (CR) and true positive rate (TPR). The p_{opt}, CR, and TPR were obtained with synthetic data (see text).

Field model

The model of the field population is a GMM in the whole representation space. We explored GMMs with different numbers of components (60, 80, 100, 120, 140, 160, and 180) and chose the model with 100 components which minimises the BIC (both in the *Gaia* and DANCe datasets).

Cluster model

To model the astrometry of the cluster population we used a GMM. We explored the number of components between one and four and chose the one that minimised the BIC. The model of the photometry is a principal curve in the space defined in the representation space. We ran the model considering several p_{in} thresholds (0.5, 0.6, 0.7, 0.8, and 0.9), and for each we computed the optimum threshold (p_{opt}), the contamination and completeness using synthetic data. In Table 3.3, we show the p_{in}, p_{opt}, contamination, completeness, and number of members for each independent analysis (*Gaia* and DANCe).

Classification of incomplete sources

We used the field and cluster models described in this section to compute membership probabilities for the incomplete sources (i.e. the sources that lack one or more magnitudes of the representation space). Then, we used the optimum threshold to classify all the sources between members and non-members.

There are very few incomplete sources in the *Gaia* catalogue and none of them is classified as a member. The number of incomplete sources classified as members in the DANCe catalogue is $4-8$, depending on the p_{in}. In general, they lack z and/or y photometry, and the brightest ones are also classified as members by the analysis with *Gaia*.

Final membership list

In Tables C.2 and C.3 (available at the Centre de Données astronomiques de Strasbourg, CDS) we provide the posterior membership probabilities obtained with the different p_{in} for all the sources in the *Gaia* and DANCe catalogues, respectively. For the DANCe catalogue, we also provide the astrometry and photometry we computed. In the following paragraphs, we describe the strategy we used to choose the most convenient member list for our requirements.

The membership probabilities obtained with different p_{in} values have to be compared with care. The relation between different membership probabilities (obtained with different p_{in}) is not linear, and lower p_{in} values tend to provide higher membership probabilities. In general, the models computed with lower p_{in} values permit a greater inclusion of sources initially classified as 'field' into the cluster class during the training of the model. This results in lists of members that can include a significant number of contaminants. On the contrary, models computed with higher p_{in} are more restrictive, include fewer additional sources into the cluster model, and thus, tend to have lower contamination, but at the same time can be incomplete.

The membership probabilities we computed are not absolute but are closely related to the model used, which at the same time depends on the representation space and the p_{in} parameter (desired degree of completeness and contamination). In consequence, the comparison between the *Gaia* and DANCe membership probabilities is not straightforward, especially due to the different representation spaces of each catalogue (e.g. DANCe does not have parallaxes).

To study cluster properties such as the mass function, we need a unique list of members, the cleanest and most complete possible. To this end, we first have to choose a p_{in} for each study (*Gaia* and DANCe), and then combine the two lists. We began with the *Gaia* catalogue which is expected to have a more robust membership analysis since it includes a very discriminating variable: the parallax. We used a Kolmogorov-Smirnov (KS) test in different variables of the representation space (proper motions, parallax, and photometry) to see if the distributions of these variables obtained with different p_{in} were compatible with each other. The goal was to see if we could find signs of strong contamination or incompleteness in one or several of the lists compared to the others. We started by taking the sources classified as members (i.e. those with $p > p_{opt}$)

obtained with the model trained with $p_{in} = 0.9$ as a reference. This is the most conservative and the least contaminated, but also probably the most incomplete list of members. Then, we compared this list of members with all the rest ($p_{in} = 0.5, 0.6, 0.7$, and 0.8, one at each time). The KS test showed that for the lists of $p_{in} = 0.5$ and 0.6, there was evidence that the distribution of their proper motions and parallax values did not come from the same distribution as that obtained with the list of $p_{in} = 0.9$ with a p-value lower than the significance level 0.01. On the contrary, for the distribution of the astrometric variables coming from the lists of $p_{in} = 0.7$ and 0.8, the KS test showed no evidence to reject the conclusion that they came from the same distribution as the one obtained with $p_{in} = 0.9$ with p-values of $0.4 - 0.5$. Then, we investigated the reason for the incompatibility of the lists of $p_{in} = 0.5$ and 0.6 compared to the rest. We found that the parallax and proper motions distributions obtained with the lists of $p_{in} = 0.5$ and 0.6 had significantly more extended wings than the distributions obtained with the lists of higher p_{in}. We interpreted this as contamination, and therefore we discarded these two lists. The remaining lists were compatible according to the KS test so we chose the list of $p_{in} = 0.7$, which had the largest number of members (see Table 3.3).

To select the optimum p_{in} for the DANCe analysis we also applied a KS test to find which distributions were compatible with the one obtained with $p_{in} = 0.9$. In this case, there was no evidence to reject the hypothesis that the distributions of all the variables analysed for the lists from all p_{in} came from the same distribution as those of $p_{in} = 0.9$ since all the p-values were > 0.3. Then, to check the consistency between the *Gaia* and DANCe lists, we took the members of *Gaia* $p_{in} = 0.7$ as a reference and compared them with the members recovered in the different DANCe lists, in the region where both studies are complete ($14.5 \lesssim G \lesssim 19$ mag). We found that all the DANCe lists recovered roughly the same number of *Gaia* members ($250 - 266$ from 285, $\sim 90\%$). On the contrary, the number of members in DANCe that were not in *Gaia* decreased with increasing p_{in}. These sources have parallaxes that are in general incompatible with the *Gaia* members (beyond 3σ), and thus we believe that most of them are contaminants (representing $30 - 35\%$ of the DANCe members). In short, for the DANCe analysis, we did not find any strong argument for discarding any list. Therefore, we decided to keep the one with the largest number of members, the one with $p_{in} = 0.5$, keeping in mind that it includes contamination of the order of $30 - 35\%$ estimated from the comparison with the *Gaia* members. This contamination rate is larger than the one we estimated with synthetic data (see Table 3.3) and the reason is that the *Gaia* catalogue contains parallaxes which are very valuable to identify the cluster members. In the rest of this work, we use the *Gaia* list with a $p_{in} = 0.7$

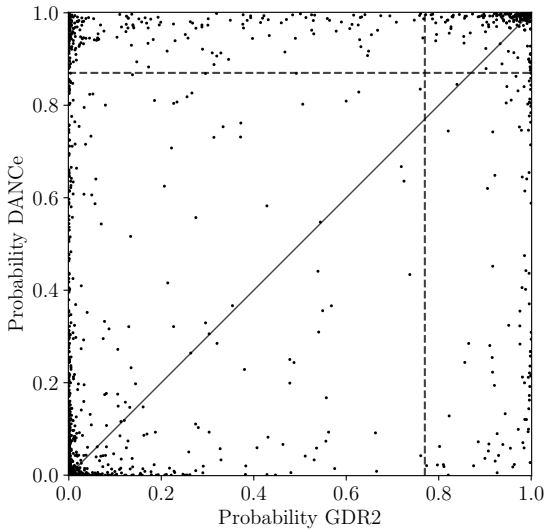

Figure 3.3. Comparison between the membership probabilities recovered by the *Gaia* and DANCe classifiers, for objects in both catalogues. The diagonal line represents the one-to-one relation, and the horizontal and vertical dashed lines show the optimum probability thresholds.

and the DANCe list of $p_{in} = 0.5$. These two lists amount to a final compilation of 819 members, which are analysed in more detail in the coming sections.

3.3.2 *Internal validation*

In this section, we compared the two membership analyses obtained with the *Gaia* and the DANCe catalogues. We cross-matched the two catalogues (which contain members and field stars) and found 1 211 272 sources in common. In Figure 3.3 we compare the membership probabilities obtained with the two catalogues. The diagonal line represents the one-to-one relation, and the vertical and horizontal dashed lines represent the optimum thresholds. We see that most of the sources are clustered in the bottom left (field) and top right (cluster) regions of the diagram. Nonetheless, some sources are classified as members by one study and not by the other.

To investigate the differences between the two classifiers we represented the number of members as a function of the magnitude (Fig. 3.4). We distinguish between the members obtained with both classifiers (red), the *Gaia* members only (blue), and the DANCe members only (green). Here we discuss the four possible cases regarding the results of the two membership analyses.

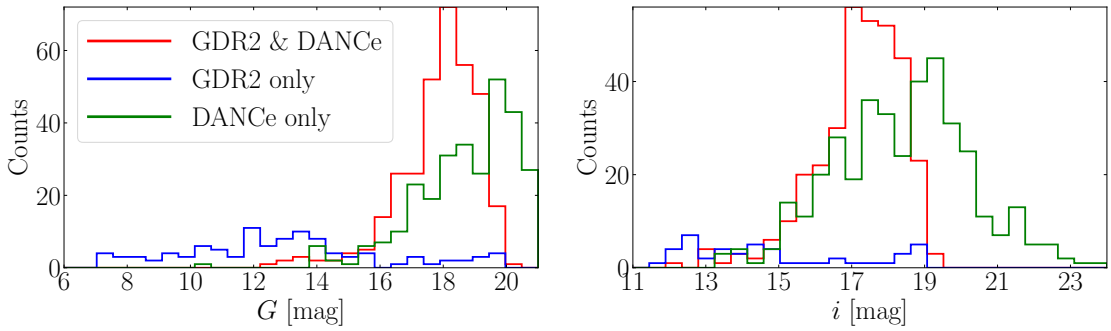

Figure 3.4. *G* and *i* (left and right) magnitude distributions of the sources classified as members in the *Gaia* and DANCe studies (red), classified as members by *Gaia* but not by DANCe (blue), and classified as members by DANCe but not by *Gaia* (green).

– *Members in Gaia and DANCe.*
331 sources appear as members in both analyses (red in Fig. 3.4). In the magnitude range where both catalogues are complete, the majority of members are classified as such by the two analyses.

– *Members in Gaia only.*
In the magnitude range where both analyses are complete, we see that the members obtained only with *Gaia* have a low and flat distribution. This can be interpreted as the *Gaia* members list having very low contamination, which does not depend on the magnitude. The reason is that the parallax is the most discriminating variable for classifying these members. Although the uncertainties on the parallax depend on the magnitude, they are at the level required to distinguish the cluster from the field in the entire magnitude range. At magnitudes > 18 we see a slight increase, but it is not significant.

– *Members in DANCe only.*
385 sources appear as members in DANCe but not in *Gaia* (green in Fig. 3.4). Of these sources, 120 objects (31%) do not have the five-parameter solution in *Gaia* and 186 (48%) have parallax uncertainties $> 10\%$. We discussed in the previous section that we find a $\sim 30\%$ of contamination in the region where both studies are complete. This is significantly higher than the value we found in other clusters (i.e. the Pleiades and Ruprecht 147; see Sarro et al. 2014; Olivares et al. 2019, respectively), but this is expected given the lower galactic latitude and significantly lower proper motion of IC 4665. Besides, we see that the number of members recovered only by DANCe increases as a function of magnitude in the region where both analyses

are complete. We interpret this as a dependence of the contamination on the magnitude. The DANCe analysis does not use the parallax and thus it is expected that photometry plays a major role, especially in this cluster with low proper motions.

– *Non-members in Gaia and in DANCe.*
All the remaining sources are classified as field stars by both studies. Most of them have extremely low membership probabilities, which clearly identify them as field population. Several sources have rather high probabilities but fall below the threshold. This means that we cannot definitely discard them as members and that we could consider them as candidate members depending on the scientific case. The sources that are spread along the rest of the diagram may suffer from the problems already discussed, or simply the observables in the two catalogues are too different. To clarify the membership of the uncertain cases we would need either a longer temporal base-line to improve the proper motions or spectroscopy to study their properties (i.e. radial velocities and low gravity due to youth).

In short, we see that in general, the two independent analyses agree rather well, especially in the magnitude range were both are expected to perform well. The members obtained with both catalogues occupy the same space in the vector point diagram (see Fig. 3.5, left). The members coming from the DANCe catalogue typically have a larger dispersion and larger uncertainties, expected by the different precision of both catalogues. In the space of parallaxes (Fig. 3.5, right) we see that the members from the *Gaia* DR2 analysis are very highly concentrated around the median value (2.84 mas with a standard deviation of 0.36 mas). The majority of the DANCe members also have parallaxes compatible with the cluster distribution although this parameter was not used in the membership analysis. Others have parallaxes significantly different (at 3σ level) and they are either problematic measurements (because they are very faint) or contaminants. Future releases of the *Gaia* catalogue will help to clarify these cases.

When we introduced the *Gaia* catalogue in Section 3.2.1, we mentioned that we did not filter the data in any manner to be the most complete possible. Here, we discuss the RUWE goodness of fit indicator of the members found in this study. Our sample contains sources with a RUWE in the range $0.8 - 16.3$, and only 9% of them have a RUWE larger than the recommended threshold (1.40). However, we insist that all the sources with a RUWE larger than the recommended value do not always have an incorrect solution, and future releases of *Gaia* or complementary observations will determine this.

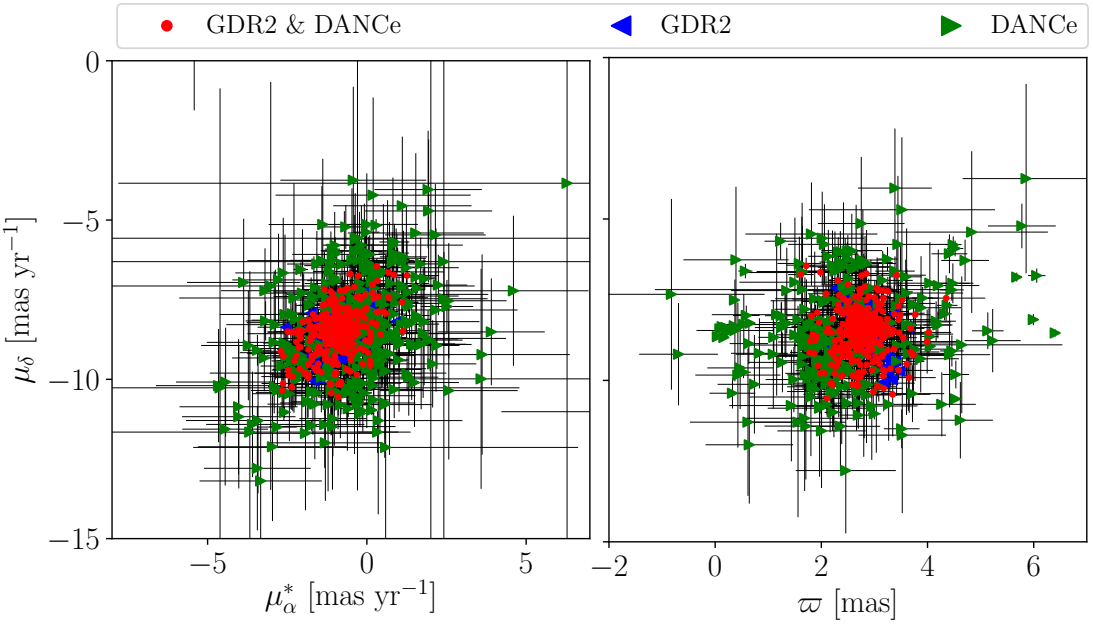

Figure 3.5. Vector point diagram (left) and parallax–proper motion diagram (right) of the IC 4665 open cluster. The members are shape- and colour-coded according their origin: *Gaia* and DANCe analysis (red circles), only *Gaia* analysis (blue left-pointing triangles), and only DANCe analysis (green right-pointing triangles).

3.3.3 *External validation*

In this section, we compared our list of 819 members with other studies in the literature and found that 409 (50%) are new members. We cross-matched each of the lists of members reported in the literature with ours using a maximum separation of 1″. In Figure 3.6, we compare the members we found with two of the most representative membership studies of IC 4665: Lodieu et al. (2011), based mainly on photometry, and Cantat-Gaudin et al. (2018), which used the *Gaia* DR2 astrometry. As a general trend, purely photometric studies tend to have more contamination than spectroscopic ones or ones based on *Gaia* astrometry.

de Wit et al. (2006)

These authors photometrically selected 691 low-mass stellar and 94 brown dwarf candidate members over an area of 3.82 square degrees centred on

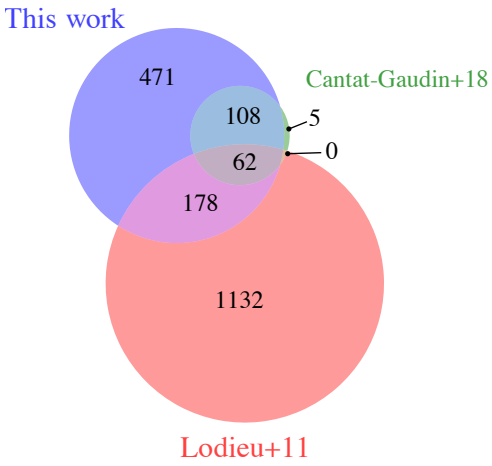

Figure 3.6. Venn diagram comparing the members in this work to previous studies in the literature (i.e. Lodieu et al. 2011; Cantat-Gaudin et al. 2018).

the cluster. In addition, they applied a filter for bright stars based on the proper motions from Tycho-2 (Høg et al. 2000) and UCAC2 (Zacharias et al. 2000) public catalogues. We detected some astrometric offsets between their positions and ours and consequently extended the cross-match search radius to 2″. We confirmed 195 of their members and rejected the rest of their candidates which have very low membership probabilities in our study. Therefore, we estimated a contamination rate of up to 75% in their study compatible with their own estimate. We believe that one of the reasons of their high amount of contamination is a problematic photometric calibration (their *i*- and *z*-band photometry display an offset of $\sim$ 1 mag compared to values from Pan-STARRS).

Manzi et al. (2008)

These authors did not attempt to do a comprehensive census of the cluster. Instead, they photometrically selected candidates from the literature and then spectroscopically confirmed 37 of them. They aimed to determine the age of IC 4665 using the lithium depletion boundary method. We confirmed 29 of their members (78%) and discarded the remaining eight (two of which were classified as not fully secure members by the authors). These eight members were discarded because their *Gaia* DR2 parallaxes and/or proper motions are far from the cluster distribution, although their photometry falls on the cluster sequence. Therefore, these sources are either interlopers or have a problematic astrometric solution in *Gaia* DR2.

Jeffries et al. (2009)

These authors aimed to study the pre-main sequence lithium depletion for low-mass stars in IC 4665. For this purpose, they selected 40 members according to several spectroscopic criteria. We confirmed 30 of their members (75%) and rejected the remaining ten. This study has 12 members in common with Manzi et al. (2008), and only one of these sources was rejected by our study. Again, the ten members were excluded from our list of members because their *Gaia* DR2 astrometry is incompatible with that of the cluster, but the same reasoning we discussed in the comparison with the members of Manzi et al. (2008) applies.

Cargile and James (2010)

These authors used a photometrically selected sample of members in the central region of the cluster (one square degree) to study the age and distance of IC 4665. Their sample contained 382 candidates members, 49 of which were confirmed by our study. From this, we estimated their contamination to be 87%.

Lodieu et al. (2011)

These authors used photometry from UKIDSS and CFHT to identify members in IC 4665. They presented a sample of 1 372 members in the magnitude range $15 < i < 20.4$, which they used to study the luminosity and mass functions. Only 240 of their candidates (17%) are classified as members in our work (see Fig. 3.6). The majority of the rejected candidates have extremely low membership probabilities in our analysis (both in *Gaia* and DANCe). We believe the reason for their high amount of contamination ($\sim$ 80%) is the same photometric offset as for de Wit et al. (2006) since they used the same data. These two works constituted the most exhaustive studies, especially regarding the low-mass regime, previous to the results we present here. Given the high levels of contamination found by the present analysis, we hereafter do not attempt any comparison of their luminosity and mass function.

Bravi et al. (2018)

These authors used the Gaia ESO Survey to study the IC 4665 open cluster. They carried out spectroscopic observations of 567 sources in the region of the cluster. They used spectroscopic criteria to exclude obvious contaminants, and then they computed membership probabilities using the radial velocity distribution of the cluster and the field. They ended up with 29 sources with membership probability values higher than 0.5. Of these sources, 24 have probability values higher than > 0.8. From the 29 candidates with $p > 0.5$, 20

were confirmed by our study (15 have probabilities > 0.8 according to their study), and the remaining nine were definitely rejected from our study. As for the previous spectroscopic surveys, we discarded these nine members because of the *Gaia* DR2 astrometry, which is incompatible with that of the cluster.

Gaia Collaboration et al. (2018b)

To demonstrate the power of *Gaia* DR2 in highlighting the fine structures of the HR diagram, these authors selected members for several open clusters. Their ambitious goal required selecting only the sources with the highest precision in astrometry and photometry, and among other filters, they restricted the selection to sources brighter than $G = 18$. One of the clusters of their study is IC 4665, for which they provided a list of 174 members based only on the astrometric solution of *Gaia* DR2. They claimed that their list was not complete, but that it contained potential members, i.e. that it had an extremely low contamination rate.

To make a fair comparison with this study, we only considered the members from our sample that are in the same magnitude and spatial range (brighter than $G = 18$ mag and within 2.4° radii around the centre of the cluster). This selection results in 267 members, 215 of which are classified as members by our analysis with the *Gaia* catalogue and the rest come from the analysis via the DANCe catalogue alone. The study of Gaia Collaboration et al. (2018b) and ours have 162 members in common, which is 93% of their list. From the 12 objects classified as members by these authors and not by our study, there are four that have probabilities > 0.5 but fall below the optimum threshold we adopted, and eight that have lower probabilities. Of these eight members, only one was also classified as a member by a similar study (Cantat-Gaudin et al. 2018). These small differences are part of the Poissonian noise of the membership analysis. Besides, we find 53 members not detected by these authors that are spread throughout the parameter space (proper motions, parallax, and magnitude), following the cluster distribution. Some of these 53 members could have been discarded by the authors in their data filtering.

Cantat-Gaudin et al. (2018)

These authors provided a membership analysis for a large number of clusters making use of the recent *Gaia* DR2 data. To avoid large uncertainties, they restricted the selection to the sources brighter than $G = 18$ mag. They used an unsupervised membership algorithm to derive membership probabilities using only the astrometry of *Gaia* DR2, and they found 175 members of IC 4665.

To make a fair comparison with this study, we only considered the members of our sample which are brighter than $G = 18$ mag and occupy the same spatial region of the sky ($\sim 2^\circ$ radius around the centre of the cluster). This results in 244 potential members, 205 of which come from the analysis of the *Gaia* catalogue and the rest only from the analysis of the DANCe catalogue. The study of Cantat-Gaudin et al. (2018) and our study have 170 members in common, which is 97% of their list. From the five objects classified as members by these authors and not by our study, there are four that have probabilities > 0.5 but fall below the optimum threshold we adopted, and one that has a probability of $p = 0.2$. Again, these small differences are part of the uncertainties of the membership analysis. Besides, we find 35 members not detected by Cantat-Gaudin et al. (2018), 17 of which are also classified as members by Gaia Collaboration et al. (2018b). These members are randomly distributed within the proper motions and parallax distributions. We found three very bright members with G magnitudes 7.5, 9.5, and 10.5, and the rest fainter than $G = 14.5$ mag. The DANCe members not classified by *Gaia* in this magnitude range (39 sources with $14.5 < G < 18$ mag) are likely to be contaminants.

3.4 RESULTS

In this section, we analyse the list of members of IC 4665 we obtained in the previous section. First, we compare the empiric isochrones with theoretical evolutionary models (Sect. 3.4.1). Then, we determine the apparent magnitude distribution (Sect. 3.4.2) and the mass function (Sect. 3.4.3), which we compare to other clusters and theoretical models. Finally, we also analyse the spatial distribution of the cluster (Sect. 3.4.4).

3.4.1 *Isochrones*

The empirical isochrones provide key information for comparing and constraining the theoretical evolutionary models. In this study, we used the membership analysis of IC 4665 to report the empirical isochrone of a 30 Myr old open cluster. First, we fitted a principal curve to the members in several apparent CMDs. Then, we manually shifted the principal curve to reach the lower edge of the distribution, which is supposed to correspond to the single-star ZAMS, and we applied manual offsets were needed to better fit the lower edge of the cluster sequence. The empirical isochrones we provide are thus, the lower envelope sequence of the members and do not correspond to the principal curve, which indicates the mean position of the sequence. In Figure 3.7, we

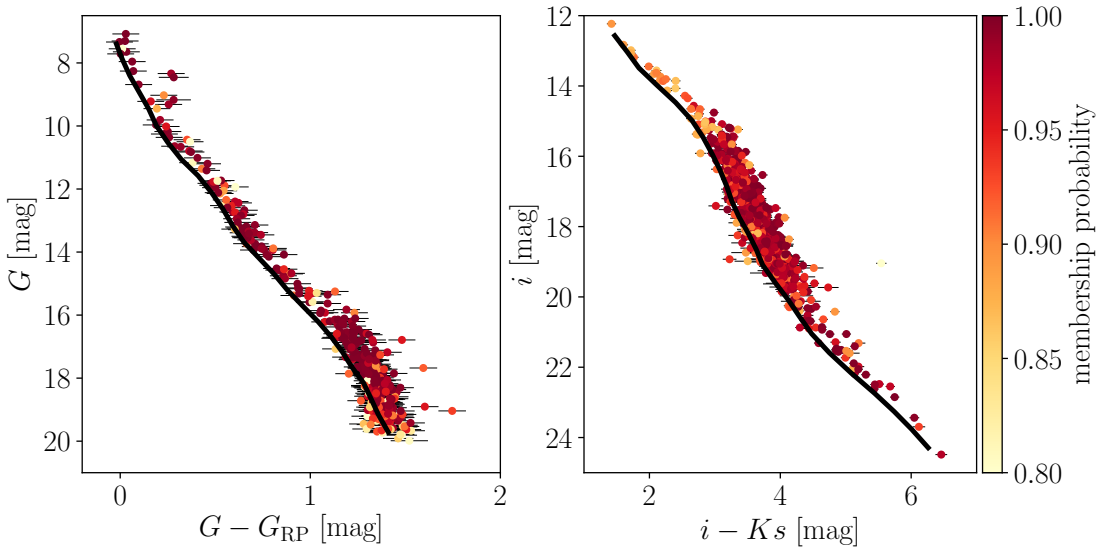

Figure 3.7. Apparent color-magnitude diagrams (CMDs) of the IC 4665 open cluster. The members are colour-coded according to their membership probability, and the empirical isochrone is overplotted (black line).

represent the empirical isochrone we obtained at 30 Myr together with the IC 4665 members and we report it in Tables C.4 and C.5.

In Figure 3.8, we compare the observed sequence of IC 4665 and the empirical isochrones to the 30 Myr models of PARSEC-COLIBRI (Marigo et al. 2017) and BT-Settl (Allard 2014) in several CMDs. We applied a distance modulus of 7.7 mag to the models, obtained from the median parallax of the *Gaia* DR2 members. We used the 88 sources with a measured extinction in *Gaia* to compute a median extinction of the cluster $A_G = 0.62$ mag (which corresponds to $A_V = 0.72$ mag using the factors in Table C.1) and a standard deviation of 0.38 mag. We corrected the theoretical models with this median extinction value.

As a general result, we see that the models show a major improvement compared to previous versions, especially in the y, J, H, Ks bands (see e.g. the comparison of the Pleiades by Bouy et al. 2015) even at such a young age. The brightest stars are only covered by the PARSEC isochrones, while the faintest are only covered by the BT-Settl models. Between $i = 11 - 15$ mag, both models agree fairly well with each other and with the observations. However, the PARSEC models start to differ from the observations at $i > 15$ mag, and in this magnitude range, the BT-Settl models are believed to be more accurate. Despite the global improvement of the models in all the photometric bands, we still find

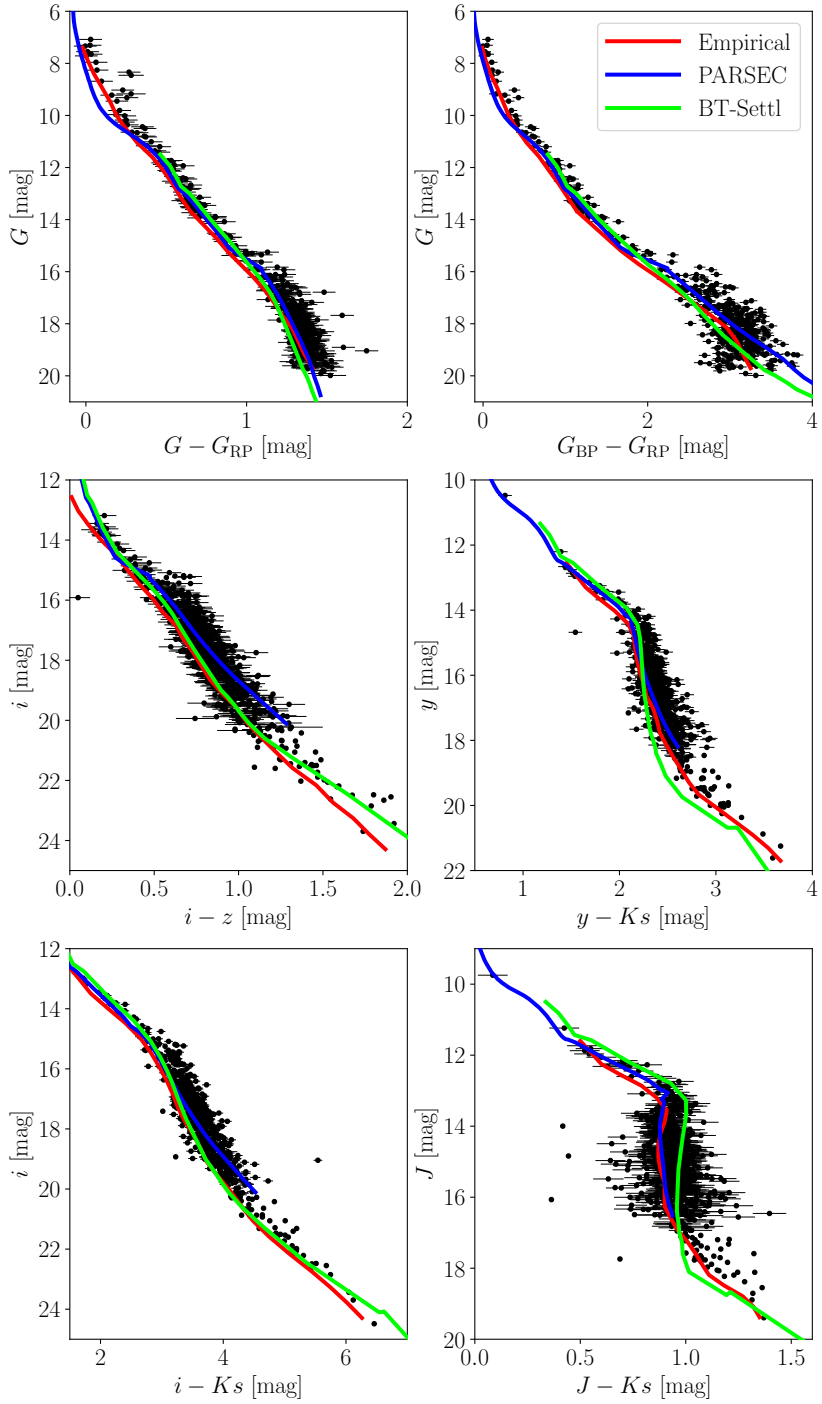

Figure 3.8. Comparison of the observations of the IC 4665 sequence (black dots) and the empirical sequence (red lines) to the models of PARSEC+COLIBRI (blue line) and the BT-Settl (green line) for an age of 30 Myr in several CMDs. The models are shifted with a distance modulus of 7.7 mag and an extinction of $A_V = 0.72$ mag.

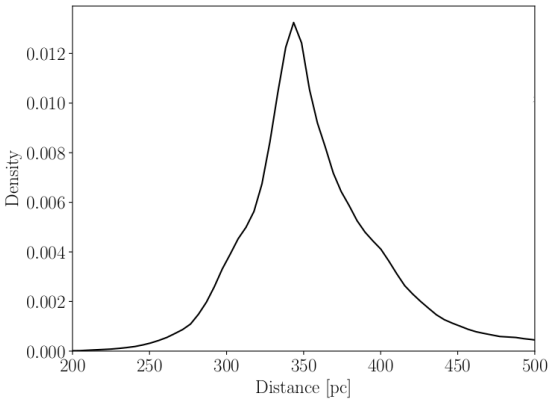

Figure 3.9. Distance distribution of IC 4665 obtained with the *Gaia* members.

a space for improvement in some of them, especially the ones involving the redder bands (see middle right and bottom-right panels of Fig. 3.8). For this, low-contaminated samples combined with accurate photometric measurements along a wide magnitude range are essential.

Regarding the *Gaia* DR2 photometry, it is noticeable that the G_{BP} band shows a larger spread for magnitudes > 18 mag. In the near-infrared, our measurements come mostly from 2MASS, which has relatively large errors beyond 14 mag, which in turn explains the larger dispersion between $14 < J < 17$ mag. Beyond this value, the measurements come from our own deeper images, and both the photometric uncertainties and the dispersion of the isochrone are significantly smaller.

To build the absolute CMDs, we first converted individual apparent magnitudes to absolute magnitudes as described in Section 2.3.1. For the sources obtained with the *Gaia* membership analysis, we used *Kalkayotl* to infer individual distances. We chose a Cauchy prior, which is recommended by the manual for clusters. The location of the prior was set to 350 pc (the approximate distance of the cluster), and the scale to 100 pc (to have a loose prior). In Figure 3.9, we show the distance distribution of the cluster obtained with the *Gaia* members. The median distance is 351 pc and the standard deviation is 55 pc.

In Figure 3.10, we show the absolute CMD of IC 4665 where we overplotted the PARSEC and the BT-Settl models, and a mass scale. We have candidate members down to masses of ~ 0.02 $M_\odot$, well within the substellar regime. We see that the PARSEC models start to differ for masses < 0.7 $M_\odot$, and in this low-mass regime, the BT-Settl models reproduce the observations more closely. For this reason, to convert magnitudes to masses, we use the PARSEC

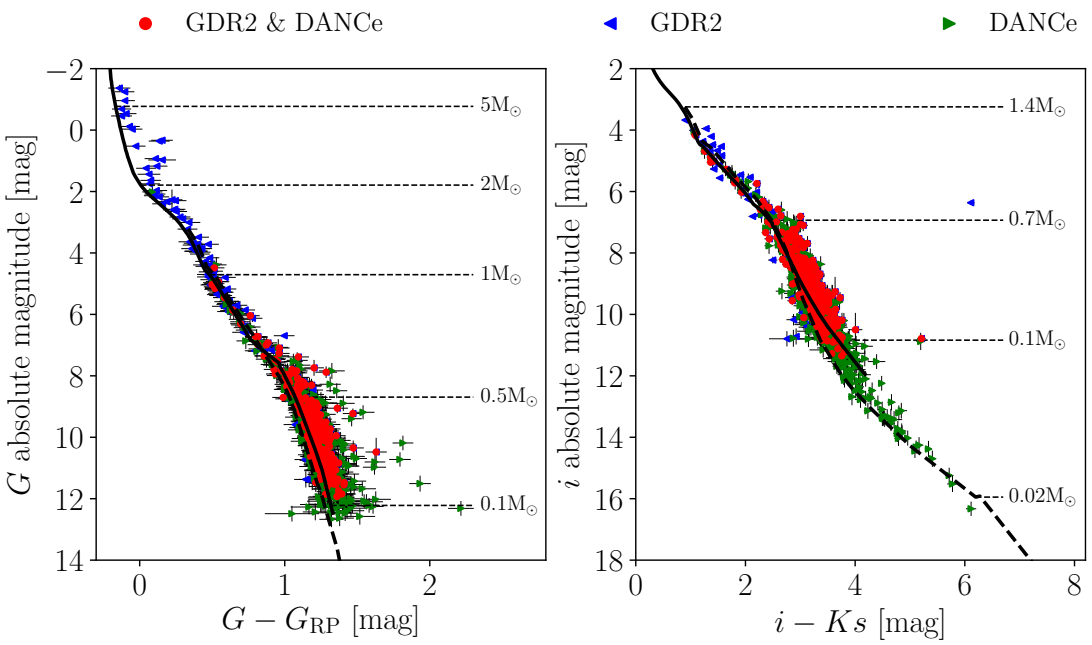

Figure 3.10. Absolute CMDs of the IC 4665 open cluster. The PARSEC+COLIBRI (solid line) and the BT-Settl (dashed line) isochrones of 30 Myr are overplotted. The members are shape- and colour-coded according to their membership classification: red circles for members in *Gaia* and DANCe analysis, blue left-pointing triangles for members only in *Gaia*, and green right-pointing triangles for members only in DANCe.

models for the high-mass stars and the BT-Settl models for low-mass stars (see Sect. 3.4.3).

3.4.2 *Apparent magnitude distribution*

The apparent magnitude distribution is a direct measurement of the number of sources observed at different brightnesses. This function is important because it does not depend on evolutionary models or distance estimates, and thus its validity does not expire (unless selection problems are present in the sample). The magnitude distribution of IC 4665 was obtained independently for the *Gaia* and DANCe members because of the different photometric bands and completeness of each catalogue. We convoluted each distribution with a Gaussian KDE with a bandwidth of 0.3 mag. We estimated the effect of contamination and completeness as a function of the magnitude using synthetic data, as in Olivares et al. (2019). Given that the contamination rate estimated this way is

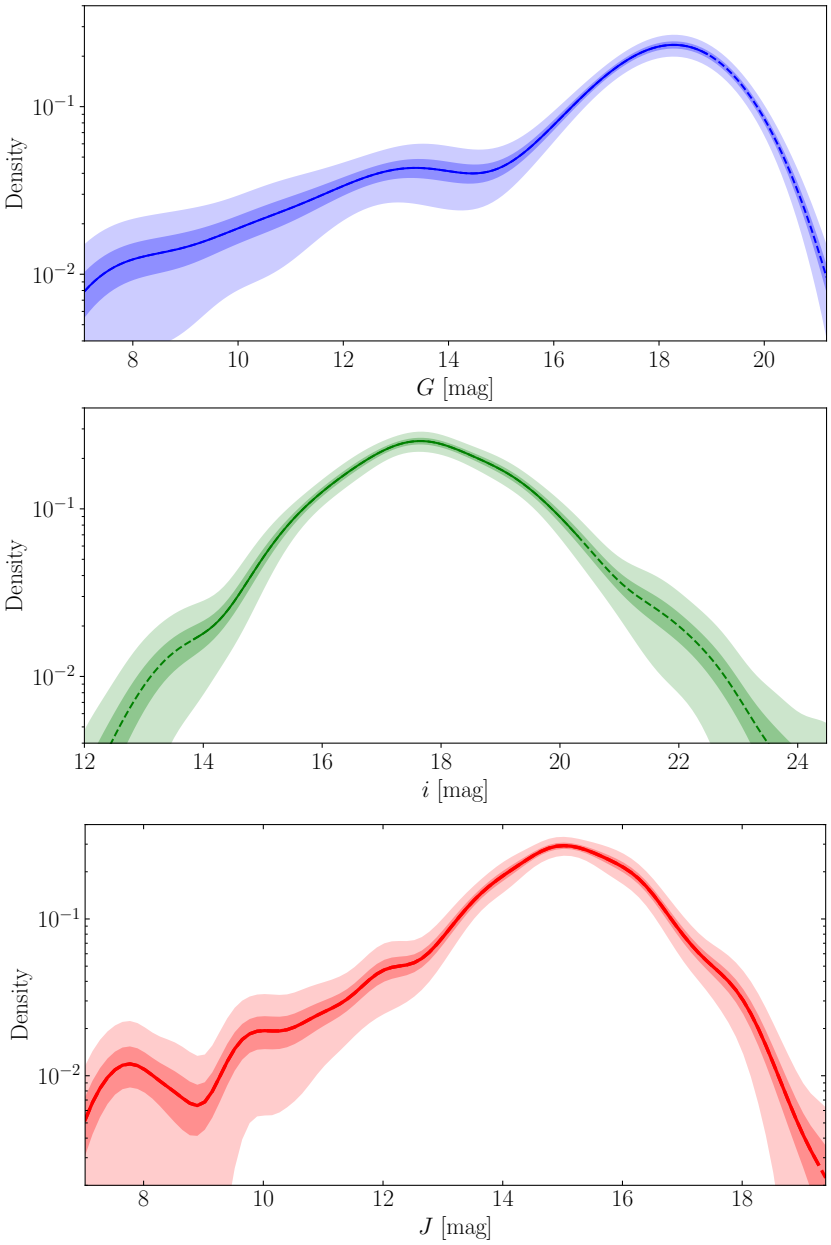

Figure 3.11. Apparent magnitude distributions of the members we found in IC 4665. Top: G magnitude distribution of the the members found with the *Gaia* catalogue (blue). Middle: i magnitude distribution of the members found with the DANCe catalogue (green). Bottom: J magnitude distribution with the members from both surveys (red, 99% of all the members have photometry in J). The shaded regions indicate the 1σ (dark) and 3σ (light) uncertainties estimated from bootstrap. The dashed lines indicate the region of incompleteness in each filter.

less than 15%, we realised that when we correct for these two effects the magnitude distribution we obtain is compatible with the original distribution within the uncertainties. For this reason, we decided to work with the magnitude distribution we obtained directly from the observations. In Figure 3.11, we show the magnitude distribution of IC 4665 in the G band for the *Gaia* members, in the i band for the DANCe members, and in the J band for all the members. These functions are available in Tables C.6, C.7 and C.8, respectively.

The apparent magnitude distribution peaks at $G = 18.2$ mag for the *Gaia* members, at $i = 17.6$ mag for the DANCe members, and at $J = 14.9$ mag for the entire sample. In all cases, this corresponds to a mass of about 0.2 $M_\odot$, according to the PARSEC and BT-Settl models and assuming an age of 30 Myr.

At $G \sim 13.5 - 15.5$ mag there is a flattening of the apparent magnitude distribution that corresponds to the Wielen dip (Wielen, Jahreiß and Krüger 1983). This feature has been reported in other open clusters such as the Pleiades (Lee and Sung 1995; Belikov et al. 1998), Praesepe and Hyades (Lee, Sung and Cho 1997), NGC 2516 (Jeffries, Thurston and Hambly 2001), NGC 2547 (Naylor et al. 2002), and Ruprecht 147 (Olivares et al. 2019). Kroupa, Tout and Gilmore 1990 explained this dip as the result of a change in the opacities in the corresponding mass range.

A change in slope seems to happen around $i \sim 21$ mag ($J \sim 17.2$ mag), which could indicate that different formation mechanisms are at work for ultracool objects in this mass range. This change in slope is nevertheless beyond our estimated limit of completeness and is not statistically significant. It is important to note that in Figure 3.11 we show the completeness in each filter (Table 3.2) which can be significantly different in terms of luminosity and mass. In consequence, while the change of slope at $J \sim 17.2$ mag is inside the completeness of the J photometry, other bands such as the i band are not complete, and thus, the membership analysis is not complete in this magnitude range.

3.4.3 *Present-day system mass function*

We estimated the mass of each source with *Sakam* (see Sect. 2.3.2). We used the PARSEC model to infer masses for the *Gaia* DR2 members and the BT-Settl model for the DANCe members. To compute the present-day system mass function (PDSMF), we convoluted the distribution of individual masses with a Gaussian KDE with a bandwidth of 0.3 (in logarithmic scale) as described in Section 2.3.3. The completeness limit in mass was propagated from the most restrictive completeness in apparent magnitude (see Table 3.2). The mass function obtained with the DANCe analysis was renormalised so that the mass

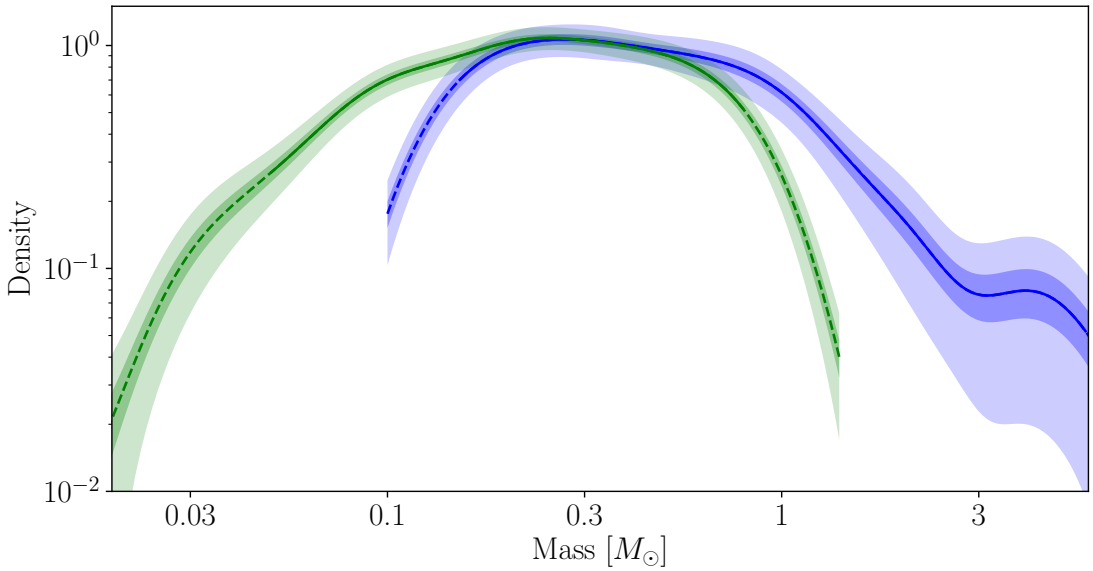

Figure 3.12. PDSMF of IC 4665 obtained from the *Gaia* (blue) and DANCe (green) members. The shaded regions indicate the uncertainty estimated from bootstrap (1σ dark and 3σ light) and the dashed lines the regions of incompleteness.

distribution functions had the same area in the region where both studies are complete (i.e. $0.15 - 0.8$ $M_\odot$).

Figure 3.12 shows the PDSMF of IC 4665 for the *Gaia* and DANCe members. We see that the two functions overlap reasonably well. There are some deviations (even inside the complete range), but they are smaller than 3σ. The robustness of our methodology, especially in the error propagation, results in a mass function with an accuracy significantly better than in the past (i.e. de Wit et al. 2006; Lodieu et al. 2011).

Several noticeable details are present in the mass function. At 3 $M_\odot$ we observe a feature that has not been reported in the literature before. It is not clear whether this is a real feature of the mass function or an artefact and the uncertainties are especially large in this mass range where there are very few members (low number statistics). Several sources of error could be responsible, in particular, the following:

- the uncertainties or errors of the transformation from apparent magnitudes to masses since it is not observed in the magnitude distribution (Fig. 3.11);
- multiplicity: the *Gaia* DR2 catalogue excluded many binary stars. Since massive stars are more often in multiple systems than their lower mass

counterparts (e.g. Lada 2006), we might be missing a larger fraction of massive members because of multiplicity;

– variability: massive stars can also display photometric variability, which is not included in our algorithm to determine individual masses. Slowly pulsating variable stars appear at three solar masses and beyond. However, they are small-amplitude variables (0.1 in V) and should not have a major impact on our selection.

The Wielen dip reported in the magnitude distribution (Fig. 3.11) is expected around 0.75 $M_\odot$ in the mass distribution but is not observed. If confirmed, this result would support the hypothesis of Kroupa, Tout and Gilmore 1990 explaining this feature as a change in opacity rather than a change in the mass function. We nevertheless note that this dip may have been masked by the KDE bandwidth. Olivares et al. (2019) indeed reported a Wielen dip in their mass function in the range $0.6 - 0.8$ $M_\odot$ with a typical scale of $\Delta \log_{10} m \sim 0.13$, smaller than our bandwidth of 0.3 (in $\log_{10} m$).

The function is rather flat between 0.1 and 1 $M_\odot$ having a maximum at 0.28 $M_\odot$. For masses < 0.1 $M_\odot$ the distribution drops. The change in slope at the very low-mass end mentioned above is not visible in the mass function.

The highest mass object has a maximum a posteriori estimate of 6.2 $M_\odot$ and the lowest mass object has a maximum a posteriori estimate of 13 M_J according to the PARSEC and BT-Settl models respectively, and assuming an age of 30 Myr. To compute the brown dwarf-to-star ratio we sampled the posterior mass distribution of each member. Then we used these samples to compute the ratio of brown dwarfs to stars within the completeness region of our sample ($6 - 0.05$ $M_\odot$) and using a mass threshold of 0.08 $M_\odot$. We did a bootstrap over all the members with 100 repetitions, and we obtained a median ratio of 0.067 ± 0.005. This value is lower than has been seen in other nearby young clusters, such as IC 348 and Taurus (Scholz et al. 2012a, and references therein). However, these studies are complete down to lower masses ($\sim 0.02 M_\odot$).

In Figure 3.13, we compare the PDSMF we obtained for the 30 Myr open cluster IC 4665 and for the Pleiades (120 Myr; Bouy et al. 2015). To facilitate the comparison, we normalised the mass function of IC 4665 over the whole mass range where it is complete. Then, we normalised the Pleiades mass function so that it had the same area in the mass range $0.05 - 0.6$ $M_\odot$, where both functions are complete. We see that in general, the two functions match fairly well within the uncertainties and the main differences are observed at the extremes of the distributions. For the high-mass domain, IC 4665 has more massive stars than the Pleiades. In this range, the number of members is quite small (only 12 objects have masses > 3 $M_\odot$ in IC 4665) leading to rather large statistical

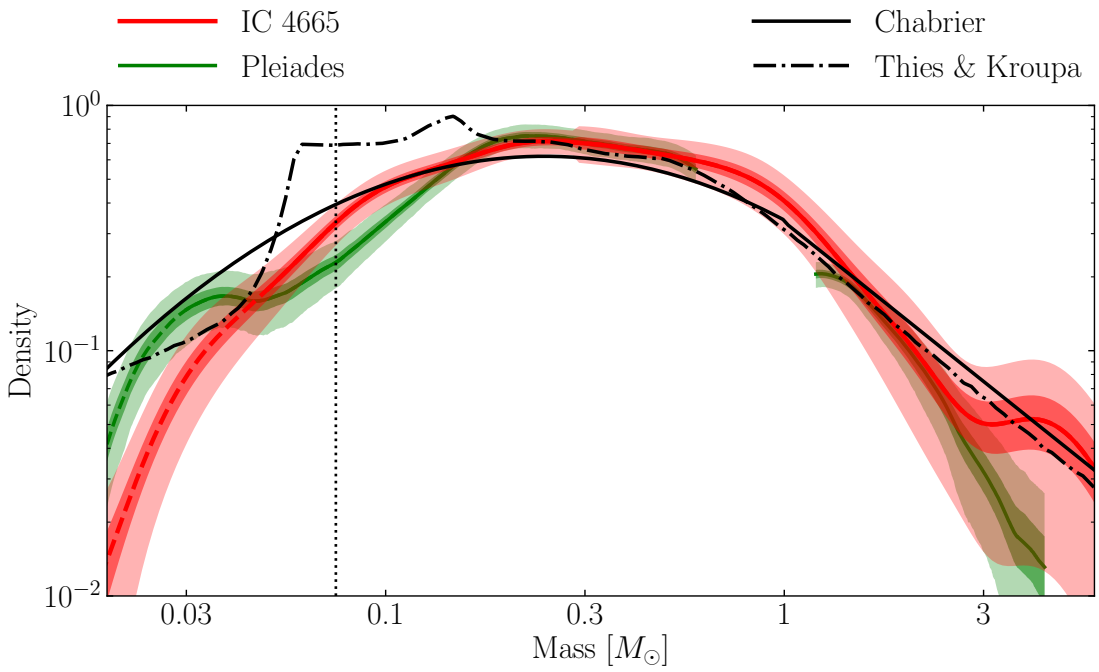

Figure 3.13. PDSMF of IC 4665 (red) and the Pleiades (green). The shaded regions indicate the uncertainties estimated from bootstrap (1σ dark and 3σ light). Overplotted are the models from Chabrier 2005 (black solid line) and Thies et al. 2015 (black dot-dashed line). The vertical dotted line indicates the hydrogen burning limit (0.075 $M_\odot$).

uncertainties. Additionally, multiplicity (more frequent among high-mass stars) and variability affect the luminosities and might contribute to the differences observed. Regarding the low-mass regime, we see that both functions are compatible (within 3σ uncertainties) down to the IC 4665 completeness limit ($\sim$ 0.05 $M_\odot$). Nonetheless, we observe that between 0.046 and 0.16 $M_\odot$ the mass function of IC 4665 might display a slight overdensity compared to the Pleiades, but only at the 1σ level. For masses lower than 0.05 $M_\odot$, the Pleiades mass function exhibits a change in slope, which the authors related to a different mechanism of star formation for this regime of masses. In the case of IC 4665, we did not detect this change in slope, perhaps because it is beyond the completeness limit of the catalogue or because it is masked by the uncertainties in evolutionary models.

In Figure 3.13, we overplotted the system IMF of two models, namely Chabrier (2005) and Thies et al. (2015), normalised in the same mass range as the mass function of IC 4665. In the high-mass regime ($>$ 1 $M_\odot$), both models assume a power law IMF with Salpeter slope that is compatible within the uncertainties

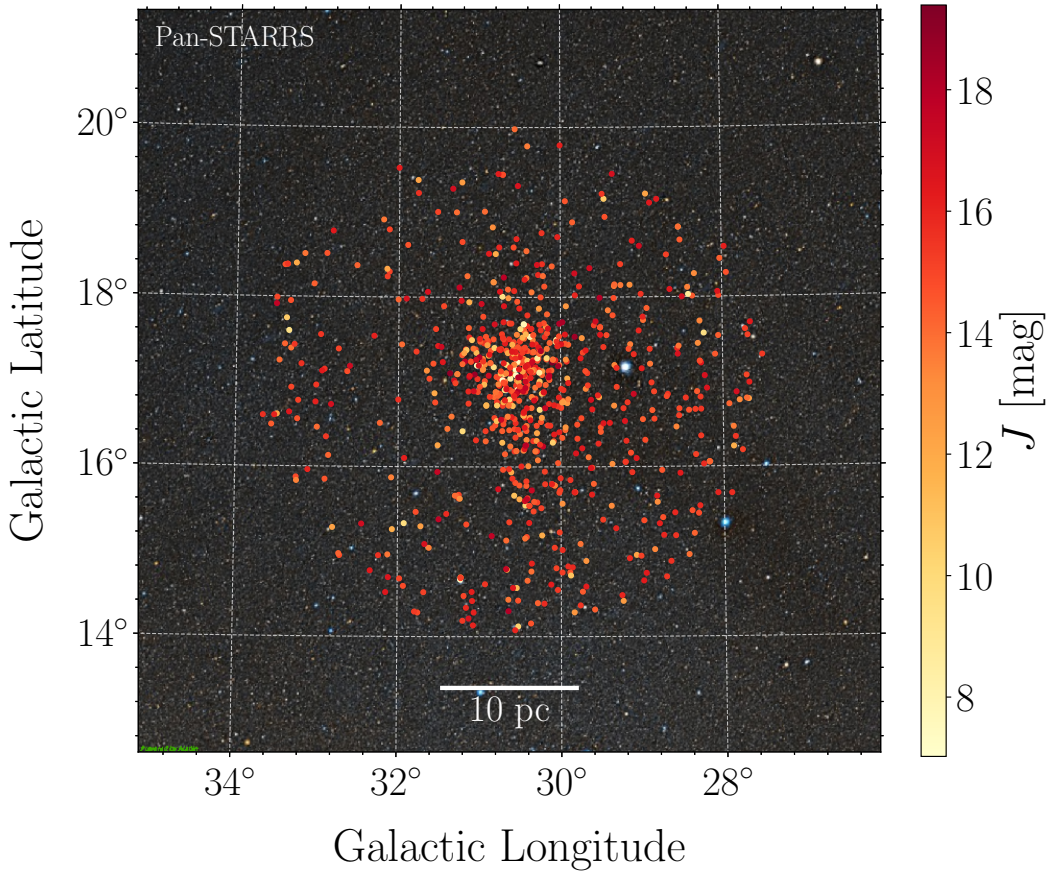

Figure 3.14. Spatial distribution of the members of IC 4665. The members are colour-coded according to their magnitude in J band. Background image credit: Pan-STARRS.

with the empirical mass function of IC 4665. For intermediate and low masses, we see that the mass function of IC 4665 is compatible with the model of Chabrier (2005) between $0.1 - 1$ $M_\odot$. For lower masses, the model predicts too many stars compared to our results. The model of Thies et al. (2015) is compatible with the empirical mass function between $0.2 - 1$ $M_\odot$, but between $0.05 - 0.2$ $M_\odot$ it also predicts too many stars. Below 0.05 $M_\odot$ the model approaches the empirical mass function and beyond this limit, our survey is not complete.

3.4.4 *Spatial distribution*

The spatial distribution of open clusters provides relevant information on their formation and early evolution. In Figure 3.14, we show the spatial distribution of the members of IC 4665 in galactic coordinates. At first glance, we can intuit some structures that depart from a pure spherical symmetry (e.g. the cluster seems elongated towards the Galactic south). In this section, we apply a statistical treatment to quantitatively assess the probability that the structures we might see are significant.

We follow the same approach as in Olivares et al. 2018, and we fit a series of parametric models to the projected spatial distribution of the cluster (i.e. in the plane of the sky). We used the same algorithm as these authors, *PyAspidistra*[2], which computes the Bayesian evidence of each model, the posterior distribution of the parameters which characterise the model, and the Bayes Factor for each pair of models. Here, we consider the same set of models as Olivares et al. 2018: the Elson, Fall and Freeman (1987) model (hereafter EFF), the Generalised Density Profile (hereafter GDP, also known as Nukker, Küpper et al. 2010), the King 1962 model (hereafter King), the Generalised King model (hereafter GKing, Olivares et al. 2018), the Optimum Generalised King model (herafter OGKing, Olivares et al. 2018), and the Restricted Generalised Density Profile (herafter RGDP, Olivares et al. 2018). For each model, the *PyAspidistra* algorithm infers the coordinates of the cluster centre, its ellipticity, and mass segregation.

Using the equatorial coordinates (J2000), the median distance of the cluster (350 pc), and the J band we ran *PyAspidistra* and obtained the Bayesian evidence for each model and the Bayes Factor for each pair of models (see Table C.10). The RGDP model is the one that shows the largest evidence in all the family models considered (spherical, elliptical and segregated). The three families of models have very similar evidences and therefore we cannot definitely discard the possibility of ellipticity or mass segregation. Moreover, our results could be biased due to the contamination in the members and the size and shape of our initial catalogues, as we discuss below.

The median parameters of each spherical model are reported in Table 3.4. The parameters α_c and δ_c correspond to the coordinates of the cluster centre in RA and Dec, respectively. The core radius (r_c) is the unit scale of the density profile, therefore it differs for each model. The α, δ, and γ parameters correspond to the exponents of the different models. The tidal radius (r_t) is only defined for the family of King's models. We refer the interested reader to Olivares et al. (2018) for a detailed discussion of these parameters. We see that the centre of the cluster is well determined by all the models at RA = 266.6°, Dec = 5.4°. All

2 https://github.com/olivares-j/PyAspidistra

Table 3.4. Median parameters for the spherically symmetric distributed models. We assumed the median distance of the cluster (350 pc) as the distance estimate.

Model	α_c [°]	δ_c [°]	r_c [pc]	γ	α	β	r_t [pc]
EFF	$266.573^{+0.070}_{-0.069}$	$5.439^{+0.092}_{-0.101}$	$2.27^{+1.22}_{-0.36}$	$2.129^{+0.314}_{-0.090}$	–	–	–
GDP	$266.580^{+0.051}_{-0.067}$	$5.439^{+0.111}_{-0.056}$	$2.10^{+0.52}_{-0.95}$	$0.18^{+0.32}_{-0.13}$	$0.20^{+0.59}_{-0.15}$	$1.81^{+0.16}_{-0.32}$	–
GKing	$266.585^{+0.049}_{-0.061}$	$5.432^{+0.102}_{-0.061}$	$1.87^{+0.44}_{-0.97}$	–	$0.21^{+0.64}_{-0.15}$	$1.67^{+0.18}_{-0.41}$	92^{+306}_{-59}
King	$266.573^{+0.073}_{-0.069}$	$5.442^{+0.090}_{-0.105}$	$2.12^{+0.91}_{-0.34}$	–	–	–	190^{+620}_{-140}
OGKing	$266.576^{+0.067}_{-0.066}$	$5.452^{+0.098}_{-0.086}$	$1.55^{+0.47}_{-0.44}$	–	–	–	55^{+50}_{-16}
RGDP	$266.583^{+0.053}_{-0.070}$	$5.433^{+0.112}_{-0.062}$	$1.98^{+0.43}_{-0.93}$	–	$0.22^{+0.58}_{-0.15}$	$1.83^{+0.18}_{-0.25}$	–

the models also agree to a core radius of $\sim$ 2 pc and the small dispersion is expected since this parameter has a different interpretation in each model. Only the family of King models are defined in terms of a tidal radius. The median values of the tidal radius reported in Table 3.4 vary from one model to another and have extremely large uncertainties. The King model with more evidence is the OGKing model which predicts a $r_t = 55$ pc, three times larger than the radius analysed in this study (18 pc). This is probably the main reason why we failed to closely constrain this parameter (see also the discussion on the main caveats at the end of the section). However, we note that to date, this study of IC 4665 is the one with the largest radius. Our estimate of the tidal radius is much larger than previous values (e.g. de Wit et al. 2006 reported a tidal radius of 1° corresponding to $\sim$ 6 pc at the distance of the cluster; however, this value was computed with a highly contaminated sample).

Here we list some of the caveats and limitations of our study of the spatial distribution.

- Our members come from a catalogue that was circularly selected, and the ends of the catalogue can clearly be seen in Figure 3.14. This can bias our results to favour a circular over an elliptic model.

- The spatial coverage of the DANCe catalogue (see Sect. 3.2.2 and Bouy et al. 2013) implies that the faintest members are more likely found in the centre. This region is where we have the highest number of images, and also the deepest ones and the ones with the longest time baseline. As a consequence, the proper motions are in general more precise in this area, which in turn influences the membership probabilities. This can have an impact both on the study of the shape (circular or elliptical) and on the study of the mass segregation.

– The tidal radius and the contamination rate are degenerate: a high contamination rate increases the density of members and the models need a larger tidal radius to explain the observations. This is especially critical at the outskirts, where we believe we might have higher contamination. The majority of our contaminants come from the DANCe catalogue with an estimated contamination rate of $\sim$ 30% compared to the *Gaia* members.

– Our members come from a catalogue that was truncated to a radius of $\sim$ 18 pc, similar to the expected tidal radius. It is highly difficult to estimate the tidal radius without having information beyond it. All these difficulties are reflected in the Bayesian evidence of each model: the family of King's models have less evidence. The truncation in radius could also bias the study on the ellipticity and segregation of the cluster.

3.5 CONCLUSIONS

In this chapter, we presented an exhaustive study of the properties of the IC 4665 open cluster. We combined the recent *Gaia* DR2 data with the deep, ground-based observations of the COSMIC DANCe project to search for members. We used the methodology described in Section 2.2 to derive Bayesian posterior probabilities for all the sources in our catalogues and found 819 members, 50% of which are new. Our members have magnitudes in the range $7 < J < 19.4$ mag, which correspond to masses of 6.2 $M_\odot$–13 M_J, according to the PARSEC and BT-Settl evolutionary models and assuming an age of 30 Myr. Using this sample we provided the empirical isochrones of the cluster, an estimate for the distance, the magnitude distribution, the present-day system mass function with unprecedented accuracy for this cluster, and a study of the spatial distribution.

Comparing our members with previous studies in the literature, we found that most of the previous studies were based on highly contaminated (up to 80%) or incomplete samples. The low motion of this cluster compared to the field (< 10 mas yr^{-1}) complicates the membership analysis. For this reason, we found a higher contamination rate in this study compared to others which use the same methodology applied to clusters with larger proper motions (Sarro et al. 2014; Olivares et al. 2019). Using synthetic data, we estimated a contamination rate of 10% for the *Gaia* members and a 13% for the DANCe members. Comparing the two studies, we estimated a contamination rate of the DANCe catalogue of up to 30% in the region of completeness. The main reason for the underestimated contamination rate in the DANCe study is the lack of parallaxes. To date, this study provides the most accurate membership analysis

by far, and thus, offers the possibility to revisit other fundamental parameters such as age. This list of members is also extremely useful to select members for follow-up studies such as a search for discs (see Chapter 6), a search for exoplanets, or spectroscopic characterisation of the ultracool dwarfs.

We found that the mass function of IC 4665 in the intermediate-mass range ($0.1 - 1$ $M_\odot$) is comparable to that of the Pleiades (Bouy et al. 2015) and to models of the IMF (Chabrier 2005; Thies et al. 2015). For higher masses, the observations have a slightly steeper slope than the models (Salpeter slope), although they are compatible at a 3σ level. In the mass range, $0.05 - 0.2$ $M_\odot$ the models predict too many low-mass stars. For masses lower than 0.05 $M_\odot$, the Pleiades have a higher proportion of members than IC 4665, but at this mass regime our study is not complete so we are missing members.

Combining our comprehensive census of the cluster with the *Gaia* DR2 parallaxes we estimated the distance of the cluster to be of 350 pc, this value is similar to what other studies recently derived (Gaia Collaboration et al. 2018b). We found that the best surface density profile for IC 4665 is the Restricted Generalised Density Profile (RGDP) model with a core radius of 2 pc. According to our study of the spatial distribution, we cannot definitely discard the possibility of ellipticity or mass segregation in this young open cluster. In the future, we aim to include a study on the velocity distribution that would allow us to characterise the kinematic and dynamic state of the cluster in the 6D space phase.

4

IMF AT 1–10 MYR: UPPER SCORPIUS AND ρ OPHIUCHUS

4.1 CONTEXT

The Scorpius-Centaurus complex (also referred as Sco-Cen or Sco OB2) is the closest OB association to the Sun. de Zeeuw et al. (1999) used the *Hipparcos* catalogue (Brown et al. 1997) to study the high mass population of this association and found 521 members. This region comprises three well-known subgroups namely, Upper Scorpius (USC), Upper Centaurus-Lupus (UCL), and Lower Centaurus-Crux (LCC). Although there are nearby dark clouds with ongoing star formation: the ρ Ophiuchi (ρ Oph) molecular cloud and the Lupus dark clouds, there are no signs of star formation in the Scorpius-Centaurus (Sco-Cen) association as a whole. The USC association is the youngest subgroup of the Sco-Cen association. Several works have been devoted to the study of the substellar population and the formation history of this region. The pioneering works of Preibisch and Zinnecker (1999) and Preibisch et al. (2002) determined an age of 5 Myr with a small age spread. They suggested a scenario in which the star formation in USC was triggered by a supernova explosion in Upper Centaurus-Lupus. Soon after ($\sim 10^5$ yr), the star formation was halted by the strong winds and the ionisation pressure of the massive stars formed in USC. About 1.5 Myr ago, the most massive star in USC exploded finally destroying and dispersing the molecular cloud surrounding USC and triggering the star formation in ρ Oph.

More recently, several studies pointed to a more complex scenario in which the age of USC is older ($\sim$ 10 Myr) with a spread of several million years (Pecaut, Mamajek and Bubar 2012). Other studies have suggested that the age spread correlates with position (Pecaut and Mamajek 2016) or effective temperature (Rizzuto et al. 2016). However, this age spread and the overall age distribution in USC are still under debate (Fang, Herczeg and Rizzuto 2017). The main difficulty for a robust and reliable age determination in USC comes from the interpretation of HR diagrams. First, theoretical evolutionary models are known to be less reliable at young ages (Baraffe et al. 2002). Additionally, the stellar variability at visible and infrared wavelengths inherent to youth leads to a significant spread in the CMD (and hence the HR diagram) that can mimic an age dispersion. Age determinations from the HR diagram are therefore not straightforward. Dynamical ages, on the contrary, should provide a more

reliable alternative as they do not rely on theoretical isochrones and are not affected by variability or extinction. In the future, we plan to determine the dynamical age of USC with the method described in Chapter 5.

Preibisch et al. (2002) provided the first determination of the mass function of USC over the stellar mass range between $20 - 0.1$ $M_{\odot}$. Since then, many studies have been devoted to the search of substellar objects (Mužić et al. 2012; Ducourant et al. 2017; Luhman et al. 2018; Lodieu et al. 2018) and to constrain the mass function in this substellar mass regime (Lodieu et al. 2007; Lodieu 2013; Slesnick, Hillenbrand and Carpenter 2008). Recently, Damiani et al. (2019) studied the stellar population of the Sco-Cen with the *Gaia* DR2 catalogue and visually identified several subgroups in the spatial distribution. They found that different kinematic populations appeared mixed in projected sky positions. In the region of USC, they identified two compact populations in the proper motion-parallax ($\mu_b - \varpi$) space, namely "USC-near" ($\varpi \sim 7$ mas) and "USC-far" ($\varpi \sim 6 - 6.5$ mas). Additionally, they found two diffuse populations (D1 and D2) occupying the whole area covered by the Sco-Cen complex. The D1 population is more concentrated in UCL but has a moderate density of stars in USC and the D2 population is mostly concentrated over USC.

In this chapter, we aim at revisiting the census of stellar and substellar objects over a large area of the sky, including the USC association and the ρ Oph star-forming region. Our comprehensive and homogeneous sample of members is especially suited for studies of the mass function and the spatial and kinematic distribution and the perfect input for age determination. These are important diagnostics to determine the star formation history of the region and the stellar (and substellar) formation mechanisms. This chapter is structured as follows. In Section 4.2, we present the observational dataset used to study the USC and ρ Oph associations. In Section 4.3, we describe the parameters of the membership algorithm and present the final list of members we obtained. In Section 4.4, we analyse the 6D structure, the age, the apparent magnitude distribution, and the luminosity and mass functions. At the end of this section, we discuss which are the formation mechanisms that can explain the large population of planetary-mass objects we found. Finally, we review the main conclusions of this work in Section 4.5.

4.2 DATA

We used the *Hipparcos*, *Gaia* DR2, and DANCe catalogues to study the region of USC and ρ Oph included in the area

$$\begin{aligned} 235^\circ < \mathrm{RA} < 252^\circ, \\ -29.5^\circ < \mathrm{Dec} < -16.7^\circ. \end{aligned} \tag{4.1}$$

These catalogues provide different astrometric and photometric parameters, precisions, and completeness limits. The *Hipparcos* catalogue provides the astrometry and photometry for the brightest stars which saturate in the other two catalogues. The *Gaia* catalogue provides an extremely precise five-parameter astrometric solution plus photometry in three bands for a large number of sources up to magnitude $G \sim 20$ mag. The DANCe catalogue provides proper motions and multi-filter photometry for sources which escape to the *Gaia* detection limit. In the following sections, we describe the details of how we obtained each of them and we review their main properties.

4.2.1 *The Hipparcos catalogue*

We downloaded all the *Hipparcos* sources in the area defined by Equation 4.1. The result is a catalogue of positions, parallaxes, proper motions, and B, V photometry for 574 sources. The median errors are 1.3 mas in parallax, around 1 mas yr^{-1} in proper motions, and tens of millimagnitude in photometry. According to Brown et al. 1997, the *Hipparcos* catalogue is complete up to $V = 7 - 8$ mag. Additionally, it is worth noting that for magnitudes $V > 7$ mag the astrometric errors start to increase significantly and then, the membership analysis is less performant and reliable in this magnitude range (increasing the contamination and decreasing the members' completeness). For this reason, we use $V = 7$ mag as the *Hipparcos* completeness limit.

4.2.2 *The Gaia catalogue*

We downloaded all the *Gaia* DR2 sources inside the spatial limits of Equation 4.1 and we kept only those with the five-parameter solution (see Appendix B.2). This sample contains positions, proper motions, parallaxes, and G, G_{BP}, G_{RP} photometry for 7 980 587 sources and the median errors are of ~ 0.5 mas in parallax, $\lesssim 1$ mas yr^{-1} in proper motions, and tens of millimagnitudes in photometry. The *Gaia* uncertainties are strongly dependent on the magnitude and we only provide a global estimate for reference. We used the same completeness limits than in the previous chapter, i.e. $7 < G < 19$ mag.

Inside the area defined by Equation 4.1 there is the NGC 6121 globular cluster with proper motions $\mu_\alpha^* = -12.48$ mas yr^{-1}, $\mu_\delta = -18.9$ mas yr^{-1} (Baumgardt et al. 2019), very similar to USC and ρ Oph. To avoid contamination from the NGC 6121 members in our sample, we selected a circular region of 12′ around the globular cluster centre (RA= 245.896°, Dec= −26.527°). With this selection, we removed 55 216 sources, a tiny fraction ($\sim$ 1%) of the catalogue. Therefore, there is a low probability that we lose members of USC and ρ Oph and, at the same time, we avoid a large fraction of potential contaminants. We did not apply this selection criterion to the *Hipparcos* catalogue since the members of the globular cluster are beyond the *Hipparcos* detection limit. Another globular cluster (Messier 80) is present in the field of our survey. At a distance of 10 kpc, its members have very small proper motions ($\mu_\alpha^* = -2.9$ mas yr^{-1}, $\mu_\delta = -5.6$ mas yr^{-1}, Baumgardt et al. 2019) and therefore, it is not expected to be a major source of contamination in our analysis.

4.2.3 *The DANCe catalogue*

We searched in the public archives mentioned in Section 2.1.1 for wide-field images inside the limits of Equation 4.1. The data found in these public archives was complemented with our own observations in the Las Campanas Swope telescope and its Direct CCD camera, DECam mounted on the Blanco telescope at the CTIO, the NEWFIRM camera mounted on the 4 m telescope at the KPNO and CTIO, the HSC mounted on the Subaru telescope at the NAOJ, and the WFC mounted on the INT. Table 4.1 gives an overview of the various cameras used for this study. Several observations found in the archives were discarded after a visual inspection because of their poor quality, limited sensitivity, or acquisition problems. Finally, we collected 80 818 individual images of 18 different instruments and obtained over the past 20 years. This is 12 times more images than the compilation we did for IC 4665 (Sect. 3.2). The raw and processed images add up to almost 120 TB and were processed and analysed on a dedicated HPC server. Over a 1.3 billion individual detections were extracted in these images. Table 4.2 gives a comparison with other popular surveys and we see that the DANCe survey of USC is comparable to the all-sky *Gaia* DR2 catalogue in terms of volume and number of sources.

The DANCe catalogue of this region contains proper motions and photometry (g, r, i, z, Y, J, H, Ks) for 40 882 164 unique sources. To optimise the number of sources with complete photometry (essential for the membership analysis, see Sect. 2.2) and accelerate the computational time of the membership algorithm, we selected the area where the coverage of most instruments was best (see Fig. 4.1). We did an elliptical selection centred in (RA = 243.5°, Dec = −23.1°)

Table 4.1. Instruments used in the DANCe catalogue of USC and ρ Oph.

Telescope	Instrument	Filters	Platescale [pixel^{-1}]	Field of view	Epoch Min./Max.	Images	Ref.
ESO VISTA	VIRCAM	z, J, H, K	$0''.34$	$1.2^\circ \times 1.1^\circ$	2010–2018	18 598	(1)
ESO VST	OmegaCAM	$u, g, r, i, z, H\alpha$	$0''.21$	$1^\circ \times 1^\circ$	2014–2017	3 302	(2)
ESO VLT	VIMOS	R, I, Z	$0''.205$	$28' \times 32'$	2007-2011	261	(3)
ESO VLT	HAWK-I	y, J, H, K^a	$0''.106$	$7.5' \times 7.5'$	2008–2015	2 752	(4)
ESO (2.2 m)	WFI	B, V, R, I^a	$0''.24$	$34' \times 33'$	2000–2017	1 562	(5)
CTIO (Blanco)	DECam	u, g, r, i, z, y^a	$0''.27$	1.1° radius	2012–2018	3 744	(6)
CTIO (Blanco)	ISPI	J, H, K^a	$0''.3$	$10.25' \times 10.25'$	2005–2010	2 214	(7)
CTIO (Blanco)	NEWFIRM	J, H, K^a	$0''.4$	$28' \times 28'$	2010–2011	1 348	(8)
KPNO (Mayall)	NEWFIRM	J, H, K^a	$0''.4$	$28' \times 28'$	2013–2014	247	(8)
CFHT	MegaCam	u, g, r, i^a	$0''.18$	$1^\circ \times 1^\circ$	2004–2016	1 395	(9)
CFHT	WIRCam	y, J, H, K^a	$0''.3$	$20' \times 20'$	2007–2017	6 579	(10)
CFHT	CFH12K	B, V, r, i, z	$0''.21$	$42' \times 28'$	2000–2002	438	(11)
INT	WFC	B, V, R, I, Z, g, r, i^a	$0''.33$	$34' \times 34'$	2000–2014	430	(12)
UKIRT	WFCAM	z, y, J, H, K^a	$0''.4$	$40' \times 40'^b$	2005-2012	34 837	(13)
SDSS	SDSS Imaging Camera	u, g, r, i, z	$0''.396$		2005–2009	2 112	(14)
Subaru	HSC	r, i, Y	$0''.17$	1.8° radius	2015–2017	160	(15)
Subaru	Suprime-Cam	g, r, i, z, V, R, I^a	$0''.2$	$34' \times 27'$	2004–2011	804	(16)
Palomar 48"	PTF	g, r	$1''.0$	$3.^\circ3 \times 2.^\circ2^c$	2010–2014	35	(17)

[a] as well as narrow and medium bands

[b] the chip layout has large gaps between detectors, and the coverage of the focal plane is only partial

[c] one of the 12 detectors is dead

References. (1) Emerson, McPherson and Sutherland (2006); (2) Kuijken et al. (2002); (3) Le Fèvre et al. (2003); (4) Pirard et al. (2004); (5) Baade et al. (1999); (6) Flaugher et al. (2010); (7) van der Bliek et al. (2004); (8) Autry et al. (2003); (9) Boulade et al. (2003); (10) Thibault et al. (2002); (11) Cuillandre et al. (2000); (12) Ives (1998); (13) Casali et al. (2007); (14) Alam et al. (2015); (15) Miyazaki et al. (2018); (16) Miyazaki et al. (2002); (17) Rahmer et al. (2008).

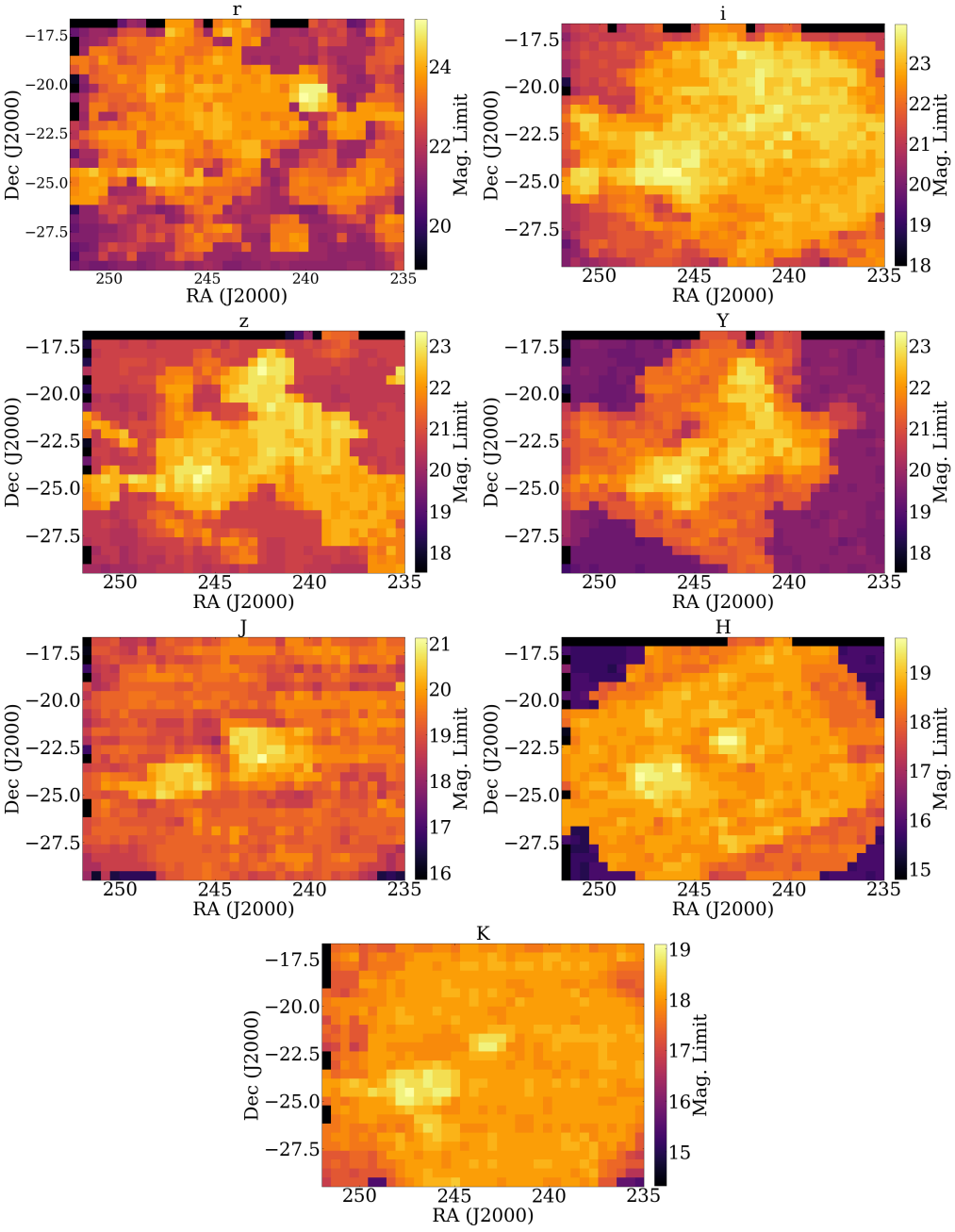

Figure 4.1. Spatial coverage of different filters of the DANCe catalogue.

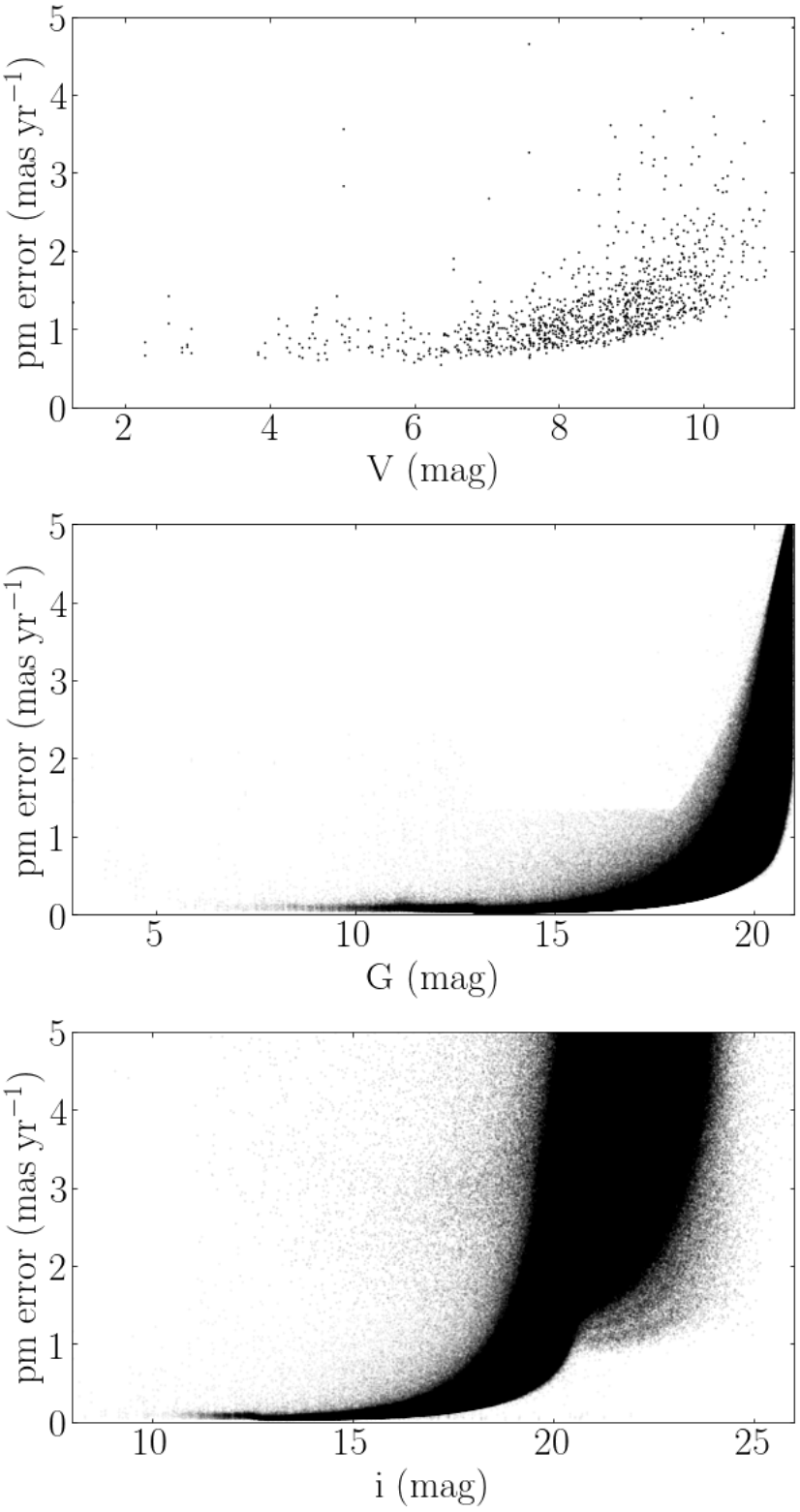

Figure 4.2. Estimated proper motion error as a function of magnitude for the *Hipparcos* (top), *Gaia* (middle), and DANCe (bottom) catalogues in the area covered by this study.

Table 4.2. Volume of data and number of sources for several large surveys.

Survey	Volume
2MASS	14 TB
SDSS	50 TB
Gaia DR2	100 TB
COSMIC-DANCE (USC)	120 TB

Table 4.3. Number of measurements and completeness limits for each photometric band in the DANCe catalogue.

Band	Num. sources		Completeness	
			Bright limit	Faint limit
g	13 372 552	(48%)	13.5	23.6
r	19 691 445	(70%)	13.5	23.5
i	26 171 446	(93%)	13.5	23.0
z	20 806 112	(74%)	13.2	22.5
Y	19 815 079	(71%)	12.1	21.7
J	13 968 999	(50%)	8.0	19.3
H	13 604 180	(48%)	8.0	18.6
Ks	2 732 406	(45%)	8.0	18.1

Notes. The total number of sources is 28 062 542.

with a semi-major axis of 8.5° in RA and a semi-minor axis of 6.4° in Dec. This selection roughly follows the coverage of the UKIDSS near-infrared survey (Lawrence et al. 2007) which was also used to define our own DECam and HSC surveys.

Similarly to what we did for the *Gaia* catalogue, we excluded the region occupied by the globular cluster NGC 6121 with the same selection criterion. The final catalogue contains 28 062 542 sources and has a median precision of < 1 mas yr^{-1} in proper motions for sources brighter than $i < 20$ mag. In Figure 4.2 we compare the precisions in the proper motions computed in DANCe as a function of the magnitude to the ones reported by *Hipparcos* and *Gaia* in the same area. We see that in the magnitude range $i = 20 - 25$ mag, beyond the detecion limit of *Gaia*, the DANCe catalogue provides proper motions with relatively good precision for a large number of sources. The precision in photometry is of the order of tens of millimagnitudes. In Figure 4.3,

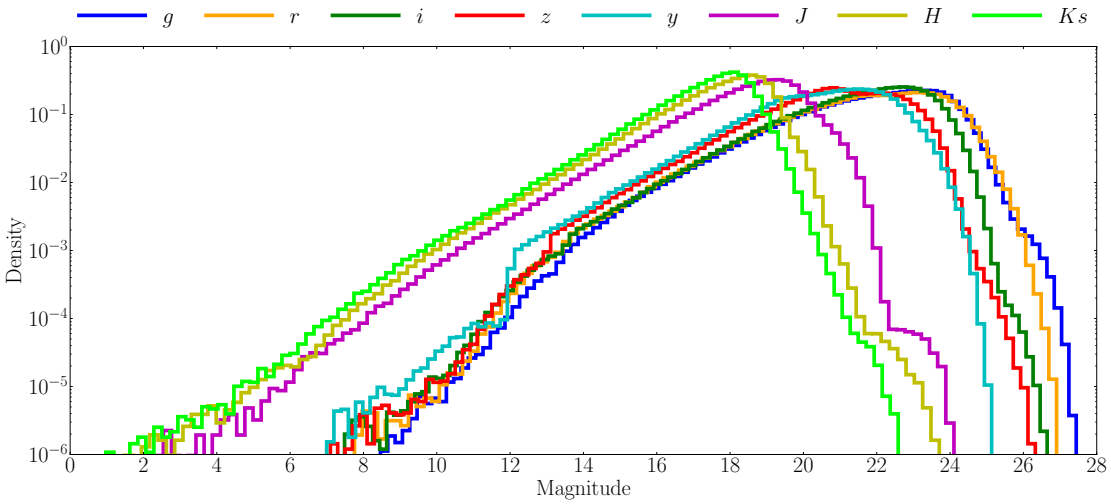

Figure 4.3. Density of sources as a function of magnitude for all the sources in the DANCe catalogue.

we show the density distribution of sources as a function of magnitude for different filters. We use the maximum of this distribution as the completeness limit in each band (reported in Table 4.3). We note that this is an approximate estimate of the completeness limit which is dependent on the extinction and is spatially variable in the DANCe catalogue.

4.3 MEMBERSHIP ANALYSIS

In this section we apply the membership algorithm described in Section 2.2 to the catalogues described in the previous section. Due to the different properties and completeness of the three catalogues, we did an independent analysis for each of them. In Section 4.3.1 we describe the parameters of the membership algorithm. In Section 4.3.2 we compare the members we obtained with the *Hipparcos*, *Gaia*, and DANCe analysis, and in Section 4.3.3 we compare our final list of members to other studies.

4.3.1 *Parameters of the membership algorithm*

To find a list of members for the USC and ρ Oph regions we used the membership algorithm described in Section 2.2 which we also applied to the IC 4665 open cluster in Section 3.3. This region, however, has several difficulties compared to the open cluster.

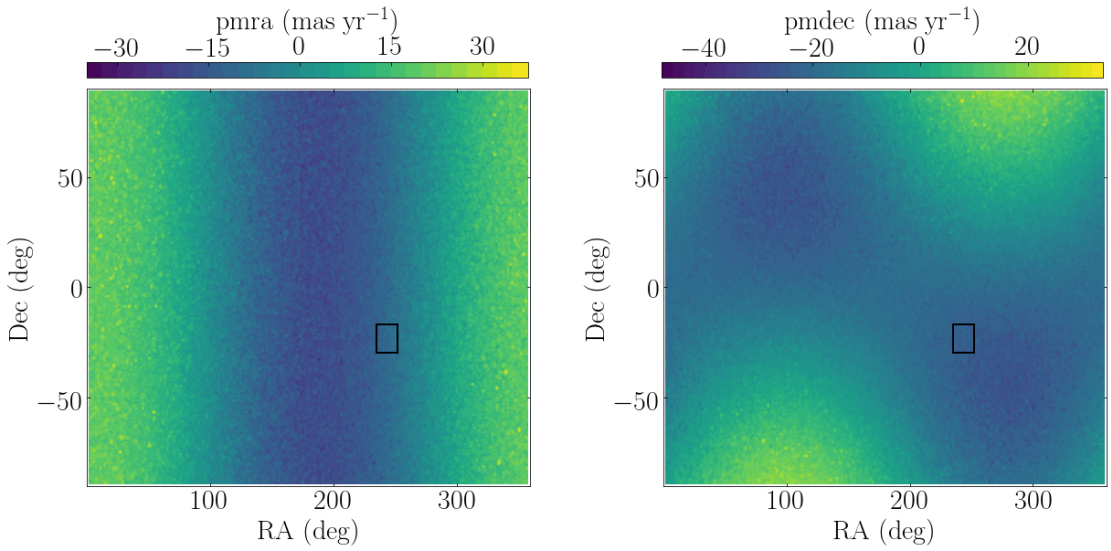

Figure 4.4. Proper motions for sources comoving with USC and ρ Oph. The area analysed in this chapter is indicated by a black rectangle.

– Young associations and star-forming regions have, in general, spatial and kinematic structures more complex than open clusters. In the following paragraphs, we describe the modifications we did to the cluster model to represent this richer substructure of USC and ρ Oph.

– The area of the sky analysed in this chapter is much larger than in the case of IC 4665, necessarily implying that the membership algorithm is computationally more expensive. Since our algorithm works in the space of the observables (proper motions and parallaxes) we checked that the projection effects were relatively low in our data. For that, we simulated members with the same 3D Cartesian velocities than the real members of the association and placed them randomly in the sky. Then, we converted their 3D velocities to proper motions and we show their distribution as a function of the 2D sky position in Figure 4.4. We can see that the area we analysed (black rectangle) is not affected by strong variations.

– The area of ρ Oph is still embedded in the parent molecular cloud which produces that the extinction of this region is variable: high at the centre of ρ Oph but moderate-low in USC (see Fig. 4.12). Our membership algorithm was not designed to deal with high levels of extinction which necessarily implies that we miss the most extincted objects.

Initial members

We compiled a list of published members in the literature. Taking the members from Damiani et al. (2019), Luhman et al. (2018), Mužić et al. (2012), Ducourant et al. (2017), and Lodieu et al. (2018) we collected 2 865 candidate members of USC and ρ Oph in the area defined in Equation 4.1. We cross-matched this list with each of our three catalogues to obtain the initial list to start each analysis. In the case of *Hipparcos*, we excluded Antares (α Sco) since it is a giant star and therefore it falls out of the empirical pre-main-sequence isochrone. For the analysis with *Gaia* and DANCe we excluded the most extinguished members since they confuse our empiric isochrone.

Representation space

For the analysis with *Hipparcos* we searched for members in the space of `pmra`, `pmdec`, `parallax`, V, $B-V$, where all the sources in the catalogue have complete observations. For the analysis with *Gaia* we used the same representation space as in Chapter 3 but excluding the G_{BP} band which is less accurate for cool dwarfs. The representation space is `pmra`, `pmdec`, `parallax`, $G_{\rm RP}$, $G-G_{\rm RP}$. In this space, 7 768 856 sources (97%) have complete observations. For the analysis of the DANCe catalogue, the representation space we used is `pmra`, `pmdec`, i, J, H, $i-Ks$. We combined the i band in the optical which is the band with the largest coverage (see Table 4.3) with the IR bands J, H, Ks where the ultracool dwarfs are best detected. With this representation space, 10 483 667 sources have observations in all the photometric bands, which represents a 37% of the catalogue. We decided not to include the g, r, z, and Y bands in the representation space because they reduced the number of sources with complete photometry, specially for the coolest objects.

Field model

The model of the field population is a GMM in the whole representation space. We explored models with different number of Gaussians and used the BIC criterion to chose the final model. Since the *Hipparcos* catalogue has a very reduced number of sources, we explored models with a number of components between 1 and 20, and selected six as the optimum choice according to the BIC. For the *Gaia* catalogue, we explored models between 20 and 180 Gaussians and chose 60 as the optimum choice according to the BIC. Finally, for the DANCe catalogue, we explored models between 60 and 300 and chose 100 components.

Table 4.4. Performance of the membership analysis obtained with different internal probability thresholds (p_{in}) for the three catalogues considered, namely *Hipparcos*, *Gaia*, and DANCe.

	Hipparcos				*Gaia*				DANCe			
p_{in}	p_{opt}	Memb	CR (%)	TPR (%)	p_{opt}	Memb	CR (%)	TPR (%)	p_{opt}	Memb	CR (%)	TPR (%)
0.5	0.97	116	17	92	0.95	2 762	1.1	99.2	0.77	2 556	2	98
0.6	0.96	108	7	95	0.96	2 698	0.9	99.2	0.78	2 458	2	99
0.7	0.94	112	7	96	0.96	2 678	1.0	99.4	0.83	2 342	1.5	99
0.8	0.95	103	5	96	0.96	2 661	0.9	99.6	0.88	2 185	0.9	99
0.9	0.96	78	3	98	0.96	2 623	0.9	99.6	0.83	2 086	0.9	99

Notes. For each internal probability threshold (p_{in}) we show the corresponding optimum probability threshold (p_{opt}), number of members (Memb), contamination rate (CR) and true positive rate (TPR). The p_{opt}, CR, and TPR were obtained with synthetic data (see text).

Cluster model

The proper motion distribution of the region of USC and ρ Oph is much more complex than that of the open cluster analysed in Chapter 3. While the open cluster had a symmetric nearly Gaussian distribution in astrometry (see Fig. 3.5), the star-forming region shows a rich substructure far from a Gaussian distribution (see Fig. 4.7) indicative of multiple kinematic populations. To model this complex distribution we used a GMM where the Gaussians are not necessarily concentric as it was the case in Chapter 3. Additionally, we explored models with larger numbers of Gaussians (between 1 and 10). Since the *Hipparcos* catalogue contains a very reduced number of sources, we found that one Gaussian was enough to model the cluster proper motions and parallaxes. The *Gaia* and DANCe catalogues are much larger and the number of Gaussians selected according to the BIC criterion was of $5-7$ for *Gaia* and $5-6$ for DANCe.

We ran the model with different p_{in} thresholds ($0.5, 0.6, 0.7, 0.8$, and 0.9) and for each we computed the optimum threshold, p_{opt}, using synthetic data. In Table 4.4, we show p_{in}, p_{opt}, and the number of members for each independent analysis (*Hipparcos*, *Gaia* DR2, and DANCe).

Final list of members

The Tables with the membership probabilities obtained with the analysis with different p_{in} values as well as the astrometry and photometry used in the

Hipparcos, *Gaia*, and DANCe catalogues will soon be available at CDS. Choosing the best solution (the best p_{in}) is a non-trivial decision and it depends on the aim of the study. Since our goal is to obtain the magnitude distribution and mass function, we need the most complete list of members. For this reason, we prefer solutions with low p_{in} values which are more complete although they can also be slightly more contaminated.

First, we compared the *Gaia* solutions and found that 2 603 (94%) were the same in all the lists. Additionally, the contamination rate and true positive rate computed with synthetic data were very similar in the five studies so we had no prior reason to prefer one list to the rest. We note that the contamination rate is around 1% only and the true positive rate always higher than 99%, according to our synthetic data analysis. Therefore, we chose the list of $p_{in} = 0.5$ as the final list of *Gaia* since it was the one with the largest number of members. Following an analogous procedure with the DANCe solution, we also chose the list of $p_{in} = 0.5$.

We compared the five solutions of *Hipparcos* and saw that 77 sources were shared among all the solutions. When we excluded the solution of $p_{in} = 0.9$ which was too restrictive (and therefore incomplete) we saw that 100 sources were shared among all the other solutions. Then, we took the *Gaia* final solution of $p_{in} = 0.5$ as reference and compared the different *Hipparcos* solutions to it. They had 65 members in common except for the *Hipparcos* solutions of $p_{in} = 0.8,\ 0.9$ which missed more *Gaia* members due to their higher incompleteness. The solution of $p_{in} = 0.5$ appeared to be significantly more contaminated than the rest according to our analysis with synthetic data. Finally, we chose the list obtained with $p_{in} = 0.7$ as a compromise between low contamination and high completeness. Although the contamination rate is slightly higher (7%) than for the *Gaia* and DANCe analysis, it is still relatively low. To this final list, we added the giant star Antares manually.

4.3.2 *Internal validation*

In this section, we do an internal validation and we compare the members obtained independently with the three different catalogues, namely *Hipparcos*, *Gaia*, and DANCe. We split this comparison into two steps. First, we analyse the overlap at the bright end between *Hipparcos* and *Gaia* and second, we analyse the overlap at the faint end between *Gaia* and DANCe.

There are 563 sources with a counterpart in the *Hipparcos* and *Gaia* catalogues and the membership probability obtained in each case is compared in Figure 4.5 (left panel). The sources classified as field stars by both studies are clustered at the bottom left of this diagram and the sources classified as cluster members

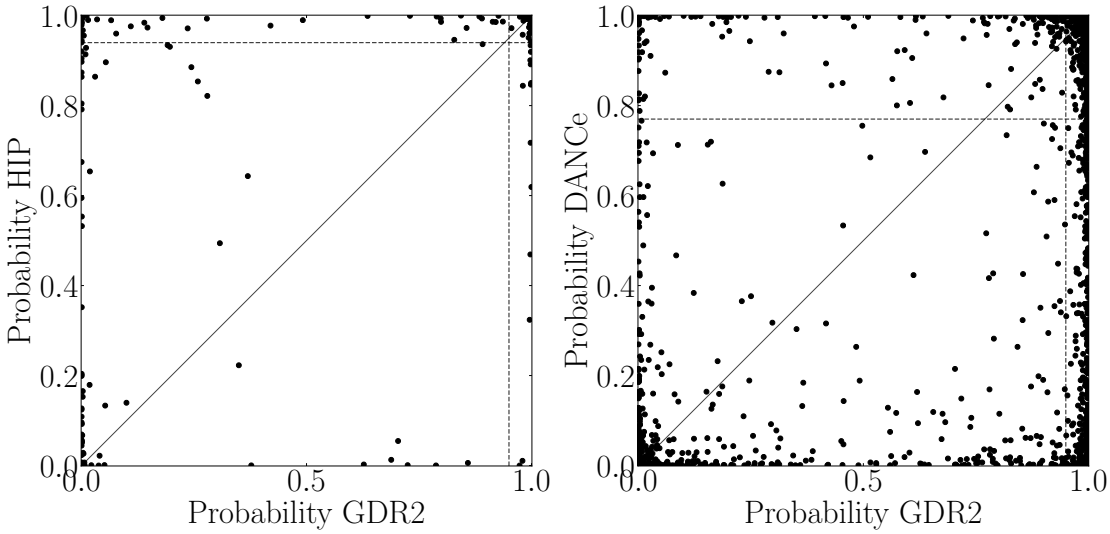

Figure 4.5. Comparison between the membership probabilities recovered by the *Gaia* and *Hipparcos* classifiers (left) and the *Gaia* and DANCe classifiers (right), for objects in both catalogues. The diagonal line represents the one-to-one relation, and the horizontal and vertical dashed lines show the optimum probability thresholds.

at the top right. These two populations represent the majority of the sources and few stars are classified as members in only one of the two studies. In the following paragraphs, we discuss these cases. In Figure 4.6 we represent the number of members as a function of magnitude recovered by each catalogue to illustrate the discussion.

– *Members in Hipparcos and Gaia.*
There are 65 sources classified as members by the two studies (yellow in Fig. 4.6 top panels). In the magnitude range where both catalogues are complete ($7 < G < 9$ mag), the majority of sources detected by both catalogues fall in this category.

– *Members in Hipparcos only.*
There are 48 sources classified as members with *Hipparcos* and not with *Gaia* (cyan in Fig. 4.6 top panels). From these, 18 stars (38%) are not in *Gaia* or are brighter than $G < 6$ mag where the *Gaia* astrometry is less reliable (Lindegren et al. 2018a). Another eight stars (17%) have a high membership probabilities in *Gaia* ($p > 0.75$) and are possibly members which are just below the optimum probability threshold ($p_{opt} = 0.95$). There are six stars with proper motions compatible with the association and which are likely binaries according to the photometry. The 16 remaining stars are on the

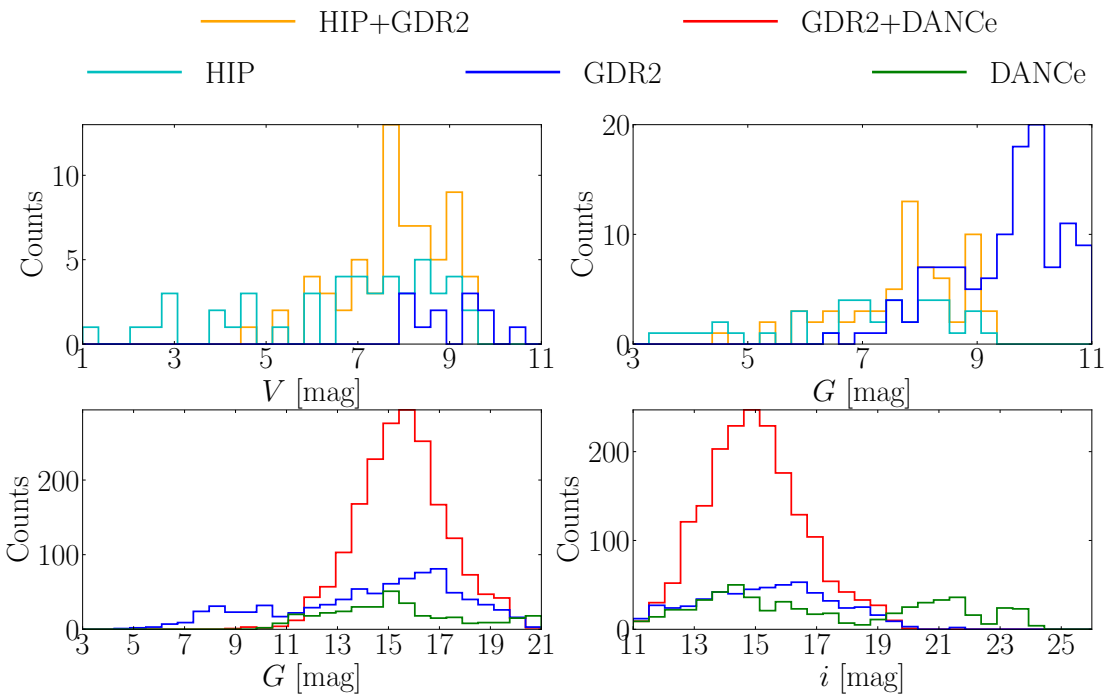

Figure 4.6. Top: V and G (left and right) magnitude distributions of the sources classified as members in the *Hipparcos* and *Gaia* studies (yellow), classified as members by *Hipparcos* but not by *Gaia* (cyan), and classified as members by *Gaia* but not by *Hipparcos* (blue). Bottom: G and i (left and right) magnitude distributions of the sources classified as members in the *Gaia* and DANCe studies (red), classified as members by *Gaia* but not by DANCe (blue), and classified as members by DANCe but not by *Gaia* (green).

photometric sequence in *Gaia* but are more dispersed in the astrometry. We checked that three of them have a large RUWE (> 1.4) and the *Gaia* astrometry is doubtful. The 13 others can not be definitely discarded and, in any case, they represent an 11% contamination which is similar to the one we estimated with synthetic data.

– *Members in Gaia only.*
There are 2 697 sources classified as members in *Gaia* and not in *Hipparcos* (blue in Fig. 4.6 top panels) but only 13 have a counterpart in *Hipparcos*. Ten of them have high membership probabilities with *Hipparcos* ($p \gtrsim 0.5$) and are probably members that fall just below our optimum probability threshold ($p_{opt} = 0.95$). Another has significantly different astrometry between the two surveys. Finally, there are two sources which are at the

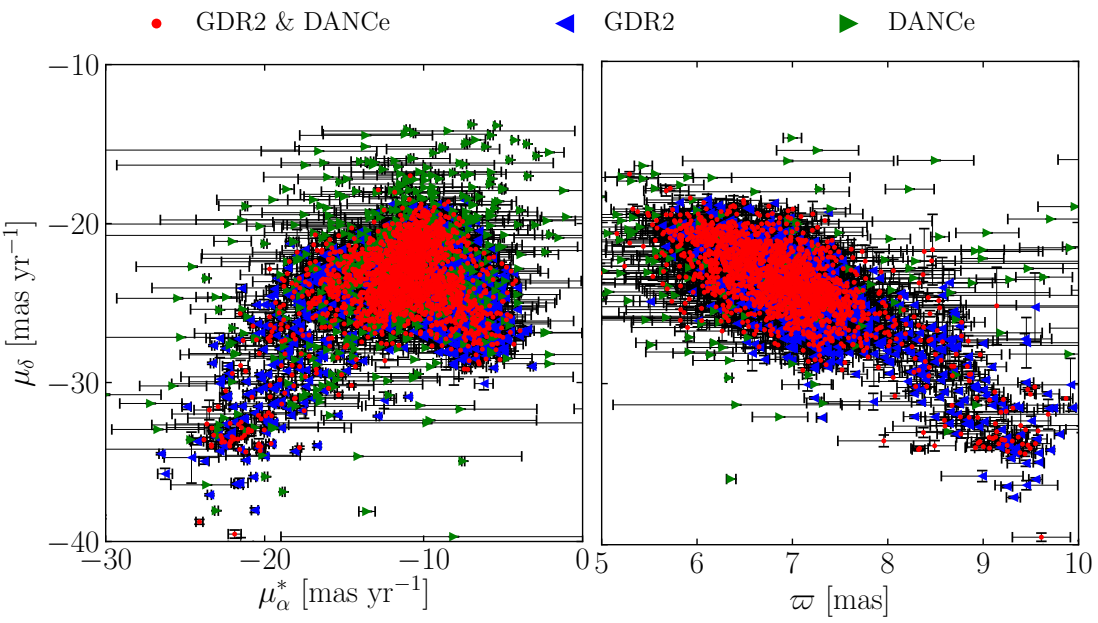

Figure 4.7. Vector point diagram (left) and parallax–proper motion diagram (right) of USC and ρ Oph. The members are shape- and colour-coded according their origin: *Gaia* and DANCe analysis (red circles), only *Gaia* analysis (blue left-pointing triangle), and only DANCe analysis (green right-pointing triangle).

very limits of the astrometric distributions of the cluster population and therefore, their membership is more uncertain.

In the second part of the internal validation, we compare the membership probabilities of the 5 555 948 sources with a counterpart in the *Gaia* and DANCe catalogues. Similarly to the validation in the bright domain, we see that the majority of sources are clustered at the bottom left (field stars) and top right (cluster members) corners of Figure 4.5 right. Here we discuss different cases in which sources are classified as members by both or only one of the studies.

– *Members in Gaia and DANCe.*
There are 1 913 sources classified as members by the *Gaia* and DANCe studies (red in Fig. 4.6 bottom panels). These are the great majority of sources in the region where both studies are complete ($7 < G < 9$ mag).

– *Members in Gaia only.*
There are 851 sources members in the *Gaia* analysis and not in DANCe (blue in Fig. 4.6 bottom panels). From these 301 (35%) are missing one or

several photometric bands of the representation space, which results in lower probability after marginalisation. The great majority are either bright and saturated in the DANCe images or are in the surroundings of the area covered by DANCe (implying that they have less observations, more missing photometry, and larger uncertainties). Another important fraction 353 (41%) seem to have a high extinction in the $i - Ks$ colour (see blue triangles on the right panel of Fig. 4.14) and are indeed very concentrated in the region of ρ Oph where the extinction in higher. Figure 4.14 shows the absolute CMD in the photometric representation space used in the *Gaia* (left) and DANCe (right). It illustrates how the extinction vector has a larger angle compared to the empiric isochrone in the DANCe space than in the Gaia space, making the DANCe analysis more sensitive to extinction. Another 45 stars (5%) are not classified as members by DANCe according to our probability threshold but have membership probabilities larger than 0.5, suggesting that they are indeed members. The rest 152 objects are spread in the space of positions and are probably part of the diffuse populations (see Sect. 4.4.1) that are modelled slightly differently in the *Gaia* and DANCe studies.

– *Members in DANCe only.*
There are 645 sources members in the DANCe analysis and not in *Gaia* (green in Fig. 4.6 bottom panels). From these, 297 (46%) do not have the five-parameter solution in the *Gaia* DR2 catalogue. Other 191 (30%) have a parallax < 5 mas (i.e. distances > 200 pc). From these, 60 have large parallax errors ($> 10\%$) or a large RUWE (> 1.4) indicating their *Gaia* astrometry is doubtful and they can not definitely be discarded as members. The other 131 objects are likely contaminants and constitute a 5% of contamination compared to *Gaia*. This contamination rate is a bit larger than the one we estimated with synthetic data (see Table 4.4) because the DANCe analysis lacks the parallaxes. We do not have any strong argument to discard the remaining objects. Some of them have relatively high membership probabilities in the *Gaia* study and the rest can be attributed to the different models of the cluster population.

4.3.3 *External validation*

A large number of studies have been covering the area of USC and ρ Oph and an individual comparison of our members with each of them is not practical. In this section, we selected some of the most recent studies with special attention to those focused on the substellar regime. In each case, we cross-matched our

list of 3 455 members with their list of members using a maximum separation of 1″. We found that 700 of our members (20%) were not previously identified by any of these studies and thus, are likely new members.

Damiani et al. (2019)

This is the most complete study of the entire Sco-Cen association based on *Gaia* DR2 data. A total of 2 397 members of their study are covered by our data, 98% of which are also identified as members in our study. The majority of members we miss have high membership probabilities (> 0.5) in our study but are below our probability threshold. Additionally, we found 751 members which have the five-parameter astrometric solution in *Gaia* and which were not identified by these authors. This represents an increase of a 30% to the number of members that Damiani et al. (2019) found in the area covered by our study.

Lodieu et al. (2018)

Lodieu et al. (2018) combined photometry and spectroscopy to identify planetary-mass objects in USC. They found 22 objects with spectral type later than M9 from which 15 are also identified as members in this work. There is one source with proper motions very discrepant from the mean which is probably a contaminant. Two other sources do not have i photometry which is a very important band for our membership algorithm since $i - Ks$ is the only colour in the representation space we used. Additionally, four other sources are scattered around the empirical isochrone in the $i - Ks$ space. We have checked that these six stars are consistent in the proper motion space and with the empirical isochrone in the IR (with the $J - Ks$ and $H - Ks$ colours). Therefore, they are likely members that our algorithm is missing because at the ultracool regime the density of members is very low and the observational uncertainties high.

Mužić et al. (2012)

In the context of the SONYC (standing for substellar objects in nearby young clusters) project, Geers et al. (2011) and Mužić et al. (2012) obtained deep optical and near-infrared images to select members of ρ Oph which were later used for spectroscopic follow-up. They spectroscopically confirmed 23 candidates, eight of which are also identified as members in our study. Since all these members are located at the core of ρ Oph, they are highly extincted which is the most likely reason why we miss an important fraction of their members (65%). However, it is worth noting that the majority of these objects have proper motions rather far away from the locus of members, suggesting that they might

be contaminants or that they belong to the overlapping dispersed populations rather than to ρ Oph.

Ducourant et al. (2017)

Ducourant et al. (2017) combined multi-epoch images to measure proper motions in a way similar to the present work. The authors used their proper motion measures to identify 82 members of ρ Oph from which we recover 26 in our study. More than half of the members we missed do not have *i*-band photometry in DANCe or are highly extincted, two extremely unfavourable situations for our algorithm. Some others appear to be contaminants according to our improved proper motions. There are a few objects which have proper motions not so different from the cluster distribution but with very low probabilities. The reason is that this association has a wide distribution in proper motions making the separation between the cluster and field populations more difficult.

4.4 RESULTS

The ultimate goal of this section is to estimate the mass function of USC and ρ Oph. This is a multi-step process which involves first transforming apparent to absolute magnitudes and eventually converting the absolute magnitudes to masses. This last step can be achieved using theoretical evolutionary models, with several important drawbacks. First, the models are fairly uncertain at such young ages (see e.g. Baraffe et al. 2002 for a detailed discussion) and various models predict significantly different luminosities and masses. Second, the luminosity of ultracool objects varies fairly rapidly over the first 10 Myr of their life, and the uncertainty on the age (or ages) in these regions translates in significant uncertainties on the mass function.

The large area covered by our study includes populations at different evolutionary stages. On the one hand, there is still star formation going on in the core of ρ Oph where the age must be less than 3 Myr (Greene and Meyer 1995). On the other hand, the age of USC is not well established and different methods result in different ages ranging between $5 - 12$ Myr. Age estimates based on the analysis of the HR diagram show a large dispersion and tend to predict older ages than other methods based on, for example, eclipsing binaries or expansion rates (David et al. 2019; Pecaut and Mamajek 2016; Feiden 2016). For this reason, at the beginning of this section, we made an effort to study the age of the USC association from kinematics (in Section 4.4.1) and from CMDs and the HR diagram (in Section 4.4.2). In Section 4.4.3, we show the magnitude distribution in different filters. In Section 4.4.4, we present an estimate of the

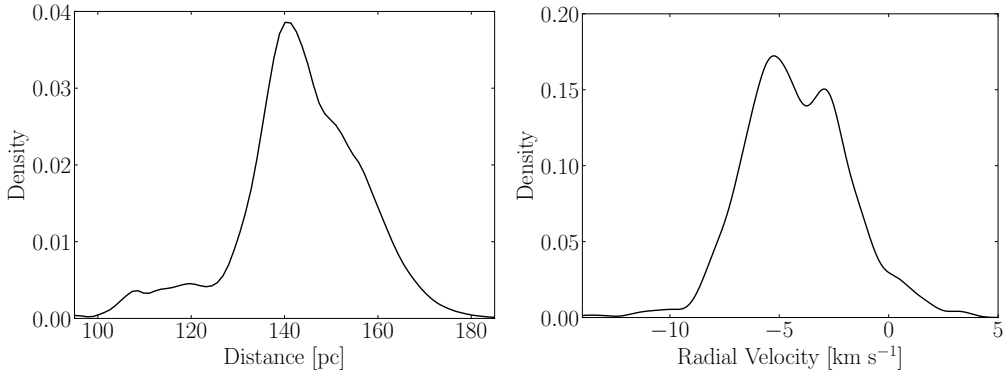

Figure 4.8. Left: Distance distribution of USC and ρ Oph members obtained with the *Gaia* analysis. The individual distances have been obtained with *Kalkayotl*. Right: Radial velocity distribution of USC and ρ Oph members obtained with the *Gaia* analysis with APOGEE radial velocities. Only the sources which are within three times the median absolute deviation have been considered.

luminosity and mass function of this region and in Section 4.4.5, we discuss the frequency of different formation mechanisms to explain the presence of the large population of substellar objects we identified.

4.4.1 *Structure in the 6D phase space*

To study the 6D phase space we need the 2D sky positions and proper motions plus the parallax and radial velocity. The list of members obtained with the *Gaia* catalogue have the five-parameters solution and thus, allow us to study the 3D distributions in positions once the parallaxes are converted to distances. Although 98% of the sample has parallax errors of less than 10%, we decided to infer Bayesian distances with the *Kalkayotl* algorithm to properly estimate and account for uncertainties in the individual distances. We tested a uniform and a Gaussian prior and found very similar results, with differences smaller than the individual distance uncertainties. Eventually, we kept the distances obtained with the Gaussian prior with a locus and scale of 145 pc and 45 pc, corresponding to the median and three times the standard deviation of the distribution of distances obtained inverting the parallax. For each source, we report the median of the a posteriori distribution and the percentiles p_{16} and p_{84}. In Figure 4.8 left panel, we show the distance distribution of the region obtained by sampling all the individual distance distributions. The median distance of the entire region is of 143 pc with a standard deviation of 14 pc. A group of 257 stars located in front of the main group at $100 - 125$ pc stands out. These are very spread in sky positions and have kinematics indistinguishable from

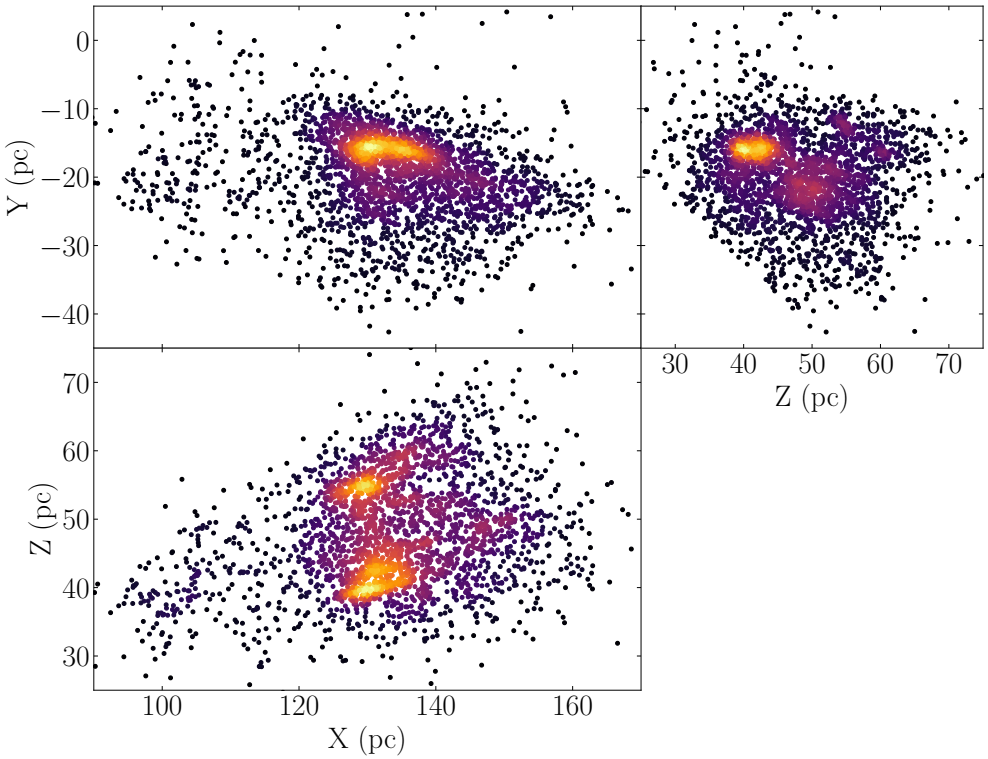

Figure 4.9. 2D projections of the heliocentric Cartesian positions of the *Gaia* members of USC and ρ Oph. The sources are colour-coded with the density (in arbitrary units).

the rest of the region. The majority of these stars were identified by Damiani et al. (2019) to be part of a diffuse population (D1) which is more concentrated in UCL but overlaps with USC.

We used the Bayesian distances to obtain the 3D Cartesian heliocentric positions X, Y, Z, where X points towards the Galactic centre, Y towards the direction of Galactic rotation, and Z towards the north Galactic pole. In Figure 4.9, we show the 2D projections of the positions of *Gaia* members. We can immediately see that this region has a complex spatial structure with different overdensities. It is most elongated in the radial direction (X) which is closely aligned to the line of sight. This direction is where the uncertainties are larger but a basic deconvolution of the uncertainties shows that the larger dispersion in the radial direction is not only due the uncertainties (see Table 4.5). At $X < 120$ pc, we see the diffuse population (D1 according to Damiani et al. 2019) which is in front of the main group. When we represent the two compact popu-

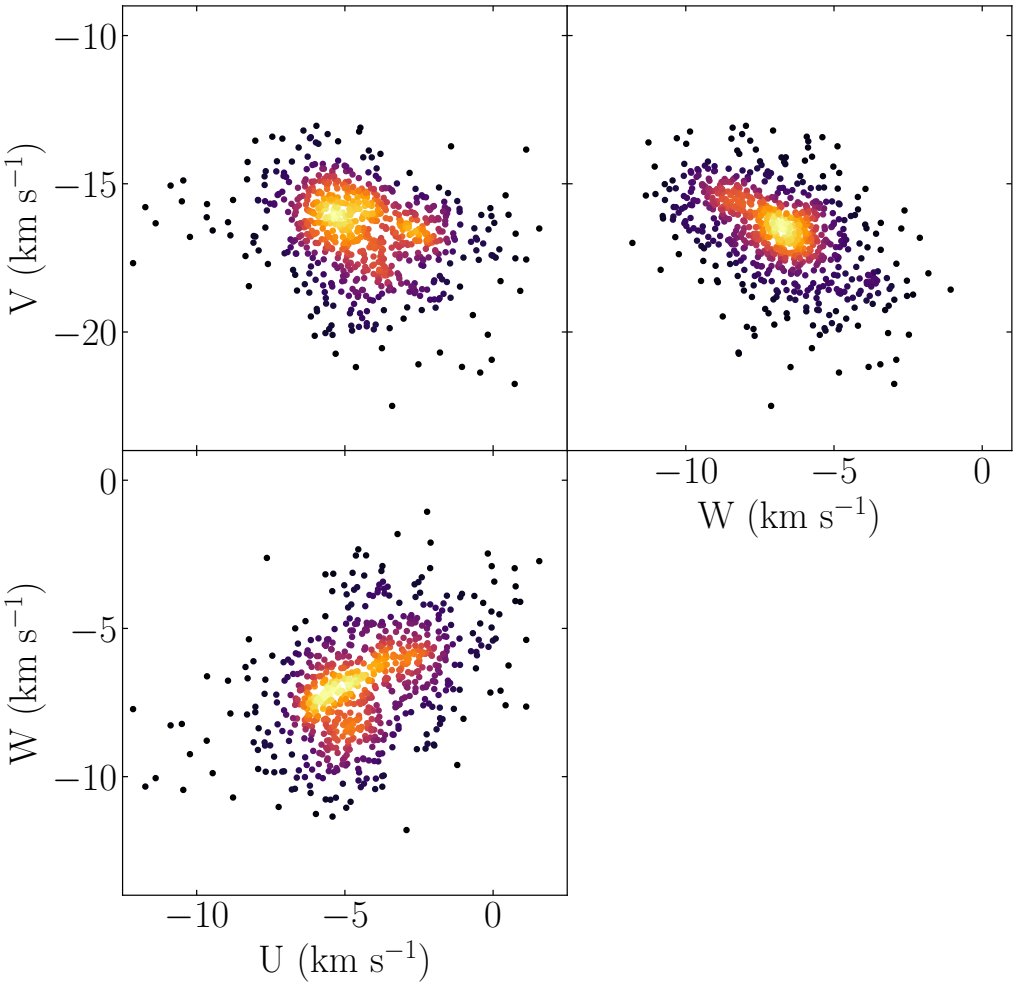

Figure 4.10. 2D projections of the heliocentric Cartesian velocities of the *Gaia* members of USC and ρ Oph with radial velocity in APOGEE. The sources are colour-coded with the density (in arbitrary units).

lations identified by Damiani et al. (2019), namely "USC-near" and "USC-far", in our 3D map we find that they are relatively mixed. These two populations were identified in the proper motion-parallax ($\mu_b - \varpi$) plane but their selection should be revised in the Cartesian 6D space phase.

To study the 3D spatial kinematics, we need to complement the *Gaia* astrometry (positions and proper motions) with radial velocities. The *Gaia* DR2 catalogue provides a radial velocity measurement for 254 sources (9% of the

Table 4.5. Parameters of the distribution in positions (in pc) and in velocities (in km s^{-1}) of the *Gaia* members of USC and ρ Oph.

Positions											
X	Y	Z	$\sigma_{obs,X}$	$\sigma_{obs,Y}$	$\sigma_{obs,Z}$	$\sigma_{err,X}$	$\sigma_{err,Y}$	$\sigma_{err,Z}$	$\sigma_{int,X}$	$\sigma_{int,Y}$	$\sigma_{int,Z}$
133.43	−18.85	47.23	12.76	6.37	8.36	2.31	0.33	0.83	10.45	6.04	7.53
Velocities											
U	V	W	$\sigma_{obs,U}$	$\sigma_{obs,V}$	$\sigma_{obs,W}$	$\sigma_{err,U}$	$\sigma_{err,V}$	$\sigma_{err,W}$	$\sigma_{int,U}$	$\sigma_{int,V}$	$\sigma_{int,W}$
−4.53	−16.5	−6.88	2.00	1.43	1.74	0.08	0.27	0.17	1.92	1.16	1.57

Notes. Columns indicate: (1–3) median of the distribution, (4–6) standard deviation, (7–9) median errors, and (10–12) a rough estimate of the intrinsic dispersion, computed as $\sigma^2_{int} = \sigma^2_{obs} - \sigma^2_{err}$.

Gaia members) with a median radial velocity error of > 2 km s^{-1}. To study the kinematics of the region, we need a higher precision, below the km s^{-1}, and ideally of the order of the precision in tangential velocities (~ 0.2 km s^{-1}). We searched the Apache Point Observatory Galactic Evolution Experiment (APOGEE) radial velocity catalogue (Jönsson et al. 2020) DR16 and obtained a radial velocity measurements for 765 sources (28% of the *Gaia* members) with a median velocity error of only 40 m s^{-1}. Around 25% of the stars have more than one measurement of the radial velocity. In this case, we computed the final error in radial velocity as the squared sum of the APOGEE error and the radial velocity scatter. With this procedure, the median uncertainties in the radial velocity are ~ 0.1 km s^{-1}. We used the median radial velocity of the sample, -4.4 km s^{-1}, and three times the median absolute deviation of 2 km s^{-1} to filter radial velocity outliers. We identified 31 objects (4%) in the sample which might be spectroscopic binaries or contaminants. We estimated a contamination rate of ~ 1% in the *Gaia* members with synthetic data (see Table 4.4), which is comparable to the fraction of radial velocity outliers. In Figure 4.8 right panel, we show the radial velocity distribution of the radial velocity confirmed members. The distribution is clearly bimodal with one peak around -5 km s^{-1} and another at -3 km s^{-1}. We verified that these two peaks do not correspond to separated structures in the space of positions. On the contrary, the radial velocity is strongly correlated with the U velocity and the two peaks in the radial velocity distribution also correspond to the different structures seen in Figure 4.10.

We converted the *Gaia* astrometry plus the APOGEE radial velocities to the 3D Cartesian heliocentric velocities U, V, W with a peculiar solar motion of $(U_\odot, V_\odot, W_\odot) = (11.1, 12.24, 7.25)$ km s^{-1} (Schönrich, Binney and Dehnen 2010). In this system, U points towards the Galactic centre, V towards the direction of Galactic rotation, and W towards the north Galactic pole. In Figure 4.10, we show different 2D projections of the 3D heliocentric velocities for the subset of 734 radial velocity confirmed candidates. The median velocity and standard deviation of this sample are reported in Table 4.5 and are similar to the ones observed in other young associations (e.g. β Pic, see Section 5) and to molecular clouds in nearby, low-mass star-forming regions (Hennebelle and Falgarone 2012, , and references therein). The precision of the 3D velocities is excellent, with uncertainties of the order of 100 m s^{-1} and should be enough to perform a study of the substructure of this region. In this thesis, we only did a preliminary examination of the 6D structure and leave for the future a more robust analysis with more elaborated algorithms and with a larger coverage of radial velocities. We have already started a survey to collect ground-based radial velocities for the members identified in USC. So far, we have spectra from the STELLA échelle

spectrograph (SES) mounted on the STELLA 1.2 m telescope in Tenerife, the Network of Robotic Echelle Spectrographs (NRES) mounted on a 1 m telescope at Las Cumbres Observatory (LCO), and the CHIRON spectrograph mounted on a 1.5 m telescope in CTIO.

In Chapter 5, we describe a robust methodology to study the dynamical age of young associations. Here, we do a much more simple attempt to estimate an expansion age and leave a more exhaustive analysis for the future. In Figure 4.11, we show the velocity as a function of the position in the three Galactic directions, namely towards the Galactic centre (X, U), towards the direction of rotation (Y, V), and perpendicular to the Galactic plane (Z, W). In each case, we fitted a linear relationship where a positive slope indicates an expansion and a negative slope a contraction. We can see that in the two coordinates on the Galactic plane (top and middle panels) the slope is positive indicating an expansion. In the vertical direction (bottom panel) the slope is zero, indicating no sign of contraction nor expansion. We converted the two positive slopes into an expansion age using the relation

$$\tau = \gamma^{-1} \cdot \kappa^{-1}, \tag{4.2}$$

where $\gamma = 1.022\,712\,165$ s pc km^{-1} Myr^{-1} is a conversion factor and κ is the slope of the linear fit. With this relationship, we obtained an expansion age of $\tau_X = 24 \pm 6$ Myr and $\tau_Y = 7.0 \pm 0.5$ Myr in the direction of the Galactic centre and the direction of the Galactic rotation, respectively. We propagated the uncertainties in the fit to the expansion age however, these might be underestimated (see Chapter 5 for an extended discussion on the age uncertainty). The age we obtained in the radial direction is larger than the age of USC and also has a large uncertainty. This direction is strongly correlated with the line of sight where we found evidence of substructure (see the radial distribution in Fig. 4.8 right) and the expansion age should be computed for each population once the structure is well defined. On the contrary, in the direction of rotation we obtained a very precise age which is compatible with other independent age estimates (e.g. based on eclipsing binaries, David et al. 2019).

Wright and Mamajek (2018) did a very similar analysis to the one presented here and only found signs of expansion in the Y direction with a slope of $\kappa_Y = 0.074^{+0.025}_{-0.027}$. This value is smaller to what we obtained and thus, corresponds to an older expansion age 13 ± 5 Myr. The main differences between the two studies are the selection of members and the astrometric and spectroscopic precision. They used a hundred candidate members from the literature and the astrometry from *Gaia* Data Release 1 (*Gaia* DR1) plus a compilation of radial velocities with a median error of 2.3 km s^{-1}.

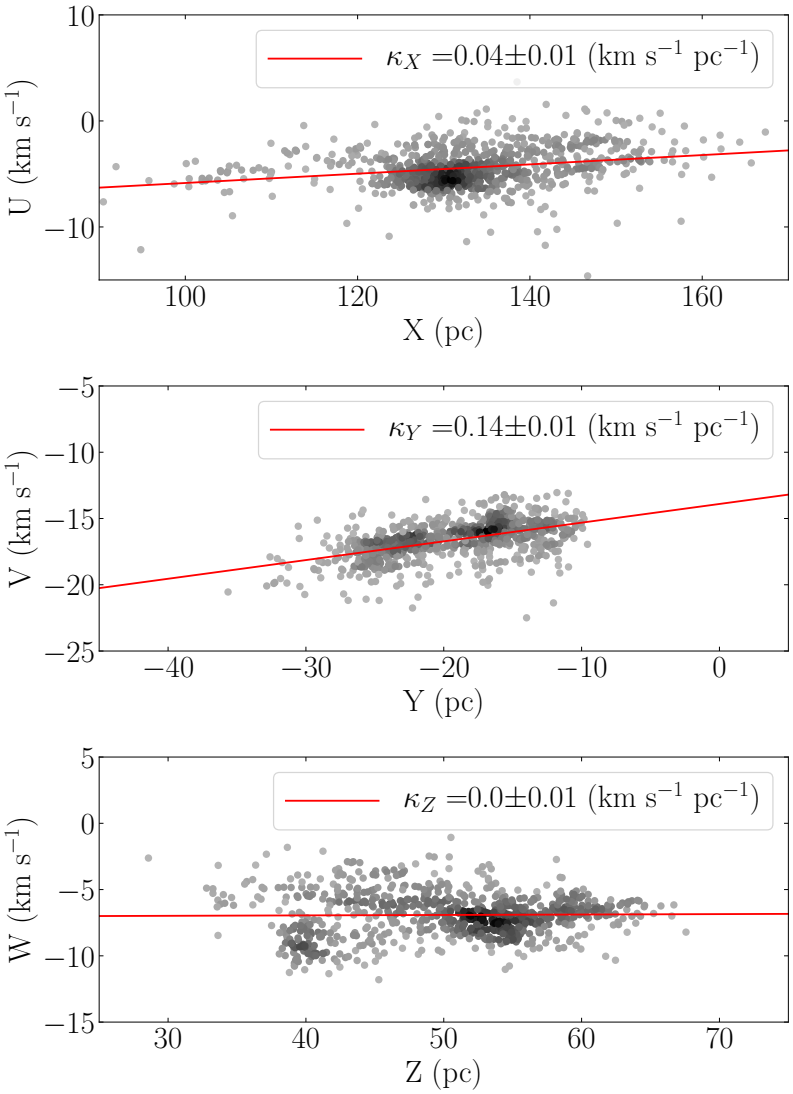

Figure 4.11. Position versus velocity in the three Galactic Cartesian coordinates for the *Gaia* members of USC and ρ Oph.

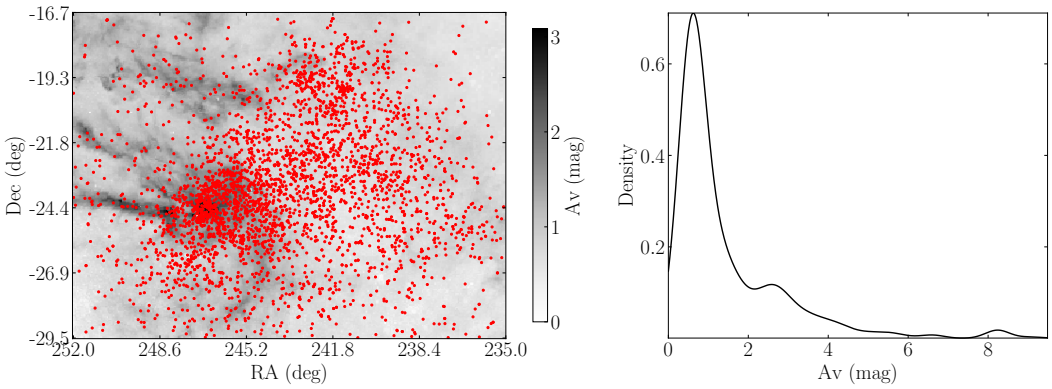

Figure 4.12. Left: Sky positions of the members we find overplotted on the dust map from Green et al. (2019) within the closest 300 pc. Right: A_V distribution obtained with the dust map from Green et al. (2019) within the closest 300 pc.

4.4.2 *Isochrones*

In this section, we compare our list of members with theoretical evolutionary models which we later used (Section 4.4.4) to tentatively infer the individual mass of each source. The extinction plays a crucial role in this comparison, especially in this region where there are molecular clouds and the extinction is variable (see Figure 4.12). Ideally, we would like to compare the theoretical isochrones with the members dereddened by their individual extinction but unfortunately, this information is not available for most of the sources. There are 690 of our members in the *Gaia* catalogue which have the line-of-sight extinction in the G band (A_G) but the Gaia DPAC consortium does not recommend to use these values on an individual basis at this stage of the mission. We computed their median extinction in the G band, $A_G = 1$ mag, which corresponds to $A_V = 1.2$ mag using the conversion factors in Table C.1. Luhman et al. (2018) provided an extinction in *Ks* for 1 462 of our members, 22% from near-IR spectra and the rest from photometry. This sample has a median $A_K = 0.07$ mag which corresponds to $A_V = 0.6$ mag, half of the extinction we obtained with the A_G parameter. However, it is important to mention that this study avoided the region of ρ Oph which has the largest extinction. Finally, we used the 3D dust map from Green et al. (2019) to compute the extinction in each sky position within 300 pc. In Figure 4.12 right, we represent the distribution of the extinctions obtained with this 3D dust map which has a median of $A_V = 0.8$ mag. We note that the great majority of sources have a rather small extinction ($A_V < 1$ mag) and the sources with $A_V > 1$ mag are concentrated in the region of ρ Oph. We also note that the extinctions estimated with the 3D

map are overestimated for stars located in front of the cloud. The individual extinctions obtained with the three methods have large differences (of the order of one magnitude). Hence, we decided not to use the individual extinctions from any previous study, and we inferred them with a Bayesian algorithm in Section 4.4.4.

In Figure 4.13, we compare our list of members with theoretical evolutionary models at different ages within the range constrained by previous studies, i.e. $3-8$ Myr, where the lower limit corresponds to the young region of ρ Oph (Greene and Meyer 1995) and the upper limit is a recent age estimate of USC based on eclipsing binaries (David et al. 2019). We show CMDs with different filters both in the optical and in the IR. The upper panels show the members obtained with *Gaia* and the PARSEC isochrones (Marigo et al. 2017) are overplotted. We see that while the models represent well the observed sequence of the association at intermediate magnitudes, they are brighter than the observations between $G \sim 7-12$ mag. This leads to an overestimation of the age when only massive stars are considered as suggested by other works (Rizzuto et al. 2016; Fang, Herczeg and Rizzuto 2017). The middle and bottom panels correspond to the members we identified with the DANCe catalogue and in this case, the BHAC15 isochrones (Baraffe et al. 2015) are shown instead of PARSEC because the latter do not reach sufficiently low luminosities. While in some diagrams the isochrones seem to represent fairly well the sequence of the association (e.g. $i, i-Ks$ bottom left panel) in others there are significant differences (e.g. $y, y-Ks$ middle right panel). In all the panels, the BHAC15 isochrones show a feature at the faint extreme which is not visible in the observations, possibly because of the relatively large dispersion and uncertainties in this luminosity range. In this figure, we show the extinction vector in each panel instead of correcting the individual extinctions. However, we have checked that the extinction cannot be responsible for the differences observed in any of these diagrams.

In Figure 4.14, we converted the apparent to absolute magnitudes as described in Section 2.3.1. For the members obtained with *Gaia* we used the individual Bayesian distances computed in Section 4.4.1 and for the DANCe members we sampled the distance distribution of the association obtained with the *Gaia* members. The PARSEC and BHAC15 isochrones of 8 Myr are overplotted and a mass-scale is indicated. We see that the aforementioned features in the theoretical evolutionary models which are not visible in the empiric sequence correspond to about 2 $M_\odot$ and 0.01 $M_\odot$. However, these features are included within the dispersion of our observations and we do not have enough resolution to see them. Necessarily, this has a negative impact in the transformations from magnitudes to luminosities and masses, enlarging even more the uncertainties

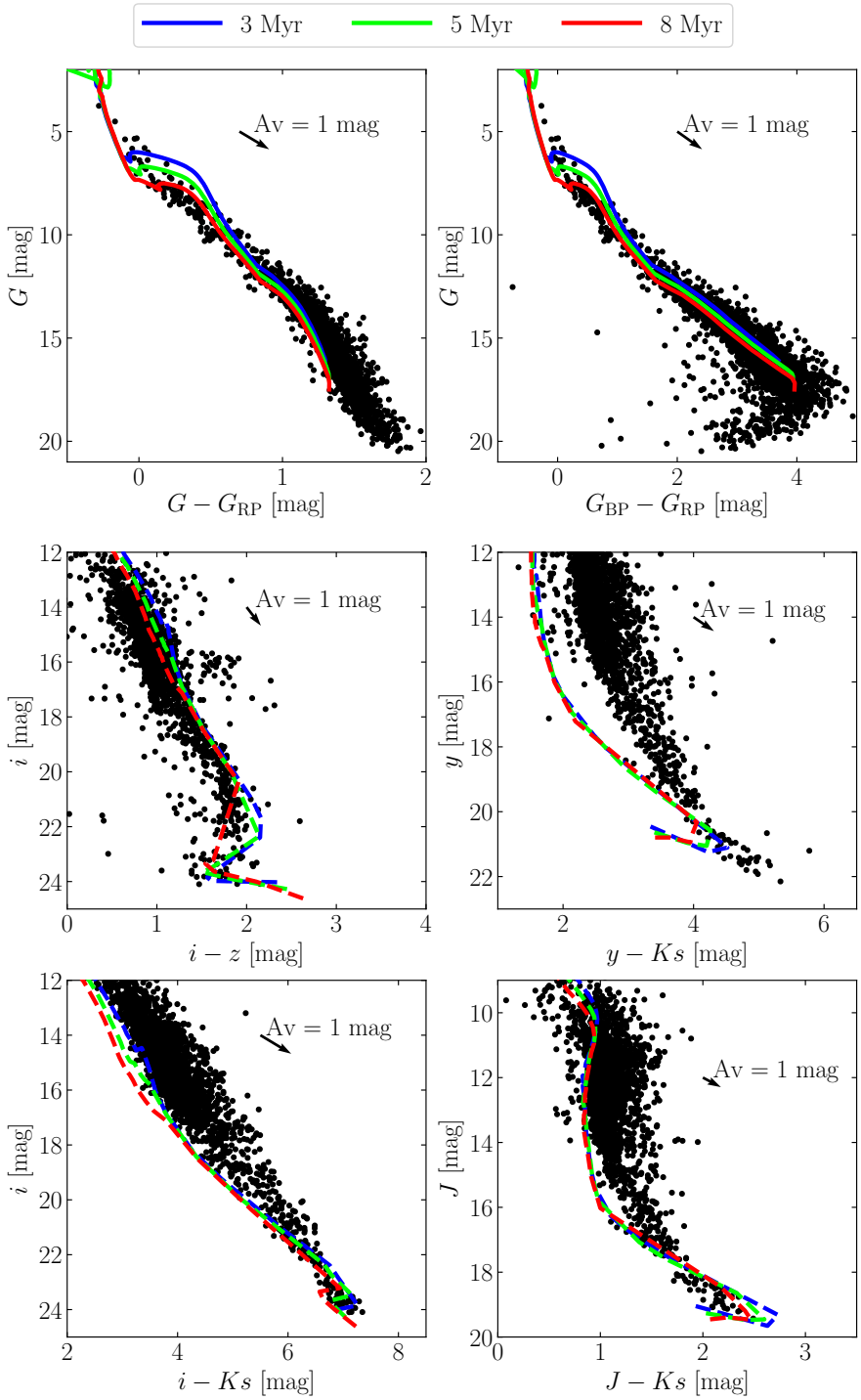

Figure 4.13. Apparent CMDs of the *Gaia* members (top panels) and the DANCe members (middle and bottom panels). The PARSEC isochrones (solid lines) at different ages are overplotted on the top panels and the BHAC15 isochrones (dased lines) are overplotted on the middle and bottom panels. A distance modulus of 5.8 mag is applied to all the theoretical isochrones. The extinction vector is indicated in each panel.

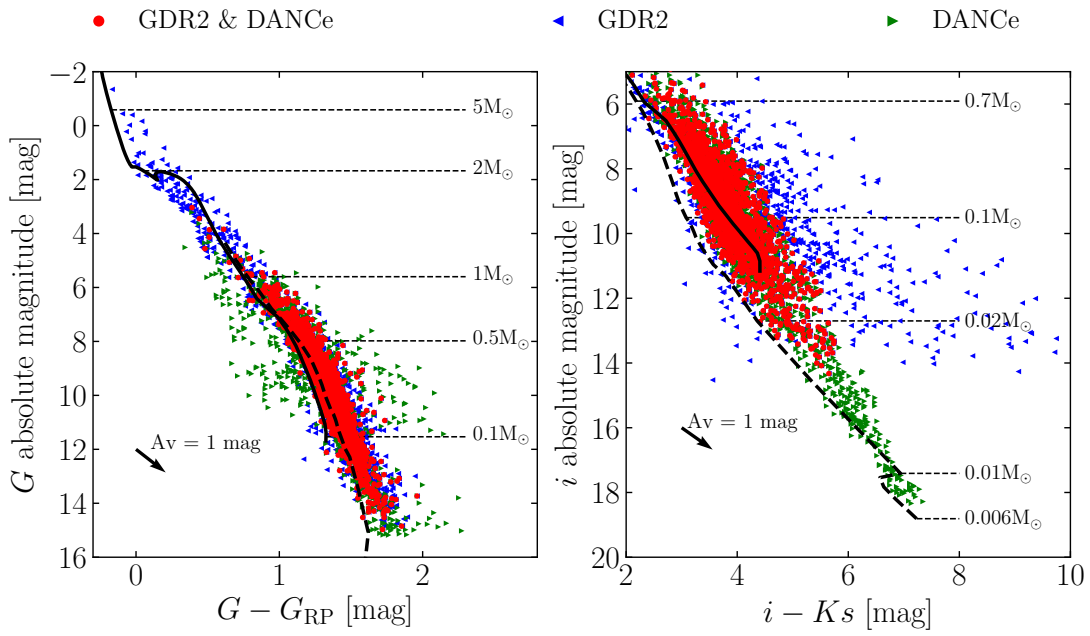

Figure 4.14. Absolute CMDs of the USC association and the ρ Oph star forming region. The PARSEC+COLIBRI isochrone of 8 Myr (solid line) and the BHAC15 isochrone of 8 Myr (dashed line) are overplotted. The members are shape- and colour-coded according to their membership classification: red circles for members in *Gaia* and DANCe analysis, blue left-pointing triangles for members only in *Gaia*, and green right-pointing triangles for members only in DANCe.

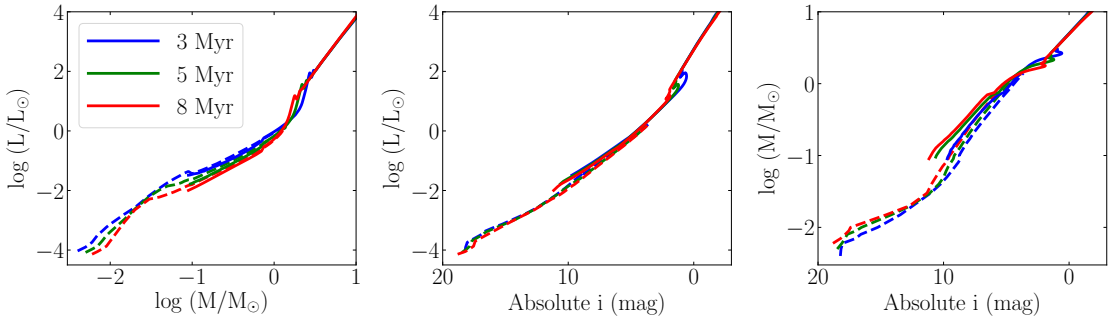

Figure 4.15. Mass-luminosity relation (left), absolute magnitude-luminosity relation (middle), absolute magnitude-mass relation (right) for the PARSEC (solid lines) and BHAC15 (dashed lines) evolutionary models at the three ages considered in this study.

and producing artificial patterns in the mass function. In Figure 4.15, we show the mass-luminosity, magnitude-luminosity, and magnitude-mass relations we used in Section 4.4.4 to infer individual luminosities and masses. It illustrates the significant differences between the various models and should be kept in mind when interpreting the luminosity and mass distributions. These differences are most unfortunate since no single grid of models covers the entire mass domain and one must necessarily combine two sets of models to study the entire mass (luminosity) domain.

4.4.3 *Apparent magnitude distribution*

We obtained the apparent magnitude distribution in the G band for the *Hipparcos* and *Gaia* members and in the i band for the DANCe members as described in Section 2.3.3. We convoluted each distribution with a Gaussian KDE with a bandwidth of 0.5 mag for *Hipparcos* and 0.3 mag for *Gaia* and DANCe according to the rules from Scott (Scott 1992) and Silverman (Silverman 1986). In the case of sources from the *Hipparcos* catalogue, we converted the V_T magnitudes to G magnitudes using the relation from Evans et al. (2018), their Table A.2. We estimated the uncertainties in the magnitude distribution from a bootstrap of 100 repetitions and the completeness limits are the ones defined in Section 4.2. We normalised the *Gaia* and *Hipparcos* magnitude distributions so that they cover the same integrated area in the magnitude range $G = 6 - 7$ mag. Although we initially considered the conservative magnitude limit of $G = 7$ for the bright end of *Gaia* (Gaia Collaboration et al. 2018c), we extended it to $G = 6$ mag (Lindegren et al. 2018a) to have a significant overlap between the *Hipparcos* and *Gaia* members. The resultant distributions are shown in Figure 4.16.

A large fraction of members (95%) have J, H, Ks photometry thanks to the combination of the deep images of the DANCe catalogue with the 2MASS catalogue that observed the brightest sources saturated in the DANCe images. Then, we also computed the magnitude distribution along the 20 magnitudes covered by the J band ($-2.7 < J < 17.4$ mag, see Fig. 4.16 bottom panel) and we provide it in Table C.11. The magnitude distribution is a direct product of the observations and the membership analysis and thus, is independent of theoretical models. Therefore, it constitutes an excellent test for the different mechanisms of star formation. In the following sections, we converted this magnitude distribution to a luminosity and mass function with the currently available evolutionary models.

The peak of the distribution is at $G = 15.6$ mag for the sample of *Gaia* members, at $i = 14.7$ mag for the sample of DANCe members, and at $J =$

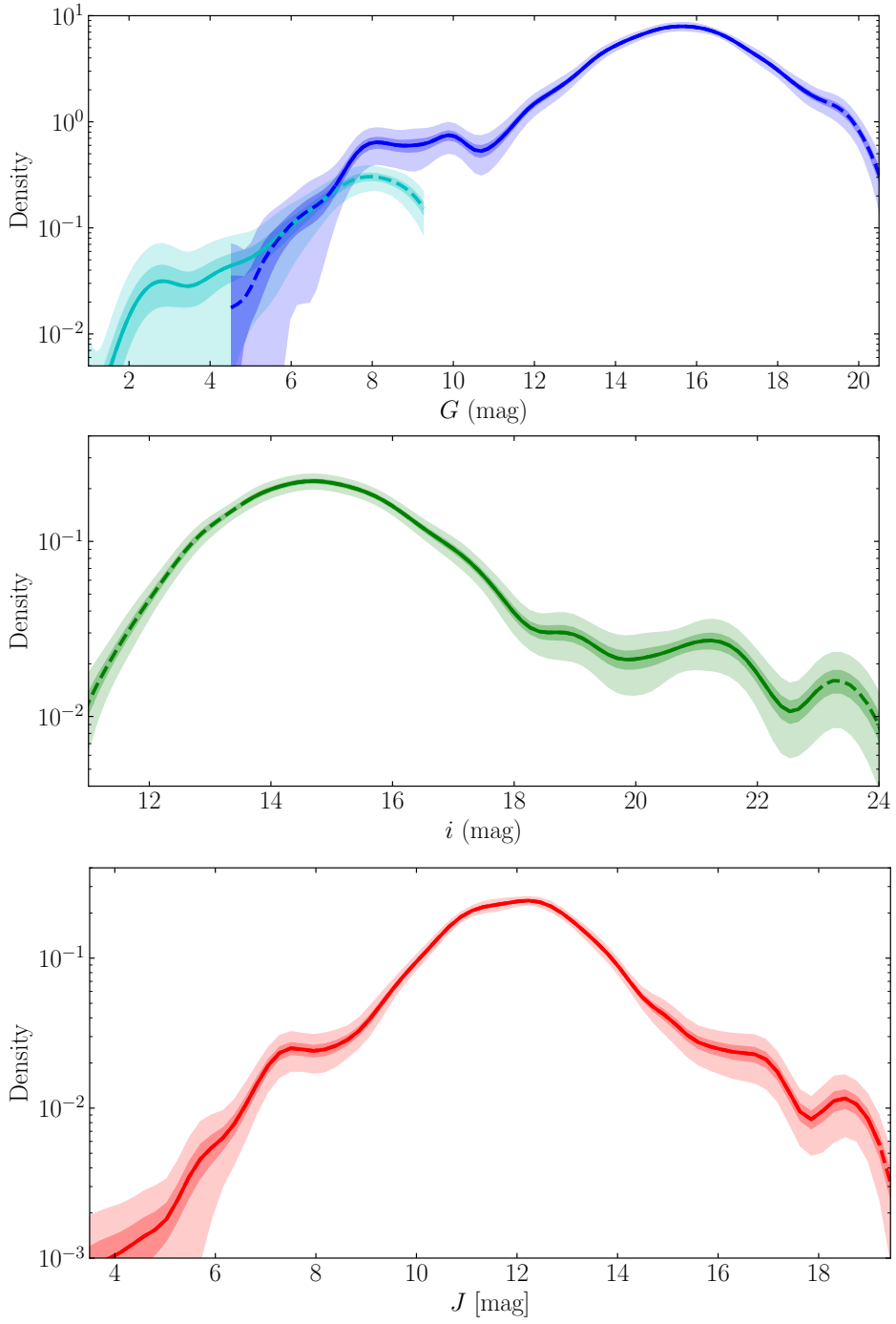

Figure 4.16. Apparent magnitude distributions of the members we found in the USC association and the ρ Oph star forming region. Top: G magnitude distribution of the the members found with the *Hipparcos* catalogue (cyan) and the *Gaia* catalogue (blue). Middle: i magnitude distribution of the members found with the DANCe catalogue (green). Bottom: J magnitude distribution with the members from the three surveys (red, 95% of all the members have photometry in J). The shaded regions indicate the 1σ and 3σ uncertainties estimated from bootstrap (1σ dark and 3σ light). The dashed lines indicate the region of incompleteness in each catalogue.

12.2 mag for the entire sample, which corresponds to $0.08 - 0.2$ $M_\odot$, depending on the age and model considered. We observe no hints of the Wielen dip which should be around apparent magnitude $G \sim 13$ mag. On the contrary, we find a plateau at apparent magnitude $G = 8 - 10.6$ mag ($J = 7.5 - 8.5$ mag) which we can not identify with any known feature in the luminosity distribution. This shape is similar to the magnitude distribution in IC 4665 but the plateau is at different magnitudes (after correcting for the distance modulus) and at different masses (according to the evolutionary models; in IC 4665 the plateau was at ~ 0.75 $M_\odot$ while in this case, we find it at $1.2 - 1.9$ $M_\odot$). At the low-mass end, the magnitude distribution is approximately flat between $18.4 < i < 21.5$ mag ($15.5 < J < 17$ mag), corresponding to the transition between brown dwarfs and planetary-mass objects. Then, it drops and rises again around $i \sim 23.5$ mag ($J \sim 18.5$ mag), suggesting that a secondary peak exists at planetary masses, although the exact mass is strongly dependent on the age and model considered and varies between 6 and 8 M_J. Our incompleteness beyond this magnitude limit does not allow us to study the extension of this rise and the exact location of the peak. Our magnitude distribution shows a very rich population of substellar objects. It is important to remember that the number of substellar objects identified in the present analysis is only a lower limit given that we are missing the sources with high extinction.

We investigated the impact of contamination and completeness in the magnitude distribution using synthetic data. We found that when we corrected the magnitude distribution for these two effects, the differences were smaller than the uncertainties we computed with the bootstrap analysis. This is due to the small contamination rates we measured (see Table 4.4). Remarkably, the contamination rate at the faint end is of less than 4% in the range where our survey is complete ($i < 23.5$ mag).

We compared our magnitude distribution to other studies in the literature which also covered the planetary mass regime. The comparison in magnitudes has the great advantage that is not affected by the uncertainties of models. On the contrary, the brightness of a PMS star varies with time and equally mass objects are brighter at younger stages. Having this limitation in mind, in Figure 4.17, we compared our magnitude distribution to three different regions, namely USC, the 1 Myr open cluster NGC 1333, and the 3 Myr association σ Ori. We took the lists of members of these regions and computed the magnitude distribution with the same method than for our study. We corrected the apparent magnitudes with the distance modulus of each region computed with the *Gaia* DR2 parallaxes. Our magnitude distribution is compatible within the uncertainties with the studies from Lodieu et al. However, our uncertainties are significantly smaller due to the larger number statistics of our sample

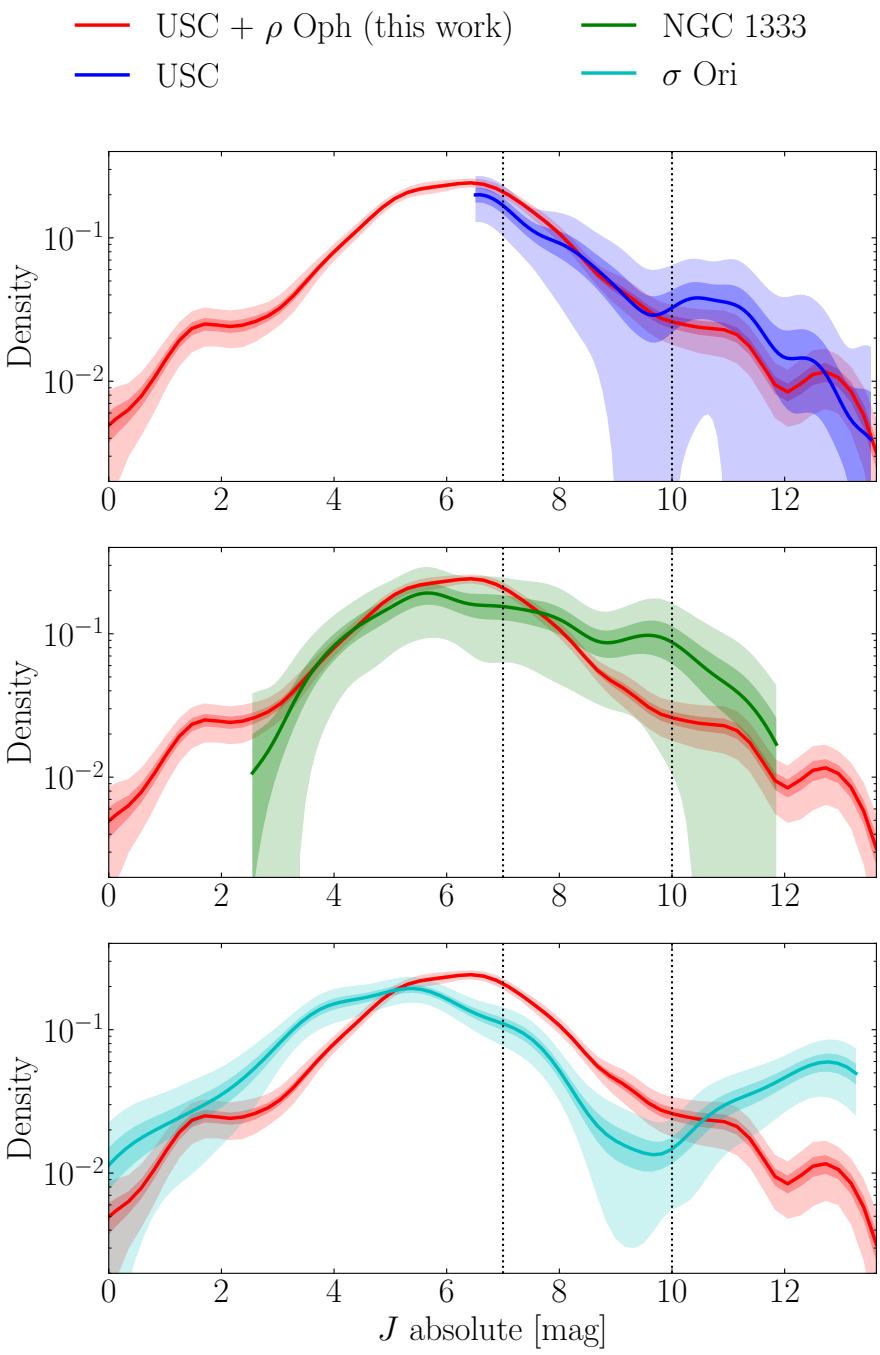

Figure 4.17. J magnitude distribution obtained in this work for USC and ρ Oph (red) compared to other studies namely, USC (blue, top panel, members from Lodieu 2013 and Lodieu et al. 2018), NGC 1333 (green, middle panel, members from Scholz et al. 2012a, Scholz et al. 2012b and Winston et al. 2009) and σ Ori (cyan, bottom panel, members from Peña Ramírez et al. 2012, Hernández et al. 2014 and Caballero et al. 2019). The vertical dotted lines indicate the transition from stars to brown dwarfs (hydrogen burning limit at 75 M_J) and the transition between brown dwarfs and free-floating planets (deuterium burning limit at 13 M_J).

(an order of magnitude larger than theirs). The magnitude distributions of NGC 1333 and σ Ori are shifted towards brighter sources with respect to our results, most likely due to the younger ages of these two regions (1 Myr and 3 Myr, respectively). NGC 1333 has a larger fraction of substellar objects (brown dwarfs and free-floating planets) compared to our magnitude distribution but the large uncertainties in NGC 1333 (due to low number statistics) make the two distributions compatible at a 3σ level. One possibility to explain these differences are the highly extinct members of ρ Oph which are missing in our sample. Eventually, if the possibility of observational biases is excluded, these differences could be due to different environments. Finally, the σ Ori association also has a larger fraction of free-floating planets than our sample. However, this sample could be more contaminated since the proper motions of this cluster are very small (< 2 mas yr^{-1}) and different young associations are aligned in the same line of sight.

4.4.4 *Luminosity and present-day system mass function*

We estimated the individual mass and extinction of each source with *Sakam* (see Sect. 2.3.2). Since there is not a single set of evolutionary models which covers the entire mass range of our study, we were forced to use different models for the high and low-mass regimes. We used the PASEC isochrones to infer luminosities and masses for the *Hipparcos* and *Gaia* members and the BHAC15 models for the DANCe members. We note that these two sets of models differ in the range where they both are computed (see Fig. 4.15) which inevitably has consequences in the luminosity and mass functions. In all cases, we considered the isochrones at three different ages, namely 3, 5, and 8 Myr to study the impact of the age uncertainty on the luminosity and mass functions. Similarly to what we did for the apparent magnitude distribution, we sampled the a posteriori luminosity/mass inferred with *Sakam* taking into account the uncertainties. We convoluted this distribution with a KDE with a bandwidth of 0.2 (in logarithmic scale) in all the cases. We normalised the *Hipparcos* and *Gaia* luminosity/mass function in the luminosity/mass range equivalent to $G = 6 - 7$ mag. The low-mass limit of *Gaia* is given by the end of the PARSEC isochrone ($\gtrsim 0.09$ M$_\odot$) and not by the *Gaia* detection limit. Sources with masses close to the end of the isochrone have poor luminosity/mass estimates and the luminosity/mass function is biased in this range. For this reason, we decided to estimate the low-mass completeness of the luminosity/mass function with *Gaia* as the maximum of the function. We propagated the DANCe completeness limits (Table 4.3) to luminosity and mass and normalised the *Gaia* and DANCe

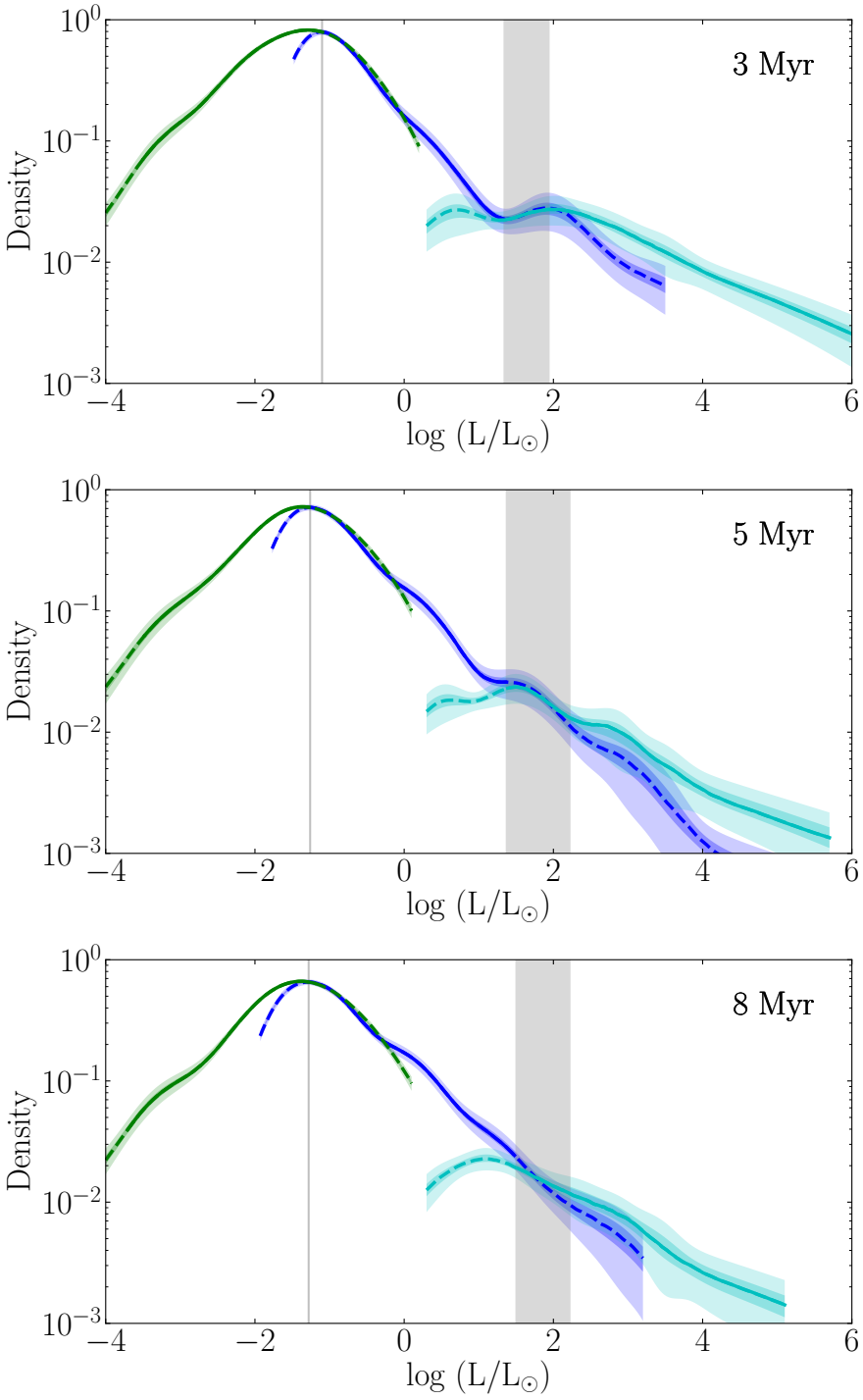

Figure 4.18. Luminosity function of USC and ρ Oph obtained assuming an age of 3 Myr (top), 5 Myr (middle), and 8 Myr (bottom). The list of members from the *Hipparcos* (cyan), *Gaia* (blue), and DANCe (green) membership analysis have been treated independently. The dashed lines indicate the regions where the surveys are incomplete and the shaded areas the 1 and 3σ uncertainties. The vertical grey shaded areas indicate the areas used to normalise the functions.

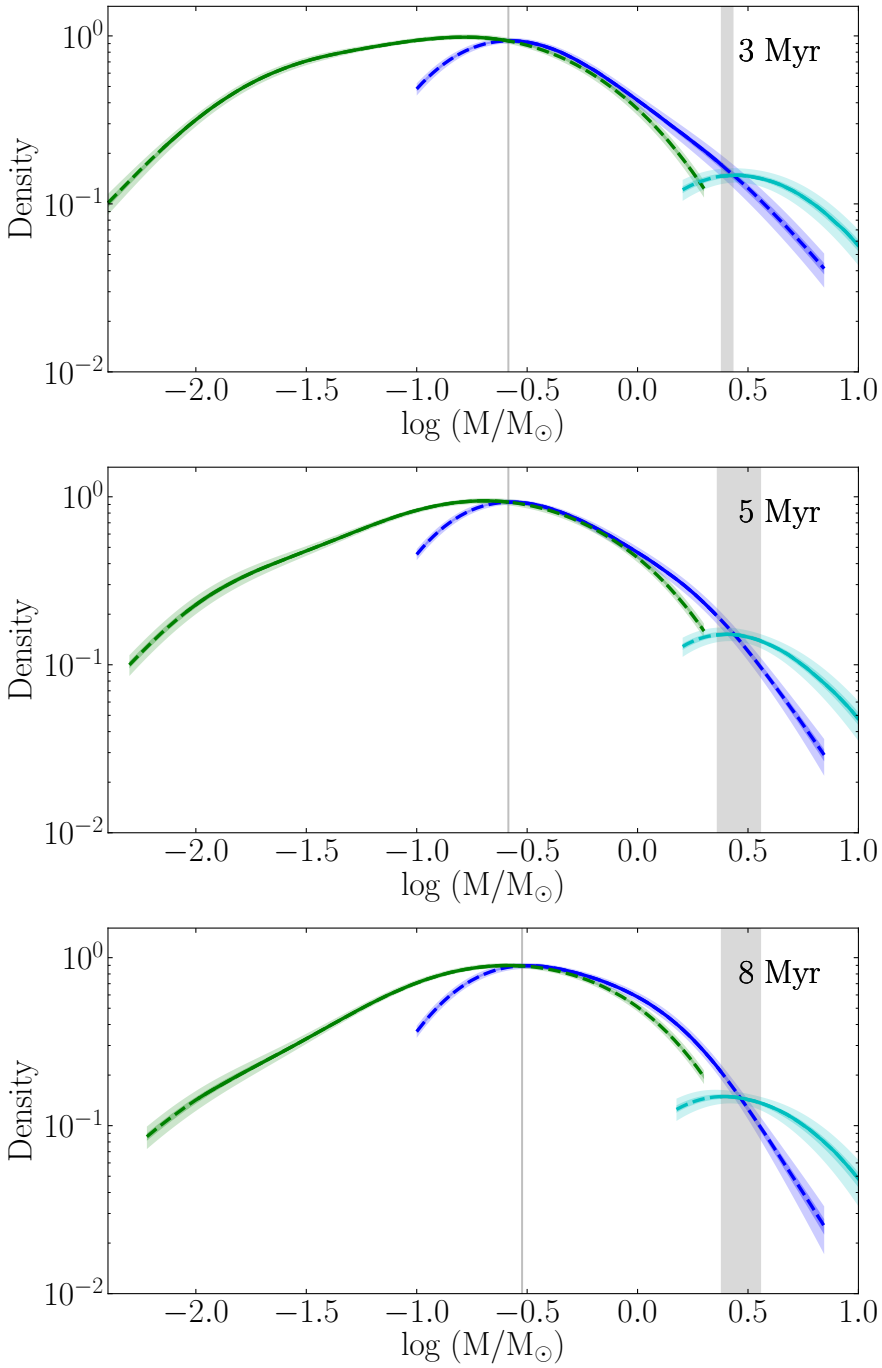

Figure 4.19. Same as Figure 4.18 for the PDSMF.

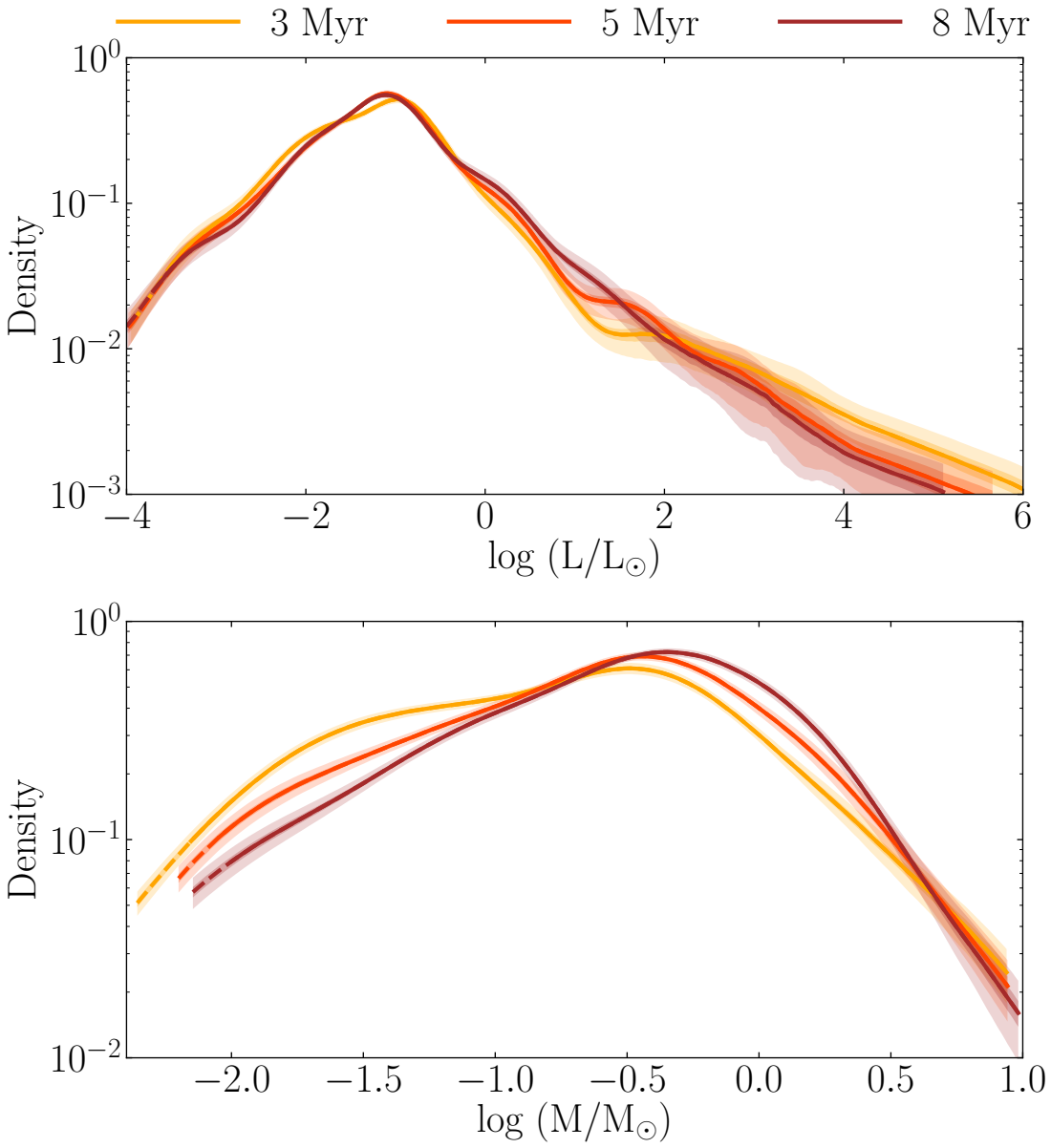

Figure 4.20. Luminosity function (top) and PDSMF (bottom) obtained assuming different ages. This functions have been obtianed combining the members of the *Hipparcos*, *Gaia*, and DANCe surveys.

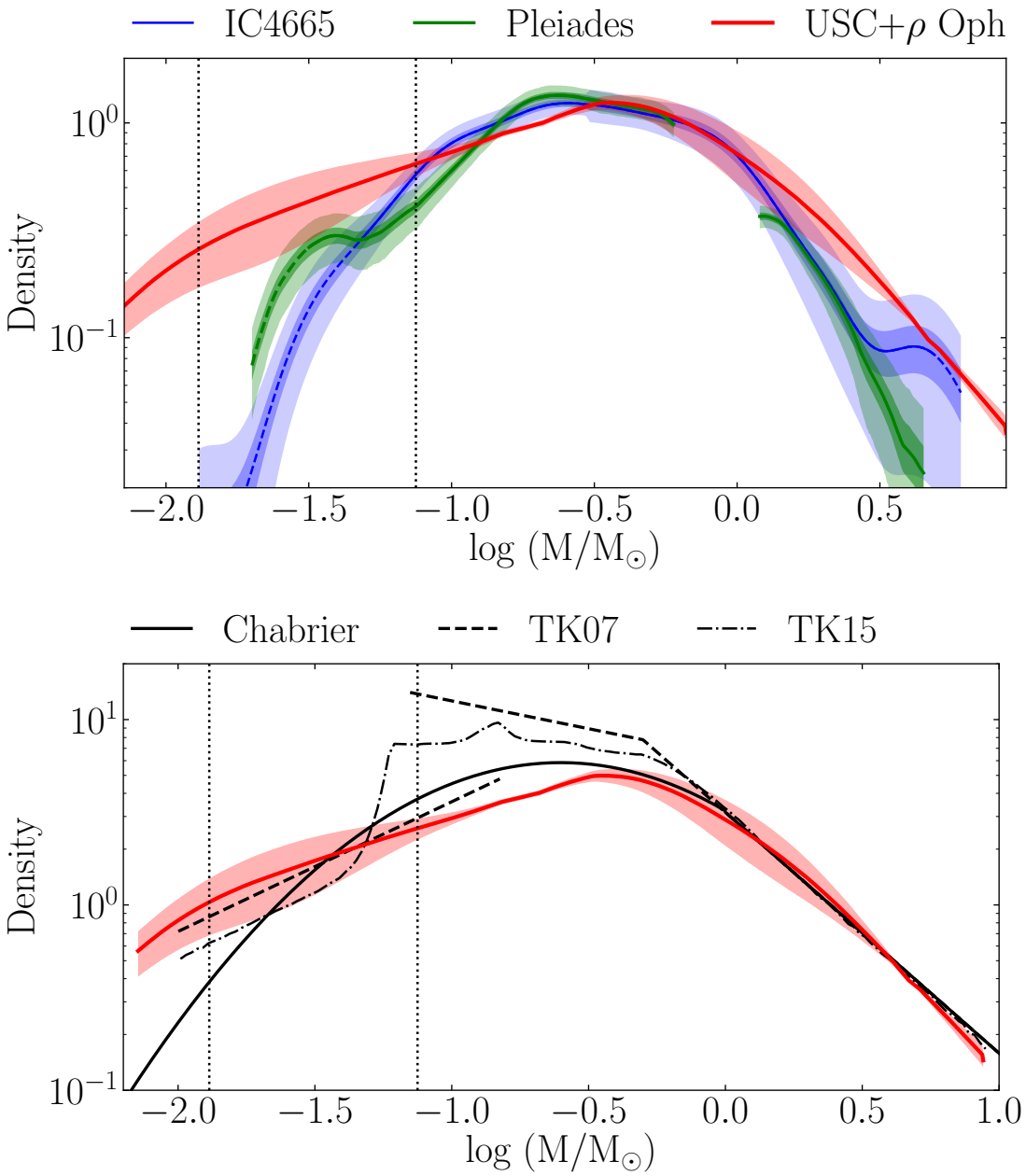

Figure 4.21. Top: PDSMF of USC and ρ Oph ($1-10$ Myr) compared to IC 4665 (30 Myr) and the Pleiades (120 Myr). Bottom: PDSMF of USC and ρ Oph ($1-10$ Myr) compared to the theoretical model of Chabrier (2005), Thies and Kroupa (2007), and Thies et al. (2015).

functions in the area where both studies are complete. This area is very small but enough to obtain a joint final function.

In Figure 4.18 we show the luminosity function and in Figure 4.19 the PDSMF obtained at different ages. These functions are continuous due to the normalisation we did at the edges of different catalogues but have uneven variations, especially in the overlap between the *Hipparcos* and *Gaia* catalogues. To obtain a smooth function which we can compare to other star-forming regions and models, we re-computed the luminosity and mass functions sampling at the same time the members of the three different catalogues. To avoid sampling twice objects repeated in different catalogues, we established the intersections of the luminosity and mass functions in Figures 4.18 and 4.19 as the limits in the lists of members. For example, to compute the mass function at 3 Myr years, we sampled the *Hipparcos* members with masses > 2.5 M$_\odot$, the *Gaia* members with masses in the range $0.26 - 2.5$ M$_\odot$ and the DANCe members with masses < 0.26 M$_\odot$. In Figure 4.20, we show the resultant distributions and these functions are reported in Tables C.12 and C.13.

The luminosity functions obtained with isochrones at different ages present variations however, in this discussion, we focus on the main conclusions which are valid for the three ages explored. No matter the age, the luminosity distribution peaks at $\log(L/L_\odot) \sim -1$. The bump observed at $\log(L/L_\odot) \sim 1 - 2$ coincides with a feature in the magnitude-luminosity relation (see Fig. 4.15). At luminosities between $\log(L/L_\odot) \sim -2.7$ and -3.2 we observe a change of slope which corresponds to the bump we observed in the magnitude distribution between $19 < i < 22$ mag. This feature is most evident at 8 Myr and almost not visible at 3 and 5 Myr. We note that the magnitude-luminosity is smooth in this range of luminosities. The rise at $i \sim 23$ mag found in Figure 4.16 is not seen in the luminosity distribution. The uncertainties added in the transformation from apparent magnitude to luminosity and mass (because of the propagation of the uncertainties on the distance and models, see Fig. 4.13) probably smooth this feature out, illustrating the need to work on direct observations and the need for improved models.

Analogously to what we did for the luminosity function we analyse the PDSMF paying special attention to the features which are independent of the age of the isochrone used to convert magnitudes to masses. We computed the median mass function of the three ages (which is almost identical to the mass function at 5 Myr) and the standard deviation. Our mass function shows a large fraction of free-floating planets similar to what other studies found (e.g. Lodieu 2013; Scholz et al. 2012b; Peña Ramírez et al. 2012) but our sample is around an order of magnitude larger than these previous studies. This allows us to have a major precision in the mass function and to better constrain the fraction of stars,

brown dwarfs and planets. The fraction of substellar objects that Scholz et al. (2012b) found in NGC 1333 is significantly higher than what we found in USC. Our sample is missing the most extinct objects which were not identified with our membership algorithm and which could explain these differences (at least partially). Then, if no other observational biases are present in any of the two samples, these results would indicate that different environments lead to the formation of different fractions of substellar objects. However, this hypothesis should be confirmed with more observations.

In Figure 4.21 (top), we compare the mass function we obtained in USC and ρ Oph to the mass function of IC 4665 (30 Myr) we obtained in Chapter 3 and the mass function of the Pleiades (120 Myr, Bouy et al. 2015). We normalised the three functions in the mass range where the three studies are complete, namely between $0.05 - 0.6$ $M_\odot$. Comparing the mass function at different ages we can study the evolution of the mass function with time. It is noticeable that the mass functions of IC 4665 and the Pleiades have a lower fraction of high mass stars ($\gtrsim 3$ $M_\odot$). First, the uncertainties in this mass range are larger due to low number statistics (especially in the case of IC 4665) and also some of the most massive stars in the older clusters might have already left the main sequence and are missing in our studies. At intermediate and low-mass stars the three functions are compatible within the uncertainties (note that this is the mass range in which they where normalised). Additionally, the peak of the mass function ($0.3 - 0.5$ $M_\odot$, $\log(M/M_\odot) = -0.5$ to -0.3) is in good agreement with what we found for IC 4665 (0.28 $M_\odot$). Finally, in the substellar regime, the mass function of USC and ρ Oph shows a larger fraction of objects. The mass functions of the Pleiades and IC 4665 are not complete in this mass range and then we cannot extract robust conclusions. However, if these differences were confirmed, this could indicate that the lowest mass objects evaporate from their parent clusters due to dynamical interactions.

In Figure 4.21 (bottom), we overplotted the theoretical mass function of Chabrier (2005), Thies and Kroupa (2007) and Thies et al. (2015) on our mass function of USC and ρ Oph. We normalised the functions in the high mass regime (> 1 $M_\odot$) where they all have a Salpeter slope. Indeed, our observational mass function, is best fit at high masses by a slope of $\Gamma = 1.388 \pm 0.006$. The peak of the mass function ($0.3 - 0.5$ $M_\odot$, $\log(M/M_\odot) = -0.5$ to -0.3), is similar to the characteristic mass of theoretical models (0.25 $M_\odot$, Chabrier 2005). In the mass range $0.08 - 0.3$ $M_\odot$ ($\log(M/M_\odot) = -1.1$ to -0.5), there is a statistically significant lack of objects with respect to all models considered. In the substellar regime, find a good agreement with the slopes of Thies and Kroupa (2007) and Thies et al. (2015) but we observe an over-density of objects with respect to the Chabrier (2005) IMF. While the Chabrier (2005) IMF can be interpreted as

Table 4.6. Fraction of free-floating planets (FFP), brown dwarfs, and stars in USC and ρ Oph.

Age (Myr)	f_{FFP}	f_{BD}	f_*
3	0.05	0.26	0.69
5	0.03	0.19	0.78
8	0.02	0.15	0.83
Chabrier 2005	0.009	0.16	0.83

Notes. These values have been obtained integrating the mass function shown in Fig. 4.20 (bottom panel) with the mass limits < 0.013 $M_\odot$ (FFP), $0.013 - 0.075$ $M_\odot$ (brown dwarfs), and > 0.075 $M_\odot$ (stars).

Table 4.7. Summary of the fractions expected for the principal mechanisms of free-floating planets formation.

Mechanism	Fraction	Ref.
Core collapse	$18 - 45\%$	this study
Planetary system ejection	$11 - 27\%$	this study
Perturbation in stellar cluster	$\sim 10\%$	Parker and Quanz 2012

a result of core-collapse formation, Thies and Kroupa (2007) and Thies et al. (2015) included other mechanisms of formation of substellar objects. Our better agreement with these latter IMFs confirms that substellar objects do not only form by core-collapse. In the next section, we investigate the possible origin of such objects.

We discovered a large new population of high-probability free-floating planets with $\sim$ 150 objects. Our analysis with synthetic data concludes that the contamination in this mass range is minimal ($< 4\%$). At the same time, we miss many embedded objects in this mass range which can only increase the number of free-floating planets. Therefore, the present analysis demonstrates that there is a much richer population of free-floating planets than predicted by core-collapse models, and provides additional evidence that low-mass brown dwarfs and planetary-mass objects must form in several ways.

4.4.5 *Constrains on the formation of free-floating planets*

In the previous section, we found a rich new population of planetary-mass objects which greatly exceeds the number of such objects predicted by core-collapse theories. This is seen in Figure 4.21, where the density of substellar

objects we obtain is systematically and significantly (in the statistical sense) larger than the IMF of Chabrier (2005), no matter the age assumed. In this section, we aim at studying how many of these objects are likely to have formed around more massive objects (i.e. stars and brown dwarfs) and have later been ejected. We follow a similar approach as Veras and Raymond (2012) in which the fraction of free-floating planets which have been ejected from a stellar system (N_{FFP}/N_{stars}) depends on the fraction of stars that form giant planets (f_{giant}) and on the fraction of such planets that become unstable and are eventually ejected ($f_{ejected}$).

$$\frac{N_{FFP}}{N_{stars}} = f_{giant} \cdot f_{ejected} \tag{4.3}$$

The number of stars and free-floating planets is given by our membership analysis, for which we inferred the masses in the previous section. We can classify these sources in stars ($M > 0.075$ M$_\odot$), brown dwarfs ($0.075 > M > 0.013$ M$_\odot$), and planets ($M < 0.013$ M$_\odot$). For simplicity, we considered stars and brown dwarfs in the same category since our purpose here is to study the number of free-floating planets which are formed surrounding a more massive object. We estimate $N_{FFP}/N_{stars} = 0.02 - 0.05$, depending on the age assumed (see Table 4.6) by integrating the mass function (Fig. 4.20) over the corresponding mass ranges.

The fraction of stars which form giant planets (f_{giant}) is constrained by planets surveys (Fernandes et al. 2019; Clanton and Gaudi 2017; Bowler 2016; Suzuki et al. 2016; Mayor et al. 2011). These studies show that this fraction is dependent on both the mass of the star and the planet. Our survey covers the mass range from 10 M$_\odot$ to 4 M$_J$ so as a first approximation, we are interested in an average fraction within this mass range. Bowler (2016) estimated an overall occurrence rate of $0.6^{+0.7}_{-0.5}$% for $5 - 13$ M$_J$ planets at $30 - 300$ AU, which was not significantly different for BA stars, FGK stars, and M dwarfs. Another recent study, Fernandes et al. (2019), estimated an occurrence rate of $6.2^{+1.5}_{-1.2}$% for planets more massive than Jupiter. Since the occurrence rate decreases with increasing mass, this latter value should be taken as an upper limit in our study where we did not detect objects lighter than 4 M$_J$. For this discussion, we take the conservative occurrence rate range of $0.6 - 6.2$%.

The number of ejected planets per system depends on the fraction of systems that become unstable and on the number of planets in that system. The fraction of giant planets that become unstable is of the order of $\sim$ 90% (Jurić and Tremaine 2008; Chatterjee et al. 2008; Raymond, Armitage and Gorelick 2010). A minimum of two planets per system is needed for an instability to happen, but the number could be much higher. The number of ejected planets scales with the number of planets involved in the instability. To get a rough estimate, we

considered a simplified scenario in which any time a planetary system forms, it forms three planets and one of them is ejected (Veras and Raymond 2012), leading to $f_{ejected} \sim 0.9$.

Finally, we constrained for all the terms in Equation 4.3. The right-hand side of this equation is reduced to the fraction of stars which form giant planets which we estimated to be $f_{giant} \cdot f_{ejected} = 0.005 - 0.05$. From our members, we obtained that the fraction of free-floating planets to stars is of $N_{FFP}/N_{stars} = 0.02 - 0.05$. With these values, we can compute the following extreme case situations. First, if we take the occurrence rate from Bowler (2016), we see that only $11 - 27\%$ of the free-floating planets found in our analysis come from planetary system ejections. Instead, with the occurrence rate from Fernandes et al. (2019) we see that all the free-floating planets we found can originate from ejections in planetary systems. However, we must remember that the occurrence rate of Fernandes et al. (2019) should be regarded as an upper limit in the present analysis since their occurrence rate applies to planets of one Jupiter mass or more, most of which are beyond the sensitivity limit of our study. A more accurate estimate of the occurrence rate of planets in the mass range of our study is needed to better constrain the fraction of free-floating planets formed in planetary systems, but the simple assumptions made above suggest that a quarter to a third of them could have been ejected.

We followed a similar approach to estimate the fraction of planetary-mass objects expected from core collapse. In this case, we integrated the theoretical IMF from Chabrier (2005) with the same integration limits as our observational mass function and found a fraction of 0.009 free-floating planets. Therefore, we expect that $18 - 45\%$ of the free-floating planets we detected have been formed from gravitational collapse. This range has been obtained considering the fraction of free-floating planets in our sample according to the 3 and 8 Myr evolutionary models.

Other mechanisms that have been proposed to explain the presence of such objects are dynamical ejections in multiple star systems (Sutherland and Fabrycky 2016) and perturbations in the birth cluster (Parker and Quanz 2012; Winter et al. 2020). In Table 4.7 we review the fractions expected for each mechanism. While it is still early to quantify the contribution of each mechanism to the overall final population, our new improved IMF definitely confirms that core-collapse is not enough to explain the observed abundance of free-floating planets. Ejection from the planetary system must play a significant role and possibly contribute at the same level as core-collapse to the formation of free-floating planets. Given that planets less massive than the free-floating ones identified in our study are even much more common, one can expect to have large numbers of free-floating Jupiter-or-less sized planets roaming the Galaxy.

4.5 CONCLUSIONS

In this chapter, we presented a comprehensive study of the USC association and the ρ Oph star-forming region. We combined the *Gaia* DR2 astrometry with deep ground-based observations from the COSMIC DANCe project to search for members. We computed membership probabilities for all the sources in the area covered by our survey and found 3 455 high-probability members, covering a magnitude range of 14 mag ($5.4 < J < 19.4$ mag), which correspond to an approximate mass range of $0.004 - 10$ $M_\odot$, according to evolutionary models. Our members cover objects of different nature including stars, brown dwarfs, and planetary-mass objects. We estimated that a 20% of the members we found are new, comparing our sample with the most recent studies of this region.

We used this sample to do a preliminary analysis of the 6D structure of this association which will be used as a starting point in the future to study the history of the formation of this region and to determine robust dynamic ages. The latter will be of uttermost importance since the age of the various subgroups in USC is not yet well established and is a major source of uncertainty on the determination of the luminosity and mass functions. We also compared the empirical isochrones defined by our members with the theoretical evolutionary models of PARSEC and BHAC15 and found features in the models which are not found in our observations. Some of them might be explained by limitations in the observations (e.g. the binarity and the spread in age widen and blurry the observed isochrone) while others might be due to the uncertainties in the models, especially large at young ages and for low-mass stars.

We determined the PDSMF in the mass range from 4 M_J to 10 $M_\odot$, using theoretical evolutionary models of $3 - 8$ Myr. In all cases, we found that the high mass regime is well represented by a power-law IMF with a Salpeter slope of $\Gamma = 1.388 \pm 0.006$. For intermediate masses, our observations are compatible with the log-normal mass function from Chabrier (2005). However, in the substellar mass regime (brown dwarfs and planetary-mass objects) we found a significant excess of objects compared to the prediction of the log-normal mass function. On the contrary, the mass functions of Thies and Kroupa (2007) and Thies et al. (2015) show a better agreement to our results. The mass function from Chabrier (2005) represents the number of objects formed by core-collapse (the dominant mechanism to form stars) and only accounts for the $18 - 45$% of the objects we observed, while Thies and Kroupa (2007) and Thies et al. (2015) included other mechanisms to form substellar objects. Under simple assumptions based on the current knowledge of planetary systems, we estimated that $11 - 27$% of the free-floating planets could have been formed in planetary systems and later have become unstable and ejected. These

numbers, although very preliminary and tentative, show that ejection might be responsible for a significant fraction of free-floating planetary-mass objects. We also must remember that our study is missing the most embedded sources and that the above-mentioned results should be regarded as lower limits. The comprehensive census of members we presented constitutes an excellent sample for future follow-up studies. For instance, to revisit the age of the association, to spectroscopically characterise the planetary mass population and improve the evolutionary models, and to search for protoplanetary discs.

Part III

PROPERTIES OF STELLAR GROUPS

In this part, we present two complementary studies motivated by the censuses obtained in IC 4665, USC and ρ Oph, presented in the previous chapters. They address very important and complementary aspects of star formation and the early evolution of open clusters and associations.

In Chapter 5 we present a method to determine dynamical traceback ages of young associations. As we have seen in Chapter 4, the age is a fundamental parameter and the currently large uncertainties regarding the age of most nearby associations are a serious limitation to derive the mass function and interpret the results. In the course of this thesis, and with the expertise acquired over my Master's degree, we improved and extended the dating method based on dynamical traceback presented in Miret-Roig et al. 2018. For the development and validation of the method, we focused on a well known and previously well studied young local association, namely the β-Pictoris moving group, but with the ultimate goal of applying the method to USC in the future. The dynamical traceback age is additionally not only useful to estimate the age of associations but also the evolution of stars in the 6D phase space and to study the star formation history of the members of USC.

In Chapter 6 we combined the WISE and Spitzer photometry to search for debris discs among the IC 4665 members found in Chapter 3. Discs are also ubiquitous to the star and planetary formation process. The improved censuses obtained during this thesis gives a new opportunity to study in particular the disc frequency among stars at various stages of evolution, with direct implications on star and planet formation theories. The methodology was developed and validated in IC 4665 and is ready to be applied to other samples such as the members we found in the region of USC and ρ Oph. The presence of discs around some of the free-floating planets discovered in this thesis would add further indications about their origin, as ejected planets are not expected to harbour discs.

5 DYNAMICAL AGES

5.1 CONTEXT

The age is one of the most fundamental parameters to study stellar formation and evolution. There are several methods to determine stellar ages (e.g. lithium evolution, isochrone fitting, gyrochronology, stellar activity) however, all of them are valid only for a specific age range (or even mass range). Additionally, many of these techniques rely on theoretical evolutionary models which are known to be less reliable at young ages (Baraffe et al. 2002). Dynamical ages[1], on the contrary, have the advantage that they are independent of stellar evolutionary models and are not affected by variability or extinction. These qualities make them a privileged technique to study the age of young associations.

During my Master thesis, I designed a method to determine the dynamical traceback age of young local associations (Miret-Roig et al. 2018). These are small aggregates of stars (a few dozens) that share dynamical properties. For this reason, it is assumed that they were born at the same time and place (from the same molecular cloud) and, therefore, they share the same chemical composition (de Zeeuw et al. 1999; Jayawardhana 2000). The method is based on an orbital traceback analysis and the main assumption is that the stars were formed together, in the past, at a time when the association was most concentrated. This assumption is supported by the lithium and isochronal ages where there is no evidence of a significant age spread (Mamajek and Bell 2014; Messina et al. 2016).

Several authors in the literature have used different techniques to traceback the positions and motions of the stars (linear trajectories, epicyclic approximation, orbital integration with a Galactic potential) and different definitions of the size of the association (e.g. standard deviation of the positions in a privileged direction, in 3D, the maximum distance between members, pairwise encounters). Historically, the main limitations of the traceback analysis were the observational uncertainties in proper motions and the lack of trigonometric parallaxes and radial velocities to derive distances and spatial velocities (Ortega et al. 2002, 2004; Song, Zuckerman and Bessell 2003). After the *Gaia* DR2 we have a large and uniform sample of stars with extremely precise parallaxes and proper motions. Several authors measured radial velocities of members of these young

1 The term "kinematical ages" is sometimes used for similar purposes.

local associations (e.g. Torres et al. 2006; Shkolnik et al. 2012; Gagné and Faherty 2018), but these measurements are highly heterogeneous in quality and systematic errors or differences of unknown origin exist between the various studies. Currently, the main limitations of the traceback analysis are: 1) the availability of a homogeneous and precise dataset of radial velocities; 2) the design of a new strategy for the selection of kinematic members adequate for the high-quality data at hand, and 3) a statistically robust approach for analysing the orbits and to establish a dynamical traceback age. In this study, we made a special effort to prepare a clean sample with precise and uniform data.

In this work, we focused on one of the best-known associations in the solar neighbourhood, the β Pictoris (β Pic) moving group. It was discovered a couple of decades ago when Barrado y Navascués et al. (1999) identified the first two companions to the β Pic star and Zuckerman et al. (2001) identified an additional set of 17 co-moving stars. Since then, many studies have contributed to increase the number of members of this association (e.g. Torres et al. 2006, Malo et al. 2013, Binks, Jeffries and Maxted 2015, Riedel et al. 2017a, and Gagné and Faherty 2018). Today, there are a few hundreds of candidate members of the β Pic moving group, making it one of the richest young local associations. Its proximity ($\sim$ 40 pc) and observational characteristics (it is visible both from the southern and northern hemispheres) facilitated the discovery of members with a large diversity of stellar masses and very interesting properties, such as discs, confirmed exoplanets, and exocomets (Kalas and Jewitt 1995, Kalas, Liu and Matthews 2004, Lagrange et al. 2010, Lagrange et al. 2019, Chauvin et al. 2012, and Kiefer et al. 2014). β Pic has an estimated age of $\sim$ 20 Myr (Barrado y Navascués et al. 1999, Barrado y Navascúes 2001, Mamajek and Bell 2014, Binks and Jeffries 2014), which is of particular interest for the study of several astrophysical processes, such as disc evolution and planet formation. However, different methods lead to a relatively broad range of values and errors ranging from 10.8 Myr to 40 Myr (see Table 5.5 for a review of the literature age estimates of β Pic).

This chapter is based on the work presented in Miret-Roig et al. (2020) and is structured as follows. In Section 5.2, we present the spectroscopic observations we carried out and the process for measuring precise radial velocities for new and archival data. We also describe our method for selecting a bona fide sample of kinematic members from our initial list of candidates from the literature. In Section 5.3, we describe the algorithm used to derive the dynamical age and analyse in detail the orbits of the bona fide members. In Section 5.4, we discuss the results obtained and we present our conclusions in Section 5.5.

5.2 DATA AND SAMPLE SELECTION

In this section, we present a compilation of confirmed members and new candidates reported in the literature over the past decade. To have a sample with homogeneous stellar parameters, we used the 5D astrometric solution (positions, parallaxes, and proper motions) of the *Gaia* DR2 catalogue. We complemented these data with a set of radial velocities (from our own observations plus archival data) analysed using the same methodology. In this study, we used the radial velocities published in the literature and the *Gaia* DR2 catalogue only to compare with our own determinations. In Table 5.1, we review the selection process from the initial compilation to the final sample.

Our initial sample is based on Torres et al. (2008), Schlieder, Lépine and Simon (2012), Malo et al. (2013), Malo et al. (2014a), Gagné et al. (2015b,a), Alonso-Floriano et al. (2015), Messina et al. (2017), Gagné et al. (2018) and Gagné and Faherty (2018). This results in a sample of 236 stars after removing the sources in common between the studies. Binaries and multiple systems are counted as one single object unless they have been resolved in previous studies. These authors used different algorithms based on the kinematics (and included the photometry in some cases) to identify new candidates or confirm members of β Pic. Most of these studies are pre-*Gaia* or were carried with partial information (missing parallaxes or radial velocities). For this reason, it has been necessary to develop a tool to reject kinematic outliers with our homogeneous and precise astrometry and spectroscopy (see Sect. 5.2.3).

5.2.1 *Proper motions and parallaxes*

We used the proper motions and parallaxes of the *Gaia* DR2 catalogue which constitute the most recent and precise astrometric measurements available to date for our sample. To identify the *Gaia* DR2 counterparts of the stars in our sample we used the 2MASS source identifier (which are given in the original tables used to construct our initial sample) and the `TMASS_BEST_NEIGHBOUR` table available in the *Gaia* archive. For 42 sources we did not find a counterpart with this procedure, so we manually refined the match considering position and magnitude. Finally, we found proper motions and parallaxes for 222 stars in our initial sample. There are eight sources in *Gaia* DR2 with only the two-parameter solution and six that are not in *Gaia* DR2 (see App. A.1). The median of the uncertainties of this sample is $\sim$ 0.1 mas yr^{-1} in proper motions and 0.08 mas in parallax which lead to a median error in the tangential velocity of 0.19 km s^{-1}, obtained by taking into account the correlations among the astrometric parameters (see Table 5.1).

Table 5.1. Number of sources at each step of the data selection process (see Sect. 5.2).

	# Members	ground-based RV error (km s^{-1})	*Gaia* RV error (km s^{-1})	*Gaia* V_{tan} error (km s^{-1})
Candidate members from literature	236	0.5*	0.6 (55)	0.19 (222)
High quality RV (this work)	81	0.3	0.6 (31)	0.08 (79)
6D data (*Gaia* astrometry + high quality RV)	79	0.3	0.6 (31)	0.08
Suspected SB (this work) 2				
SB from literature 35				
Single 42				
Single following kinematic criteria (see Sect. 5.2.3)	27	0.3	0.6 (13)	0.05
Confirmed by orbital analysis (bona fide sample)	26			

Notes. Columns 3–4 indicate the median radial velocity error obtained from ground-based surveys and from the *Gaia* DR2 catalogue, respectively. For comparison, in column 5 we indicate the median tangential errors obtained with the *Gaia* DR2 parallaxes and proper motions, obtained taking into account the correlation among the astrometric parameters. The number of *Gaia* sources used to estimate the median velocity errors is indicated in brackets in each case.
(*) median radial velocity errors published in the literature for the 137 stars with radial velocity previous to this work. This sample is inhomogeneous and may be affected by systematic errors among different studies.

Table 5.2. Spectra analysed in this study from our spectroscopic observations plus archival data.

Spectrograph	R	$\Delta\lambda$ (nm)	# Spectra total/this work
FEROS	48 000	350 – 920	167 / 45
ELODIE	45 000	385 – 680	45 / 0
HARPS	115 000	378 – 691	138 / 0
SOPHIE	75 000	387 – 694	62 / 62
UVES	110 000	300 –1100	277 / 0
CAFE	62 000	407 – 925	34 / 34

Notes. Number of spectra analysed and number of new spectra obtained in this study with different instruments. The total number of spectra analysed is 723 and 141 of them are new. The (maximum) resolving power and spectral range of each spectrograph are indicated.

5.2.2 *Radial velocities*

The scarcity and quality of the radial velocities of β Pic stars are currently two of the main limitations for deriving an accurate estimate of the dynamical age of the association. Even though many radial velocity measurements are available in the literature (e.g. Torres et al. 2006, Kharchenko et al. 2007, Shkolnik et al. 2012, Elliott et al. 2014, Gagné and Faherty 2018), we re-analysed the spectra available in public archives to ensure that all the radial velocities are derived using the same methodology. The consistency and homogeneity of the individual measurements are indeed particularly important in a dynamical traceback analysis (see e.g. Miret-Roig et al. 2018).

New spectroscopic observations

We performed spectroscopic observations of β Pic stars with three different instruments. The Fiber-fed Extended Range Optical Spectrograph (FEROS) spectrograph (Kaufer et al. 1999) mounted on the ESO/MPG 2.2 m telescope operated at La Silla (Chile) was used to collect the spectra of 43 stars as part of programme 103.A-9009 (PI: W. Brandner). These observations were performed in OBJCAL mode that allows for simultaneous acquisition of the target spectrum and the calibration lamp during July and August 2019. We observed 8 stars with the Calar Alto Fiber-fed Echelle spectrograph (CAFE) spectrograph (Aceituno et al. 2013; Lillo-Box et al. 2020) mounted on the 2.2 m telescope of the Calar Alto Observatory (programme: H18-2.2-015, F19-2.2-002, PI: D. Barrado). The

observations were carried out from July to October 2018, right after the upgrade of the instrument. The data were processed using the new instrument pipeline described in Lillo-Box et al. (2020), which performs the basic reduction and extracts the radial velocities. Finally, another 14 stars were observed with the SOPHIE spectrograph (Perruchot et al. 2008) mounted on the 1.93 m telescope of the Observatoire de Haute-Provence (OHP) (programmes: 2018A–PNPS005, 2019A–PNPS008, PI: H. Bouy). These spectra were obtained in August 2018 and May 2019 and were processed with the instrument standard data reduction pipeline which measures radial velocities by numerical cross-correlation techniques. The median SNR of our observations is 25.

Spectroscopic archival data

In addition to the observations conducted by our team, we did an exhaustive search for the spectra available in public archives. As shown in Table 5.2, a total of 582 spectra have been collected from the ESO and the ELODIE archives. We reanalysed all these data (see next section *Radial velocities determination*) and provide radial velocities for a large number of stars. Table 5.2 shows the instruments that have been used in this study and the respective number of spectra analysed in each case. We specify the number of new spectroscopic observations presented in this work which constitutes a 20% of all the spectra. We note that some sources have been observed several times with the same or various instruments. In fact, the 723 spectra correspond to 81 different stars, 54% of which have been observed once, 18% twice, and the rest three or more times. In the following section, we describe how we combined the different radial velocity measurements for the same star.

Radial velocities determination

The observed and downloaded spectra were reduced using the official pipeline available for each instrument. We derived radial velocities by cross-correlating the reduced spectra of the stars with the closest mask to its spectral type. We used six different masks of spectral types A0, F0, G2, K0, K5, and M5, along with the iSpec routines for this purpose (Blanco-Cuaresma et al. 2014; Blanco-Cuaresma 2019). This procedure follows the cross-correlation technique (Baranne et al. 1996; Pepe et al. 2002) and fits a Gaussian profile to the cross-correlation function to derive the radial velocity and associated uncertainty. We discard the radial velocity measurements resulting from a poor fit to the cross-correlation function due to, for example, a low SNR of the spectrum or a mismatch between the spectral type of the star and the adopted mask. We used the effective temperatures given in *Gaia* DR2 as a rough estimate of the spectral

type of the star to choose the corresponding mask. For each star, we computed the radial velocity scatter from the results obtained with three different masks: the closest mask (M) to the spectral type of the star, one before (M−1), and one after (M+1). We added this number in quadrature to the formal uncertainty returned from the iSpec routines. The later step accounts for the observed fluctuation on the radial velocity results derived from different masks[2].

We derived radial velocities for 81 stars of our initial sample of β Pic candidates by combining our own observations with archival spectra (Table available at CDS). In the case of multiple radial velocity measurements for the same star, we proceed as follows. For each radial velocity solution (for a given star), we generated a sample of 10 000 synthetic measurements from a Gaussian distribution where the mean and variance correspond to the radial velocity and its uncertainty. We repeated this process for all radial velocity measurements of the star. Then, we took the mean of the joint distribution of synthetic radial velocities as our final result for the radial velocity of the star. The uncertainties on the resulting radial velocity were computed from the 16% and 84% percentiles of the joint distribution of synthetic radial velocities. We note that for ten of the stars (12% of the radial velocities we determine), our radial velocity is the first measurement ever taken. This is an important product of our work since these data can be used to assess the membership and to study the dynamics of the association in 6D. Additionally, six of them are in our final bona fide sample of 26 stars (see Sect 5.2.3).

In Table 5.1, we compare the quality of our radial velocities with the *Gaia* DR2 catalogue and with previous ground-based spectroscopic surveys. We found a radial velocity in the literature for 137 sources in our initial sample. These measurements come from a variety of different surveys with different qualities and methods to determine the radial velocity. On the contrary, our measurements are homogeneous and about 40% more precise than this compilation which is crucial for the success of our work. The radial velocities we determined are twice as precise as the *Gaia* DR2 radial velocities and we have a measurement for a larger number of sources. We identified and discarded 35 sources which have been classified as binaries in previous works. To include the binaries in our study, we would need to determine the radial velocity motion of the centre of mass and that is beyond the scope of this work.

Figure 5.1 shows the comparison of the radial velocities derived in our study with the ones in *Gaia* DR2 and the ones in other spectroscopic surveys in the

2 This method provided an overestimated uncertainty for the β Pic star since it is a fast rotator ($v \sin i =$ 120 km s $^{-1}$, Lagrange et al. 2019) and only the A0 mask provides reasonable cross-correlation function fit. The formal error returned by the iSpec routines is 2.2 km s $^{-1}$, a 60% smaller than the final uncertainty we obtain from different masks (5.5 km s $^{-1}$).

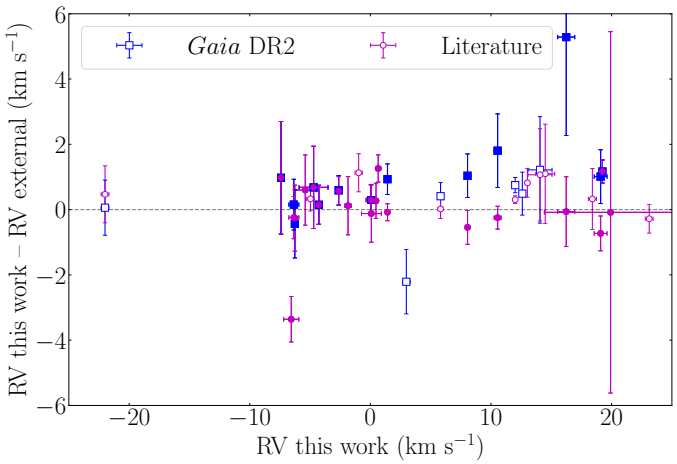

Figure 5.1. Radial velocity residuals between this work and external measures: *Gaia* DR2 (blue squares) and previous spectroscopic measures in the literature (magenta open circles). For this comparison, we used the 42 single stars with 6D data (see Table 5.1). Our final sample of 26 stars is represented by the filled markers. We note that our radial velocity uncertainties (horizontal error bars) are smaller than the markers in most of the cases. The largest uncertainty corresponds to the β Pic star (see footnote 2).

literature for the 42 single stars with 6D data in our sample. We found hints of binarity in two sources (2MASS J19312434 − 2134226 and 2MASS J22571130 + 3639451) and we discarded them from the analysis (see App. A.2). The median difference and root mean square error between the *Gaia* DR2 radial velocities and our measurements are 0.7 km s^{-1} and 1.0 km s^{-1}, respectively. We obtained these values by disregarding the source with a radial velocity difference of about 5 km s^{-1}. The *Gaia* DR2 radial velocity of this star is based only in two transits, which is probably the reason for its large uncertainty. If we compare the radial velocities from the literature and our sample, we obtain a median difference and root mean square error of 0.3 km s^{-1} and 0.9 km s^{-1}, respectively. Since we believe that the homogeneity and precision of our radial velocities are superior to any other sample, we only use our measurements in the current analysis.

5.2.3 *Kinematic sample selection*

In this section, we present the kinematic selection that we designed to discard kinematic outliers in our sample. Kinematic outliers in the context of the present study refer to sources with a velocity significantly different than the group,

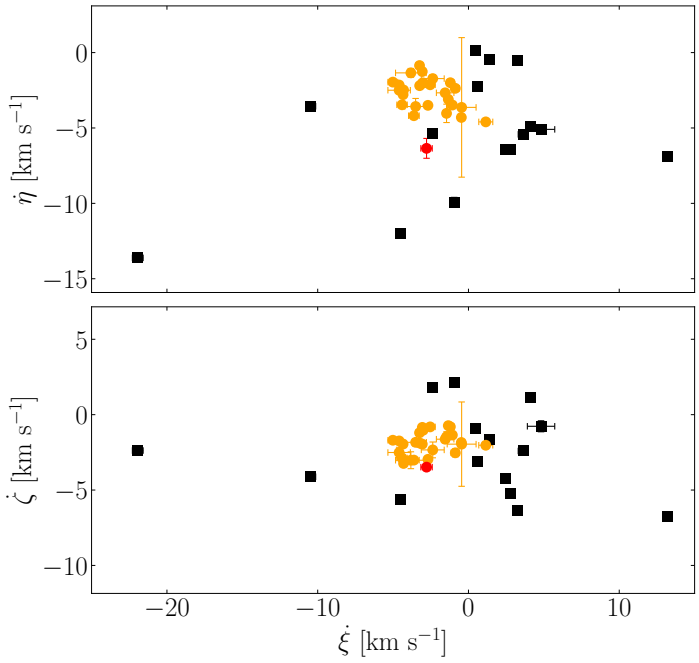

Figure 5.2. Present velocity distribution in the Galactic plane (top) and in the vertical plane (bottom) of the sample of 42 single sources with 6D data. The sample of 26 kinematically selected members is represented by the orange dots and the kinematically rejected sources are the black squares. The source 2MASS J11493184 − 7851011 (red dot) is retained by our kinematical criteria but is discarded due to its orbit (see text).

either because they are non-members or because they have variable velocity due to multiplicity, for example. First, we introduce the notation we adopted to refer to position and velocity coordinate systems. We used the curvilinear heliocentric coordinates (ξ', η', ζ') defined in Asiain, Figueras and Torra (1999) to place the stars in the configuration space. This coordinate system is centred at the current position of the Sun ($R_\odot = 8.4$ kpc) and rotates around the Galactic centre with a frequency of the circular velocity of $\omega_\odot = 28.81$ km s^{-1} kpc^{-1} (Irrgang et al. 2013). It has the advantage that it minimises the variation in each component of the configuration space. The radial component ξ' points towards the Galactic anti-centre, the azimuthal component η' is measured along the circle of radius $R_\odot$ and is positive in the sense of the galactic rotation, and the vertical component ζ' is defined positive towards the north Galactic pole. We also refer to the corresponding velocities as $\dot{\xi}', \dot{\eta}', \dot{\zeta}'$. The second reference

system considered in this work is the Cartesian heliocentric system. The spatial components X, Y, Z, along with the velocity components U, V, W, are defined with X, U pointing towards the Galactic centre, Y, V towards the direction of Galactic rotation, and Z, W towards the north Galactic pole. We use a peculiar solar motion of $(U_\odot, V_\odot, W_\odot) = (11.1, 12.24, 7.25)$ km s^{-1} (Schönrich, Binney and Dehnen 2010).

In Figure 5.2 we represent the velocity distribution of the 42 single stars with *Gaia* astrometry and radial velocities from this work. We see that some sources have a significant scatter. Most of them were classified as members of β Pic with pre-*Gaia* astrometry or with no radial velocity information and clearly appear to be kinematic outliers with our extremely precise data. We discarded the kinematic outliers in the 3D velocity distribution $(\dot{\xi}', \dot{\eta}', \dot{\zeta}')$ in a similar way to what we did in Miret-Roig et al. (2018). The major improvement is that in this work we used a robust estimator of the covariance matrix (the Minimum Covariance Determinant from Sklearn, Pedregosa et al. 2011) to fit the central location ($\vec{\boldsymbol{\mu}}$) and the covariance matrix ($\boldsymbol{\Sigma}$) of the velocity ellipsoid of the association. Then, we computed the Mahalanobis distance of each object defined as:

$$D_M(\vec{\boldsymbol{x}}) = \sqrt{(\vec{\boldsymbol{x}} - \vec{\boldsymbol{\mu}})^T \boldsymbol{\Sigma}^{-1} (\vec{\boldsymbol{x}} - \vec{\boldsymbol{\mu}})}. \tag{5.1}$$

In Figure A.1, we show the distribution of Mahalanobis distances. We used the percentile p_{65} to discard the kinematic outliers and retain 27 kinematic members (dots in Fig. 5.2). This threshold is empiric and represents the best compromise between rejecting kinematic outliers which hinder the traceback analysis and keeping kinematic members in the final sample. When we computed the orbits of our targets (see Sect. 5.3.1) we immediately saw that one of them (2MASS $J11493184 - 7851011$, red circle in Fig. 5.2) had an orbit that is significantly different from the main group and thus, we discarded this object. This star has kinematics similar to β Pic but it is at $> 3\sigma$ in positions compared to β Pic. We also checked that this object has the largest Mahalanobis distance to the centre of the velocity distribution. We refer to App. A.2 for a detailed discussion, source-by-source, of the kinematically rejected sources. The final sample contains 26 bona fide members of β Pic and their 3D positions and velocities are given in Table C.14 (available at CDS).

5.2.4 *Bona fide β Pic sample*

In this paper, we made a substantial effort to prepare a robust sample of β Pic members with the best precision possible in their determination of the positions in the 6D space phase. Then, we used this valuable data to identify and remove

Table 5.3. Parameters of the distribution in positions (in pc) and in velocities (in km s^{-1}) of the 26 bona fide kinematic members of β Pic in the present ($t = 0$ Myr).

Positions											
X	Y	Z	$\sigma_{obs,X}$	$\sigma_{obs,Y}$	$\sigma_{obs,Z}$	$\sigma_{err,X}$	$\sigma_{err,Y}$	$\sigma_{err,Z}$	$\sigma_{int,X}$	$\sigma_{int,Y}$	$\sigma_{int,Z}$
47.49	−7.89	−17.92	16.04	13.18	7.44	0.11	0.04	0.05	15.93	13.14	7.39
Velocities											
U	V	W	$\sigma_{obs,U}$	$\sigma_{obs,V}$	$\sigma_{obs,W}$	$\sigma_{err,U}$	$\sigma_{err,V}$	$\sigma_{err,W}$	$\sigma_{int,U}$	$\sigma_{int,V}$	$\sigma_{int,W}$
−8.74	−16.16	−9.98	1.49	0.54	0.70	0.24	0.11	0.11	1.25	0.43	0.59

Notes. Columns indicate: (1–3) central location of the distribution, (4–6) robust standard deviation, (7–9) median errors, and (10–12) a rough estimate of the intrinsic dispersion, computed as $\sigma^2_{int} = \sigma^2_{obs} - \sigma^2_{err}$.

kinematic outliers. In this section, we review the main characteristics of our final sample.

The relative error in the parallax of these members is less than 1% which allows us to compute the distance as the inverse of parallax. We note that four stars have a parallax error $< 0.1\%$ at distances up to 50 pc. The median relative errors in proper motions are of 0.3% in right ascension (μ_{α^*}) and 0.09% in declination (μ_δ). The precision in μ_{α^*} and μ_δ is similar but a few members have μ_{α^*} close to zero which increases the relative error. The β Pic star is the brightest source ($G = 3.7$ mag) and causes a fraction of the pixel used in the standard *Gaia* DR2 analysis to be saturated. Hence, measurements of its centroid position and the resulting astrometry are less precise than for fainter sources ($G > 6$ mag) (Lindegren et al. 2018b).

In Table 5.3, we provide the median heliocentric position and velocity of β Pic. The observational uncertainties in positions (σ_{err}) are of the order of tenths of parsecs and thus, the observed dispersion (σ_{obs}) can be interpreted as an intrinsic dispersion (σ_{int}). The dispersion in the Galactic plane (X, Y components) is twice the vertical dispersion (Z). When we look at the velocity dispersion, we find that the median errors in velocity (σ_{err}) are significantly smaller than the velocity dispersion observed (σ_{obs}), indicating the presence of an intrinsic cosmic dispersion (σ_{int}). Therefore, the dispersion we observe in Figure 5.2 is intrinsic and not due to observational errors. The velocity ellipsoid is elongated in the radial direction (towards the Galactic centre) with a dispersion that is twice that of those in the other two directions. The typical velocity dispersions observed in molecular clouds are of the order of 0.5 to 1 km s^{-1} in nearby, low-mass star-forming regions (Hennebelle and Falgarone 2012; Heyer and Dame 2015, and references therein), similar to the velocity dispersion we find in β Pic.

5.3 TRACEBACK ANALYSIS

In this section, we describe our methodology to perform the traceback analysis which is based on the work of Miret-Roig et al. (2018), with some improvements.

5.3.1 *Towards a dynamical age estimate*

We considered the same 3D Milky Way potential as in Miret-Roig et al. (2018) to integrate the equations of motion. This model is based on the Allen and Santillan (1991) potential which consists of a spherical central bulge, a disc, and a massive spherical halo, but with updated parameters taken from Irrgang et al. (2013, their Table 1). Hereafter, we refer to this model as new A&S and we compare it with other axisymmetric models in Section 5.3.3. In Figure 5.3, we

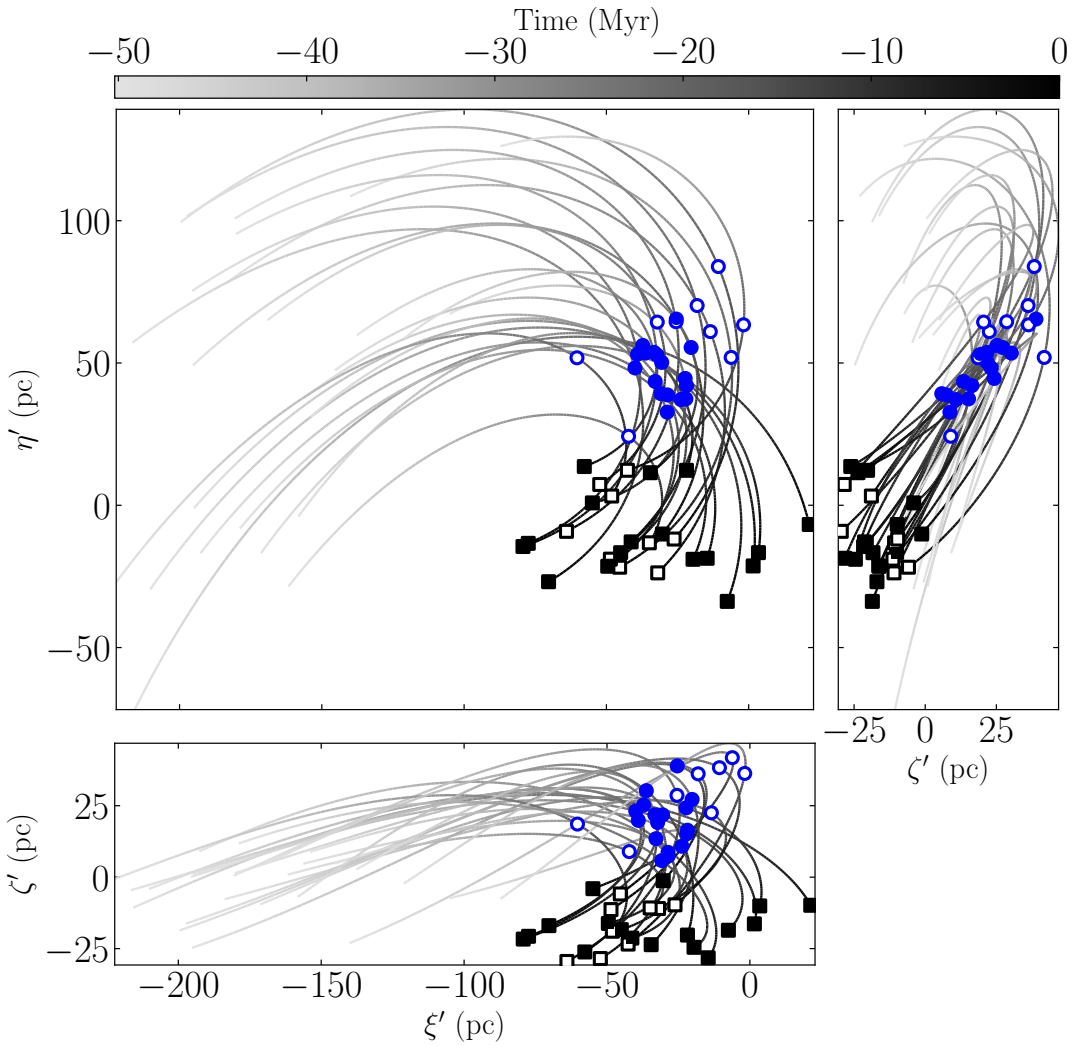

Figure 5.3. Orbital projection in the Galactic plane (top left) and in the two vertical planes (bottom left and top right) of our bona fide sample of 26 members of β Pic, integrated back in time 50 Myr, under the new A&S potential. The orbits are colour-coded with the backwards time, the black squares represent the positions in the present ($t = 0$ Myr), and the blue dots represent positions at birth time ($t = -18.5$ Myr). The filled markers correspond to the core of β Pic defined in Section 5.3.2.

show the 2D orbital projections in the Galactic plane and the two vertical planes of the 26 bona fide members in our sample. The orbits have been integrated back in time 50 Myr.

Following the example of other studies (e.g. Fernández, Figueras and Torra 2008; Ducourant et al. 2014; Mamajek and Bell 2014; Riedel et al. 2017a; Miret-Roig et al. 2018), we define the dynamical age as the time at which the members of the association were most concentrated in space. The algorithm to measure the degree of concentration, hereafter the size of the association, is of uttermost importance and different strategies to compute the size have been used in the literature. These different methodologies have significantly contributed to the large spread in the dynamical traceback ages determined. In general, the size of the association is estimated with the empiric standard deviation in the spatial coordinates. However, it is very sensitive to the presence of outliers, i.e. members which significantly deviate from the mean position of the association which are not necessarily contaminants. In this section, we present three strategies to estimate the size of the association as a function of time. Some of them are based on classical functions used in the literature (i.e. the variance) and others are novel, representing the overall variance of the association, and independent of the coordinates chosen. In the following, we define the three functions we use to estimate the size of the association in a way that they all have units of length.

- The size in the radial, azimuthal, and vertical directions ($S_{\xi'}$, $S_{\eta'}$, $S_{\zeta'}$) are the squared root of the diagonal terms of the covariance matrix in each direction.
- The Trace Covariance Matrix Size (S_{TCM}) is defined as:

$$S_{TCM} = \left[\frac{\mathrm{Tr}(\mathbf{\Sigma})}{3}\right]^{1/2}. \tag{5.2}$$

- The Determinant Covariance Matrix Size (S_{DCM}) is defined as:

$$S_{DCM} = [\det(\mathbf{\Sigma})]^{1/6}. \tag{5.3}$$

Each of these expressions is computed from the covariance matrix of the association in the configuration space. We used two different algorithms to estimate the covariance matrix, namely the empirical covariance estimation, and the robust covariance estimation, both from the Sklearn packages (Pedregosa et al. 2011). Whereas the first corresponds to the classical maximum likelihood estimator, the second is less sensitive to outliers in the dataset.

The size estimators $S_{\tilde{\xi}'}$, $S_{\eta'}$, and $S_{\zeta'}$, when computed with the empirical covariance estimation, correspond to the classical standard deviation in each direction. The other two size estimators (S_{TCM} and S_{DCM}) can be interpreted from the eigenvalues of the covariance matrix. The trace of the association often referred to as the total variance of the covariance matrix, coincides with the sum of its eigenvalues. In Equation 5.2, we introduce a factor of $1/3$ (in a 3D space) so that we can interpret the S_{TCM} estimator as the arithmetic mean of the variance in the individual components. In any case, this multiplicative factor changes the absolute value of the size estimator but not the locus of the minimum, which is our main interest. The determinant of the covariance matrix, also known as the generalised variance, can be interpreted as the geometric mean of the eigenvalues of the covariance matrix. Then, the volume of the association is proportional to the squared root of the determinant of the covariance matrix. Finally, we define the diagonal of the Determinant Covariance Matrix Size (S_{dDCM}) analogously to the S_{DCM} size but only considering the diagonal terms, that is, neglecting the correlations among the three spatial components. This is not a good estimator of the size of the association since it neglects part of the information included in the covariance matrix. However, it can be understood as a geometric mean of the size estimators $S_{\tilde{\xi}'}$, $S_{\eta'}$, $S_{\zeta'}$, so we include it only for comparison.

In Figure 5.4 we show the six parameters defining the size of β Pic ($S_{\tilde{\xi}'}$, $S_{\eta'}$, $S_{\zeta'}$, S_{DCM}, S_{dDCM}, S_{TCM}) computed with the empirical covariance estimate and the robust covariance estimate as a function of time. Remarkably, the minimum size obtained with the empirical covariance estimate (top panels) depends on the size estimator, whereas we find a minimum at similar times for all the size estimators considered with the robust covariance estimate (bottom panels). This is because the robust covariance estimate gives less weight to sources with a large dispersion, attenuating the impact of outliers.

Going forward, we only considered the size estimates computed with the robust covariance estimates. In the left bottom panel of Figure 5.4, we show the dispersion in the radial, azimuthal, and vertical direction, independently. We see that the vertical component does not provide useful information for constraining the age of the association, while the two components in the Galactic plane have a minimum at a similar time. In this panel, we highlighted the azimuthal component ($S_{\eta'}$) which is the size estimator we used in Miret-Roig et al. (2018), although in that study we used the empiric covariance estimate (top panel).

In the middle bottom panel, we add the size from the determinant of the covariance matrix (S_{DCM}) and, for comparison, the inaccurate size using only the diagonal values of this matrix (S_{dDCM}), that is, with and without correlations, respectively. Both curves have close minima with a time difference of ~ 1 Myr

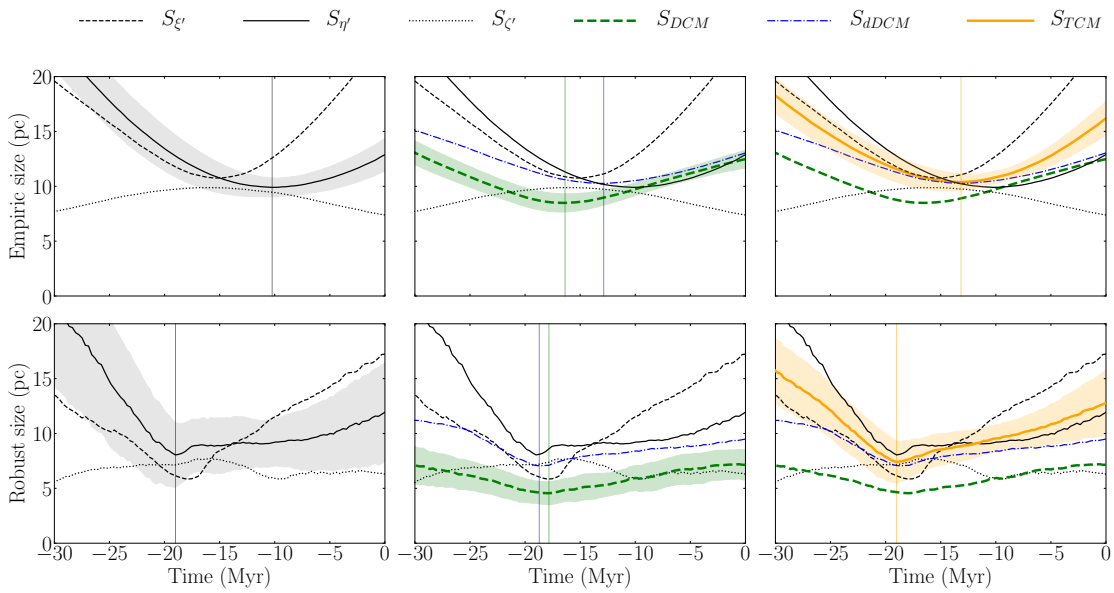

Figure 5.4. Size of the β Pic association as a function of backwards time computed with the empirical covariance estimate (top panels) and the robust covariance estimate (bottom panels). The association size estimates considered in this study are indicated in the legend and described in the text. The lines represent the median of 1 000 bootstrap repetitions and the shaded areas represent the 1σ uncertainties. The orbits were integrated using the new A&S potential.

and are also similar to the age obtained with the $S_{\eta'}$ size estimator. The correlations reduce the value of the determinant and in consequence, the absolute value of S_{DCM}, estimating a birth size of the association of $\sim$ 5 pc. In the right bottom panel, we include the size estimator from the trace (S_{TCM}) which also has a minimum at a similar time. As mentioned before, the S_{TCM} and S_{DCM} sizes correspond to the arithmetic and geometric mean of the eigenvalues of the covariance matrix, respectively. These two statistics are related by an inequality in which the arithmetic mean is always larger than the geometric mean and they are only equal if all the individual values are the same. This corresponds to an isotropic covariance matrix, which is not the case in our study.

Currently, thanks to the excellent astrometric precision of *Gaia* and the homogeneous precise radial velocity sample derived in this work, the observational uncertainties are no longer what dominates the uncertainties in the dynamical age. We propagated the present uncertainties with an analytic approximation (Miret-Roig et al. 2018) and estimated that the dispersion due to observational uncertainties is $\lesssim$ 2 pc at the time of minimum size. At birth, the association had a S_{TCM} size of $\sim$ 7 pc (see Fig. 5.4), which is similar to what has been observed

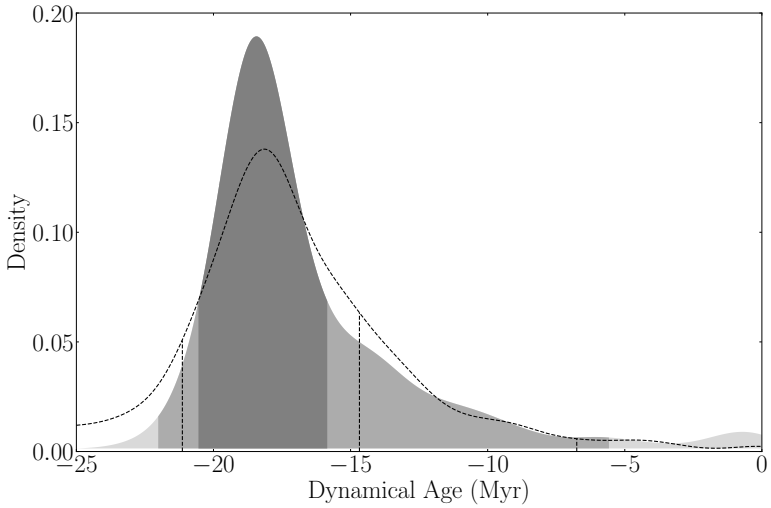

Figure 5.5. Dynamical age distribution of the bona fide β Pic members, obtained with the robust estimate of the covariance matrix. The distribution obtained with the S_{TCM} size estimator is colour-coded with the 68%, 95%, and 99.7% highest-density intervals. The distribution obtained with the S_{DCM} size estimator is shown in dashed lines and the same highest density intervals are shown. The orbits were integrated using the new A&S potential and we computed 1 000 bootstrap repetitions.

in star-forming regions such as Ophiuchus (Cánovas et al. 2019), Taurus (Galli et al. 2019), and Corona Australis (Galli et al. 2020).

As mentioned, the sample selection (i.e. the presence of contaminants or unidentified binaries) is extremely important. To estimate the impact of the sample selection on the age, we took 1 000 random samples of the 26 bona fide β Pic members and estimated the dynamical age with each. Then, determined the dynamical age and a robust uncertainty from the distribution of ages. In Figure 5.5, we report a kernel density estimate of the age distribution with a bandwidth of 1 Myr; this value is smaller and of the order of the age uncertainties. In Table 5.4, we report the mode and the 68%, 95%, and 99.7% highest density intervals[3] of the age distribution. Considering the S_{TCM} size estimator and the 68% highest density interval, we find a dynamical age of β Pic of $18.5^{+2.0}_{-2.4}$ Myr (see Table 5.4). With the S_{DCM} size estimator, we obtain a similar age, $17.6^{+3.5}_{-2.9}$ Myr. We note that the two values agree within a 1 Myr difference which is significantly smaller than the age uncertainty.

3 The highest density interval is defined such that all points within the interval have a higher probability density than all points outside the interval. We used the ArviZ python package (Kumar et al. 2019) to compute it.

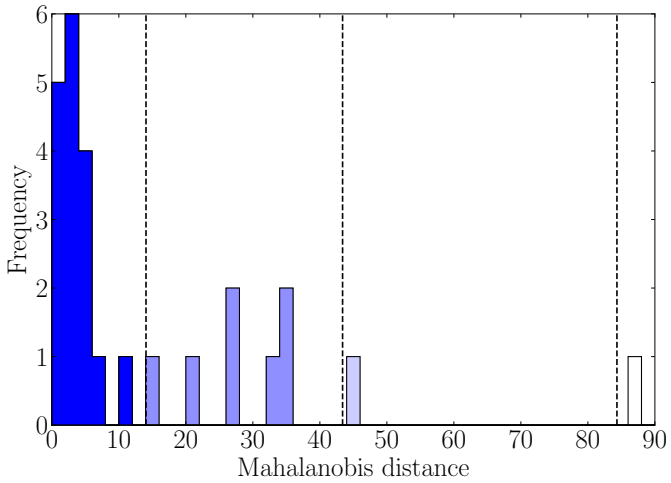

Figure 5.6. Histogram of the Mahalanobis distance to the centre of the 3D positions distribution (ξ', η', ζ') of the 26 selected kinematic members of our sample, computed with the robust metric. The vertical dashed lines indicate the position of the percentiles p_{68}, p_{95}, and $p_{99.7}$.

5.3.2 *Signs of substructure at birth time*

When we look at Figure 5.3, we see that at birth, some stars appeared to be more concentrated and forming a core (filled dots), while a few members appeared to be more dispersed (empty dots). To identify these two populations, we computed the Mahalanobis distance (see Equation 5.1) with the robust central location and covariance of the 3D spatial distribution (ξ', η', ζ'). In Figure 5.6, we show the distribution of the Mahalanobis distances. We used the percentile p_{68} to separate the core from the peripheral stars which result in 17 core stars and 9 peripheral stars (see Table C.14). These stars were selected at birth in the space of positions where they appear most concentrated (see Fig. 5.3). Interestingly, in the present, the stars forming the core appear more dispersed than those originally more dispersed. In the velocity space, both populations are mixed in the present and at birth (see Fig. 5.7).

It is worth mentioning that if we use only the 17 core stars to study the dynamical age, we obtain an age very similar to the value we obtained in Section 5.3.1. With the S_{TCM} size, we find an age estimate of $18.8^{+1.7}_{-2.1}$ Myr and with the S_{DCM} size of $17.6^{+3.5}_{-1.2}$ Myr. As expected, in this case, where all the stars are well concentrated at birth time, the age is independent of the covariance estimate used (empirical or robust). Additionally, the small bump we observe

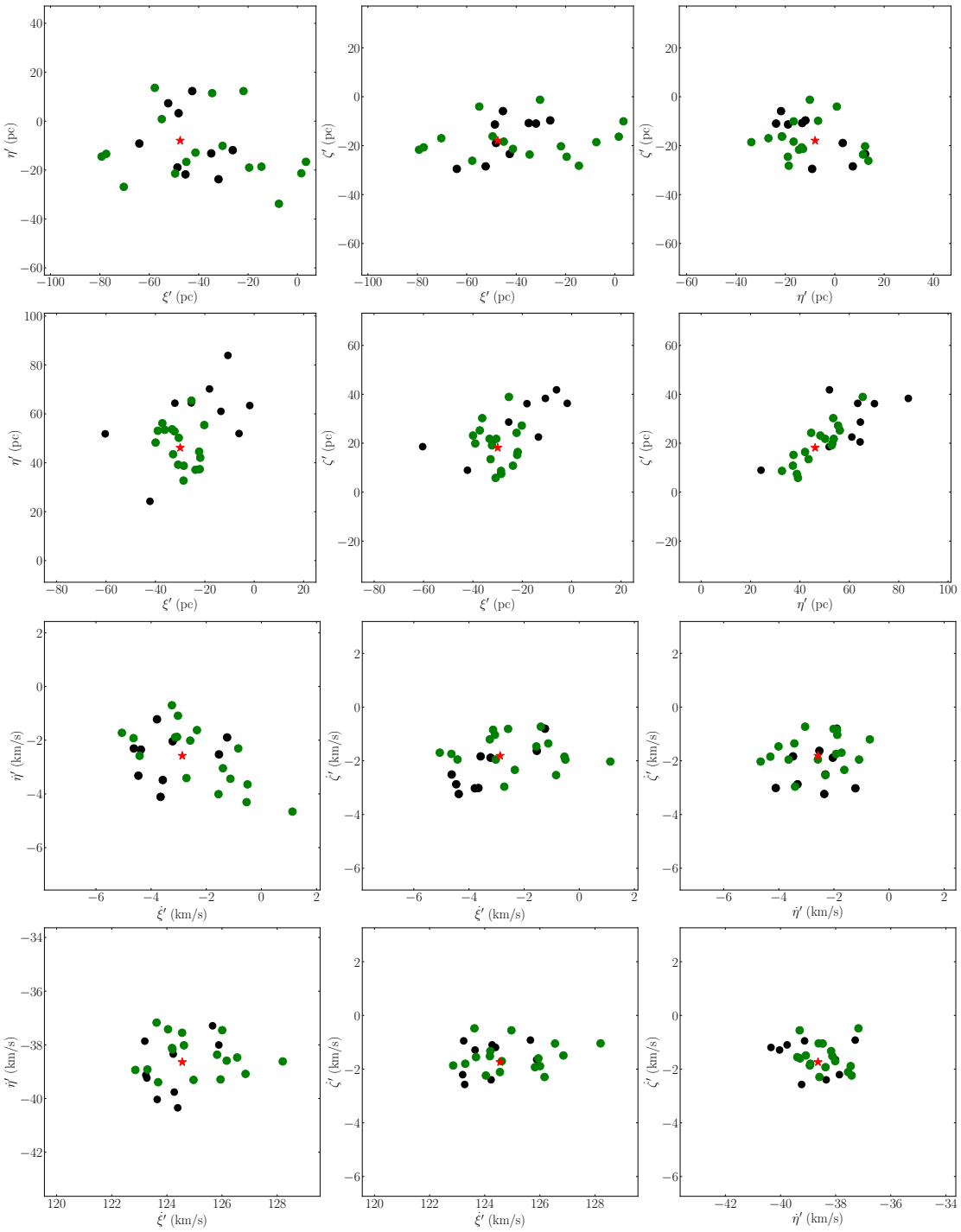

Figure 5.7. Top: 2D projections of the distribution in positions in the present. Top middle: 2D projections of the distribution in positions at birth time. Bottom middle: 2D projections of the distribution in velocities in the present. Bottom: 2D projections of the distribution in velocities at birth. In all the cases we show the 17 core stars (in green) and the other 9 stars more dispersed in black. The red star represents the locus of the distribution.

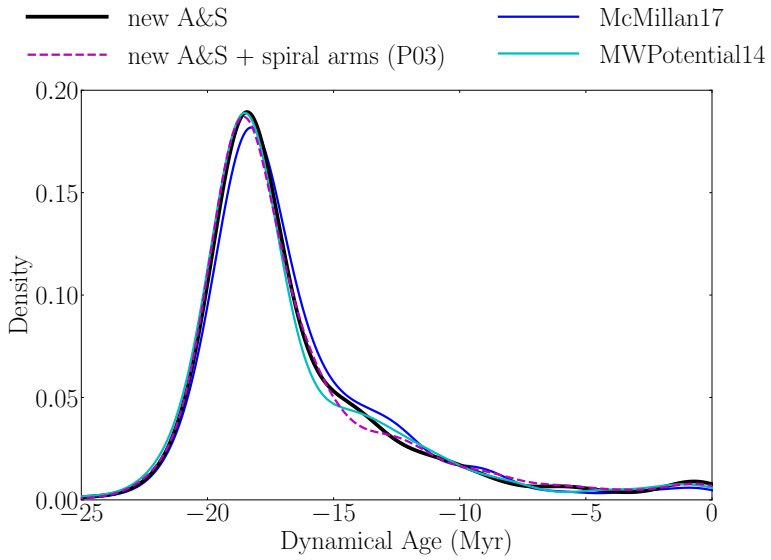

Figure 5.8. Dynamical age distribution of β Pic obtained with the S_{TCM} size estimator and different axisymmetric potentials (solid lines) and with the new A&S + spiral arms (P03) potential (dashed line).

in Figure 5.5 at ~ -15 Myr disappears with the age distribution obtained only with the 17 core stars. In short, if we use the core sample of 17 stars to trace back the age of β Pic we find variations of less than 1 Myr compared to the value we obtained in Section 5.3.1, with all the covariance and size estimates considered in this study. This is the first time that the spatial distribution of β Pic is analysed in detail and these results should be revisited with a larger sample of members.

5.3.3 *Effect of the Galactic potential*

In this section, we discuss the effect of considering different Galactic axisymmetric potentials and including non-axisymmetric structures such as spiral arms, on the dynamical age. First, we considered two additional axisymmetric potentials, namely McMillan (2017, hereafter McMillan17) and Bovy (2015, hereafter MWPotential14). These two models together with the new A&S model have similar rotation curves in the range of radius relevant here with only slight differences in the mass distribution as can be seen in their respective rotation curves (Figure D.1 in Gaia Collaboration et al. 2018a for a comparison of new A&S and McMillan17 and Figure 8 in Bovy 2015 for MWpotential14).

Table 5.4. Dynamical age (in Myr) obtained with the robust metrics for different potentials. We report the mode and the highest density interval for probabilities of 68%, 95%, and 99.7%.

Potential	Size estimator	$p_{0.15}$	$p_{2.5}$	p_{16}	mode	p_{84}	$p_{97.5}$	$p_{99.85}$
new A&S	S_{DCM}	-32.0	-27.6	-21.1	-17.6	-14.7	-6.8	0
McMillan17	S_{DCM}	-43.9	-29.3	-20.2	-17.7	-14.6	-8.1	0
MWPotential14	S_{DCM}	-46.5	-27.8	-21.2	-17.7	-14.6	-6.1	-1.5
new A&S + spiral arms (P03)	S_{DCM}	-46.4	-29.3	-20.8	-17.9	-14.4	-7.6	0
new A&S	S_{TCM}	-25.2	-22.0	-20.5	-18.5	-15.9	-5.6	0
McMillan17	S_{TCM}	-26.3	-22.2	-19.7	-18.2	-15.2	-8.6	0
MWPotential14	S_{TCM}	-26.3	-23.7	-20.7	-18.7	-16.2	-7.6	0
new A&S + spiral arms (P03)	S_{TCM}	-26.4	-22.3	-20.2	-18.5	-15.9	-5.6	0

We also used a non-axisymmetric potential which accounts for the spiral arms in addition to the axisymmetric potential described in Sect. 5.3.1. The 3D spiral model is the PERLAS spiral arms from Pichardo et al. (2003, hereafter new A&S + spiral arms (P03)). The locus is the one following Drimmel and Spergel (2001) and has a pitch angle of 15.5°. We take a pattern speed of $\Omega_P = 21$ km s^{-1} kpc^{-1} and a mass of 0.04% of the disc mass. These values are in agreement with the values proposed in Antoja et al. (2011). Recently, Eilers et al. (2020) estimated a density contrast at the solar radius of 20% which is similar to the amplitude of the arms used here which leads to a contrast of around 23% (Antoja et al. 2011).

In Figure 5.8 we present the dynamical age distribution obtained with different axisymmetric potentials and with the non-axisymmetric potential with spiral arms. In Table 5.4 we report the percentiles of the dynamical age distribution for each of the potentials considered. The variations in the dynamical age due to the Galactic potential are minimal, and they are all compatible with the value we obtained in Section 5.3.1. Therefore, we conclude that the variations in the dynamical age produced by different Galactic potentials are much lower than our main source of uncertainty, that is, the membership. This is valid for the potentials we have tested, the parameters of which are constrained by recent observations of the Milky Way and can be explained for the short integration times given the low age of the association. Given that the different Galactic potentials considered here lead to changes in the dynamical age smaller than the current uncertainties, we decided to keep the results obtained with the new A&S potential which has fewer parameters.

5.4 DISCUSSION

In the previous section, we discussed different strategies to determine the dynamical traceback age of β Pic. All of them are compatible, with differences of $\lesssim 1$ Myr, significantly smaller than the age uncertainties. Going forward, we adopt an age of $18.5^{+2.0}_{-2.4}$ Myr, obtained for the sample of 26 bona fide members, with the S_{TCM} size, and with the axisymmetric potential. Our study provides the first traceback age which conforms with other dynamical ages recently published in the literature, such as the expansion or the forward-modelling algorithms and with ages based on evolutionary models such as the lithium depletion or the isochronal ages. In Table 5.5, we present a compilation of previous age estimates published in the literature and we see that our determination is compatible with the majority of them. The first reliable age determination of the β Pic star and its moving group was an isochronal age presented in Barrado y Navascués et al. (1999), 20 ± 10 Myr, which is in full agreement with our current estimate.

Table 5.5. Literature age estimates for β Pic. This table is an udated version of Table 1 from Mamajek and Bell (2014).

Reference	Age	Method
Barrado y Navascués et al. 1999	20 ± 10 Myr	CMD isochronal age (KM stars)
Zuckerman et al. 2001	12^{+8}_{-4} Myr	H-R diagram isochronal age (KM stars)
Ortega et al. 2002	11.5 Myr	Dynamical (Traceback) age
Song, Zuckerman and Bessell 2003	12 Myr	Dynamical (Traceback) age
Ortega et al. 2004	10.8 ± 0.3 Myr	Dynamical (Traceback) age
Torres et al. 2006	18 Myr	Dynamical (Expansion) age
Makarov 2007	31 ± 21 Myr	Dynamical (Traceback) age
Mentuch et al. 2008	21 ± 9 Myr	Li depletion
Macdonald and Mullan 2010	~ 40 Myr	Li depletion (magnetoconvection models)
Binks and Jeffries 2014	21 ± 4 Myr	Li depletion boundary
Malo et al. 2014b	26 ± 3 Myr	Li depletion boundary
Malo et al. 2014b	21.5 ± 6.5 Myr ($15 - 28$ Myr)	H–R diagram isochronal age (KM stars)
Mamajek and Bell 2014	22 ± 3 Myr	CMD isochronal age (FG stars)
Mamajek and Bell 2014	$13 - 58$ Myr	Dynamical (Expansion) age
Bell, Mamajek and Naylor 2015	24 ± 3 Myr	CMD isochronal age
Messina et al. 2016	25 ± 3 Myr	Li depletion boundary (rotation models)
Miret-Roig et al. 2018	13^{+7}_{-0} Myr	Dynamical (Traceback) age
Crundall et al. 2019	$18.3^{+1.3}_{-1.2}$ Myr	Dynamical (Forward-modelling) age
Ujjwal et al. 2020	19.38 Myr ($5.5 - 54.5$ Myr)	CMD isochronal age
This work	$18.5^{+2.0}_{-2.4}$ **Myr**	**Dynamical (Traceback) age**

The earliest traceback studies of β Pic obtained an age of $11 - 13$ Myr (Ortega et al. 2002, Song, Zuckerman and Bessell 2003, Ortega et al. 2004), which is younger than what we find here. These differences are most probably due to the large observational uncertainties of the pre-*Gaia* astrometry and, thus, to the presence of a significant number of kinematic contaminants. Those authors used the maximum size between stars to determine the age of the association. We did not consider this size estimator in our study but it is clearly sensitive to the presence of outliers in the dataset.

Miret-Roig et al. (2018) measured a dynamical age of β Pic of 13^{+7}_{-0} Myr with a method that is very similar to the one presented in this work. We believe that the main differences between these two studies are 1) the precision of the 6D space phase positions, 2) the new sample selection based on a robust estimate of the 3D velocities covariance matrix, and 3) the new orbital analysis which uses an improved size estimator of the association.

In our previous study, we used the *Gaia* DR1 astrometry and a compilation of radial velocities from the literature without any treatment. Here, we use the improved precision of *Gaia* DR2 and a uniform sample of radial velocities. The median uncertainty in the DR1 parallaxes and proper motions were 0.3 mas and 0.2 mas yr^{-1}, respectively, compared to the values 0.05 mas and < 0.1 mas yr^{-1} now available from the DR2. We discarded ten objects from our previous sample for being classified as binaries and five others do not have a radial velocity measurement in our work. These leaves only six objects in common between the two works (23% of our new sample). The black solid line in Figure 5.4 ($S_{\eta'}$) corresponds to the methodology used in Miret-Roig et al. (2018) (their blue curve in Fig. 7). We see that with the empiric covariance (top panel) matrix we still find younger dynamical traceback ages. On the contrary, the size estimator $S_{\eta'}$, if we use a robust estimate of the covariance matrix, we recover a similar age to the one reported in Section 5.3.1.

Another technique used in the literature to measure a kinematic age consists of studying if the association is under expansion. Torres et al. (2006) found a linear relationship between the velocity and the position in the direction of the Galactic centre, which results in an age of ~ 18 Myr. In a similar approach, Mamajek and Bell (2014) found an age of 21^{+10}_{-5} Myr, taking into account the positions and velocities in the Galactic plane. Both results are compatible with what we obtain here. Besides, we used our new accurate sample to estimate an expansion age of β Pic. We fitted a line between the Cartesian heliocentric positions XYZ and velocities UVW. We find evidence of expansion in the direction towards the Galactic centre and in the direction of Galactic rotation with slopes of $\kappa_X = 0.057 \pm 0.006$ km s $^{-1}$ pc^{-1} and $\kappa_Y = 0.033 \pm 0.008$ km s $^{-1}$ pc^{-1}, respectively. In the vertical direction, we find a slope of $\kappa_Z = -0.02 \pm 0.02$ km s $^{-1}$ pc^{-1},

which is slightly negative but compatible with zero. These coefficients result in an expansion age[4] of 17 ± 2 Myr and 29 ± 4 Myr in the radial and azimuthal directions. If we combine these measures with a weighted mean as done by Mamajek and Bell (2014), we obtain an expansion age of 20 ± 4 Myr, in excellent agreement with our traceback age.

Recently, Crundall et al. (2019) provided a new tool (Chronostar) to determine a dynamical age applying the forward-modelling technique and obtained an age of $18.3^{+1.3}_{-1.2}$ Myr. It is interesting to see how similar the results of their study are to ours despite the different sample of members (we have 15 members in common, 25% of their sample) and method used. These results prove that both methods are complementary. Their method allowed them to detect the β Pic members among a large catalogue of field stars while ours provides a deeper orbital analysis allowing us to discover, for example, the existence of a central core and a more dispersed structure at birth time.

Finally, it is important to mention that the age estimates in the literature based on the Li depletion or isochronal fitting obtained values very similar to the one obtained here and, in general, with a lower dispersion than the dynamical age estimates obtained up to now (see Table 5.5). If we exclude the work of Macdonald and Mullan (2010) which obtained an age of $\sim$ 40 Myr, twice the other works, we obtain a median value of 21 ± 4 Myr which is in good agreement with the age we measured. This is an important result since our method is independent of evolutionary models and these are two very different strategies.

5.5 CONCLUSIONS

In this work, we measured a dynamical, traceback age of the β Pic moving group of $18.5^{+2.0}_{-2.4}$ Myr which is compatible with ages based on evolutionary models. Our age estimate is the first traceback age that reconciles the ages determined by the traceback method with other dynamical ages (expansion, forward modelling), lithium depletion ages, or isochronal ages.

The precision in the dynamical traceback age we achieved in this study is thanks to the combination of the *Gaia* DR2 astrometry and the uniform radial velocity sample of single stars that we produced in this work. We measured the radial velocity of 81 candidate members of β Pic uniformly. For ten sources, our measure is the first radial velocity estimate. This is an important result of our work, allowing us to identify 15 kinematic outliers from our initial sample and two new potential spectroscopic binaries.

4 To compute the expansion age we used the relation $\tau = \gamma^{-1}\kappa^{-1}$, where $\gamma = 1.022\,712\,165$ s pc km^{-1} Myr^{-1}.

Our improved algorithm to determine the age (based on our previous work, Miret-Roig et al. 2018) provides a more rigorous kinematic sample selection and an improved orbital analysis. We showed the importance of using a robust estimate of the covariance matrix (instead of an empirical one) to minimise the impact of outliers (sources which deviate from the central locus of the association which are not necessarily contaminants). We explored different size estimators computed from the covariance matrix to determine the dynamical age (the standard deviation in different directions, the determinant, and the trace). All of them provide dynamical ages with differences of less than 1 Myr, meaning that they are compatible given the uncertainties when computed from the robust covariance matrix. Our thorough orbital analysis allowed us to propose the existence of a central core of 17 stars which appeared more concentrated at birth time.

In this study, we show that different potentials (i.e. axisymmetric and including the effect of spiral arms) lead to changes in the dynamical age that are within the current uncertainties. Nowadays, the major source of uncertainty in the dynamical, traceback age is the sample selection and the errors in the radial velocity estimates. For this reason, we stress the importance of choosing samples with accurate radial velocity data, with uncertainties comparable to the imminent early *Gaia* Data Release 3 (*Gaia* eDR3). This is crucial to reject kinematic contaminants and binaries and to ensure the success of a traceback analysis.

6 DEBRIS DISCS

6.1 CONTEXT

Debris discs are the result of collisions between planetesimals and their detection, therefore, implies that the planet formation process was successful in forming bodies of a few hundred or a few thousands of kilometres (see e.g. Hughes, Duchêne and Matthews 2018 for a recent review on debris discs). Stars hosting debris discs are excellent places where to image planets and discs simultaneously since debris discs are optically thin, see e.g. Fomalhaut (Kalas et al. 2008), β Pictoris (Lagrange et al. 2010), HR8799 (Marois et al. 2008), in opposition to protoplanetary discs which are optically thick. Besides, the study of debris discs can give us clues on the composition of exoplanets as well as their orbits and masses (e.g. Hughes, Duchêne and Matthews 2018).

The first debris disc was discovered around Vega using the IRAS by Aumann et al. (1984). After that, several studies have been devoted to searching for debris discs in the solar vicinity (e.g. Moór et al. 2006; Rhee et al. 2007; Zuckerman et al. 2011). One of the main questions addressed by these studies is the temporal evolution of debris discs, only possible if accurate age measurements are available which is in general not common for isolated stars. The easiest way to tackle this issue is to study debris discs hosted by stars members of a known association or open cluster where the age estimates are much more reliable. In the past decade, a number of studies reported the frequency of IR excesses in clusters of different ages (e.g. Gorlova et al. 2006, Gorlova et al. 2007, Siegler et al. 2007). These joint efforts complemented by others based on field stars suggested a debris disc fraction decay inversely proportional to the age (Rieke et al. 2005).

IC 4665 is among the sample of young open clusters examined in the literature to search for debris discs. This is a young open cluster with an estimated age of $27.7^{+4.2}_{-3.5}$ Myr (Manzi et al. 2008) and an average distance of 350 pc (Miret-Roig et al. 2019). Several works have studied the cluster population (Hogg and Kron 1955; Prosser and Giampapa 1994; de Wit et al. 2006; Jeffries et al. 2009; Lodieu et al. 2011). Recently, Miret-Roig et al. (2019) updated the cluster census using photometric and astrometric information, providing a list of more than 800 highly probable cluster members. Smith, Jeffries and Oliveira (2011) searched for debris discs in IC 4665 based on *Spitzer* observations. These latter authors

started from a sample of 75 members and obtained a disc fraction of 27^{+9}_{-7}%. The authors also reported a disc fraction for solar-type stars (F5–K5) of 42^{+18}_{-13}% which they claimed to be higher than what had been found in other clusters of similar ages, although compatible within the uncertainties (e.g. Gorlova et al. 2007 found an F0–F9 fraction of 33^{+13}_{-09}% for the 30 Myr NGC 2547 open cluster).

In this work, we take advantage of the census we did in Chapter 3 to revisit the study of debris discs in this cluster. This chapter is based on the work of Miret-Roig, Huélamo and Bouy (2020) and is structured as follows. In Section 6.2 we describe our sample and dataset which combines photometry from DANCe, WISE, and *Spitzer*. In Section 6.3 we present our empirical method to detect IR excesses with CMDs. In Section 6.4 we confirm our candidates by comparing their spectral energy distribution (SED) to models of photospheric emission. In Section 6.5 we discuss the candidates individually, and in Section 6.6 we compute the disc fraction and compare it to other studies. Finally, in Section 6.7 we present our conclusions.

6.2 DATA

We start from a list of 819 candidate members of IC 4665 (Miret-Roig et al. 2019) covering a magnitude range of 12.4 mag ($7 < J < 19.4$ mag). This sample has been selected combining photometry and astrometry from the *Gaia* DR2 and the DANCe catalogues in a Bayesian membership algorithm. The resulting sample is expected to be significantly more complete and reliable than the one previously used by Smith, Jeffries and Oliveira (2011) to study debris discs in this cluster. Their sample contained 40 spectroscopic low-mass members from Jeffries et al. (2009), 33 brighter stars selected with proper motions and B, V photometry from the Tycho-2 catalogue (Høg et al. 2000), and two additional members from Prosser and Giampapa (1994). The recent *Gaia* DR2 astrometry allows discarding as non-members at a high level of confidence 24 of their 75 targets (32%), hence motivating a re-analysis of the cluster disc frequency.

6.2.1 *Photometric database*

We used all the optical and IR photometry available in the DANCe catalogue[1], i.e. $G, G_{BP}, G_{RP}, g, r, i, z, y, J, H, Ks$. We also cross-matched (using a cross-match radius of $1''$ our sample with the AllWISE catalogue (Wright et al. 2010) and found 704 sources with a counterpart in the $W1$ (3.4 μm), $W2$ (4.6 μm), $W3$ (12.1 μm), and $W4$ (22.2 μm) bands.

1 http://vizier.u-strasbg.fr/viz-bin/VizieR?-source=J/A+A/631/A57

Table 6.1. *Spitzer* program IDs used in this study.

Instrument	Program ID
IRAC	13102, 40601, 80072
MIPS	3347, 40601

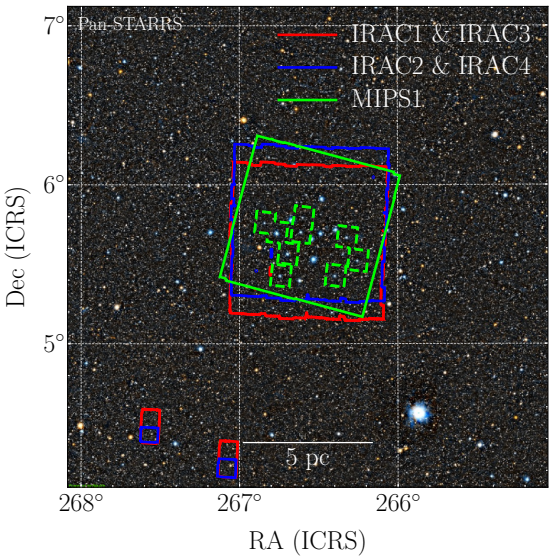

Figure 6.1. Footprint of the various bands of *Spitzer*. Two MIPS programs cover this cluster namely, program ID 40601 (solid green line) and program ID 3347 (dashed green line). Background image credit: Pan-STARRS.

We queried the *Spitzer* Heritage Archive for all the IRAC1 (4.6 μm), IRAC2 (4.5 μm), IRAC3 (5.8 μm), IRAC4 (8.0 μm), and MIPS1 (24 μm) data within a radius of 3° the estimated size of the cluster, around the centre. The program IDs of the observations in this area are given in Table 6.1 and the footprints of the various bands are displayed in Figure 6.1. The majority of the data come from program ID 40601 which has been analysed in Smith, Jeffries and Oliveira (2011), but a significant number of images were added from program ID 3347 over part of the area. Our reduction began from the S18.25.0 pipeline-processed artefact Corrected Basic Calibrated Data (CBCD) in the case of IRAC, and from the S18.12.0 pipeline-processed Basic Calibrated Data (BCD) in the case of MIPS. The self-calibration recommended in the *Spitzer* Data Analysis Cookbook was applied in the case of MIPS to remove artefacts as well as bright and dark latents present in the BCD images. We then combined these into deep mosaics using the recommended version 18 of MOPEX (MOsaicker and Point source

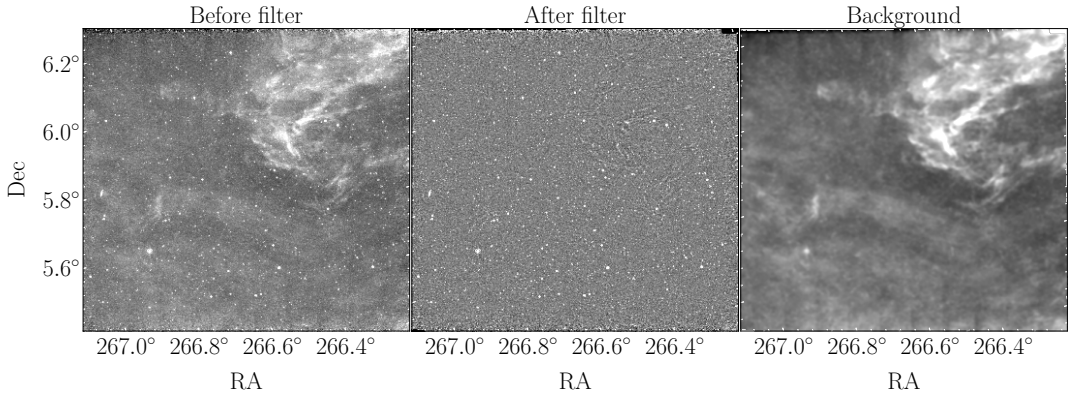

Figure 6.2. MIPS 24 μm image before (left) and after (center) the nebulosity filtering. The background computed by the nebulosity filter is shown on the right panel.

EXtractor) provided by the *Spitzer* Science Center using the standard parameters (see the MOPEX User's Guide for details on the data reduction).

In the case of IRAC, point sources were detected using SExtractor (Bertin and Arnouts 1996), and their PRF-fitting photometry was measured using APEX, the photometry package that is part of MOPEX. According to the manual, the colour corrections tabulated in the IRAC and MIPS handbooks are marginal for our sources ($T_{\rm eff} > 4\,000$ K) and we, therefore, neglected them.

In the case of MIPS, an extra step was performed before extracting the sources and measuring their photometry. The presence of a bright extended nebulosity (see Fig. 6.2) indeed compromises the detection and measurements as the background estimations implemented in SExtractor and APEX are not optimised to deal with such extended emission. We, therefore, applied the nebulosity filter described in Irwin (2010) to the pipeline produced mosaic. A spatially variable PSF was then computed using PSFEx (Bertin 2013) and the final PSF photometry was extracted using SExtractor again. We verified that the SExtractor PSF and APEX fluxes were in good agreement within the uncertainties, but kept SExtractor measurements as it detected and deblended more sources than APEX. To calibrate the fluxes of SExtractor we used the APEX photometry as a reference and computed a linear fit which resulted in a zero point of 140.89 ± 0.12 Jy. We applied this zero point to all the SExtractor fluxes, and its uncertainty was added quadratically to the flux error.

To convert fluxes into magnitudes we used the magnitude zero points provided in the instruments handbooks. For IRAC they are 280.9 Jy, 179.7 Jy, 115.0 Jy, and 64.9 Jy for bands 1, 2, 3, and 4, respectively and for MIPS1 it is 7.17 Jy. As explained in the instruments handbooks, the estimated level of accuracy of the photometric measurements is of 3% for IRAC and 4% for MIPS1.

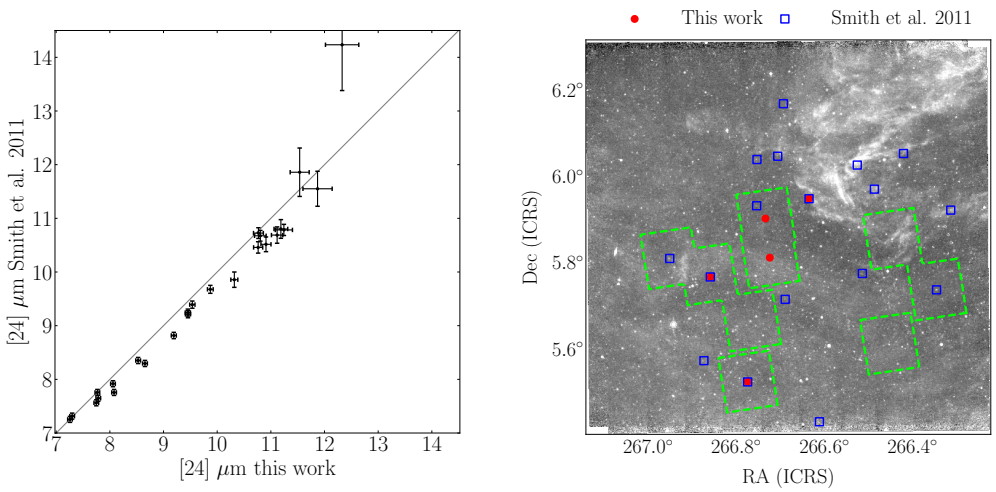

Figure 6.3. Left: Comparison between the MIPS1 photometry obtained in this work and that published on Smith, Jeffries and Oliveira (2011) for the common sources. Right: Spatial distribution of the sources with excess in this work (red dots) and in Smith, Jeffries and Oliveira (2011) (blue squares). The areas limited by green lines indicate the coverage of the *Spitzer* program ID 3347 which was not included in Smith, Jeffries and Oliveira (2011).

Therefore, we also added these uncertainties in quadrature to the statistical flux uncertainties. We estimated the global offset of our sources compared to *Gaia* DR2 and AllWISE to be $\lesssim 2''$ in all bands. The sources were then cross-identified with our input catalogue using a $2''$, radius as maximum separation. The number of matches in each case is reported in Table 6.2. In Table C.15 we provide the photometry used for the sources candidates of hosting a debris disc. An extended version of this table including all the photometric bands for all the members of IC 4665 is available at CDS.

We compared the photometry obtained with the one published in Smith, Jeffries and Oliveira (2011). The photometric measurements obtained in the four IRAC channels are consistent within the uncertainties except for a few objects close or above saturation. When we compared the MIPS1 photometry we found that for several sources their magnitudes are systematically brighter than our measurements (see Fig. 6.3, left). We checked that our SExtrator PSF fits are good, as demonstrated by the very low levels of residuals and good reduced χ^2. We find several reasons to explain these differences. First, we used a more recent version of the pipeline (both MOPEX and APEX). In particular, it includes a significant background improvement thanks to the self-calibration of the data mentioned above. Second, we used a superior background subtraction with the nebulosity filter compared to the standard pyramidal median filtering used in

Table 6.2. Number and percentage of members of IC 4665 detected for each photometric band before and after filtering the photometry. The total number of members is 819.

	Initial		After filtering	
Filter	Num.	Pct.	Num.	Pct.
G	727	89%	727	89%
G_{BP}	698	85%	698	85%
G_{RP}	699	85%	699	85%
g	566	69%	566	69%
r	695	85%	695	85%
i	766	94%	766	94%
z	755	92%	755	92%
y	789	96%	789	96%
J	815	100%	815	100%
H	781	95%	781	95%
Ks	778	95%	778	95%
W1	704	86%	577	70%
W2	704	86%	560	68%
W3	704	86%	148	18%
W4	704	86%	18	2%
IRAC1	218	27%	218	27%
IRAC2	219	27%	219	27%
IRAC3	204	25%	202	25%
IRAC4	200	24%	199	24%
MIPS1	45	5%	45	5%

SExtractor and MOPEX that produces local over-estimations that can severely affect the final photometry in regions of variable extended emission. Indeed, in Figure 6.3 (right) we see that several of Smith, Jeffries and Oliveira 2011 sources with 24 μm excess are in regions of nebulosity. We also note that other sources are in regions where our images are more sensitive since we combined the data of two programs (areas limited by green lines). Finally, we emphasise that we provide PSF photometry for all the objects while Smith, Jeffries and Oliveira (2011) measured aperture photometry when their PSF fit failed.

6.2.2 *Photometry filtering*

Photometric measurements can be affected by several problems (e.g. saturation, blending with a nearby source, cosmic rays, etc.) which can alter the true values and lead to unreliable measurements. Such contaminated photometric measurements can lead to a false IR excess detection or prevent the detection of a real excess. To minimise the impact of dubious photometric measurements, we applied filtering criteria specifically designed for each instrument.

The WISE photometry is well-known to be affected by a large number of artefacts which are identified and flagged in the AllWISE catalogue. Filtering these sources is essential to discard unreliable photometry. In this work we applied the following filtering:

- "cc_flags". We only keep sources with 0 flag, which means that they are unaffected by any of the known artefacts.
- "ext_flg". We only keep sources with 0 flag, which means that they are point-source objects, excluding extended objects.
- "ph_qual" is the photometric quality flag. We consider flags A (SNR $\geq$ 10) and B ($3 <$ SNR < 10) as good quality photometry, flags C ($2 <$ SNR < 3) as bad quality photometry, and flag U (SNR < 2) as an upper limit. The bad quality photometry and the upper limits are shown throughout our analysis but are not considered as reliable measurements.

For *Spitzer* observations, we discarded any detection with SNR < 3. Detections with $3 <$ SNR < 5 are considered to be marginal and they should be considered with caution.

In Table 6.2 we report the number of sources detected in each band before and after the filtering process. Despite their better sensitivity, the *Spitzer* images include less sources simply because they cover a smaller area ($1 \times 1^{\circ}$, see Fig. 6.1). Another important remark is that WISE detections are the most affected by our filtering criteria, especially at large wavelengths ($W3$ and $W4$) where many sources are only detected as upper limits. In Figure 6.4 we see the magnitude distribution of the members of IC 4665 in the mid-infrared photometric bands. There are 45 sources with MIPS1 photometry in the magnitude range 7.2 – 12.4 mag. The detection limit of the $W4$ channel at 22 μm is slightly shallower and there are 18 sources in the magnitude range between $7 - 8.6$ mag.

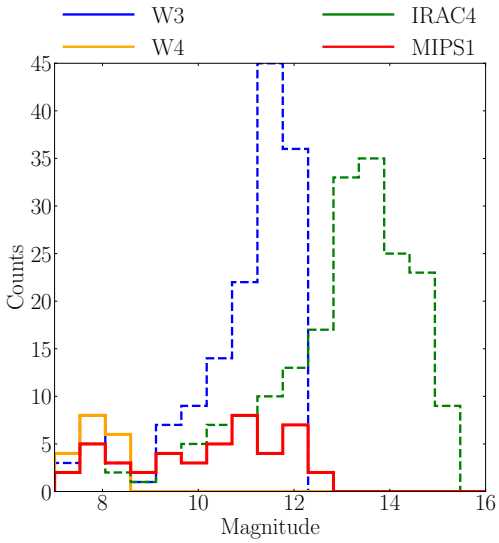

Figure 6.4. Magnitude distribution of the members of IC 4665 for the filters *W*3 (12 μm), *W*4 (22 μm), IRAC4 (8 μm), and MIPS1 (24 μm).

6.2.3 *Completeness*

One of the goals of this study is to measure the debris disc fraction of IC 4665. For that, defining a sample for which the photometric surveys are complete is crucial to interpret the results and compare with other studies. Establishing the completeness of photometric surveys can be a complex task, especially when variable extended emission is present (see Fig. 6.2).

In the following, we derive an estimate of the completeness limits of the photometric filters MIPS1 and *W*4. We take the maximum of the magnitude distribution of all the sources in the field of view (members and field stars) as the completeness limit. These distributions show a maximum of around 11.8 mag for MIPS1 and around 8.5 mag for *W*4. We find no significant variations in the areas affected by the extended emission and, as a first approximation, use these numbers for the entire survey. To convert the completeness in magnitude to a fundamental parameter such as the mass, we used the BT-Settl atmospheric models of Allard (2014). At the age and distance of IC 4665, we find that the magnitude limit of MIPS1 corresponds to a temperature of 4 000 K and a mass of 0.75 $M_\odot$. This corresponds to a spectral type of mid-K (Table A5 from Kenyon and Hartmann 1995). The BT-Settl models do not cover the hottest objects and can not be used to convert the *W*4 completeness limit in magnitude into a mass. Therefore, we followed a different approach and transformed the *W*4 magnitude to a $G - Ks$ colour using an empirical relation defined by the

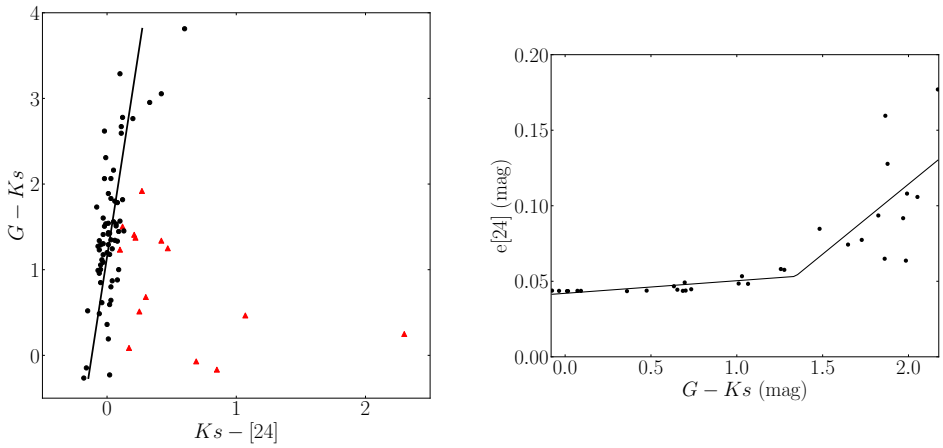

Figure 6.5. Left: $(G - Ks) - (Ks - [24])$ CMD of the Pleiades members with good 24 μm photometry from Table 2 of Gorlova et al. (2006). Only the sources classified as non-excess sources by the authors (black points) are used in the fit (Equation 6.1). Right: Photometric uncertainties at [24] μm as a function of the $G - Ks$ colour (Equation 6.2).

members of IC 4665. The limiting magnitude of $W4 = 8.5$ mag corresponds to an intrinsic $G - Ks \sim 0.2$ mag (assuming an extinction $A_V = 0.46$ mag). This colour corresponds to an effective temperature of 8 400 K and a mass of 1.75 $M_\odot$ according to the PARSEC-COLIBRI models (Marigo et al. 2017). This is equivalent to a spectral type of mid-A (Kenyon and Hartmann 1995).

6.3 INFRARED EXCESS DETECTION

To identify cluster members with debris discs, we used CMDs to detect IR excesses at different wavelengths, an entirely empirical method. We chose to analyse the WISE and *Spitzer* data independently because of their significantly different wavelength coverage, spatial resolution and sensitivities.

6.3.1 *MIPS 24 µm data*

The photometric colour $Ks - [24]$ has been commonly used in the literature to detect sources with 24 μm excess emission (e.g. Gorlova et al. 2006; Stauffer et al. 2010). We followed the methodology of these works and used CMDs to discern between the excess and non-excess population. The only difference is that we used the photometry of the recent *Gaia* DR2 G filter which is more precise, uniform, and extended than the Johnson V filter.

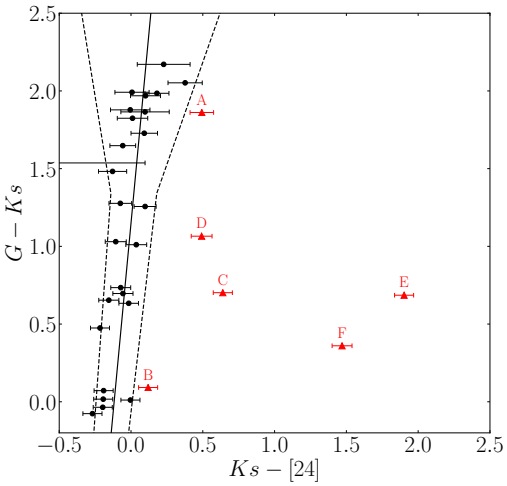

Figure 6.6. $(G - Ks) - (Ks - [24])$ CMD of the members of IC 4665 with 24 μm photometry. The locus of photospheric emission is indicated by the solid line and the 3σ uncertainties are represented by the dashed lines. The members with IR excess are indicated as red triangles.

To detect sources with IR excess, it is essential to first outline the location of the sources with photospheric colours (i.e. those which do not have an IR excess). We used the *Spitzer* observations in the Pleiades of Gorlova et al. (2006) to define the photospheric sequence in the $(G - Ks) - (Ks - [24])$ CMD. We note that this is the same approach that Gorlova et al. (2007) used for the $30 - 40$ Myr cluster NGC 2547. Indeed, several authors have found similar relations in young clusters (e.g. Stauffer et al. 2010 for the Hyades, and Plavchan et al. 2009 for nearby young stars). We used only the reliable 24 μm photometry for the Pleiades sources classified as not having excess by the authors (sources in their Table 2 with no asterisk). Equivalently to what they did, we fitted a linear polynomial relation (see Fig. 6.5 left) and obtained:

$$(Ks - [24]) = 0.102(\pm 0.013) \times (G - Ks) - 0.12(\pm 0.02) \tag{6.1}$$

We used this relation to define the photospheric emission locus in our data. To establish a confidence interval in which we believe that there is no emission excess, we fitted the uncertainties of the MIPS1 photometry with a segmented linear function with two slopes to account for the fact that at high S/N the measurements are dominated by photon noise and at low S/N by Poisson noise (see Fig. 6.5 right). The point of change in trend is a free parameter of the fitting process.

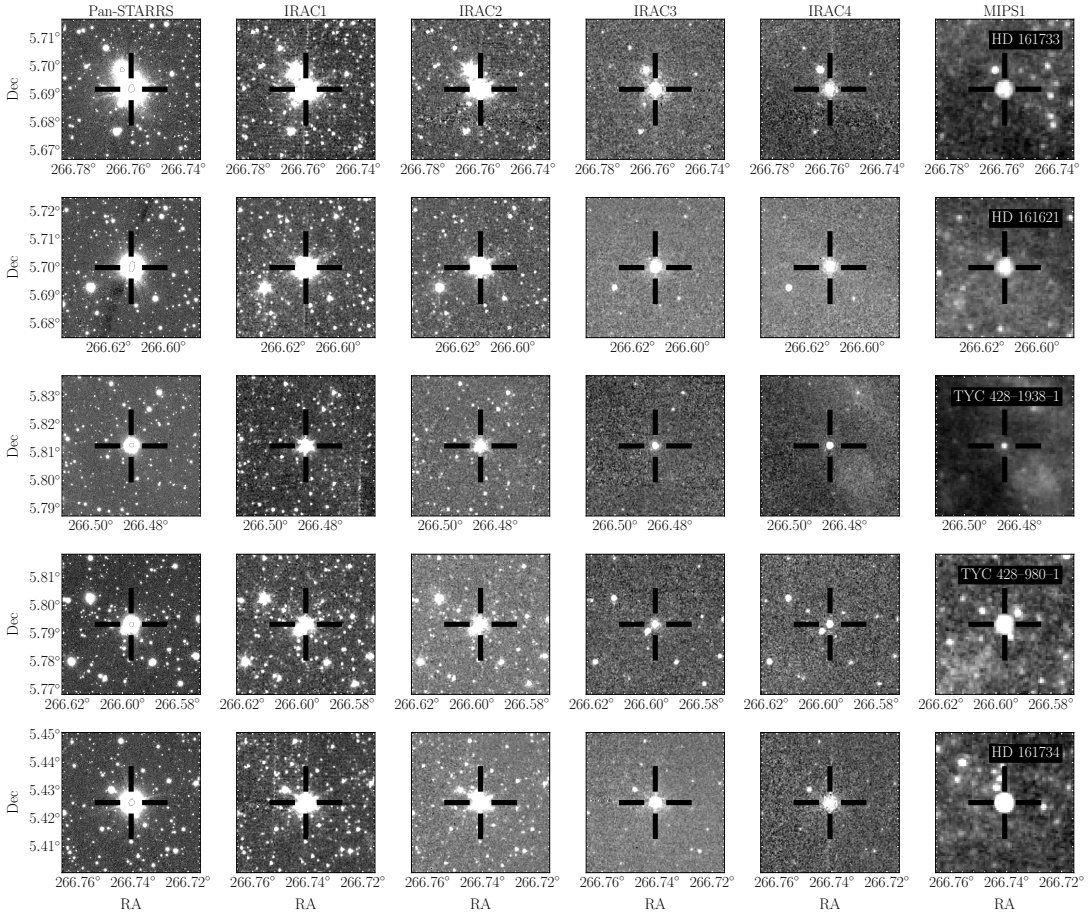

Figure 6.7. Multifilter *Spitzer* images of the sources with IR excess.

$$\mathrm{e}[24] = \begin{cases} c1 + k1 \times (G - Ks), & (G - Ks) < 1.34 \\ c2 + k2 \times (G - Ks), & (G - Ks) \geq 1.34. \end{cases} \tag{6.2}$$

The parameters of the fit are $c1 = 0.042(\pm 0.018)$ mag, $c2 = -0.07(\pm 0.05)$ mag, $k1 = 0.008(\pm 0.011)$, and $k2 = 0.09(\pm 0.03)$.

We used the fit of the photospheric sequence (Equation 6.1) and the fit of the MIPS1 uncertainties (Equation 6.2) to detect sources with infrared excess in the $(G - Ks) - (Ks - [24])$ CMD (see Figure 6.6). We considered that sources with a colour $Ks - [24]$ larger (within the uncertainties) than the photospheric emission locus plus the 3σ uncertainties of the 24 μm photometry have an excess in the 24 μm emission. According to this criterion, we found 4/45 candidates with excesses in the 24 μm emission. Half of these (HD 161733 and TYC 428-1938-1)

had already been reported by Smith, Jeffries and Oliveira (2011) and the other half (HD 161621 and TYC 428-980-1) are new candidates. In Figure 6.7 we see that all the candidates have a clear detection in all the *Spitzer* photometric bands.

In the case of Smith, Jeffries and Oliveira (2011), they detected 15 additional sources with 24 μm excesses not present in our analysis. Four of them are simply not classified as members by Miret-Roig et al. (2019) and thus were not considered in this study. We have checked that three out of these four do not show any excess at 24 μm according to our photometry. The fourth object (HD 161734) has WISE+*Spitzer* excesses in our photometry (see Figs. 6.6, 6.8, and 6.9) but it had a low membership probability ($p = 0.002\%$) with *Gaia* in Miret-Roig et al. (2019) and therefore was not initially considered in this work. We refer to Section 6.5 for a more detailed discussion of this object. For the remaining 11 sources the MIPS 24 μm photometry is significantly discrepant between the two studies (as shown in Fig. 6.3), which explains why they found an excess and we did not.

6.3.2 *IRAC* 3.6 − 8.0 *μm data*

Similarly to what we did in Section 6.3.1 with the MIPS photometry, now we use the four channels of IRAC to search for possible candidates with a near-infrared excess. In Figure 6.8 we represent the CMDs $Ks - [3.6], Ks - [4.5], Ks - [5.8], Ks - [8.0]$ against $G - Ks$. None of our members has an excess on any of the IRAC bands. There are a few points in each CMD which seem to be much redder than the mean photospheric locus but none of them shows an excess in two consecutive bands. These are spurious or blended detections in the images or have a high χ^2 of the PSF fit.

The source HD 161734 shows an increasing excess in the CMDs of the IRAC channels. This excess was also detected by Smith, Jeffries and Oliveira (2011) in the 5.8 and 8.0 μm channels.

6.3.3 *WISE* 3.4 − 22 *μm data*

Similarly to what we did in Section 6.3.1 for MIPS and in Section 6.3.2 for IRAC, here we present CMDs using the WISE photometry (see Fig. 6.9). The photometric measurements classified as "good" are represented by black dots, according to the criteria defined in Section 6.2.2. In these panels we have also represented data classified as "bad" (grey crosses) to illustrate the loss of sensitivity at longer wavelengths, resulting in the overlap of good and bad quality data in $W3$ (mainly for the coldest objects) and $W4$ (almost along the

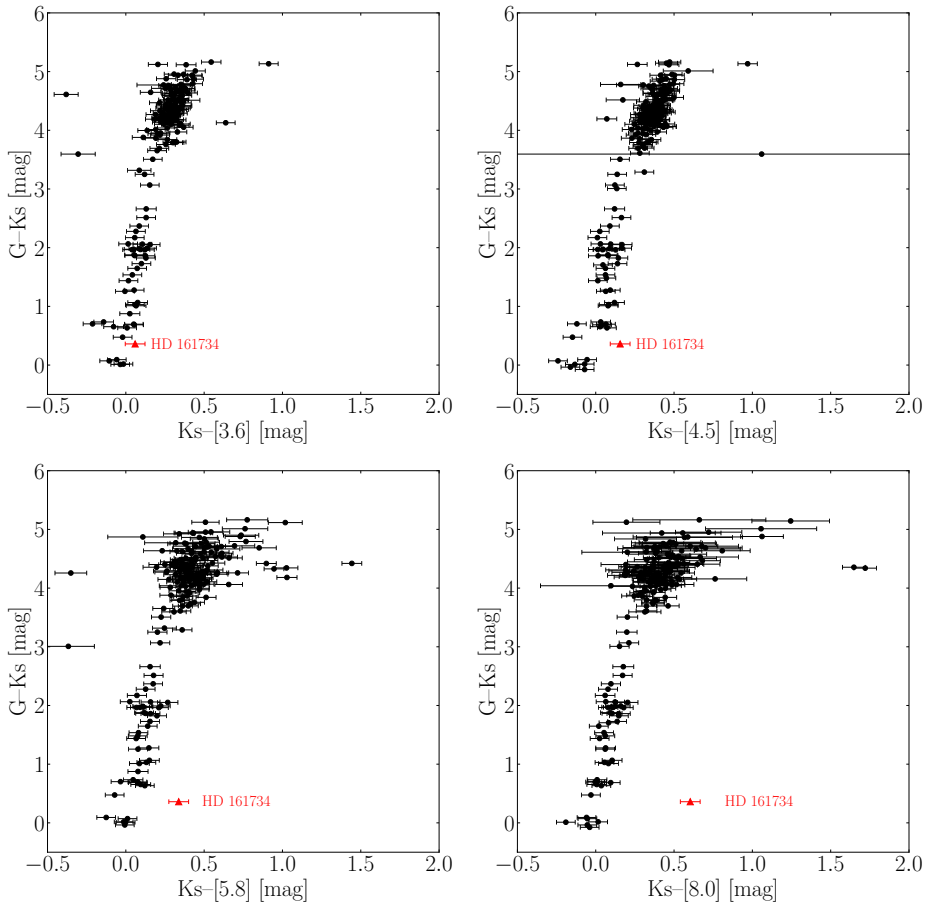

Figure 6.8. Colour-colour diagrams of the IRAC channels. Black dots indicate sources with high signal-to-noise ratio (SNR>5) and the red triangle indicates the source with IR excess.

whole cluster sequence). In the bands $W1$ (3.4 μm) and $W2$ (4.6 μm) we do not see any source with a significant excess, with the exceptions of TYC 428-980-1 which is flagged as an extended source by the WISE catalogue (probably due to the blending of nearby sources, see Fig. 6.10), and HD 161734 which shows an increasing excess in all the WISE bands.

In addition to HD 161734, in the $W3$ (12 μm) band, we see two objects redder than the photospheric sequence defined by the majority of sources. One is HD 161261, a good candidate to host a debris disc since it also displays an

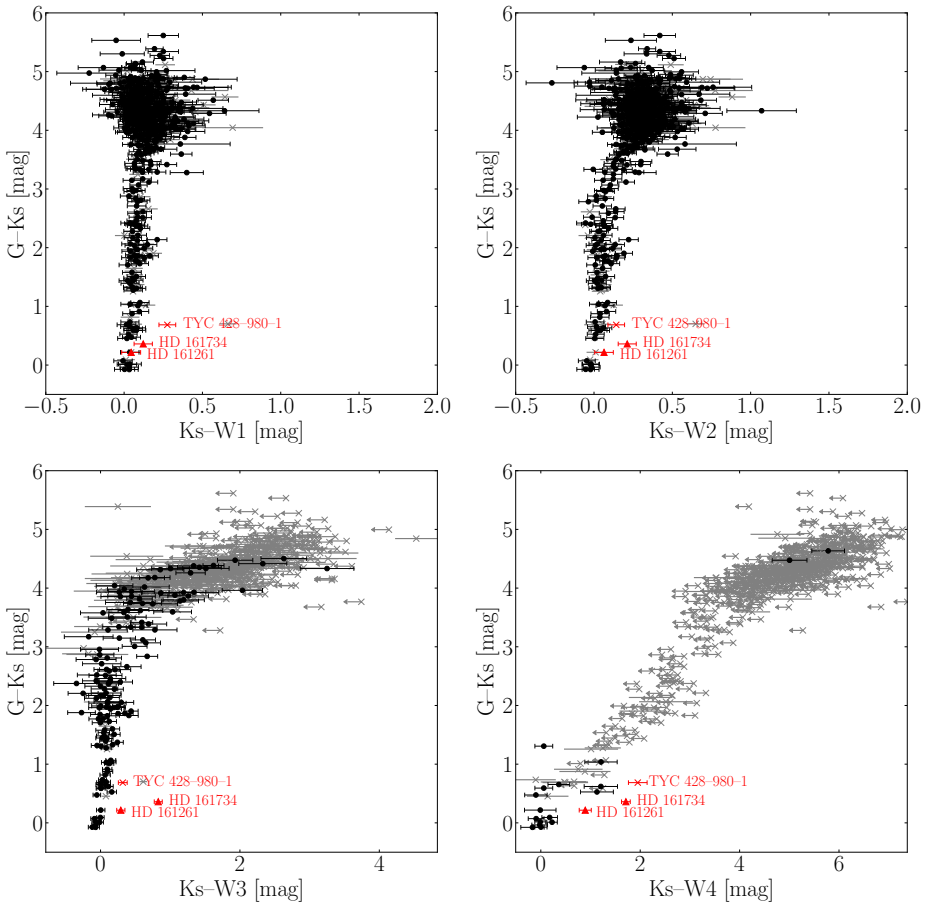

Figure 6.9. Colour-colour diagrams of the WISE photometric bands. Black dots indicate sources with good photometric quality, grey crosses indicate low-quality photometry or upper limits, and red triangles indicate an IR excess. The source TYC 428–980–1 (red cross) shows an IR excess but is flagged as an extended object (see text).

excess in $W4$ (22 μm). Moreover, the WISE images of this source look clean (see Fig. 6.10). The second source is TYC 428-980-1 which, as mentioned above, it was initially discarded for being flagged as an extended object by the WISE catalogue. However, if we look at the WISE images (Fig. 6.10), we see that the source appears blended in the $W1$ and $W2$ bands, but not in $W3$ and $W4$, where the object shows an increasing excess. In Section 6.5 we discuss this object more

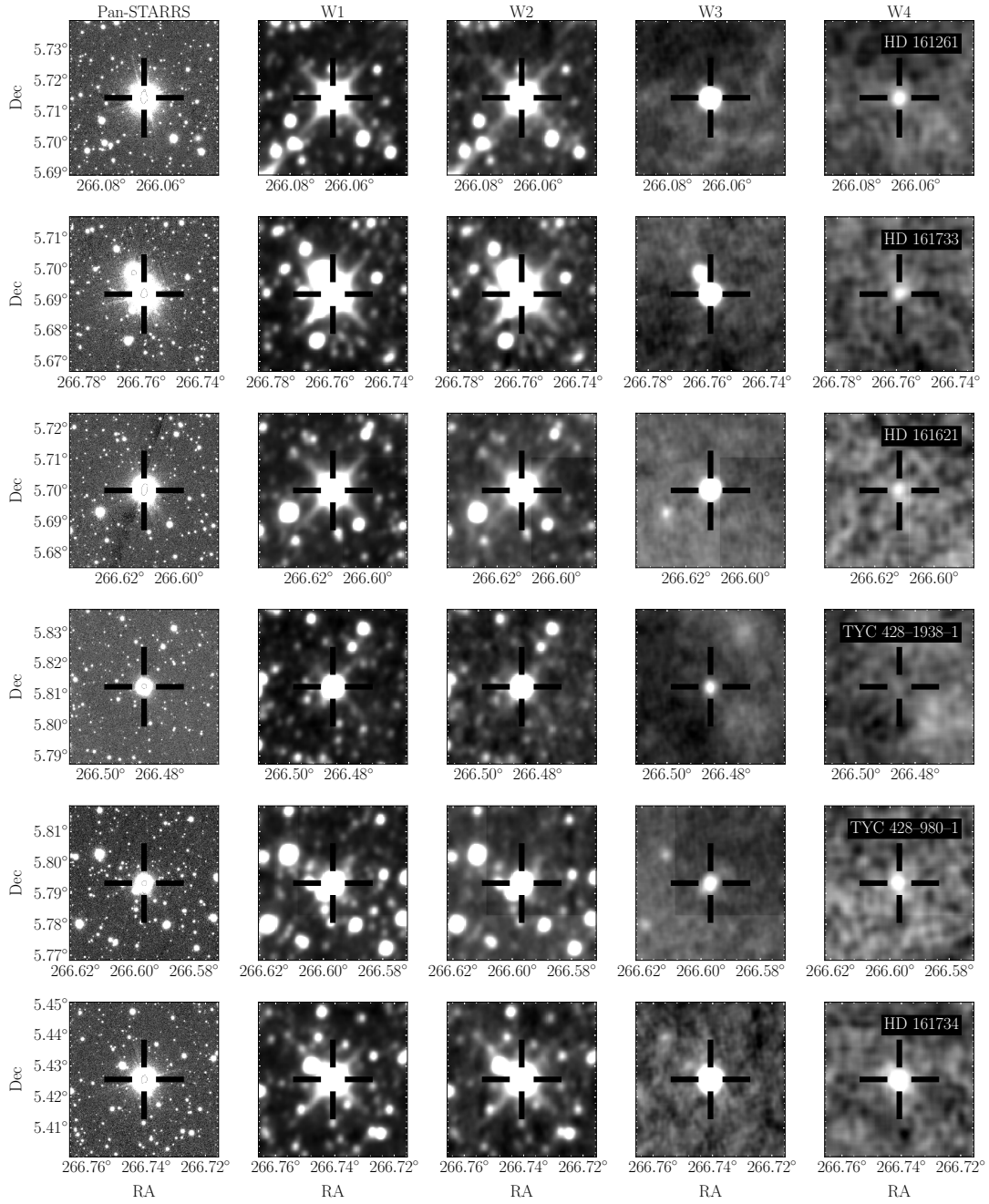

Figure 6.10. Multifilter WISE images of the IC 4665 sources with IR excesses.

in detail, and explain if the visual binary detected at shorter wavelengths might be unresolved in *W*3 and *W*4, with the subsequent contamination of the derived photometry.

As commented above, in bands $W3$ and $W4$ there is a significant increase in the amount of "bad" photometric measurements and upper limits. This is due to the limited sensitivity of WISE, and the increasing amount of diffuse emission present at those wavelengths.

There are a few sources at the limit of sensitivity which have not been flagged by WISE as "bad" and seem to have an excess. We have checked the images and discarded them because they do not show any detected source.

6.4 SPECTRAL ENERGY DISTRIBUTION

We used the Spanish Virtual Observatory (SVO) tool VOSA[2] (VO SED analyser, Bayo et al. 2008) to further investigate the sources that show significant excesses in the CMDs. We fitted their SEDs to (i) confirm if the mid-IR excesses are automatically detected by the tool, and (ii) characterise the central sources more in detail.

We used all the photometry described in Sect. 6.2 excluding the filtered photometry, upper limits, and saturated measurements. In addition, we used the VO SED analyser (VOSA) interface to search for all the ultraviolet (UV) photometry available. Since several targets are early-type stars, and the filters in the bluest part of the spectrum are important to complete the SED. We computed Bayesian distances inferred using *Kalkayotl* and the *Gaia* DR2 parallaxes. The resultant values are reported in Table 6.3. The extinction towards IC 4665 is not yet well constrained. The 3D dust map from Green et al. (2019) reports an extinction of $A_V = 0.46^{+0.12}_{-0.06}$ mag at the position and distance of the cluster. Recently, Miret-Roig et al. (2019) estimated a median extinction of $A_V = 0.72$ mag with the *Gaia* DR2 A_G and Anders et al. (2019) determined individual extinction values for our targets between 0.09 and 0.74 mag. As a consequence, we leave the extinction as a free parameter between 0 and 1 mag.

To find the model that best reproduces the observed SEDs, we used the option 'Chi-square Fit'. This option calculates the synthetic photometry from theoretical spectra for the filters with observed data, and applies a statistical test to find the model that best reproduces the data. The fitting algorithm is able to detect possible IR excesses and then these points are no longer considered in the final fit. We used the theoretical atmospheres models of Kurucz (ODFNEW/NOVER models, Castelli, Gratton and Kurucz 1997) with solar metallicity. We allow VOSA to find the best $\log g$ in the interval $4 - 5$, and the best temperature in the range $5\,000 < T_{\rm eff} < 20\,000$ K.

2 http://svo2.cab.inta-csic.es/theory/vosa/

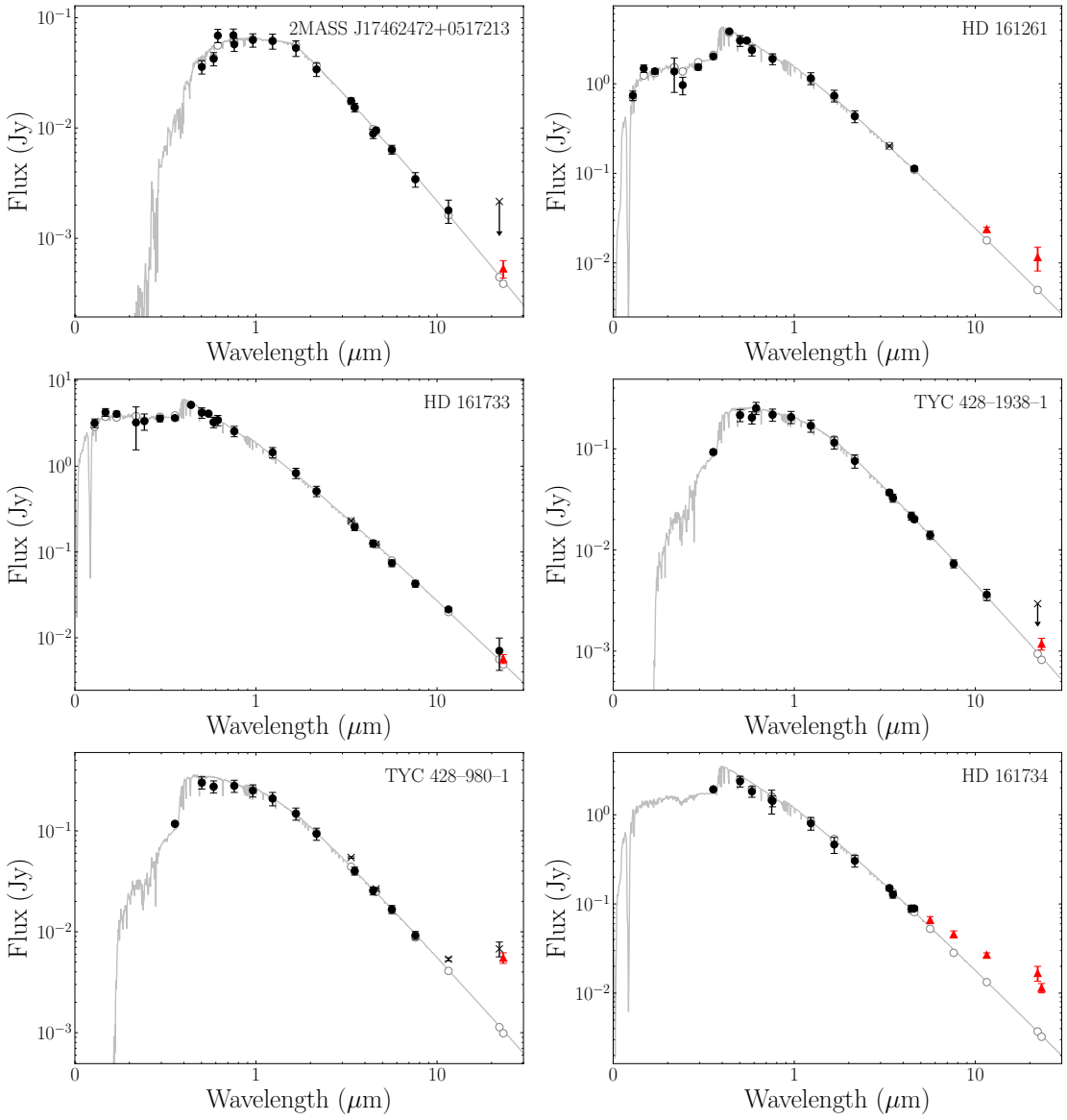

Figure 6.11. SEDs of the sources for which we have detected an IR excess. The black dots indicate the photometric measurements fitted, the grey crosses indicate the photometric measures not used in the fit, the red triangles indicate a photometric excess. We report the 3σ uncertainties, some of which are smaller than the markers. For the bands in DANCe, we have the imposed a minimum uncertainty of 0.05 while there are some WISE/Spitzer sources with an uncertainty smaller than this. The grey line represents the best fitted Kurucz model.

Table 6.3. List of candidates for which we have detected an IR excess. Columns indicate: (1) Object ID; (2) spectral type; (3) Bayesian distance; (4–5) *Gaia* DR2 *G*-band magnitude and extinction; (6–7) photometric effective temperature from *Gaia* DR2 and Smith, Jeffries and Oliveira (2011); (8–12) extinction, effective temperature and the 96% confidence level, $\log g$, and reduced χ^2 parameter of the best fit SED; (13–14) significance of the *W*4 and 24 μm excess defined as $\left(\frac{F_{obs}-F_{phot}}{\sigma_{obs}}\right)^2$; (15) binary flag (from literature); (16) new candidate to host a debris disc. *We note that eventually we reject the source HD 161621 as a candidate (see text).

Object	SpT (Ref.)	d (pc)	G (mag)	A_G (mag)	$T_{\rm eff,\,GDR2}$ (K)	$T_{\rm eff,\,S11}$ (K)	$A_{V,\rm SED}$ (mag)	$T_{\rm eff,SED}$ (K)	$T_{\rm eff,SED}$ 96% CL (K)	$\log g$	χ^2	S_{W4}	S_{24}	Bin	New
HD 161261	B9 (1)	356 ± 17	8.26	0.62	9 132	8 842	0.6	12 000	11 250 – 13 000	4.5	10.0	32.8		?	Y
HD 161733	B7 (2)–B8 (1)	322 ± 13	7.96	0.43	9 124	8 740	0.65	15 000	14 000 – 16 914	5.0	5.2	2.3	12.6	?	N
HD 161621	A0 (1)	314 ± 11	9.45	0.61	7 886		0.4	8 250	7 250 – 11 000	4.0	9.0			Y	Y*
TYC 428-1938-1	A (3)	338 ± 15	11.01	0.77	6 197	7 840	0.7	7 500	6 031 – 8 463	4.5	0.9		47.4	N	N
TYC 428-980-1	A2 (3)	340 ± 11	10.36		7 310		0.35	7 750	6 750 – 10 250	4.0	0.6	25.0	417.1	N	Y
2MASS J17462472+0517213	G2–G3 (4)	336 ± 10	12.67	0.78	5 155	5 459	0.65	5 750	5 000 – 6 500	5.0	3.8		20.8	N	N
HD 161734	B8 (5)–A0 (1)	447 ± 20	8.82	0.75	8 478	8 420	0.9	13 000	10 705 – 14 000	4.5	5.9	150.0	320.3	?	N

References. (1) Cannon and Pickering (1993); (2) Kraicheva et al. (1980); (3) Giampapa, Prosser and Fleming (1998); (4) Allain et al. (1996); (5) Gray and Corbally (2002)

In Figure 6.11, we present the observed SEDs together with the best-fit models, and in Table 6.3 we summarise some of their parameters. We see that VOSA independently finds an IR excess for six of the seven candidates for which an excess was detected in colour–colour diagrams (Sect. 6.3). The excess of HD 161733 is at the limit of the VOSA detection ($\gtrsim 3\sigma$, see Sect. 6.5). In Table 6.3 we report the effective temperature measured with different techniques. The effective temperatures from *Gaia* DR2 ($T_{\mathrm{eff,\,GDR2}}$) are computed from the three photometric bands of *Gaia*, and two colours which can be strongly correlated. In addition, these temperatures were obtained with a machine-learning algorithm only trained on the range $3\,000 - 10\,000$ K. Stars outside this range (which is the case for several of our candidates) can be systematically under- or over-estimated (Andrae et al. 2018; Gaia Collaboration et al. 2018c). The effective temperatures from Smith, Jeffries and Oliveira (2011) ($T_{\mathrm{eff,\,S11}}$) are obtained from the $B - V$ intrinsic colours through a relation provided by the authors. The differences between these two temperatures are of a few hundred Kelvin, similar to what Andrae et al. (2018) found in the validation of the *Gaia* DR2 effective temperatures. Additionally, we provide the effective temperatures of the theoretical atmospheric model which best fits the observed SED ($T_{\mathrm{eff,\,SED}}$). In all cases, the temperatures from the SED fitting have higher values with respect to the two photometric temperatures, particularly for the two hottest objects which have differences of thousands of Kelvins. In these cases, we have more confidence in the effective temperatures from our SED fitting because they rely on a larger amount of photometric measurements from different instruments (i.e. not correlated), covering a large fraction of the spectra (UV-IR), and are derived using the individual parallaxes for each object. Additionally, our effective temperatures better match the spectral types determined in the literature (see second column of Table 6.3).

6.5 CANDIDATES OF HOSTING A DEBRIS DISC

We detected six stars with mid-IR excesses in one or several of the *Spitzer* and WISE bands. In this section, we discuss them one by one.

HD 161261

HD 161261 displays excesses in *W*3 and *W*4 and the images show a clear detection in both cases. This source is not in the $1 \times 1^{\circ}$ central region of the cluster and thus is not covered by *Spitzer*. It is a new debris disc candidate. The effective temperature of the best theoretical atmospheric model is 12 000 K, significantly higher than the values obtained by *Gaia* DR2 and Smith, Jeffries

and Oliveira (2011). However, it matches well with the spectral class B9 from Cannon and Pickering (1993).

Interestingly, this source is classified as a rotating ellipsoidal variable by the General Catalogue of Variable Stars (Samus' et al. 2017), which implies that it could be a close binary system. However, we find neither any confirmation of the existence of this binary system nor any hint on the properties of the possible companion.

HD 161733

HD 161733 shows a small excess in MIPS 24 μm data (see Fig. 6.6). It is also detected in *W*4, but the uncertainties of the photometry are large, hindering a confirmation of this excess with WISE. The best fit SED corresponds to a model of $T_{eff} = 15\,000$ K, significantly hotter than the photometric temperatures of *Gaia* DR2 and Smith, Jeffries and Oliveira (2011) but consistent with the strong helium lines present in its spectrum (e.g. Levato and Malaroda 1977; Hubrig and Mathys 1996), and the spectral classification found in the literature (e.g. Kraicheva et al. 1980; Cannon and Pickering 1993). The algorithm of VOSA did not detect an IR excess for this source when both *W*4 and MIPS1 are considered. We find that the MIPS 24 μm observation shows a significance excess of 3.5σ, at the limit of the algorithm detection. Indeed, if we neglect the *W*3 and *W*4 photometry (*W*1 and *W*2 are filtered in Sect. 6.2.2), VOSA automatically detects an excess with MIPS. Smith, Jeffries and Oliveira (2011) also detected a 24 μm excess for this source.

The multiplicity of this source has been discussed in different works and the results are not conclusive. It was included in the catalogue of spectroscopic binaries of Kraicheva et al. (1980) based on radial-velocity studies (Abt, Bolton and Levy 1972; Pédoussaut and Carquillat 1973). However, the works of Crampton et al. (1976) and Morrell and Abt (1991) did not report any RV variability after the analysis of several spectra. According to the work of Kraicheva et al. (1980), the masses of the primary and the secondary are 4.3 $M_\odot$ and 0.8 $M_\odot$, respectively. This mass ratio cannot explain the excess we observe since the contribution of a 0.8 $M_\odot$ star to the SED of a 4.3 $M_\odot$ star is negligible. These authors also determined an orbital period of the system of 7.3 ± 0.8 days and a separation of ~ 1.4 AU. However, the nature of the spectroscopic binary is not confirmed and more observations are needed to characterise this source.

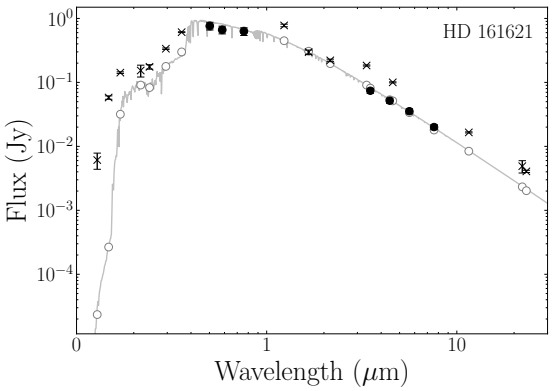

Figure 6.12. Same as Figure 6.11 for the source HD 161261 which does not present an IR excess. The filled black circles represent the photometric points of the primary, since in these observations the binary system is resolved.

HD 161621

HD 161621 is a visual binary star with a separation of 3.2″(Mason et al. 2001). The companion is the source TYC 428-1977-1. The two companions have very similar magnitudes ($G = 9.45$ mag; $G = 9.59$ mag), effective temperatures (7 886 K; 7 811 K), and parallaxes ($\varpi = 3.17 \pm 0.05$ mas; $\varpi = 3.29 \pm 0.04$ mas) indicating it is an equal mass binary.

This system has a WISE counterpart at a separation of 1.6″ from the primary source. This is slightly larger than our initial search and so we added the WISE photometry manually. This source is flagged as an extended object by WISE and we verified that it is not resolved by this instrument. Moreover, this system is resolved by *Gaia* and IRAC, but is unresolved by the International Ultraviolet Explorer (IUE), WISE, and MIPS; 2MASS detects the two components but the photometry is flagged as contaminated.

We only used the photometry which resolved the system (*Gaia* and IRAC) to fit a SED (see Fig. 6.12). We can see that all the unresolved channels (crosses) provided a photometric measurement systematically brighter than that predicted by the model. Our SED fit shows that the excess we detected with MIPS is due to the companion, because the excess is of 0.75 mag, exactly what we expect for an equal-mass binary. For this reason, we no longer consider this source as a candidate to host a debris disc.

TYC 428-1938-1

TYC 428-1938-1 displays an excess in 24 μm data which was already reported by Smith, Jeffries and Oliveira (2011). This source has WISE photometry but the sensitivity of $W4$ is too low to be detected in that channel (see Fig. 6.10) so we can not use WISE to confirm this excess. The SED shows a 24 μm excess compared to the photospheric emission.

TYC 428-980-1

TYC 428-980-1 displays excesses in $W3$, $W4$, and MIPS 24 μm. While the MIPS1 PSF fit shows a χ^2 of 1.3, the source is flagged as an extended object in the WISE catalogue. Figures 6.7 and 6.10 show a close source at a separation of around 12″ but $\sim$ 100 pc closer according to the *Gaia* DR2 parallaxes. Such a separation could be spatially resolved in the WISE $W1 - W3$ bands (not in $W4$), and in MIPS 24 μm. The fact that this close source is detected neither in the $W3$ band nor in the MIPS1 image implies that the detected emission is associated with the central star. The SED of this object (see Fig. 6.11) shows that the $W4$ (22 μm) and MIPS1 (24 μm) excesses are compatible, making an extremely interesting new candidate.

HD 161734

HD 161734 was not initially included in our sample because it has a low membership probability in Miret-Roig et al. (2019). However, Smith, Jeffries and Oliveira (2011) and Meng et al. (2017) detected an excess emission from the near- to mid-infrared which motivated us to study the object further. With our new IRAC and MIPS photometric reduction, we also detect an excess. Additionally, we searched the WISE photometry finding an excess consistent with what is seen with *Spitzer* (see Fig. 6.11). Smith, Jeffries and Oliveira (2011) mention in their conclusions that this source may be a binary. However, they did not mention on what they based their hypothesis and we ourselves do not find any evidence of a binary nature. Based on its near-IR excess, these latter authors also proposed that this source could have a remnant primordial disc. They were able to fit the excess with a 500 K blackbody, suggesting a dusty disc with a radius of 1.7 AU. Considering the members obtained with *Gaia* in Miret-Roig et al. (2019), the cluster has a median and standard deviation parallax of 2.84 mas and 0.36 mas, respectively. For the proper motions, the median and standard deviation are -0.91 mas yr^{-1} and 0.64 yr^{-1} in right ascension and -8.49 mas yr^{-1} and 0.68 yr^{-1} in declination. The *Gaia* DR2 astrometry

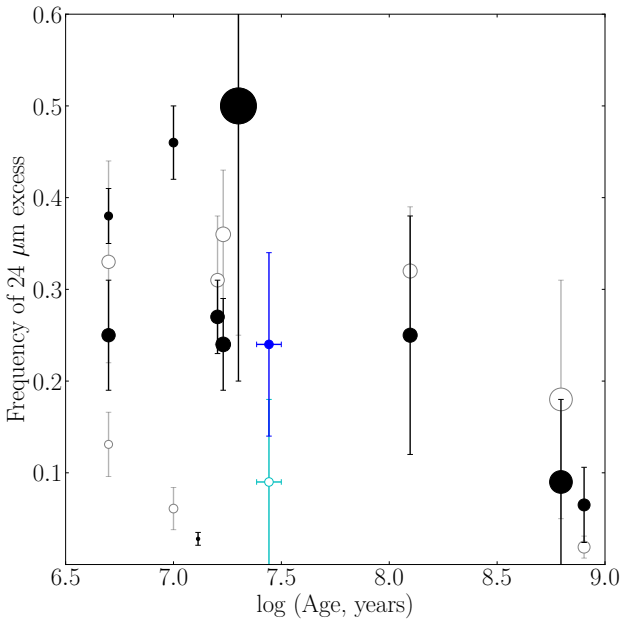

Figure 6.13. Frequency of 24 μm excess in the sample listed in Table 1 of Chen, Su and Xu (2020) for early-type stars ($2-2.5$ M$_\odot$, black filled dots) and for solar-type stars ($1-1.5$ M$_\odot$, grey empty dots). The frequencies measured in this work are marked with a blue filled dot for B–A stars and with a cyan empty dot for solar-type stars. All the markers have sizes inversely proportional to the distance of the cluster.

of HD 161734 is $\varpi = 2.1716 \pm 0.0407$ mas, $\mu_\alpha^* = -1.623 \pm 0.063$ mas yr^{-1}, and $\mu_\delta = -9.432 \pm 0.062$ mas yr^{-1}. Therefore, we see that this source has a very precise *Gaia* DR2 astrometry which is beyond the 1σ distribution of the cluster in all the spaces, especially in parallax which is a decisive variable for the membership analysis. However, we find that this source has a photometry that agrees well with the main sequence of the cluster, and the fact that it shows a clear IR excess makes it a good debris-disc candidate member. Future *Gaia* releases with improved astrometry might rise the membership probability of this source. In any case, the membership of Miret-Roig et al. (2019) has a true positive rate of $\sim 90\%$, and this source is an example of the objects that could be missing in that list of members.

6.6 DISCUSSION

We have estimated that our MIPS photometry is complete down to $[24] \lesssim 11.8$ (late-B to mid-K, see Sect. 6.2.3) in our sample. In this spectral range and the

central $1^\circ \times 1^\circ$ area covered by MIPS (37 pc^2), the disc fraction of IC 4665 is 5/32 or $16 \pm 7\%$. This fraction is smaller than the $27^{+9}_{-7}\%$ rate reported in a previous study of this cluster, covering the same field of view and magnitude range (Smith, Jeffries and Oliveira 2011). The main reasons for this difference are our improved image-processing techniques (see Sect. 6.2), the fact that we only provide PSF photometry and they mixed PSF and aperture photometry, and the different lists of members. We discarded most of their candidates because their MIPS1 photometry was systematically brighter than ours (10 sources were rejected for this reason; see Sect. 6.2), and/or they are no longer classified as members after the analysis of the *Gaia* DR2 astrometry (three sources were rejected for this reason).

Many studies in the literature provide the disc fraction for B–A stars and solar-type stars, separately, in different clusters and star-forming regions. To compare our study with these results, we have estimated these fractions in our sample. The B–A stars in IC 4665 have an intrinsic colour $G - Ks \lesssim 0.75$ mag and, in this range, the disc fraction becomes 4/17 or $24 \pm 10\%$. If we apply the same selection to the sample of Smith, Jeffries and Oliveira (2011) we obtain a disc fraction of 5/14 or $36 \pm 12\%$ for B–A stars. Therefore, in this spectral range we also obtain a smaller disc fraction, although both are consistent within the uncertainties. We only detect one candidate in the spectral range F5–K5 (solar type stars) which results in a disc fraction of 1/11 or $9 \pm 9\%$. Smith, Jeffries and Oliveira (2011) report a disc fraction of 10/24 or $42^{+18}_{-13}\%$ in the same spectral range which is discrepant with our results. Finally, we note that the disc fractions derived by us for early- and solar-type stars are compatible within the relatively large uncertainties.

In the following, we compare the disc fractions obtained in this study with other young clusters and associations. This comparison should be regarded as tentative and taken with caution given that the various studies quoted below have very different levels of sensitivity and/or completeness (see **Wyatt+2008**; Hughes, Duchêne and Matthews 2018, and references therein for a detailed discussion on the difficulties related to such comparisons). Additionally, the level of completeness and contamination in the list of members differs from one study to another and most of them are based on pre-*Gaia* members lists.

Gorlova et al. (2007) did a study analogous to the one presented here for the NGC 2547 open cluster. This is a very similar cluster in terms of age (30 Myr, Jeffries et al. 2006) and distance (400 pc). They imaged the inner $1^\circ \times 1^\circ$ regions which at the distance of the cluster corresponds to ~ 50 pc^2, and were complete down to a spectral type of late-F in MIPS1. They found a B8–A9 excess fraction of $\sim 44\%$ and an F0–F9 excess fraction of $\sim 33\%$. These values are significantly larger than what we find in IC 4665. We believe that the

same reasons we discussed to explain the differences with the study of Smith, Jeffries and Oliveira (2011) could apply to this discussion. Indeed, we checked that around 40% of their MIPS sample could be contaminants according to the *Gaia* DR2 astrometry.

Gorlova et al. (2006) studied the disc population of the intermediate age Pleiades cluster (120 Myr). They analysed *Spitzer* MIPS1 data of an area covering the central $2^\circ \times 1^\circ$ area of the cluster which at the distance of the Pleiades corresponds to an area of 14 pc^2. They were complete down to a spectral type of K3, or even M2 in the regions with less nebulosity. They estimated the debris disc fraction of B–A members to be $\sim 25\%$. The value is very similar to the one found in IC 4665 and is consistent with a slow evolution of the 24 μm excess in debris discs, with a characteristic timescale of 150 Myr (e.g. Siegler et al. 2007; Gorlova et al. 2006). However, the proximity of the Pleiades compared to IC 4665 leads to a significantly smaller spatial coverage of this cluster, hindering a proper comparison of the disc fractions.

In Figure 6.13 we compare the disc fractions obtained in this study with several nearby clusters and associations reported in a recent work by Chen, Su and Xu (2020) for early- and solar-type stars. We see that our disc fraction for B–A stars is compatible with the disc evolution trend defined by the other clusters. The disc fraction we measure at 30 Myr is compatible within the uncertainties with clusters of $15 - 20$ Myr (Upper Centaurus Lupus, Lower Centaurus Crux, and the β Pictoris moving group) and with the Pleiades at 125 Myr. In the case of solar-type stars, our disc fraction is smaller than that from clusters of ~ 20 Myr that are closer than 150 pc. Interestingly, our disc fraction is similar to the one reported in younger clusters ($5 - 10$ Myr) at similar distances (Orion OB1a and Orion OB1b).

Our *Spitzer* photometry of IC 4665 only covers the central $1^\circ \times 1^\circ$ of the cluster (see Fig. 6.1). However, according to the most complete membership analysis to date (Miret-Roig et al. 2019), the cluster has a size of at least 3° radius. We estimated that MIPS1 observations only cover 55% of the B–A stars of the cluster by comparing the spatial distribution of all the B–A members in a circle of 3° radius (whole cluster area) with the same population in the area covered by MIPS data ($1^\circ \times 1^\circ$). Therefore, the disc fractions we obtain with MIPS1 are in principle only valid for the central part of the cluster. Since we also have WISE photometry, which covers all the area occupied by the cluster (a circle of 3° radius in this case) we used it to estimate the disc fraction. We obtain a fraction of 3/14 or $29 \pm 12\%$ at 22 μm ($W4$) in the spectral range late–B to mid–A (see Sect. 6.2.3). This value is very similar to what we obtain with MIPS at the central region in the same spectral range 2/8 or $25 \pm 15\%$.

6.7 CONCLUSIONS

Here, we present a study of the debris disc population of the 30 Myr open cluster IC 4665. We identified six candidates with IR excess, two of which are new. All of them have excesses at $22 - 24$ μm but not in the NIR (except for HD 161734), which indicates the presence of dusty debris discs. Using MIPS data in the central part of the cluster, we compute a disc fraction of $24 \pm 10\%$ B–A stars. We only detect one solar-type star resulting in a fraction of $9 \pm 9\%$ in the F5–K5 spectral type range. Using WISE, we extended the search to the outskirts of the cluster, finding a similar result in the B–A range. We believe that the main differences between our results and the ones obtained in a similar study of this cluster (Smith, Jeffries and Oliveira 2011) are mainly due to (i) the fact that we used improved image-processing techniques, (ii) we only measured PSF photometry and these latter authors combined PSF and aperture photometry, and (iii) we worked with different member lists.

Comparing our disc fraction with other nearby clusters and associations we find that for early-type stars our results are compatible with regions of $15 - 20$ Myr (Upper Centaurus Lupus, Lower Centaurus Crux the β Pictoris moving group), and 125 Myr (the Pleiades). For solar-type stars, we find a disc fraction lower than generally observed at $15 - 20$ Myr. We would like to emphasise that all the studies with which we compare our results here are pre-*Gaia*, meaning that the derived memberships (and therefore disc fractions) should be revised with the new astrometry. Additionally, we emphasise the importance of image processing, especially at 24 μm where the images are strongly affected by nebulosities.

All our candidates were first detected in colour–colour diagrams and using an empirical photospheric sequence to define the non-excess locus. We also used the Kurucz atmospheric models to fit a SED and independently detect IR excess. As an extra product of this procedure, we obtained effective temperatures which are more accurate than the photometric ones available in the literature. Our candidates are good targets to be followed up with the Atacama Large Millimeter/submillimeter Array (ALMA) and with the future mission James Webb Space Telescope (JWST).

Part IV

CONCLUSIONS AND PERSPECTIVES

7

SUMMARY, CONCLUSIONS, AND PERSPECTIVES

7.1 SUMMARY AND CONCLUSIONS

This thesis contributes to the understanding of the star formation process in the solar neighbourhood. In particular, it provides a continuous mass function from substellar objects to stars for open clusters and associations of two different ages. Additionally, it contains a strategy to determine the dynamical traceback age of young local associations using an orbital traceback analysis. Finally, it includes a method to identify discs to the members of young regions using the WISE and *Spitzer* photometry.

Results on the initial mass function

The formation of stellar and substellar objects is a complex process with many physical processes involved. In the last decades, theories have made major advances but more observations are still needed to constrain the models. A fundamental parameter of models is the IMF. It has been measured in several clusters and star-forming regions but usually, it hardly reaches the substellar regime and the uncertainties are estimated in a simple way, probably underestimating the impact of contamination or incompleteness. In this thesis, we conducted a large effort to overcome these limitations and provide a continuous mass function with realistic uncertainties derived from the observations.

1. We compiled a vast database of deep, wide-field, multi-filter images encompassing a broad time scale. This has been possible thanks to a combination of a long term plan ($\sim$ 10 yr) of observations from our team, some of which have been obtained as part of this thesis, and a selection of images available in public archives. The union of all these observations is key to reach the faintest objects in the regions under study.

2. The Bayesian statistical tools developed by our team are key to identify the few cluster members (hundreds or thousands) among a vast amount of field stars (millions of Galactic and extragalactic sources). This algorithm takes into account all the information available: astrometry, photometry, and the corresponding uncertainties. Additionally, it can classify sources with missing information.

3. We computed the magnitude, luminosity and mass distributions with the members selected by the membership algorithm. Our statistical treatment allowed us to propagate the observational uncertainties consistently to the individual luminosities and masses and to account for the effect of completeness and contamination of our sample. Accounting for the uncertainties is key to obtain a realistic distribution which can be compared to models and the observational distributions in other regions.

Here, we list the main results regarding the mass functions of IC 4665 (30 Myr) and USC and ρ Oph ($1 - 10$ Myr).

- The two mass functions estimated in this thesis have a characteristic mass around $0.3 - 0.5$ $M_\odot$. This is similar to the characteristic mass of theoretical models (Chabrier 2005).
- In the high mass regime (> 1 $M_\odot$), the two mass functions are compatible with a power-law with a Salpeter slope. For the mass function of USC and ρ Oph, we fitted a power-law function with a slope of $\Gamma = 1.388 \pm 0.006$. In the case of IC 4665, we observed a feature around 3 $M_\odot$ which is likely to be caused by the low number of sources in this mass range (noisy small number statistics).
- In the mass range between $0.08 - 0.3$ $M_\odot$, the mass function of USC and ρ Oph has a statistically significant lower fraction of objects than the theoretical mass functions of Chabrier (2005), Thies and Kroupa (2007) and Thies et al. (2015). In the same mass range, the mass function of IC 4665 is compatible with the theoretical model of Chabrier (2005) but still has a deficit compared to Thies and Kroupa (2007) and Thies et al. (2015).
- In the substellar regime (< 0.075 $M_\odot$), the mass function of USC and ρ Oph revealed a large population of substellar objects, which exceeds the number expected to have formed from gravitational collapse. In this same mass regime, the census of IC 4665 is incomplete, and thus, the comparison with theoretical predictions is inconclusive.

We investigated the possible origin of the rich free-floating population we found in the region of USC and ρ Oph which greatly exceeds the number of objects expected from core-collapse theories. We found hints that between a quarter and a third of free-floating planetary-mass objects might have formed in planetary systems and later were ejected due to dynamical interactions. However, these estimates are based on simple assumptions given the current knowledge of exoplanet properties. Therefore, our results can only be tentative given the large uncertainties regarding exoplanet statistics at young ages.

Despite all the caveats aforementioned, it is clear that ejection from planetary systems is an important mechanism to form free-floating planets with a contribution possibly of the same order as that of core-collapse.

The main caveats and limitations of the mass functions we estimated are listed below.

- To convert magnitudes/luminosities to masses, we need the theoretical evolutionary models which are strongly age-dependent and uncertain at very young ages. This necessarily introduces uncertainties in our final luminosity/mass functions which are difficult to estimate. For this reason, we also provide the magnitude distributions which are independent of models and can be re-converted to luminosity/mass functions when improved evolutionary models are available.
- The region of USC and ρ Oph has a complex formation history with an age spread of several million years, leading to larger uncertainties and errors in the conversion from magnitudes to masses. For this reason, it is important to revisit the age of this region and ideally, to measure individual ages for the various subgroups to use the appropriate isochrone and re-estimate the mass of each object.
- The membership algorithm we used in this thesis is not capable of identifying deeply embedded members of the association. As a consequence, the number of objects identified in ρ Oph is a lower limit of the overall population. We expect that our census is more complete in the region of USC where the extinction is moderately low.

Results on the dynamical age

The stellar ages are a fundamental parameter to study the star formation and evolution since they place in the right timescale parameters such as the mass function, the disc evolution, and the spatial distribution which are time-dependent. Additionally, they are essential to convert luminosities to masses. For this reason, we devoted one chapter of this thesis to the study of dynamical ages. They have the great advantage of being independent of evolutionary models and are especially suited for young systems which are the targets of our studies. In this thesis, we improved a method we designed during my Master's degree to determine the dynamical age of young local associations using an orbital traceback analysis. This technique requires excellent precision in the present 3D positions and velocities. In this thesis, we used the orbital analysis to determine the dynamical traceback age of the β Pictoris moving group. The main results of this study are:

- We measured a dynamical traceback age of $18.5^{+2.0}_{-2.4}$ Myr for β Pic, which is in good agreement with ages based on evolutionary models. This value is older than previous traceback ages and we believe it is due to the large observational errors in the past.
- We measured the radial velocity of 81 candidate members of β Pic in a uniform manner. We performed and analysed our own observational spectroscopic observations plus all the spectra found in various public archives homogeneously. With this procedure, we obtained significantly better uncertainties than those provided in the literature, with an obvious direct positive impact on the traceback analysis. Our radial velocity measurements combined with the astrometry of *Gaia* DR2 result in uncertainties of $0.1 - 0.2$ km s^{-1} in the 3D Cartesian velocities.
- We studied the impact of observational uncertainties, membership, and the Galactic potential in the dynamical traceback age and concluded that the contamination in the membership is the dominant error with uncertainties of about 2 Myr. We estimated that different Galactic potentials (axisymmetric and with spiral arms) result in differences of less than 1 Myr in the age.
- We showed that the orbital traceback analysis is not only useful to estimate the age of a young association but also to study its spatial and kinematic distribution in the past and the relation between different associations.

Results on the identification of discs

One of the suggested mechanisms to explain the formation of substellar objects is that they form in circumstellar discs and are afterwards ejected. To provide observational constraints to this theory, it is important to detect and study the presence of discs in young stars. We took advantage of the first region studied in this thesis, the open cluster IC 4665, to search for discs. At 30 Myr, we expect to find debris discs which are formed by the collision of planetesimals, meaning that large bodies formed surrounding the star. However, this method is equally valid for applying to younger regions where stars are expected to be surrounded by protoplanetary discs which are the nursery of the planets. The main results regarding the detection of debris discs in IC 4665 are:

- We identified six candidates with IR excess, two of which are new. All the candidates have excesses at $22 - 24$ μm but not in the near-IR (except for HD 161734), which indicates the presence of dusty debris discs. We

detected all the candidates in CMDs, and then, we used the Kurucz atmospheric models to fit a SED and independently detect IR excess.

- We computed a disc fraction of $24 \pm 10\%$ for B–A stars, which is compatible with regions of $15 - 20$ Myr (Upper Centaurus Lupus, Lower Centaurus Crux the β Pictoris moving group), and 125 Myr (the Pleiades). We only detected one solar-type star with IR excess resulting in a fraction of $9 \pm 9\%$ in the F5–K5 spectral type range. This fraction is lower than generally observed at $15 - 20$ Myr.
- The majority of studies of the disc fraction are based in pre-*Gaia* membership selections and therefore should be revised with the new astrometry.
- We found that it is important the image processing, especially at 24 μm where the images are strongly affected by nebulosities.

7.2 FUTURE PERSPECTIVES

The results of this thesis show the potential of determining comprehensive censuses of young clusters and star-forming regions. Such censuses are the starting point of all follow-up studies, including studies of the mass function, but also of discs, exoplanets, dynamics, binaries, and many more. They also provide complete and clean target lists for the coming spectroscopic surveys, for example using WHT Enhanced Area Velocity Explorer (WEAVE) at the 4.2 m William Herschel Telescope (WHT), 4-metre Multi-Object Spectroscopic Telescope (4MOST) at Visible and Infrared Survey Telescope for Astronomy (VISTA), and Multi Object Optical and Near-infrared Spectrograph (MOONS) at the Very Large Telescope (VLT). This new generation of spectrographs will provide very precise and uniform spectra for large samples, reaching several magnitudes deeper than it was possible up to now for thousands of sources. In this thesis, we took care to set a framework of methods and tools to efficiently conduct several follow-up studies. In the following paragraphs, we describe some examples of future lines of research, some of which have already been started during this thesis.

Unravelling the star formation history of USC and ρ Oph

In Chapter 4, we showed an example of the difficulties of measuring isochronal ages of very young associations. A more reliable alternative is to measure the age based on the kinematics using an orbital traceback analysis (similar to the one we presented in Chapter 5). For that, we need precise 6D positions in the

space phase. The imminent *Gaia* eDR3 will provide a very precise astrometric solution for a large number of source. To complement this data, we have started to apply for spectroscopic observational time which we will combine with the APOGEE radial velocities, available for about 20% of the stars. So far, we obtained spectra from the SES mounted on the STELLA 1.2 m telescope in Tenerife, the NRES mounted on a 1 m telescope at LCO, and the CHIRON spectrograph mounted on a 1.5 m telescope in CTIO. As in the case of β Pic, we will also mine the public archives to gather as many high-quality spectra as possible.

The study of the 6D space phase distributions in the present is essential to identify and characterise the presence of substructures which can be related to different populations. To this end, it is important to do a multidimensional analysis, including all the information available, in a robust statistical framework. The identification of substructures in the present is an indispensable study that will complement the orbital traceback analysis.

Eventually, with the identification and age tagging of the different structures, we will be able to study the formation history of this complex and see where did the star formation begin, how it propagated and the relationship (feedback) between the various groups. Additionally, once we have individual stellar ages we can re-compute a more accurate and precise mass function from the magnitude distribution. This will give us stronger constraints on the mechanisms that formed the substellar population.

Spectroscopic characterisation of brown dwarfs and free-floating planets

Brown dwarfs and free-floating planets are impossible to identify when the age and distance are unknown because the mass-luminosity relationship is highly degenerate for ultracool objects. In this thesis, we identified a large population of substellar objects because they are part of associations and have a well-defined age and distance. However, spectra are essential to confirm their nature and youth through the accurate measurement of effective temperatures, gravities, and extinctions. Additionally, the spectra of the free-floating planets in our sample will serve to study the atmospheres of these objects with unprecedented sensitivity and details thanks to the absence of a blinding host star. These objects will become benchmark references in the study of free-floating planets and exoplanets formation, evolution and atmosphere models and therefore, privileged targets for present and future observatories such as ALMA, the JWST, the Giant Magellan Telescope (GMT), the Thirty Meter Telescope (TMT), and the European Extremely Large Telescope (E-ELT).

During this thesis, I led a successful spectroscopic proposal at the 10 m telescope Gran Telescopio Canarias (GTC) to observe substellar members of IC 4665. I participated in the observations on the nights of the 19–22 June 2019 during which we observed nine targets with the OSIRIS optical spectrograph and ten targets with the EMIR infrared spectrograph. These spectra are currently under analysis. Additionally, we submitted a similar proposal to the GTC and Subaru telescopes to study the free-floating planet candidates of USC and ρ Oph. Since this region is much closer, we can detect even cooler objects and produce a reference sample at an younger age and lower masses.

Search for exoplanets

Most of the detected planets so far have been found around isolated main-sequence stars with estimated ages around several Gyr, albeit with very large uncertainties. Only a few have been detected around young stars with well-determined ages and extensive studies are still rare. Detecting planets with well-defined ages is important to follow the system evolution. Tracing the planet properties and planet occurrence during the first stages of the life of the planet (< 1 Gyr) is crucial to disentangle the different formation and early evolution theories. While most theories indicate that giant planets can only be formed in distant orbits (> 10 au), observations have found giant planets located in very close-in orbits (< 0.5 au). Currently, planet migration is the most likely explanation to reconcile theory and observations, however, we still do not know when this migration begins, which mechanisms drive it and what are the implications in the system architecture. Migration processes are expected to take place during the first hundreds of Myr after the formation of the planetary system and thus, it is crucial to detect planets of these ages.

Taking advantage of the new census in the young open cluster IC 4665 (presented in Chapter 3), we started a program to search for planets. I led successful proposals for the CAFE spectrograph at Calar Alto, Fibre-fed Echelle Spectrograph (FIES) at Nordic Optical Telescope (NOT), and SOPHIE at OHP. At the time of writing this thesis, we obtained radial velocity measurements at 9 to 12 epochs for five stars in IC 4665. According to our preliminary results, we detected one spectroscopic binary which shows radial velocity variations of the order of tens of km s^{-1}. Additionally, we have a few candidates of hosting exoplanets which display periodic radial velocity variations of the order of tens of m s^{-1}. We are still completing the analysis of these spectra, including light curves to take variability into account and applying for more observational time to confirm the presence of a planet and better constrain the orbital parameters. With this sample, we will be able to estimate the occurrence rate of planets in

this cluster since our initial target list comes from an unbiased membership analysis. This is key to determine the planetary formation mechanisms and early evolution and will constitute an anchor for models since the age of the hosting star is well determined.

Search for protoplanetary discs in USC and ρ Oph

Stars form surrounded by discs which are planet nurseries. Thus, detecting discs hosted by stars with well-known ages is crucial to study the disc evolution and constrain the mechanisms of planetary formation. In this thesis, we presented a search for debris discs in the members we found in IC 4665 (Chapter 6), which at 30 Myr were all debris discs. In the future, we plan to apply the same techniques to the members we found in USC and ρ Oph. Since this region is much younger ($1 - 10$ Myr) we expect to detect a larger population of stars hosting protoplanetary discs, where planets are being formed in the present. Additionally, since this region comprises a large age span we will detect discs at different evolutionary stages which is crucial to study the evolution with time. The discs we detect, are excellent candidates for a follow-up with ALMA or the JWST.

Re-analysis in highly extincted regions

Our group is currently developing a novel and more complex software based on Bayesian hierarchical models that properly takes into account the extinction in the membership selection. This will represent a major advance in the censuses of very young star-forming regions which are embedded in the parent molecular cloud. In particular, in the case of ρ Oph we expect to identify many more members which currently escape from our detection, leading to an improved luminosity and mass function.

Complete censuses of very deep and wide-field areas

The Large Synoptic Survey Telescope (LSST), recently renamed as the Vera C. Rubin Observatory[1], is a 8.4 m telescope currently under construction. This telescope will image the entire southern hemisphere, providing deep and homogeneous data for a vast number of stars. This survey will be an excellent input for the kind of membership analysis we have presented in this thesis, solving the limitations in the spatial coverage and completeness we have with

1 https://www.vro.org/

the DANCe survey. Our membership algorithm combined with this survey will provide complete censuses of free-floating planets, crucial to constrain their formation mechanisms. The Euclid mission will also survey a significant fraction of the sky up to very faint magnitudes in the optical and near-infrared. In the longer term, the Nancy Grace Roman Space Telescope will survey the whole sky in the infrared up to extremely faint magnitudes as well.

All these surveys will produce extraordinary data of unprecedented quality. Although their main motivations are focusing mostly on cosmology, the tools and methodologies developed and used during my thesis will certainly be very useful to analyse them for the study of star formation.

Part V

APPENDIX

A

DYNAMICAL AGE OF β PIC

In this appendix we include additional information on the analysis of the dynamical traceback age of β Pic presented in Chapter 5.

A.1 CROSS-MATCH WITH GAIA DR2

In Section 5.2, we cross-matched our sample of candidate members of β Pic with the *Gaia* DR2 catalogue to obtain the proper motions and parallaxes. There are six sources which are not in the *Gaia* DR2 catalogue and eight which only have the two-parameter solution in *Gaia*. In this Appendix, we discuss the reasons for which these sources were not in the DR2 catalogue and the perspectives for *Gaia* eDR3, expected for the end of 2020.

There are two sources, 2MASS J05120636 − 2949540 and 2MASS J04210718 − 6306022, with magnitudes $G > 21$ mag which fail the first condition to have a five-parameter solution in *Gaia*. The other six have an `astrometric_sigma5d_max` too large and fail the third condition (equation 11 from Lindegren et al. 2018b). The `astrometric_sigma5d_max` is a parameter used to detect cases where one or several parameters from the five-parameter solution are poorly determined. These stars are very nearby and have high proper motions which could hinder the proper cross-match of the observed transits. Besides, at least two are spectroscopic binaries (2MASS J20100002 − 2801410 and 2MASS J21374019 + 0137137), a fact that could difficult the derivation of a proper AGIS solution.

There are three sources, 2MASS J00160844 − 0043021, 2MASS J03582255 − 4116060, and 2MASS J23433470 − 3646021 with a magnitude $J \gtrsim 15.8$ mag, which are fainter than the *Gaia* detection limit. It is expected that they will not appear in any of the future *Gaia* releases. We checked[1] that the other three sources, 2MASS J01112542 + 1526214, 2MASS J03323578 + 2843554, and 2MASS J05241914 − 1601153, have a `visibility_period_used` < 6 and for that reason were rejected from the five-parameter solution. In addition, they are known to be close spectroscopic binaries with separations of $0.2 - 0.6''$which can induce to an erroneous solution and are not included in *Gaia* DR2 (Lindegren et al. 2018b).

1 https://gaia.esac.esa.int/gost/

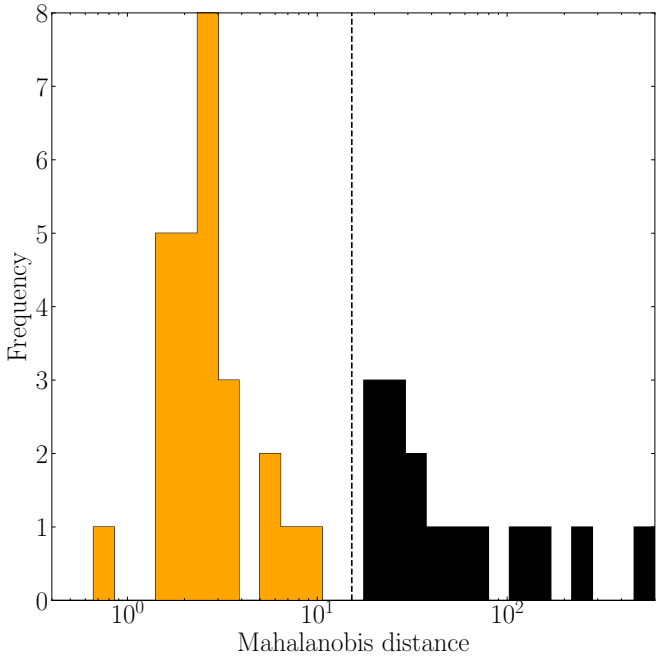

Figure A.1. Histogram of the Mahalanobis distance to the centre of the velocity distribution ($\dot{\xi}'$, $\dot{\eta}'$, $\dot{\zeta}'$) of the 42 single sources of our sample. The vertical dashed line indicates the percentile p_{65} used to select the kinematic members (see Sect. 5.2.3).

A.2 KINEMATICALLY DISCARDED SOURCES

Here, we discuss possible reasons for which the 3D velocity of the 15 kinematic outliers reported in Sect 5.2.3 was found inconsistent with the rest of members of β Pic. We also review the two suspected spectroscopic binaries found in this work and the outlier in 3D positions (which was rejected because of the different orbital motion compared to the β Pic members, see Sect. 5.2.3).

2MASS J01365516 − 0647379

This source was first classified as a candidate member of β Pic by Malo et al. (2013) with a low membership probability of 27.4%, taking into account the position, proper motion, magnitude, and colour. Later, Malo et al. (2014a) revised the membership of this source and found a probability of 99.9% includ-

ing the radial velocity of Shkolnik et al. (2012). Our radial velocity estimate (13.02 ± 0.18 km s^{-1}) is consistent with the value of Shkolnik et al. (2012) (12.2 ± 0.4 km s^{-1}). Recently, Crundall et al. (2019) also classified this source as a field contaminant based on *Gaia* DR2 astrometry and the radial velocity of Shkolnik et al. (2012).

2*MASS J*01373545 − 0645375

This source was proposed as a candidate of β Pic by Gagné et al. (2018). However, it had been previously classified as a member of the Hercules Lyra association by López-Santiago et al. (2006) and Gagné et al. (2018) could not confirm its membership because they did not consider the Hercules Lyra association in their analysis. Our radial velocity estimate (12.01 ± 0.12 km s^{-1}) is similar to a recent value from the literature (11.658 ± 0.006 km s^{-1}, Soubiran et al. 2018).

2*MASS J*02232663 + 2244069

Our radial velocity measurement (12.60 ± 0.15 km s^{-1}) is consistent with the one from the *Gaia* DR2 catalogue (12.1 ± 0.6 km s^{-1}). This source was listed as a high probability (99%) member of β Pic by Malo et al. (2013) based on a radial velocity and a proper motion which differ by 2 km s^{-1} and 6 mas yr^{-1}, respectively, from *Gaia* DR2. The different data could explain why this source was discarded by our kinematic selection and the membership of this source has been revised with our data.

2*MASS J*03573393 + 2445106

We have three spectra for this source with radial velocity measures of 13.46 ± 0.18 km s^{-1} (2018-08-12), 13.44 ± 0.18 km s^{-1} (2018-08-14), and 15.30 ± 0.14 km s^{-1} (2019-11-30). This source is rotationally variable (0.86 days, Hartman et al. 2011) which could explain the variations in the radial velocity that we measure. This source is a candidate of spectroscopic binary which requires more follow-up observations to confirm it. We also note that Crundall et al. (2019) classified it as a field contaminant.

2*MASS J*05004928 + 1527006

This source was classified as a member by Schlieder, Lépine and Simon (2012) based on a predicted radial velocity of 13.70 ± 2.03 km s^{-1}. We measure a radial velocity of 18.4 ± 0.3 km s^{-1}, similar to what has been reported in the literature (White, Gabor and Hillenbrand 2007), and significantly different to the predicted value used in the previous membership analysis. Additionally, this source has been classified as a member of the Taurus-Auriga complex (Kraus et al. 2017), and therefore is a likely contaminant in β Pic.

2*MASS J*08475676 − 7854532

This source was classified as a candidate of β Pic based on a predicted radial velocity of 13.4 ± 1.5 km s^{-1} (Malo et al. 2013). This value is significantly different from our measurement of 23.1 ± 0.3 km s^{-1} and with the literature (23.4 ± 0.3 km s^{-1} from Malo et al. 2014a). Using *Gaia*, it has been proposed as a member of η Chamaeleontis (Cantat-Gaudin et al. 2018).

2*MASS J*11493184 − 7851011

This source was classified as a β Pic candidate based on a predicted radial velocity of 10.8 ± 1.6 km s^{-1} and a predicted distance of 68 pc ($\varpi = 14.7$ mas) by Malo et al. (2014a). Our two radial velocity measurements differ by about 1.3 km s^{-1} between them but have a mean value of 14.5 ± 0.8 km s^{-1}, which is not compatible with the predicted radial velocity in that study. The *Gaia* DR2 parallax of this source is 9.92 ± 0.03 mas, indicating this source is probably a contaminant. A recent study classified this source as a ϵ Chamaeleontis (Schneider et al. 2019).

2*MASS J*13545390 − 7121476

This source was classified as a candidate member of β Pic by Malo et al. (2014a) based on proper motions values which differ of about 20 mas yr^{-1} from the values of *Gaia* DR2. This source is probably a contaminant.

2*MASS J*19312434 − 2134226

Our radial velocity measurement (-36.6 ± 1.8 km s^{-1}) is not consistent with the literature (e.g. Shkolnik et al. 2012 measured a radial velocity of $-26.0 \pm$

1.8 km s^{-1} and Malo et al. 2014a -25.6 ± 1.5 km s^{-1}) with a difference of about 10 km s^{-1}. We checked the CCF and there are hints it might be a spectroscopic binary. Besides, a recent study classified this as a member of the Argus association (Janson et al. 2017).

2*MASS J*21212873 − 6655063

This source was classified by Malo et al. (2014a) as a high probability (99.9%) member of β Pic. However, their analysis was based on pre-*Gaia* astrometry and the proper motions they used differ about 20 mas yr^{-1} from the one of *Gaia* DR2, indicating the membership should be revised.

2*MASS J*23314492 − 0244395

This source was classified as a β Pic candidate member by Malo et al. (2013). However, their analysis was based on pre-*Gaia* astrometry and the proper motions they used differ about 10 mas yr^{-1} to the ones of *Gaia* DR2.

2*MASS J*23512227 + 2344207

Our radial velocity measurement (-1.0 ± 0.3 km s^{-1}) differs by about 1 km s^{-1} from the measurement of Shkolnik et al. (2012) (-2.1 ± 0.5 km s^{-1}). Binks and Jeffries (2016) provided another measurement of the radial velocity for this source (38.6 ± 1.6 km s^{-1}), with a discrepancy of several tens of km s^{-1}. Based on their measurement, they rejected this source as a β Pic member and also suggested the possibility of a binary system to explain the differences observed. Messina et al. (2016) classified this source as a single star based on a study of photometric variability. Further work is required to confirm the binarity of this source. Additionally, other authors have classified this source as a member of other moving groups (e.g. Shkolnik et al. 2012, Klutsch et al. 2014).

2*MASS J*21183375 + 3014346

This source was classified as a candidate member of β Pic by Schlieder, Lépine and Simon (2012) with a predicted radial velocity of -15.1 ± 0.9 km s^{-1}. This value is significantly different from our radial velocity measurement (-22.0 ± 0.3 km s^{-1}). Additionally, Shkolnik et al. (2017) recently measured a radial velocity similar to ours (-22.5 ± 0.8 km s^{-1}) and rejected the β Pic membership of this source.

2*MASS J*22571130 + 3639451

This source was classified as a candidate member of β Pic by Schlieder, Lépine and Simon (2012) with a predicted radial velocity of -10.0 ± 0.9 km s^{-1} although their measured radial velocity was -20 ± 1.2 km s^{-1}. We have analysed eight spectra of this source and obtained a variable radial velocity between -10 km s^{-1} and -20 km s^{-1}, indicating this is probably an unresolved spectroscopic binary.

2*MASS J*16120516 − 4556242, 2*MASS J*17092947 − 5235197, 2*MASS J*18430597 − 4058047, *and* 2*MASS J*20105054 − 3844326

These sources were classified as new members of the β Pic moving group by Gagné and Faherty (2018) with no radial velocity measurements. The first estimation of their radial velocity provided for the first time in the present work shows that their velocity is not compatible with the velocity distribution of β Pic, suggesting they might be contaminants.

B QUERIES

In this appendix we provide the queries used to download the data analysed in Chapters 3 and 4.

B.1 IC 4665

Gaia DR2

```
SELECT
 "I/345/gaia2".ra\_epoch2000,
 "I/345/gaia2".dec_epoch2000,
 "I/345/gaia2".ra_epoch2000\_error,
 "I/345/gaia2".dec\_epoch2000_error,
 "I/345/gaia2".parallax,
 "I/345/gaia2".parallax_error,
 "I/345/gaia2".pmra,
 "I/345/gaia2".pmra\_error,
 "I/345/gaia2".pmdec,
 "I/345/gaia2".pmdec\_error,
 "I/345/gaia2".phot\_g\_mean\_mag,
 "I/345/gaia2".phot_g_mean_mag_error,
 "I/345/gaia2".phot_bp_mean_mag,
 "I/345/gaia2".phot_bp_mean_mag_error,
 "I/345/gaia2".phot_rp_mean_mag,
 "I/345/gaia2".phot_rp_mean_mag_error,
 "I/345/gaia2".radial_velocity,
 "I/345/gaia2".radial_velocity_error,
 "I/345/gaia2".teff_val,
 "I/345/gaia2".a_g_val,
 "I/345/gaia2".lum_val,
 "I/345/gaia2".a_g_percentile_lower,
 "I/345/gaia2".a_g_percentile_upper,
 "I/345/gaia2".dec_parallax_corr,
 "I/345/gaia2".dec_pmdec_corr,
 "I/345/gaia2".dec_pmra_corr,
```

```
 "I/345/gaia2".lum_percentile_lower,
 "I/345/gaia2".lum_percentile_upper,
 "I/345/gaia2".parallax_pmdec_corr,
 "I/345/gaia2".parallax_pmra_corr,
 "I/345/gaia2".pmra_pmdec_corr,
 "I/345/gaia2".ra_parallax_corr,
 "I/345/gaia2".ra_pmdec_corr,
 "I/345/gaia2".ra_pmra_corr,
 "I/345/gaia2".teff_percentile_lower,
 "I/345/gaia2".teff_percentile_upper
FROM "I/345/gaia2"
WHERE 1=CONTAINS(POINT('ICRS',
 "I/345/gaia2".ra,"I/345/gaia2".dec),
 CIRCLE('ICRS', 266.6, 5.7, 3.))
```

Pan-STARRS

```
SELECT
 "II/349/ps1".RAJ2000,
 "II/349/ps1".DEJ2000,
 "II/349/ps1".Qual,
 "II/349/ps1".e_RAJ2000,
 "II/349/ps1".e_DEJ2000,
 "II/349/ps1".Epoch,
 "II/349/ps1".Ns,
 "II/349/ps1".Nd,
 "II/349/ps1".gmag,
 "II/349/ps1".e_gmag,
 "II/349/ps1".gKmag,
 "II/349/ps1".e_gKmag,
 "II/349/ps1".gFlags,
 "II/349/ps1".rmag,
 "II/349/ps1".e_rmag,
 "II/349/ps1".rKmag,
 "II/349/ps1".e_rKmag,
 "II/349/ps1".rFlags,
 "II/349/ps1".imag,
 "II/349/ps1".e_imag,
 "II/349/ps1".iKmag,
 "II/349/ps1".e_iKmag,
```

```
 "II/349/ps1".iFlags,
 "II/349/ps1".zmag,
 "II/349/ps1".e_zmag,
 "II/349/ps1".zKmag,
 "II/349/ps1".e_zKmag,
 "II/349/ps1".zFlags,
 "II/349/ps1".ymag,
 "II/349/ps1".e_ymag,
 "II/349/ps1".yKmag,
 "II/349/ps1".e_yKmag,
 "II/349/ps1".yFlags
FROM "II/349/ps1"
WHERE (("II/349/ps1".RAJ2000>=264.8)
 AND ("II/349/ps1".RAJ2000 <= 269.8)
 AND ("II/349/ps1".DEJ2000>=3.14)
 AND ("II/349/ps1".DEJ2000<=7.4))
```

2*MASS*

```
SELECT
 "II/246/out".RAJ2000,
 "II/246/out".DEJ2000,
 "II/246/out"."2MASS",
 "II/246/out".Jmag,
 "II/246/out".e_Jmag,
 "II/246/out".Hmag,
 "II/246/out".e_Hmag,
 "II/246/out".Kmag,
 "II/246/out".e_Kmag,
 "II/246/out".Qflg
FROM "II/246/out"
WHERE 1=CONTAINS(POINT('ICRS',
 "II/246/out".RAJ2000,"II/246/out".DEJ2000),
CIRCLE('ICRS', 266.6, 5.7, 3.))
```

WISE

```
SELECT
 "II/328/allwise".RAJ2000,
 "II/328/allwise".DEJ2000,
```

```
 "II/328/allwise".W1mag,
 "II/328/allwise".e_W1mag,
 "II/328/allwise".W2mag,
 "II/328/allwise".e_W2mag,
 "II/328/allwise".W3mag,
 "II/328/allwise".e_W3mag,
 "II/328/allwise".W4mag,
 "II/328/allwise".e_W4mag,
 "II/328/allwise".ccf,
 "II/328/allwise".ex,
 "II/328/allwise".var,
 "II/328/allwise".pmRA,
 "II/328/allwise".e_pmRA,
 "II/328/allwise".pmDE,
 "II/328/allwise".e_pmDE,
 "II/328/allwise".qph
FROM "II/328/allwise"
WHERE (("II/328/allwise".RAJ2000>=264.8)
 AND ("II/328/allwise".RAJ2000 <= 269.8)
 AND ("II/328/allwise".DEJ2000>=3.14)
 AND ("II/328/allwise".DEJ2000<=7.4))
```

B.2 USC AND ρ OPH

Gaia DR2

```
SELECT "I/345/gaia2".ra,
 "I/345/gaia2".ra\_epoch2000,
 "I/345/gaia2".dec_epoch2000,
 "I/345/gaia2".ra_epoch2000\_error,
 "I/345/gaia2".dec\_epoch2000_error,
 "I/345/gaia2".parallax,
 "I/345/gaia2".parallax_error,
 "I/345/gaia2".pmra,
 "I/345/gaia2".pmra\_error,
 "I/345/gaia2".pmdec,
 "I/345/gaia2".pmdec\_error,
 "I/345/gaia2".phot\_g\_mean\_mag,
 "I/345/gaia2".phot_g_mean_mag_error,
```

```
 "I/345/gaia2".phot_bp_mean_mag,
 "I/345/gaia2".phot_bp_mean_mag_error,
 "I/345/gaia2".phot_rp_mean_mag,
 "I/345/gaia2".phot_rp_mean_mag_error,
 "I/345/gaia2".radial_velocity,
 "I/345/gaia2".radial_velocity_error,
 "I/345/gaia2".teff_val,
 "I/345/gaia2".a_g_val,
 "I/345/gaia2".lum_val,
 "I/345/gaia2".a_g_percentile_lower,
 "I/345/gaia2".a_g_percentile_upper,
 "I/345/gaia2".dec_parallax_corr,
 "I/345/gaia2".dec_pmdec_corr,
 "I/345/gaia2".dec_pmra_corr,
 "I/345/gaia2".lum_percentile_lower,
 "I/345/gaia2".lum_percentile_upper,
 "I/345/gaia2".parallax_pmdec_corr,
 "I/345/gaia2".parallax_pmra_corr,
 "I/345/gaia2".pmra_pmdec_corr,
 "I/345/gaia2".ra_parallax_corr,
 "I/345/gaia2".ra_pmdec_corr,
 "I/345/gaia2".ra_pmra_corr,
 "I/345/gaia2".teff_percentile_lower,
 "I/345/gaia2".teff_percentile_upper
FROM "I/345/gaia2"
WHERE (("I/345/gaia2".ra>=235.0)
AND ("I/345/gaia2".ra <= 252.0)
AND ("I/345/gaia2".dec>=-29.5)
AND ("I/345/gaia2".dec<=-16.7))
```

Pan-STARRS

```
SELECT
 "II/349/ps1".RAJ2000,
 "II/349/ps1".DEJ2000,
 "II/349/ps1".Qual,
 "II/349/ps1".e_RAJ2000,
 "II/349/ps1".e_DEJ2000,
 "II/349/ps1".Epoch,
 "II/349/ps1".Ns,
```

```
 "II/349/ps1".Nd,
 "II/349/ps1".gmag,
 "II/349/ps1".e_gmag,
 "II/349/ps1".gKmag,
 "II/349/ps1".e_gKmag,
 "II/349/ps1".gFlags,
 "II/349/ps1".rmag,
 "II/349/ps1".e_rmag,
 "II/349/ps1".rKmag,
 "II/349/ps1".e_rKmag,
 "II/349/ps1".rFlags,
 "II/349/ps1".imag,
 "II/349/ps1".e_imag,
 "II/349/ps1".iKmag,
 "II/349/ps1".e_iKmag,
 "II/349/ps1".iFlags,
 "II/349/ps1".zmag,
 "II/349/ps1".e_zmag,
 "II/349/ps1".zKmag,
 "II/349/ps1".e_zKmag,
 "II/349/ps1".zFlags,
 "II/349/ps1".ymag,
 "II/349/ps1".e_ymag,
 "II/349/ps1".yKmag,
 "II/349/ps1".e_yKmag,
 "II/349/ps1".yFlags
FROM "II/349/ps1"
WHERE (("II/349/ps1".RAJ2000>=235.0)
AND ("II/349/ps1".RAJ2000 <= 252.0)
AND ("II/349/ps1".DEJ2000>=-29.5)
AND ("II/349/ps1".DEJ2000<=-16.7))
```

2*MASS*

```
SELECT
 "II/246/out".RAJ2000,
 "II/246/out".DEJ2000,
 "II/246/out"."2MASS",
 "II/246/out".Jmag,
 "II/246/out".e_Jmag,
```

```
 "II/246/out".Hmag,
 "II/246/out".e_Hmag,
 "II/246/out".Kmag,
 "II/246/out".e_Kmag,
 "II/246/out".Qflg
FROM "II/246/out"
WHERE (("II/246/out".RAJ2000>=235.0)
AND ("II/246/out".RAJ2000 <= 252.0)
AND ("III/246/out".DEJ2000>=-29.5)
AND ("II/246/out".DEJ2000<=-16.7))
```

C

ADDITIONAL TABLES

In this appendix we include additional tables which have been cited in the text.

Table C.1. Factors A_λ/A_V to convert the extinction in the visual V filter to the extinction in any other photmometric band used in this study.

Band	A_λ/A_V	Band	A_λ/A_V	Band	A_λ/A_V	Band	A_λ/A_V	Band	A_λ/A_V
g	1.16529	G_{BP}	1.06794	J	0.29434	$W1$	0.07134	$I1$	0.06706
r	0.86813	G	0.85926	H	0.18128	$W2$	0.05511	$I2$	0.05591
i	0.67659	G_{RP}	0.65199	Ks	0.11838	$W3$	0.0022	$I3$	0.04948
z	0.51743					$W4$	0.0	$I4$	0.02518
y	0.43092							$M1$	0.0

Notes. From left to right, we show the factors of the Pan-STARRS, *Gaia* DR2, 2MASS, WISE, and *Spitzer* (IRAC and MIPS) photometric systems. These factors are from the PARSEC website (http://stev.oapd.inaf.it/cgi-bin/cmd).

Table C.2. *Gaia* catalogue of IC 4665 (only the first 10 rows are displayed as example).

Gaia DR2 source ID	RA [°]	Dec [°]	G [mag]	$p_{in} = 0.5$	$p_{in} = 0.6$	$p_{in} = 0.7$	$p_{in} = 0.8$	$p_{in} = 0.9$
4376249758236481664	265.96	2.82	20.35	2.5E−29	$7.2E-31$	$8.02E-30$	$7.2E-37$	$8.8E-45$
4376260409754607872	265.81	2.80	19.27	9.2E−45	$6.4E-39$	$1.75E-42$	$3.9E-58$	$1.8E-58$
4376260482773352576	265.80	2.80	18.10	1.4E−51	$3.0E-54$	$3.67E-60$	$7.5E-67$	$6.4E-80$
4376260482769778176	265.80	2.80	20.28	3.1E−18	$6.9E-20$	$2.89E-21$	$1.0E-22$	$2.5E-24$
4376260478474097664	265.80	2.80	18.62	3.4E−61	$8.3E-56$	$1.34E-79$	$9.0E-97$	$1.2E-107$
4376260650272889856	265.78	2.81	19.29	6.5E−5	$4.0E-5$	$8.33E-6$	$4.9E-6$	$1.4E-6$
4376260684632540032	265.78	2.81	19.36	1.6E−32	$6.1E-34$	$1.31E-35$	$3.0E-46$	$1.6E-48$
4376260684632546816	265.78	2.81	18.12	1.7E−62	$1.4E-43$	$2.30E-56$	$5.9E-61$	$1.7E-71$
4376260684632548736	265.79	2.81	19.03	3.7E−39	$3.4E-40$	$1.82E-45$	$2.6E-55$	$4.6E-58$
4376260684633273344	265.79	2.82	19.82	2.8E−11	$7.1E-12$	$3.89E-12$	$2.1E-15$	$5.6E-18$

Notes. Columns indicate: (1) *Gaia* DR2 source ID; (2–3) right ascension and declination; (4) *Gaia* DR2 G-band magnitude; (5–9) posterior probabilities obtained with p_{in} from 0.5 to 0.9.

Table C.3. DANCe catalogue of IC 4665 (only a subset of the most relevant columns, and the first 10 rows are displayed as example).

RA	Dec	pmRA	pmDec	g	r	i	z	y	J	H	Ks	$p_{in} = 0.5$	...	$p_{in} = 0.9$
[°]	[°]	[mas yr^{-1}]	[mas yr^{-1}]	[mag]	[mag]	[mag]	[mag]	[mag]	[mag]	[mag]	[mag]			
266.37	5.82	−4.51	−7.98	19.7	19.8	19.0	19.0	19.0	17.8	17.0	17.0	6.3E−54	...	7.1E−65
266.67	5.73	−10.19	−23.17	19.8	19.2	19.0	18.9	18.9	17.9	17.5	17.3	3.3E−86	...	3.2E−119
266.30	5.67	5.99	−8.06		21.0	19.7	19.0	18.7	17.3	16.7	16.4	1.7E−18	...	9.8E−20
266.39	6.90	0.81	−4.07	20.4	19.8	19.3	19.1	19.3				7.1E−6	...	2.4E−8
266.66	6.81	−2.51	−5.41	20.4	17.8		16.1					1.2E−4	...	4.9E−5
266.86	6.74	−6.60	−8.79									3.2E−6	...	1.3E−7
266.86	6.79	1.62	−8.71	20.4	19.9	19.6	19.4	19.2	18.2	17.5		6.2E−62	...	1.5E−69
266.89	6.92	2.66	−9.60	18.5	18.0	17.8	17.7	17.7	16.6	16.2	16.2	5.7E−51	...	2.2E−67
266.21	6.63	−5.09	−5.88	19.6	19.0	18.8	18.7	18.7	17.6	17.2	17.1	1.3E−55	...	6.0E−85
266.89	6.92	−2.22	−11.55	18.9	18.1	17.8	17.6	17.4	16.3	15.9	15.7	5.7E−29	...	8.4E−38

Notes. Columns indicate: (1–2) right ascension and declination; (3–4) proper motions; (5–12) photometry; (13 and 15) posterior probabilities obtained with p_{in} of 0.5 and 0.9.

Table C.4. Empirical isochrones of IC 4665 for the photometric bands of the *Gaia* DR2 catalogue.

G [mag]	G_{BP} [mag]	G_{RP} [mag]
7.40	7.41	7.42
7.87	7.89	7.86
8.40	8.44	8.35
8.93	9.00	8.83
9.46	9.55	9.31
9.99	10.11	9.80
10.52	10.68	10.27
11.05	11.26	10.73
11.58	11.85	11.17
12.11	12.43	11.63
12.63	13.01	12.09
13.15	13.59	12.56
13.68	14.17	13.03
14.19	14.78	13.46
14.70	15.39	13.89
15.21	16.01	14.33
15.71	16.64	14.75
16.20	17.28	15.16
16.69	17.92	15.58
17.18	18.56	16.01
17.66	19.20	16.44
18.15	19.83	16.87
18.66	20.42	17.34
19.18	20.98	17.82
19.71	21.55	18.30

Table C.5. Empirical isochrones of IC 4665 for the photometric bands of DANCe (Pan-STARRS and 2MASS).

i [mag]	*z* [mag]	*y* [mag]	*J* [mag]	*H* [mag]	*Ks* [mag]
12.57	12.56	12.55	11.60	11.20	11.10
13.03	12.98	12.92	11.92	11.47	11.37
13.49	13.38	13.30	12.25	11.73	11.65
13.97	13.79	13.65	12.55	11.96	11.86
14.47	14.20	14.02	12.86	12.23	12.07
14.98	14.64	14.42	13.19	12.51	12.33
15.46	15.05	14.79	13.55	12.82	12.64
15.94	15.45	15.14	13.88	13.16	12.98
16.40	15.85	15.50	14.20	13.53	13.32
16.85	16.22	15.88	14.54	13.90	13.67
17.28	16.61	16.27	14.89	14.26	14.02
17.73	17.00	16.64	15.24	14.61	14.36
18.19	17.41	17.03	15.58	14.95	14.68
18.64	17.81	17.40	15.91	15.32	15.01
19.09	18.19	17.78	16.26	15.66	15.36
19.59	18.60	18.16	16.60	15.97	15.67
20.08	19.03	18.52	16.92	16.31	15.96
20.55	19.42	18.90	17.27	16.65	16.26
21.05	19.83	19.29	17.62	16.94	16.57
21.59	20.27	19.66	17.92	17.22	16.84
22.16	20.70	20.10	18.19	17.51	17.08
22.74	21.18	20.50	18.48	17.84	17.30
23.26	21.58	20.90	18.79	18.19	17.52
23.77	22.00	21.30	19.08	18.48	17.76
24.29	22.42	21.70	19.38	18.75	18.03

Table C.6. Apparent G magnitude distribution of IC 4665 (normalised).

G mag	Density	$\sigma_{Density}$
7.08	0.0079	0.0024
7.65	0.0110	0.0029
8.22	0.0128	0.0031
8.78	0.0139	0.0033
9.35	0.0157	0.0033
9.92	0.0184	0.0035
10.49	0.0215	0.0040
11.06	0.0252	0.0043
11.62	0.0299	0.0043
12.19	0.0356	0.0043
12.76	0.0407	0.0048
13.33	0.0431	0.0056
13.90	0.0417	0.0057
14.46	0.0399	0.0052
15.03	0.0440	0.0048
15.60	0.0589	0.0049
16.17	0.0878	0.0057
16.73	0.1309	0.0069
17.30	0.1816	0.0088
17.87	0.2229	0.0109
18.44	0.2319	0.0116
19.01	0.1980	0.0102
19.57	0.1344	0.0077
20.14	0.0701	0.0054
20.71	0.0271	0.0033

Table C.7. Apparent i magnitude distribution of IC 4665 (normalised).

i mag	Density	$\sigma_{Density}$
12.00	0.0017	0.0010
12.50	0.0044	0.0017
13.01	0.0088	0.0026
13.51	0.0140	0.0032
14.01	0.0182	0.0034
14.51	0.0278	0.0043
15.02	0.0518	0.0063
15.52	0.0873	0.0069
16.02	0.1282	0.0078
16.52	0.1741	0.0099
17.03	0.2225	0.0106
17.53	0.2527	0.0115
18.03	0.2419	0.0111
18.54	0.2062	0.0101
19.04	0.1691	0.0098
19.54	0.1272	0.0084
20.04	0.0863	0.0074
20.55	0.0548	0.0058
21.05	0.0355	0.0049
21.55	0.0262	0.0049
22.06	0.0192	0.0039
22.56	0.0126	0.0029
23.06	0.0070	0.0020
23.56	0.0037	0.0015
24.07	0.0023	0.0012

Table C.8. Apparent J magnitude distribution of IC 4665 (normalised).

J mag	Density	$\sigma_{Density}$
7.02	0.0052	0.0021
7.40	0.0098	0.0031
7.77	0.0119	0.0035
8.15	0.0101	0.0029
8.52	0.0079	0.0028
8.90	0.0064	0.0023
9.27	0.0099	0.0031
9.65	0.0170	0.0044
10.02	0.0194	0.0046
10.40	0.0197	0.0045
10.77	0.0229	0.0047
11.15	0.0270	0.0047
11.52	0.0336	0.0052
11.90	0.0446	0.0071
12.27	0.0501	0.0074
12.65	0.0559	0.0069
13.02	0.0784	0.0082
13.40	0.1170	0.0100
13.77	0.1616	0.0121
14.15	0.2054	0.0145
14.52	0.2549	0.0136
14.90	0.2909	0.0138
15.27	0.2848	0.0131
15.65	0.2516	0.0154
16.02	0.2129	0.0159
16.40	0.1616	0.0134
16.77	0.1053	0.0102
17.15	0.0687	0.0075
17.52	0.0494	0.0063
17.90	0.0352	0.0058
18.27	0.0200	0.0044
18.65	0.0091	0.0027
19.02	0.0042	0.0016
19.39	0.0022	0.0014

Table C.9. Present-day system mass function of IC 4665 (normalised).

$\log(M/M_\odot)$	Density	$\sigma_{Density}$
−2.00	0.0026	0.0022
−1.88	0.0055	0.0040
−1.76	0.0086	0.0038
−1.64	0.0256	0.0059
−1.51	0.0738	0.0118
−1.38	0.1328	0.0154
−1.27	0.1982	0.0173
−1.14	0.3204	0.0208
−1.01	0.4604	0.0254
−0.89	0.5434	0.0278
−0.76	0.6372	0.0289
−0.63	0.7113	0.0287
−0.51	0.7029	0.0399
−0.40	0.6680	0.0367
−0.29	0.6258	0.0356
−0.17	0.5704	0.0403
−0.06	0.4742	0.0401
0.05	0.3432	0.0333
0.17	0.2055	0.0266
0.29	0.1220	0.0210
0.39	0.0730	0.0145
0.51	0.0502	0.0119
0.63	0.0526	0.0131
0.73	0.0420	0.0111
0.85	0.0203	0.0064

Table C.10. Bayesian evidences of the models considered to study the spatial distribution of IC 4665.

	Spherical						Elliptical						Segregated					
	EFF	GDP	GKing	King	OGKing	RGDP	EFF	GDP	GKing	King	OGKing	RGDP	EFF	GDP	GKing	King	OGKing	RGDP
EFF	−2354.75	0.74	2.56	4.30	1.40	0.16	2.00	1.13	21.53	187.76	22.75	0.15	0.31	0.84	10.28	7.51	> 999	0.25
GDP	1.35	−2354.45	3.46	5.82	1.90	0.22	2.71	1.53	29.12	253.93	30.77	0.21	0.41	1.14	13.90	10.16	> 999	0.34
GKing	0.39	0.29	−2355.69	1.68	0.55	0.06	0.78	0.44	8.42	73.38	8.89	0.06	0.12	0.33	4.02	2.94	493.36	0.10
King	0.23	0.17	0.59	−2356.21	0.33	0.04	0.47	0.26	5.00	43.63	5.29	0.04	0.07	0.20	2.39	1.75	293.31	0.06
OGKing	0.71	0.53	1.82	3.07	−2355.09	0.11	1.43	0.80	15.34	133.77	16.21	0.11	0.22	0.60	7.32	5.35	899.35	0.18
RGDP	6.22	4.60	15.92	26.78	8.73	−2352.92	12.46	7.03	134.00	> 999	141.57	0.95	1.90	5.24	63.96	46.75	> 999	1.55
EFF	0.50	0.37	1.28	2.15	0.70	0.08	−2355.44	0.56	10.76	93.80	11.37	0.08	0.15	0.42	5.13	3.75	630.63	0.12
GDP	0.89	0.65	2.27	3.81	1.24	0.14	1.77	−2354.87	19.07	166.27	20.15	0.14	0.27	0.75	9.10	6.65	> 999	0.22
GKing	0.05	0.03	0.12	0.20	0.07	< 1e−2	0.09	0.05	−2357.82	8.72	1.06	< 1e−2	0.01	0.04	0.48	0.35	58.62	0.01
King	< 1e−2	< 1e−2	0.01	0.02	< 1e−2	< 1e−2	0.01	< 1e−2	0.11	−2359.98	0.12	< 1e−2	< 1e−2	< 1e−2	0.05	0.04	6.72	< 1e−2
OGKing	0.04	0.03	0.11	0.19	0.06	< 1e−2	0.09	0.05	0.95	8.25	−2357.87	< 1e−2	0.01	0.04	0.45	0.33	55.48	0.01
RGDP	6.53	4.83	16.72	28.12	9.17	1.05	13.08	7.38	140.70	> 999	148.66	−2352.87	1.99	5.50	67.16	49.08	> 999	1.62
GDP	1.19	0.88	3.04	5.11	1.67	0.19	2.38	1.34	25.58	223.04	27.03	0.18	0.36	−2354.58	12.21	8.92	> 999	0.30
EFF	3.28	2.42	8.38	14.10	4.60	0.53	6.56	3.70	70.55	615.13	74.53	0.50	−2353.56	2.76	33.67	24.61	> 999	0.81
GKing	0.10	0.07	0.25	0.42	0.14	0.02	0.19	0.11	2.10	18.27	2.21	0.01	0.03	0.08	−2357.08	0.73	122.81	0.02
King	0.13	0.10	0.34	0.57	0.19	0.02	0.27	0.15	2.87	25.00	3.03	0.02	0.04	0.11	1.37	−2356.77	168.04	0.03
OGKing	< 1e−2	< 1e−2	< 1e−2	< 1e−2	< 1e−2	< 1e−2	< 1e−2	< 1e−2	0.02	0.15	0.02	< 1e−2	< 1e−2	< 1e−2	< 1e−2	< 1e−2	−2361.89	< 1e−2
RGDP	4.02	2.98	10.30	17.32	5.65	0.65	8.06	4.54	86.66	755.65	91.56	0.62	1.23	3.39	41.37	30.23	> 999	−2353.36

Notes. Natural logarithm of the evidence for each profile density (diagonal) and Bayes factors (off-diagonal elements, with the evidence for the model specified in the column header placed in the denominator, i.e. $p(D|M_{row})/p(D|M_{column})$).

Table C.11. Apparent J magnitude distribution of USC and ρ Oph (normalised).

J mag	Density	σ_{Density}
3.90	0.0010	0.0004
4.58	0.0014	0.0005
5.25	0.0024	0.0007
5.93	0.0055	0.0012
6.60	0.0105	0.0015
7.28	0.0234	0.0025
7.95	0.0241	0.0024
8.63	0.0285	0.0024
9.30	0.0494	0.0034
9.98	0.0929	0.0040
10.65	0.1624	0.0054
11.33	0.2191	0.0070
12.00	0.2387	0.0060
12.68	0.2213	0.0066
13.35	0.1495	0.0056
14.03	0.0871	0.0039
14.70	0.0474	0.0035
15.38	0.0308	0.0030
16.05	0.0247	0.0027
16.73	0.0228	0.0028
17.40	0.0129	0.0017
18.08	0.0096	0.0015
18.75	0.0106	0.0015
19.43	0.0032	0.0008

Table C.12. Luminosity function of USC and ρ Oph (normalised).

	3 Myr		5 Myr		8 Myr	
$\log(L/L_\odot)$	Density	$\sigma_{Density}$	Density	$\sigma_{Density}$	Density	$\sigma_{Density}$
−4.0000					0.0142	0.0015
−3.6496	0.0277	0.0020	0.0267	0.0019	0.0274	0.0021
−3.2993	0.0521	0.0034	0.0477	0.0030	0.0465	0.0030
−2.9489	0.0770	0.0039	0.0709	0.0034	0.0625	0.0032
−2.5986	0.1202	0.0043	0.1044	0.0039	0.0927	0.0034
−2.2482	0.2096	0.0056	0.1720	0.0050	0.1683	0.0045
−1.8979	0.3095	0.0062	0.2749	0.0064	0.2794	0.0062
−1.5475	0.3750	0.0069	0.3910	0.0074	0.3924	0.0070
−1.1972	0.4684	0.0088	0.5529	0.0088	0.5445	0.0085
−0.8468	0.4937	0.0099	0.4824	0.0091	0.4623	0.0087
−0.4965	0.2891	0.0082	0.2592	0.0070	0.2546	0.0068
−0.1461	0.1425	0.0060	0.1491	0.0053	0.1652	0.0057
0.2042	0.0849	0.0042	0.1022	0.0048	0.1186	0.0050
0.5546	0.0493	0.0030	0.0582	0.0037	0.0690	0.0036
0.9049	0.0253	0.0020	0.0293	0.0022	0.0409	0.0028
1.2553	0.0144	0.0012	0.0214	0.0016	0.0283	0.0024
1.6056	0.0125	0.0012	0.0200	0.0017	0.0183	0.0016
1.9560	0.0124	0.0014	0.0144	0.0013	0.0121	0.0014
2.3063	0.0106	0.0011	0.0097	0.0011	0.0089	0.0011
2.6567	0.0088	0.0009	0.0078	0.0011	0.0069	0.0010
3.0070	0.0071	0.0008	0.0059	0.0009	0.0053	0.0009
3.3574	0.0056	0.0007	0.0041	0.0007	0.0036	0.0007
3.7077	0.0044	0.0006	0.0030	0.0005	0.0025	0.0004
4.0581	0.0034	0.0004	0.0022	0.0003	0.0019	0.0003
4.4084	0.0027	0.0003	0.0017	0.0003	0.0015	0.0003
4.7588	0.0023	0.0003	0.0014	0.0003	0.0013	0.0002
5.1091	0.0019	0.0002	0.0012	0.0002	0.0010	0.0002
5.4595	0.0015	0.0002	0.0010	0.0002		
5.8098	0.0012	0.0002				

Table C.13. Present-day system mass function of USC and ρ Oph (normalised).

	3 Myr		5 Myr		8 Myr	
$\log(M/M_\odot)$	Density	$\sigma_{Density}$	Density	$\sigma_{Density}$	Density	$\sigma_{Density}$
−2.3979						
−2.2789	0.0664	0.0026				
−2.1598	0.0965	0.0033	0.0754	0.0034		
−2.0408	0.1349	0.0041	0.1041	0.0045	0.0730	0.0038
−1.9218	0.1807	0.0049	0.1346	0.0054	0.0921	0.0045
−1.8027	0.2313	0.0057	0.1646	0.0060	0.1124	0.0049
−1.6837	0.2808	0.0064	0.1934	0.0062	0.1351	0.0050
−1.5646	0.3249	0.0068	0.2232	0.0061	0.1631	0.0050
−1.4456	0.3601	0.0070	0.2555	0.0058	0.1986	0.0051
−1.3265	0.3868	0.0070	0.2909	0.0058	0.2421	0.0054
−1.2075	0.4071	0.0069	0.3305	0.0063	0.2905	0.0061
−1.0884	0.4254	0.0068	0.3728	0.0071	0.3425	0.0071
−0.9694	0.4496	0.0066	0.4206	0.0079	0.3945	0.0080
−0.8503	0.4858	0.0066	0.4804	0.0081	0.4521	0.0083
−0.7313	0.5350	0.0080	0.5568	0.0084	0.5232	0.0080
−0.6122	0.5852	0.0105	0.6343	0.0090	0.6072	0.0077
−0.4932	0.6093	0.0121	0.6860	0.0097	0.6832	0.0082
−0.3741	0.5838	0.0118	0.6811	0.0100	0.7225	0.0094
−0.2551	0.5104	0.0102	0.6186	0.0102	0.7056	0.0106
−0.1360	0.4114	0.0083	0.5197	0.0102	0.6372	0.0110
−0.0170	0.3148	0.0072	0.4145	0.0101	0.5389	0.0106
0.1020	0.2344	0.0068	0.3214	0.0096	0.4260	0.0098
0.2211	0.1745	0.0066	0.2403	0.0087	0.3124	0.0084
0.3401	0.1294	0.0059	0.1716	0.0073	0.2107	0.0066
0.4592	0.0944	0.0050	0.1172	0.0059	0.1318	0.0051
0.5782	0.0688	0.0043	0.0776	0.0046	0.0795	0.0043
0.6973	0.0505	0.0036	0.0511	0.0036	0.0485	0.0038
0.8163	0.0361	0.0030	0.0336	0.0029	0.0309	0.0032
0.9354	0.0249	0.0023	0.0219	0.0023	0.0194	0.0025

Table C.14. Final bona fide sample of 26 members of β Pic selected to determine the dynamical age.

2MASS ID	SpT[a] (ref)	$T_{\rm eff}$ (K)	G (mag)	X (pc)	Y (pc)	Z (pc)	U (km s^{-1})	V (km s^{-1})	W (km s^{-1})	Core
J00172353 − 6645124	M3.0V (1)	3630	11.3	14.60 ± 0.02	-18.59 ± 0.02	-28.21 ± 0.04	-10.51 ± 0.12	-16.09 ± 0.15	-8.60 ± 0.22	Y
J04593483 + 0147007	M0V (2)	3986	9.3	-21.28 ± 0.02	-6.77 ± 0.01	-9.83 ± 0.01	-12.42 ± 0.46	-16.30 ± 0.15	-9.28 ± 0.21	Y
J05004714 − 5715255	M0V (2)	4033	9.4	-1.54 ± 0.00	-21.32 ± 0.02	-16.33 ± 0.01	-11.17 ± 0.02	-16.50 ± 0.15	-9.09 ± 0.12	Y
J05471708 − 5103594	A6V (3)	7100	3.7	-3.43 ± 0.02	-16.65 ± 0.11	-10.06 ± 0.07	-11.07 ± 0.96	-15.79 ± 4.63	-9.21 ± 2.80	Y
J06182824 − 7202416	K4V (2)	4555	9.3	7.59 ± 0.01	-33.75 ± 0.03	-18.58 ± 0.02	-10.50 ± 0.14	-16.46 ± 0.61	-8.71 ± 0.33	Y
J16572029 − 5343316	M3 (4)	3612	11.3	45.37 ± 0.28	-21.65 ± 0.13	-5.88 ± 0.04	-7.35 ± 0.16	-15.87 ± 0.13	-10.49 ± 0.08	N
J17020937 − 6734447	(M4) (5)	3712	12.8	32.00 ± 0.05	-23.67 ± 0.04	-10.97 ± 0.02	-8.20 ± 0.72	-16.62 ± 0.53	-9.09 ± 0.25	N
J17024014 − 4521587	(M2) (5)	3914	10.7	30.33 ± 0.06	-10.06 ± 0.02	-1.24 ± 0.00	-8.67 ± 0.17	-16.51 ± 0.07	-10.21 ± 0.03	Y
J17444256 − 5315471	(M3) (5)	3866	12.9	48.62 ± 0.17	-18.83 ± 0.07	-11.34 ± 0.04	-7.17 ± 0.35	-16.93 ± 0.15	-10.12 ± 0.09	N
J17483374 − 5306118	(M2) (5)	3962	12.9	70.36 ± 0.29	-26.64 ± 0.11	-16.96 ± 0.07	-7.44 ± 0.12	-16.81 ± 0.09	-9.20 ± 0.06	Y
J18041617 − 3018280	(M2) (5)	3814	11.7	54.93 ± 0.15	0.82 ± 0.00	-4.03 ± 0.01	-7.83 ± 0.24	-14.52 ± 0.05	-8.45 ± 0.04	Y
J18055491 − 5704307	(M2) (5)	3884	12.4	49.55 ± 0.16	-21.31 ± 0.07	-16.18 ± 0.05	-8.58 ± 0.19	-15.54 ± 0.10	-8.09 ± 0.07	Y
J18092970 − 5430532	(M4) (5)	3826	13.4	34.91 ± 0.11	-13.14 ± 0.04	-10.76 ± 0.03	-10.23 ± 0.24	-15.13 ± 0.11	-8.05 ± 0.08	N
J18161236 − 5844055	(M3) (5)	3563	11.5	26.21 ± 0.05	-11.84 ± 0.02	-9.68 ± 0.02	-7.78 ± 0.35	-17.09 ± 0.16	-10.26 ± 0.13	N
J18281651 − 4421477	(M2) (5)	3996	12.6	77.46 ± 0.28	-13.26 ± 0.05	-20.69 ± 0.07	-6.84 ± 0.22	-16.37 ± 0.08	-8.99 ± 0.08	Y
J18283524 − 4457280	(K7) (5)	4190	11.6	79.32 ± 0.20	-14.36 ± 0.04	-21.66 ± 0.06	-6.45 ± 0.33	-16.22 ± 0.08	-8.95 ± 0.10	Y
J18420694 − 5554254	M3.0V (1)	3753	12.4	45.01 ± 0.12	-16.58 ± 0.04	-18.35 ± 0.05	-8.52 ± 0.19	-15.40 ± 0.08	-8.28 ± 0.08	Y
J19225894 − 5432170	F6V (2)	6437	6.9	41.30 ± 0.11	-12.80 ± 0.04	-21.32 ± 0.06	-8.89 ± 0.34	-15.43 ± 0.11	-8.06 ± 0.18	Y
J19233820 − 4606316	M0 (4)	4050	11.2	64.02 ± 0.19	-9.10 ± 0.03	-29.50 ± 0.09	-6.73 ± 0.74	-16.37 ± 0.12	-9.76 ± 0.35	N
J19243494 − 3442392	M4.0V (1)	4045	12.8	48.13 ± 0.22	3.22 ± 0.01	-18.92 ± 0.09	-9.47 ± 0.58	-16.14 ± 0.09	-8.88 ± 0.24	N
J19481651 − 2720319	(M2) (5)	3944	12.2	57.78 ± 0.22	13.52 ± 0.05	-26.17 ± 0.10	-7.69 ± 0.15	-14.99 ± 0.06	-9.20 ± 0.08	Y
J20013718 − 3313139	M1 (4)	3938	11.5	52.34 ± 0.13	7.26 ± 0.02	-28.47 ± 0.07	-7.68 ± 0.16	-15.78 ± 0.04	-9.13 ± 0.10	N
J20090521 − 2613265	F5V (6)	6450	7.1	42.62 ± 0.09	12.23 ± 0.03	-23.41 ± 0.05	-6.96 ± 1.02	-14.69 ± 0.29	-10.27 ± 0.56	N
J20333759 − 2556521	M4.5V (4)	3864	13.1	34.55 ± 0.17	11.39 ± 0.06	-23.62 ± 0.12	-8.44 ± 0.76	-14.85 ± 0.26	-9.59 ± 0.52	Y
J21100535 − 1919573	M2 (4)	3770	10.8	21.87 ± 0.06	12.25 ± 0.04	-20.26 ± 0.06	-9.91 ± 0.28	-15.17 ± 0.16	-9.78 ± 0.26	Y
J22424896 − 7142211	K7V (2)	4065	9.8	19.57 ± 0.02	-18.94 ± 0.02	-24.54 ± 0.02	-10.25 ± 0.08	-15.84 ± 0.08	-7.98 ± 0.10	Y

References. (1) Riedel et al. (2017b); (2) Torres et al. (2006); (3) Gray et al. (2006); (4) Riaz, Gizis and Harvin (2006); (5) Gagné and Faherty (2018); (6) Houk (1982)

Notes. [(a)] Spectral types between parentheses were estimated from the absolute *Gaia* $G-$band magnitude.

Table C.15. Photometric bands used to detect an IR excess in Sect. 6.3. Only the sources for which we have detected an IR excess are shown. An extended version of this Table including all the photometric bands analysed in this work for all the members of IC 4665 is available at the CDS.

Obj	*G* (mag)	*Ks* (mag)	*W*1 (mag)	*W*2 (mag)	*W*3 (mag)	*W*4 (mag)	IRAC1 (mag)	IRAC2 (mag)	IRAC3 (mag)	IRAC4 (mag)	MIPS1 (mag)
HD 161261	8.26 ± 0.05	8.04 ± 0.05	$8.00 \pm 0.02^{*}$	7.98 ± 0.02	7.75 ± 0.02	7.15 ± 0.11					
HD 161733	7.96 ± 0.05	7.87 ± 0.05	$7.85 \pm 0.03^{*}$	$7.89 \pm 0.02^{*}$	7.87 ± 0.02	7.69 ± 0.15	7.92 ± 0.03	7.92 ± 0.03	7.99 ± 0.03	7.92 ± 0.03	7.75 ± 0.04
HD 161621	9.45 ± 0.05	8.75 ± 0.05	$8.09 \pm 0.02^{*}$	$8.10 \pm 0.02^{*}$	$8.14 \pm 0.02^{*}$	$8.08 \pm 0.24^{*}$	8.96 ± 0.03	8.87 ± 0.03	8.78 ± 0.03	8.74 ± 0.03	8.11 ± 0.04
TYC 428-1938-1	11.01 ± 0.05	9.95 ± 0.05	9.85 ± 0.02	9.86 ± 0.02	9.80 ± 0.05	8.64^{u}	9.87 ± 0.03	9.83 ± 0.03	9.80 ± 0.03	9.84 ± 0.03	9.46 ± 0.05
TYC 428-428-1	10.36 ± 0.05	9.68 ± 0.05	$9.40 \pm 0.02^{*}$	$9.53 \pm 0.02^{*}$	$9.36 \pm 0.04^{*}$	$7.72 \pm 0.18^{*}$	9.62 ± 0.03	9.64 ± 0.03	9.60 ± 0.03	9.58 ± 0.03	7.77 ± 0.04
HD 161734	8.82 ± 0.05	8.46 ± 0.05	8.34 ± 0.02	8.25 ± 0.02	7.64 ± 0.02	6.75 ± 0.07	8.40 ± 0.03	8.31 ± 0.03	8.13 ± 0.03	7.86 ± 0.03	6.99 ± 0.04

$^{(*)}$ measurement filtered (see Sect. 6.2.2)
$^{(u)}$ upper limit

D

RÉSUMÉ SUBSTANTIEL

INTRODUCTION

Comprendre comment se forment les étoiles est l'une des questions fondamentales à laquelle l'astronomie entend répondre. Actuellement, la plupart des études indiquent que la majorité des étoiles se forment en groupes plutôt que de manière isolée. Cependant notre compréhension des détails du processus de formation est encore très incomplète. Comment la formation d'étoiles commence-t-elle et se propage-t-elle à travers les nuages moléculaires géants ? Quel est le rôle de l'environnement local ? Quelle est l'efficacité du processus de formation stellaire ? Quelle est l'origine des masses stellaires ? Quelle fraction de la population d'étoiles se retrouve dans des structures liées par gravitation ? Ce ne sont là que quelques-unes des questions auxquelles les théories de formation stellaire doivent répondre et qui font à ce jour toujours l'objet de débats et d'intenses recherches.

Le principal défi qui entrave l'étude du processus de formation des étoiles est qu'il se produit à une échelle de temps beaucoup plus grande que l'échelle de temps humains et qu'il ne peut donc pas être étudié en temps réel. Dans cette thèse, nous discutons plusieurs méthodes indirectes, telles que la mesure de la fonction de masse, la dynamique et l'identification des étoiles hébergeant des disques, pour obtenir et déduire des informations sur différents aspects des processus de formation des étoiles. Une autre difficulté importante liée à l'étude de la formation des étoiles est que les étoiles jeunes sont toujours enfouies dans leurs nuages moléculaires et sont donc très difficiles à observer. Pour mitiger ce problème, dans cette thèse nous combinons des images obtenues dans le domaine visible avec des images obtenues dans l'infrarouge, qui permettent de sonder les nuages de gaz et de poussière. De plus, en nous concentrant sur l'étude de régions proches du système solaire, nos observations nous permettent de détecter les objets les plus faibles et les plus froids, jusque dans le domaine des masses planétaires.

OBJECTIFS

L'objectif principal de cette thèse est de déterminer la fonction de masse initiale – la distribution de masse des étoiles à la naissance – dans différentes associations et régions de formation d'étoiles proches du Soleil. La fonction de

masse est un produit direct de la formation stellaire et à ce titre constitue un paramètre d'observation fondamental pour contraindre les théories de formation stellaire et sous-stellaire. Déterminer la fonction de masse avec précision sur une large gamme de masses est extrêmement difficile, en particulier dans le régime des faibles masses où il y a peu d'observations et où les incertitudes sont grandes. À ce jour, peu d'études ont tenté de déterminer la fonction de masse des objets sous-stellaires et les incertitudes sont généralement mal encore relativement grandes et souvent sous-estiment les incertitudes liées aux méthodes d'observations elles-mêmes.

Les recensements de populations jeunes obtenus pour déterminer la fonction de masse permettent par ailleurs d'étudier d'autres paramètres astrophysiques très informatifs pour les études de la formation stellaires. C'est pourquoi, parallèlement à l'étude principale de la fonction de masse, nous consacrons une grande partie de cette thèse à deux autres types d'études complémentaires : l'âge et les disques circum-stellaires.

L'âge est un paramètre fondamental pour interpéter les mesures obtenues et les comparer avec les prédictions des modèles et des simulations numériques. Dans le cas qui nous concerne, nous verrons que les incertitudes relatives à l'âge des associations sont une source importante d'incertitudes et d'erreurs. Nous consacrons donc un chapitre à l'amélioration de méthodes existantes pour mesurer l'âge d'associations jeunes à partir de leur dynamique, au moyen d'une analyse orbitale de retraçage.

Les disque circum-stellaires sont omniprésents à la fois dans les étapes précoces de la formation des étoiles (disques protoplanétaires) et des planètes (disques proto-planétaires puis disques de débris). L'identification et la caractérisation des disques fournit donc des informations importantes et uniques sur les mécanismes de formation stellaire et planétaire. Tirant parti de nos nouveaux recensements et des relevés dans l'infrarouge moyen existant (WISE et Spitzer), nous dévelopons une stratégie qui nous permet d'identifier les étoiles possédant un disque de débris dans l'amas IC 4665. À 30 Ma, cet amas est à un stade d'évolution ou les interactions dynamiques des planètes et planétesimaux sont très actives et vont déterminer la forme des systèmes planétaires. La méthodologie mise en place pour cette étude pourra être appliquée à d'autres régions au fur et a mesure que de nouveaux recensements sont disponibles.

MÉTHODES

Cette thèse s'insère dans le contexte du projet COSMIC DANCe, pour lequel un grand nombre d'images profondes grand champ ont été obtenues sur une grande période de temps. En combinant ces données avec des images d'archives publiques, nous avons construit un catalogue astrométrique et photométrique

(optique et infrarouge proche) précis de différents amas jeunes et régions de formation d'étoiles, complémenté par le catalogue Gaia DR2. Nous avons analysé les catalogues DANCe et Gaia avec des outils statistiques bayésiens modernes pour fournir une liste complète de membres de l'amas jeune IC 4665 et des régions de formation d'étoiles ρOph et Upper Scorpius. Nous avons alors utilisé ces listes complètes de membres pour déterminer la distribution de magnitude apparente ainsi que les distributions de luminosité et de masse, en utilisant des modèles d'évolution stellaires récents pour transformer les osbervables (magnitudes apparentes) en luminosités et masses. Notre analyse statistique bayésienne nous a permis de propager les incertitudes d'observation tout au long de l'analyse et jusqu'à la fonction de masse.

En complément de l'analyse de la fonction de masse, nous avons utilisé les recensements obtenus pour d'autres études de suivi. Tout d'abord, nous avons développé une stratégie basée sur une analyse de traçage orbital pour déterminer les âges dynamiques. Cette stratégie inclue plusieurs étapes depuis l'obtention de données au télescope ou dans les archives publiques jusqu'à la détermination de l'âge dynamique. En effet, mon experience sur les âges dynamiques m'a enseigné au cours de mon master que la précision et l'homogénéité des mesures de vitesses radiales est fondamentale pour le succès de l'analyse. La première étape de notre stratége consiste donc à acquérir et analyser des spectres échelles au télescope ou dans les archives publiques pour la mesure de vitesses radiales précises. La deuxième partie consiste à combiner ces mesures avec les mouvements propres et parallaxes de Gaia DR2, pour enfin effectuer l'analyse de traçage dynamique et déterminer l'âge de l'association tout en propageant de manière rigoureuse les incertitudes et corrélations entre les mesures.

Enfin, nous avons mis en place une méthodologie pour identifier les disques circum-stellaires à partir de leur signature dans l'infrarouge moyen en utilisant la photométrie des missions WISE et Spitzer. Cette stratégie recquiert un traitement initial de la photométrie, c'est-à-dire un filtrage robuste des défauts et problèmes dans les catalogues WISE et les images Spitzer, avec en particulier un traitement adéquat des nébulosités présentes dans ces images. Ensuite, nous avons recherché les excès dans la photométrie infrarouge indicatifs de la présence de matériel circum-stellaire dans divers diagrammes couleur-couleur. Enfin, nous avons ajusté la distribution d'énergie spectrale de chaque candidat afin de confirmer ces excès infrarouges et de déterminer la température effective des étoiles concernées.

RÉSULTATS

Nous avons appliqué l'algorithme d'appartenance au cluster ouvert. Nous avons identifié :

- 819 membres dans l'amas IC 4665 de 30 Ma
- 3 455 membres dans les deux associations Upper Scorpius et Ophiuchus ($1 - 10$ Ma)

couvrant sur un très grand domaine de masse des étoiles massives de type OB jusqu'aux régimes sous-stellaire et planétaire. Les fonctions de masse observées sont assez bien représentées par une fonction de masse en loi de puissance type Salpeter dans le domaine des masses élevées. Aux masses intermédiaires, leur forme est bien représentée par une distribution log-normale avec une masse caractéristique de $0.3 - 0.5$ $M_\odot$.

Dans le domaine des très faibles masses, nos deux études ont confirmé des populations extrêmement riches d'objets sous-stellaires avec un excès significatifs d'objets paar rapport aux prédictions des modèles. Dans la région la plus proche (145 pc) et la plus jeune du Scorpion supérieur et d'Ophiuchus, notre sensibilité accrue a permis de révéler une population extrêmement riche de plusieurs dizaines de planètes errantes. Les nombres relatifs de naines brunes et de planètes errantes sont plus importants que ceux prédits par les modèles de formation par effondrement de cœurs moléclaires. En faisant des hypothèses simples basées sur les connaissances actuelles des systèmes planétaires, nous avons estimé qu'une fraction significative des naines brunes et des planètes errantes doit se former par des phénomènes d'éjection dynamique. La contribution de ces mécanismes à la population finale de naines brunes et de planètes errantes pourrait être du même ordre que la formation par contraction des coeurs moléculaires.

Afin d'améliorer l'estimation des âges des associations jeunes qui nous intéresse, nous avons amélioré et appliqué l'analyse de traçage orbital au groupe β Pictoris et obtenu un âge dynamique de $18.5^{+2.0}_{-2.4}$ Myr. Cette valeur réconcilie l'estimation d'âge dynamique avec celles basées sur le lithium et l'ajustement d'isochrone, qui jusque là étaient en conflit. Les précédentes estimations d'âge dynamique trouvaient en effet des valeurs inférieures et incompatibles avec les valeurs obtenues par l'étude du Lithium ou des isochrones. Notre méthode démontre ainsi l'importance d'un traitement amélioré et rigoureux des données, des mesures et des incertitudes.

En utilisant des données d'archives et catalogues dans l'infrarouge moyen, nous avons identifié six disques de débris dans l'amas ouvert proches IC 4665. Avec un âge où les interactions dynamiques entre planètes et planétésimaux sont très actives dans les disques circum-stellaires, ces objets constituent d'excellents

candidats pour le suivi avec des observatoires comme ALMA ou le JWST. Nous avons calculé une fraction de disque de $24 \pm 10\%$ pour les étoiles de type spectraux B–A qui est compatible avec les valeurs rapportées dans la litérature pour les régions de $15 - 20$ Ma (Upper Centaurus Lupus, Lower Centaurus Crux, β Pictoris), et pour l'amas des Pléïades (125 Ma). Nous n'avons détecté qu'une seule étoile de type solaire avec un excès infrarouge, correspondant à une fraction de $9 \pm 9\%$ pour les classes spectrales comprises entre F5–K5. Cette fraction est inférieure à celle généralement observée à $15 - 20$ Myr, mais devra être confirmée par des données plus profondes.

CONCLUSIONS ET PERSPECTIVES

La méthode de sélection des membres d'amas présentée dans cette thèse s'est avérée être un outil statistique efficace et robuste pour obtenir des recensements complets d'amas ouvertes et de régions proches de formation d'étoiles. Les objets identifiées par notre algorithme sont d'excellents candidats pour toutes sortes d'études de suivi telles que la recherche de disques, de planètes et la caractérisation des atmosphères des planètes flottantes. De plus, cet outil est prêt à être appliqué aux grands relevés du futur tels que le LSST, Euclid et le télescope spatial Nancy Grace Roman. Ces études permettront de surmonter les limites imposées au travail présent par la couverture spatiale et la sensibilité limitée des données COSMIC DANCe, et fourniront des recensements encore plus complets de planètes flottantes, cruciales pour contraindre leurs mécanismes de formation.

La méthodologie d'analyse observationnelle et analytique de traçage orbital dévelopé dans cette thèse est non seulement utile pour déterminer les âges mais aussi pour étudier l'évolution dynamique des étoiles dans l'espace des phases en 6D. Cette méthode ainsi que le nouveau recensement du Scorpion supérieur présenté dans cette thèse nous permettront d'obtenir un âge plus précis pour cette région et les structures qui la composent. Ces âges permettront alors d'affiner les estimations de masse des membres, ce qui réduira les incertitudes de la fonction de masse et fournira de meilleures contraintes en particulier sur le nombre de planètes flottantes. Un relevé spectroscopiques est déjà en cours pour compléter l'excellente astrométrie que l'imminent catalogue Gaia DR3 fournira et les vitesses radiales déjà dispnibles avec APOGEE pour environ 20% étoiles de notre échantillon. Ces données d'observation en 6D seront également essentielles pour étudier l'histoire de la formation d'étoiles de la région et comprendre où la formation d'étoiles a commencé et comment elle s'est propagée à travers le nuage moléculaire.

Nous avons également commencé d'autres études de suivi des membres les moins massifs de IC 4665 et Upper Scorpius pour étudier leurs atmosphères avec

des spectres basse-résolution optiques et infrarouges. Nous avons ainsi obtenu 19 spectres au GTC pour étudier les atmosphères des objets sous-stellaires de IC 4665, et avons soumis plusieurs demandes dans des observatoires pour étudier la population de planètes errantes Scorpion supérieur.

Nous avons également commencé un suivi de vitesse radiale de cinq membres de IC 4665 pour rechercher des exoplanètes. Entre 9 et 12 époques ont été obtenues avec différents vélocimètres (SOPHIE à l'OHP, CAFE à Calar Alto et FIES au NOT). Une analyse préliminaire de ces données a révélé une binaire spectroscopique et quelques candidats exoplanètes. Une analyse plus complète des spectres et des courbes de lumière disponibles est en cours pour confirmer leur nature.

Enfin, nous prévoyons d'appliquer la méthode présentée pour chercher des disques dans IC 4665 à Upper Scorpius où de nombreuses données dans l'infrarouge moyen sont disponibles. La fréquence et les propriétés des disques autour des membres de Upper Scorpius apportera de nouvelles contraintes fortes sur les mécanismes à l'oeuvre dans cette région, et en particulier sur les mécanismes responsables de la formation des planètes errantes.

BIBLIOGRAPHY

Abt, H. A., C. T. Bolton and S. G. Levy (1972). «IC 4665, a Cluster of Binaries». In: *ApJ* 171, p. 259.

Aceituno, J. et al. (2013). «CAFE: Calar Alto Fiber-fed Échelle spectrograph». In: *A&A* 552, A31, A31.

Alam, S. et al. (2015). «The Eleventh and Twelfth Data Releases of the Sloan Digital Sky Survey: Final Data from SDSS-III». In: *ApJS* 219.1, 12, p. 12.

Allain, S. et al. (1996). «Rotational periods and starspot activity of young solar-type dwarfs in the open cluster IC 4665.» In: *A&A* 305, p. 498.

Allard, F. (2014). «The BT-Settl Model Atmospheres for Stars, Brown Dwarfs and Planets». In: *Exploring the Formation and Evolution of Planetary Systems*. Ed. by M. Booth, B. C. Matthews and J. R. Graham. Vol. 299. IAU Symposium, pp. 271–272.

Allen, C. and A. Santillan (1991). «An improved model of the galactic mass distribution for orbit computations». In: *Rev. Mexicana Astron. Astrofis.* 22, pp. 255–263.

Alonso-Floriano, F. J. et al. (2015). «Reaching the boundary between stellar kinematic groups and very wide binaries. III. Sixteen new stars and eight new wide systems in the β Pictoris moving group». In: *A&A* 583, A85, A85.

Alves de Oliveira, C. et al. (2013). «Spectroscopy of brown dwarf candidates in IC 348 and the determination of its substellar IMF down to planetary masses». In: *A&A* 549, A123, A123.

Alves, J., M. Lombardi and C. J. Lada (2007). «The mass function of dense molecular cores and the origin of the IMF». In: *A&A* 462.1, pp. L17–L21.

Alves, J. et al. (2020). «A Galactic-scale gas wave in the Solar Neighborhood». In: *arXiv e-prints*, arXiv:2001.08748, arXiv:2001.08748.

Anders, F. et al. (2019). «Photo-astrometric distances, extinctions, and astrophysical parameters for Gaia DR2 stars brighter than G = 18». In: *A&A* 628, A94, A94.

Andrae, R. et al. (2018). «gaiai Data Release 2. First stellar parameters from Apsis». In: *A&A* 616, A8, A8.

André, P. et al. (2014). «From Filamentary Networks to Dense Cores in Molecular Clouds: Toward a New Paradigm for Star Formation». In: *Protostars and Planets VI*. Ed. by H. Beuther et al., p. 27.

André, P. (2002). «The Initial Conditions for Protostellar Collapse: Observational Constraints». In: *EAS Publications Series*. Ed. by J. Bouvier and J.-P. Zahn. Vol. 3. EAS Publications Series, pp. 1–38.

André, P. et al. (2010). «From filamentary clouds to prestellar cores to the stellar IMF: Initial highlights from the Herschel Gould Belt Survey». In: *A&A* 518, L102, p. L102.

André, P., D. Ward-Thompson and J. Greaves (2012). «Interferometric Identification of a Pre-Brown Dwarf». In: *Science* 337.6090, p. 69.

Antoja, T. et al. (2011). «Understanding the spiral structure of the Milky Way using the local kinematic groups». In: *MNRAS* 418, pp. 1423–1440.

Asiain, R., F. Figueras and J. Torra (1999). «On the evolution of moving groups: an application to the Pleiades moving group». In: *A&A* 350, pp. 434–446.

Astropy Collaboration et al. (2013). «Astropy: A community Python package for astronomy». In: *A&A* 558, A33, A33.

Aumann, H. H. et al. (1984). «Discovery of a shell around alpha Lyrae.» In: *ApJ* 278, pp. L23–L27.

Autry, R. G. et al. (2003). «NEWFIRM: the widefield IR imager for NOAO 4-m telescopes». In: *Society of Photo-Optical Instrumentation Engineers (SPIE) Conference Series*. Ed. by M. Iye & A. F. M. Moorwood. Vol. 4841. Society of Photo-Optical Instrumentation Engineers (SPIE) Conference Series, pp. 525–539.

Baade, D. et al. (1999). «The Wide Field Imager at the 2.2-m MPG/ESO telescope: first views with a 67-million-facette eye.» In: *The Messenger* 95, pp. 15–16.

Baraffe, I. et al. (2002). «Evolutionary models for low-mass stars and brown dwarfs: Uncertainties and limits at very young ages». In: *A&A* 382, pp. 563–572.

Baraffe, I. et al. (2015). «New evolutionary models for pre-main sequence and main sequence low-mass stars down to the hydrogen-burning limit». In: *A&A* 577, A42, A42.

Baranne, A. et al. (1996). «ELODIE: A spectrograph for accurate radial velocity measurements.» In: *A&AS* 119, pp. 373–390.

Barrado y Navascúes, D. (2001). «The β Pic Moving Group: a New Age Assesment». In: *Young Stars Near Earth: Progress and Prospects*. Ed. by R. Jayawardhana and T. Greene. Vol. 244. Astronomical Society of the Pacific Conference Series, p. 63.

Barrado y Navascués, D. et al. (1999). «The Age of β Pictoris». In: *ApJ* 520, pp. L123–L126.

Basri, G. and E. L. Martín (1999). «PPL 15: The First Brown Dwarf Spectroscopic Binary». In: *AJ* 118.5, pp. 2460–2465.

Bastian, N., K. R. Covey and M. R. Meyer (2010). «A Universal Stellar Initial Mass Function? A Critical Look at Variations». In: *ARA&A* 48, pp. 339–389.

Basu, S. (2012). «Brown-Dwarf Origins». In: *Science* 337.6090, p. 43.

Bate, M. R., I. A. Bonnell and V. Bromm (2002). «The formation mechanism of brown dwarfs». In: *MNRAS* 332.3, pp. L65–L68.

— (2003). «The formation of a star cluster: predicting the properties of stars and brown dwarfs». In: *MNRAS* 339.3, pp. 577–599.

Baumgardt, H. et al. (2019). «Mean proper motions, space orbits, and velocity dispersion profiles of Galactic globular clusters derived from Gaia DR2 data». In: *MNRAS* 482.4, pp. 5138–5155.

Bayo, A. et al. (2008). «VOSA: virtual observatory SED analyzer. An application to the Collinder 69 open cluster». In: *A&A* 492.1, pp. 277–287.

Bayo, A. et al. (2011). «Spectroscopy of very low mass stars and brown dwarfs in the Lambda Orionis star forming region. I. Enlarging the census down to the planetary mass domain in Collinder 69». In: *A&A* 536, A63, A63.

Beccari, G., H. M. J. Boffin and T. Jerabkova (2020). «Uncovering a 260 pc wide, 35-Myr-old filamentary relic of star formation». In: *MNRAS* 491.2, pp. 2205–2216.

Infrared Astronomical Satellite (IRAS) Catalogs and Atlases.Volume 1: Explanatory Supplement. (1988). Vol. 1.

Belikov, A. N. et al. (1998). «The fine structure of the Pleiades luminosity function and pre-main sequence evolution». In: *A&A* 332, pp. 575–585.

Bell, C. P. M., E. E. Mamajek and T. Naylor (2015). «A self-consistent, absolute isochronal age scale for young moving groups in the solar neighbourhood». In: *MNRAS* 454, pp. 593–614.

Bertin, E. (2006). «Automatic Astrometric and Photometric Calibration with SCAMP». In: *Astronomical Data Analysis Software and Systems XV*. Ed. by C. Gabriel et al. Vol. 351. Astronomical Society of the Pacific Conference Series, p. 112.

Bertin, E. and S. Arnouts (1996). «SExtractor: Software for source extraction.» In: *A&AS* 117, pp. 393–404.

Bertin, E. (2013). *PSFEx: Point Spread Function Extractor*.

Binks, A. S. and R. D. Jeffries (2014). «A lithium depletion boundary age of 21 Myr for the Beta Pictoris moving group». In: *MNRAS* 438.1, pp. L11–L15.

— (2016). «Spectroscopic confirmation of M-dwarf candidate members of the Beta Pictoris and AB Doradus Moving Groups». In: *MNRAS* 455.3, pp. 3345–3358.

Binks, A. S., R. D. Jeffries and P. F. L. Maxted (2015). «A kinematically unbiased search for nearby young stars in the Northern hemisphere selected using SuperWASP rotation periods». In: *MNRAS* 452, pp. 173–192.

Blanco-Cuaresma, S. et al. (2014). «Determining stellar atmospheric parameters and chemical abundances of FGK stars with iSpec». In: *A&A* 569, A111, A111.

Blanco-Cuaresma, S. (2019). «Modern stellar spectroscopy caveats». In: *MNRAS* 486.2, pp. 2075–2101.

Bonnell, I. A. et al. (2001). «Competitive accretion in embedded stellar clusters». In: *MNRAS* 323.4, pp. 785–794.

Bosch, J. et al. (2018). «The Hyper Suprime-Cam software pipeline». In: *PASJ* 70, S5, S5.

Boss, A. P. et al. (2007). «Working Group on Extrasolar Planets». In: *Transactions of the International Astronomical Union, Series A* 26A, pp. 183–186.

Boulade, O. et al. (2003). «MegaCam: the new Canada-France-Hawaii Telescope wide-field imaging camera». In: *Society of Photo-Optical Instrumentation Engineers (SPIE) Conference Series*. Ed. by M. Iye & A. F. M. Moorwood. Vol. 4841. Society of Photo-Optical Instrumentation Engineers (SPIE) Conference Series, pp. 72–81.

Bouy, H. et al. (2011). «The DANCE Project: Dynamical Analysis of Nearby Clusters». In: *Stellar Clusters & Associations: A RIA Workshop on Gaia*, pp. 103–107.

Bouy, H. et al. (2013). «Dynamical analysis of nearby clusters. Automated astrometry from the ground: precision proper motions over a wide field». In: *A&A* 554, A101, A101.

Bouy, H. et al. (2015). «The Seven Sisters DANCe. I. Empirical isochrones, luminosity, and mass functions of the Pleiades cluster». In: *A&A* 577, A148, A148.

Bovy, J. (2015). «galpy: A python Library for Galactic Dynamics». In: *ApJS* 216.2, 29, p. 29.

Bowler, B. P. (2016). «Imaging Extrasolar Giant Planets». In: *PASP* 128.968, p. 102001.

Bravi, L. et al. (2018). «The Gaia-ESO Survey: a kinematical and dynamical study of four young open clusters». In: *A&A* 615, A37, A37.

Brown, A. G. A. et al. (1997). «Considerations in Making Full Use of the HIPPARCOS Catalogue». In: *Hipparcos - Venice '97*. Ed. by R. M. Bonnet et al. Vol. 402. ESA Special Publication, pp. 63–68.

Caballero, J. A. et al. (2019). «Stars and brown dwarfs in the σ Orionis cluster. IV. IDS/INT and OSIRIS/GTC spectroscopy and Gaia DR2 astrometry». In: *A&A* 629, A114, A114.

Cannon, A. J. and E. C. Pickering (1993). «VizieR Online Data Catalog: Henry Draper Catalogue and Extension (Cannon+ 1918-1924; ADC 1989)». In: *VizieR Online Data Catalog*, III/135A, III/135A.

Cánovas, H. et al. (2019). «Census of ρ Ophiuchi candidate members from Gaia Data Release 2». In: *A&A* 626, A80, A80.

Cantat-Gaudin, T. et al. (2018). «A Gaia DR2 view of the open cluster population in the Milky Way». In: *A&A* 618, A93, A93.

Cargile, P. A. and D. J. James (2010). «Employing a New, BVI_c Photometric Survey of IC 4665 to Investigate the Age of This Young Open Cluster». In: *AJ* 140, pp. 677–691.

Carroll, B. W. and D. A. Ostlie (2007). *An Introduction to Modern Astrophysics*. Ed. by S. F. P. Addison-Wesley. 2nd (International).

Casali, M. et al. (2007). «The UKIRT wide-field camera». In: *A&A* 467, pp. 777–784.

Castelli, F., R. G. Gratton and R. L. Kurucz (1997). «Notes on the convection in the ATLAS9 model atmospheres.» In: *A&A* 318, pp. 841–869.

Chabrier, G. (2005). «The Initial Mass Function: From Salpeter 1955 to 2005». In: *The Initial Mass Function 50 Years Later*. Ed. by E. Corbelli, F. Palla and H. Zinnecker. Vol. 327. Astrophysics and Space Science Library, p. 41.

Chabrier, G. et al. (2014). «Giant Planet and Brown Dwarf Formation». In: *Protostars and Planets VI*. Ed. by H. Beuther et al., p. 619.

Chabrier, G. (2003). «Galactic Stellar and Substellar Initial Mass Function». In: *PASP* 115.809, pp. 763–795.

Chatterjee, S. et al. (2008). «Dynamical Outcomes of Planet-Planet Scattering». In: *ApJ* 686.1, pp. 580–602.

Chauvin, G. et al. (2012). «Orbital characterization of the β Pictoris b giant planet». In: *A&A* 542, A41, A41.

Chen, C. H., K. Y. L. Su and S. Xu (2020). «Spitzer's debris disk legacy from main-sequence stars to white dwarfs». In: *Nature Astronomy* 4, pp. 328–338.

Clanton, C. and B. S. Gaudi (2017). «Constraining the Frequency of Free-floating Planets from a Synthesis of Microlensing, Radial Velocity, and Direct Imaging Survey Results». In: *ApJ* 834.1, 46, p. 46.

Clark, P. C., R. S. Klessen and I. A. Bonnell (2007). «Clump lifetimes and the initial mass function». In: *MNRAS* 379.1, pp. 57–62.

Crampton, D. et al. (1976). «Radial velocities and distances of OB stars at the solar distance to the galactic centre.» In: *MNRAS* 176, pp. 683–692.

Crundall, T. D. et al. (2019). «Chronostar: a novel Bayesian method for kinematic age determination - I. Derivation and application to the β Pictoris moving group». In: *MNRAS* 489.3, pp. 3625–3642.

Cuillandre, J.-C. et al. (2000). «Performance of the CFH12K: a 12K by 8K CCD mosaic camera for the CFHT prime focus». In: *Society of Photo-Optical Instrumentation Engineers (SPIE) Conference Series*. Ed. by M. Iye and A. F. Moorwood. Vol. 4008. Presented at the Society of Photo-Optical Instrumentation Engineers (SPIE) Conference, pp. 1010–1021.

Damiani, F. et al. (2019). «Stellar population of Sco OB2 revealed by Gaia DR2 data». In: *A&A* 623, A112, A112.

David, T. J. et al. (2019). «Age Determination in Upper Scorpius with Eclipsing Binaries». In: *ApJ* 872.2, 161, p. 161.

Di Francesco, J. et al. (2020). «Herschel Gould Belt Survey Observations of Dense Cores in the Cepheus Flare Clouds». In: *arXiv e-prints*, arXiv:2010.09894, arXiv:2010.09894.

Drimmel, R. and D. N. Spergel (2001). «Three-dimensional Structure of the Milky Way Disk: The Distribution of Stars and Dust beyond 0.35 R_{solar}». In: *ApJ* 556, pp. 181–202.

Ducourant, C. et al. (2014). «The TW Hydrae association: trigonometric parallaxes and kinematic analysis». In: *A&A* 563, A121, A121.

Ducourant, C. et al. (2017). «Proper motion survey and kinematic analysis of the ρ Ophiuchi embedded cluster». In: *A&A* 597, A90, A90.

Dye, S. et al. (2018). «The UKIRT Hemisphere Survey: definition and J-band data release». In: *MNRAS* 473, pp. 5113–5125.

Eilers, A.-C. et al. (2020). «The Strength of the Dynamical Spiral Perturbation in the Galactic Disk». In: *arXiv e-prints*, arXiv:2003.01132, arXiv:2003.01132.

Elliott, P. et al. (2014). «Search for associations containing young stars (SACY). V. Is multiplicity universal? Tight multiple systems». In: *A&A* 568, A26, A26.

Elson, R. A. W., S. M. Fall and K. C. Freeman (1987). «The structure of young star clusters in the Large Magellanic Cloud». In: *ApJ* 323, pp. 54–78.

Emerson, J., A. McPherson and W. Sutherland (2006). «Visible and Infrared Survey Telescope for Astronomy: Progress Report». In: *The Messenger* 126, pp. 41–42.

Evans, D. W. et al. (2018). «Gaia Data Release 2. Photometric content and validation». In: *A&A* 616, A4, A4.

Fang, Q., G. J. Herczeg and A. Rizzuto (2017). «Age Spreads and the Temperature Dependence of Age Estimates in Upper Sco». In: *ApJ* 842.2, 123, p. 123.

Feiden, G. A. (2016). «Magnetic inhibition of convection and the fundamental properties of low-mass stars. III. A consistent 10 Myr age for the Upper Scorpius OB association». In: *A&A* 593, A99, A99.

Fernandes, R. B. et al. (2019). «Hints for a Turnover at the Snow Line in the Giant Planet Occurrence Rate». In: *ApJ* 874.1, 81, p. 81.

Fernández, D., F. Figueras and J. Torra (2008). «On the kinematic evolution of young local associations and the Scorpius-Centaurus complex». In: *A&A* 480, pp. 735–751.

Flaugher, B. L. et al. (2010). «Status of the dark energy survey camera (DECam) project». In: *Ground-based and Airborne Instrumentation for Astronomy III*. Vol. 7735. Proc. SPIE, p. 77350D.

Gagné, J. and J. K. Faherty (2018). «BANYAN. XIII. A First Look at Nearby Young Associations with Gaia Data Release 2». In: *ApJ* 862.2, 138, p. 138.

Gagné, J. et al. (2015a). «BANYAN. V. A Systematic All-sky Survey for New Very Late-type Low-mass Stars and Brown Dwarfs in Nearby Young Moving Groups». In: *ApJ* 798.2, 73, p. 73.

Gagné, J. et al. (2015b). «BANYAN. VII. A New Population of Young Substellar Candidate Members of Nearby Moving Groups from the BASS Survey». In: *ApJS* 219.2, 33, p. 33.

Gagné, J. et al. (2018). «BANYAN. XII. New Members of Nearby Young Associations from GAIA-Tycho Data». In: *ApJ* 860.1, 43, p. 43.

Gaia Collaboration et al. (2016). «The Gaia mission». In: *A&A* 595, A1, A1.

Gaia Collaboration et al. (2018a). «Gaia Data Release 2. Kinematics of globular clusters and dwarf galaxies around the Milky Way». In: *A&A* 616, A12, A12.

Gaia Collaboration et al. (2018b). «Gaia Data Release 2. Observational Hertzsprung-Russell diagrams». In: *A&A* 616, A10, A10.

Gaia Collaboration et al. (2018c). «Gaia Data Release 2. Summary of the contents and survey properties». In: *A&A* 616, A1, A1.

Galli, P. A. B. et al. (2019). «Structure and kinematics of the Taurus star-forming region from Gaia-DR2 and VLBI astrometry». In: *A&A* 630, A137, A137.

Galli, P. A. B. et al. (2020). «Corona-Australis DANCe. I. Revisiting the census of stars with Gaia-DR2 data». In: *arXiv e-prints*, arXiv:2001.05190, arXiv:2001.05190.

Geers, V. et al. (2011). «Substellar Objects in Nearby Young Clusters (SONYC). II. The Brown Dwarf Population of ρ Ophiuchi». In: *ApJ* 726.1, 23, p. 23.

Gehrels, N. (1986). «Confidence Limits for Small Numbers of Events in Astrophysical Data». In: *ApJ* 303, p. 336.

Giampapa, M. S., C. F. Prosser and T. A. Fleming (1998). «X-Ray Activity in the Open Cluster IC 4665». In: *ApJ* 501.2, pp. 624–642.

Goldsmith, P. F. et al. (2008). «Large-Scale Structure of the Molecular Gas in Taurus Revealed by High Linear Dynamic Range Spectral Line Mapping». In: *ApJ* 680.1, pp. 428–445.

Gorlova, N. et al. (2007). «Debris Disks in NGC 2547». In: *ApJ* 670.1, pp. 516–535.

Gorlova, N. et al. (2006). «Spitzer 24 μm Survey of Debris Disks in the Pleiades». In: *ApJ* 649.2, pp. 1028–1042.

Gray, R. O. and C. J. Corbally (2002). «A Spectroscopic Search for λ Bootis and Other Peculiar A-Type Stars in Intermediate-Age Open Clusters». In: *AJ* 124.2, pp. 989–1000.

Gray, R. O. et al. (2006). «Contributions to the Nearby Stars (NStars) Project: Spectroscopy of Stars Earlier than Mo within 40 pc-The Southern Sample». In: *AJ* 132.1, pp. 161–170.

Green, G. M. et al. (2019). «A 3D Dust Map Based on Gaia, Pan-STARRS 1, and 2MASS». In: *ApJ* 887.1, 93, p. 93.

Greene, T. P. and M. R. Meyer (1995). «An Infrared Spectroscopic Survey of the rho Ophiuchi Young Stellar Cluster: Masses and Ages from the H-R Diagram». In: *ApJ* 450, p. 233.

Großschedl, J. E., J. Alves and S. Meingast (2020). «3D dynamics of the Orion cloud complex – Discovery of coherent radial gas motions at the 100-pc scale». In: *arXiv e-prints*, arXiv:2007.07254, arXiv:2007.07254.

Hacar, A. et al. (2013). «Cores, filaments, and bundles: hierarchical core formation in the L1495/B213 Taurus region». In: *A&A* 554, A55, A55.

Hacar, Á. (2013). «Formación de núcleos densos en las nubes moleculares de Tauro y Perseo». Tesis inédita de la Universidad Complutense de Madrid, Facultad de Ciencias Físicas, Departamento de Física de la Tierra, Astronomía y Astrofísica II (Astrofísica y Ciencias de la Atmósfera), leída el 18/01/2013. Tesis formato europeo (compendio de artículos). Madrid.

Hacar, A., M. Tafalla and D. Pierce-Price (2012). *eso1209 - Photo Release - APEX Turns its Eye to Dark Clouds in Taurus*.

Hartman, J. D. et al. (2011). «A Photometric Variability Survey of Field K and M Dwarf Stars with HATNet». In: *AJ* 141.5, 166, p. 166.

Hayashi, C. and T. Nakano (1963). «Evolution of Stars of Small Masses in the Pre-Main-Sequence Stages». In: *Progress of Theoretical Physics* 30.4, pp. 460–474.

Hennebelle, P. and G. Chabrier (2008). «Analytical Theory for the Initial Mass Function: CO Clumps and Prestellar Cores». In: *ApJ* 684.1, pp. 395–410.

Hennebelle, P. and E. Falgarone (2012). «Turbulent molecular clouds». In: *A&A Rev.* 20, 55, p. 55.

Hernández, J. et al. (2014). «A Spectroscopic Census in Young Stellar Regions: The σ Orionis Cluster». In: *ApJ* 794.1, 36, p. 36.

Heyer, M. and T. M. Dame (2015). «Molecular Clouds in the Milky Way». In: *ARA&A* 53, pp. 583–629.

Høg, E. et al. (2000). «The Tycho-2 catalogue of the 2.5 million brightest stars». In: *A&A* 355, pp. L27–L30.

Hogg, A. R. and G. E. Kron (1955). «The galactic cluster IC 4665.» In: *AJ* 60, p. 365.

Hopkins, A. M. (2018). «The Dawes Review 8: Measuring the Stellar Initial Mass Function». In: *Publications of the Astronomical Society of Australia* 35.

Hopkins, P. F. (2012). «The stellar initial mass function, core mass function and the last-crossing distribution». In: *MNRAS* 423.3, pp. 2037–2044.

Houk, N. (1982). *Michigan Catalogue of Two-dimensional Spectral Types for the HD stars. Volume_3. Declinations $-40°$ to $-26°$.*

Hubble, E. (1929). «A Relation between Distance and Radial Velocity among Extra-Galactic Nebulae». In: *Proceedings of the National Academy of Science* 15.3, pp. 168–173.

Hubrig, S. and G. Mathys (1996). «The λ 3984 feature in late-B spectroscopic binaries.» In: *A&AS* 120, pp. 457–462.

Hughes, A. M., G. Duchêne and B. C. Matthews (2018). «Debris Disks: Structure, Composition, and Variability». In: *ARA&A* 56, pp. 541–591.

Iglewicz, B. and D. Hoaglin (1993). *How to Detect and Handle Outliers*. ASQC basic references in quality control. ASQC Quality Press.

Irrgang, A. et al. (2013). «Milky Way mass models for orbit calculations». In: *A&A* 549, A137, A137.

Irwin, M (2010). «A Nebulosity Filtering Algorithm». In: *UKIRT Newsletter* 26, p. 14.

Ives, D. (1998). «The INT Wide Field Camera.» In: *IEEE Spectrum* 16, pp. 20–21.

Janson, M. et al. (2017). «Binaries among low-mass stars in nearby young moving groups». In: *A&A* 599, A70, A70.

Jayawardhana, R. (2000). «New Stars on the Block». In: *Science* 288, p. 64.

Jeans, J. H. (1902). «The Stability of a Spherical Nebula». In: *Philosophical Transactions of the Royal Society of London Series A* 199, pp. 1–53.

Jeffries, R. D. (2012). «Measuring the Initial Mass Function of Low Mass Stars and Brown Dwarfs». In: *EAS Publications Series*. Ed. by C. Reylé, C. Charbonnel and M. Schultheis. Vol. 57. EAS Publications Series, pp. 45–89.

Jeffries, R. D., M. R. Thurston and N. C. Hambly (2001). «Photometry and membership for low mass stars in the young open cluster NGC 2516». In: *A&A* 375, pp. 863–889.

Jeffries, R. D. et al. (2006). «An XMM-Newton observation of the young open cluster NGC 2547: coronal activity at 30 Myr». In: *MNRAS* 367.2, pp. 781–800.

Jeffries, R. D. et al. (2009). «Low-mass members of the young cluster IC 4665 and pre-main-sequence lithium depletion». In: *MNRAS* 400, pp. 317–329.

Jönsson, H. et al. (2020). «APOGEE Data and Spectral Analysis from SDSS Data Release 16: Seven Years of Observations Including First Results from APOGEE-South». In: *AJ* 160.3, 120, p. 120.

Jordi, C. et al. (2010). «Gaia broad band photometry». In: *A&A* 523, A48, A48.
Jurić, M. and S. Tremaine (2008). «Dynamical Origin of Extrasolar Planet Eccentricity Distribution». In: *ApJ* 686.1, pp. 603–620.
Kalas, P. and D. Jewitt (1995). «Asymmetries in the Beta Pictoris Dust Disk». In: *AJ* 110, p. 794.
Kalas, P., M. C. Liu and B. C. Matthews (2004). «Discovery of a Large Dust Disk Around the Nearby Star AU Microscopii». In: *Science* 303.5666, pp. 1990–1992.
Kalas, P. et al. (2008). «Optical Images of an Exosolar Planet 25 Light-Years from Earth». In: *Science* 322.5906, p. 1345.
Kaufer, A. et al. (1999). «Commissioning FEROS, the new high-resolution spectrograph at La-Silla.» In: *The Messenger* 95, pp. 8–12.
Kenyon, S. J. and L. Hartmann (1995). «Pre-Main-Sequence Evolution in the Taurus-Auriga Molecular Cloud». In: *ApJS* 101, p. 117.
Kharchenko, N. V. et al. (2007). «Astrophysical supplements to the ASCC-2.5: Ia. Radial velocities of ∼55000 stars and mean radial velocities of 516 Galactic open clusters and associations». In: *Astronomische Nachrichten* 328.9, p. 889.
Kiefer, F. et al. (2014). «Two families of exocomets in the β Pictoris system». In: *Nature* 514.7523, pp. 462–464.
King, I. (1962). «The structure of star clusters. I. an empirical density law». In: *AJ* 67, p. 471.
Kippenhahn, R., A. Weigert and A. Weiss (2012). *Stellar Structure and Evolution*.
Klutsch, A. et al. (2014). «Reliable probabilistic determination of membership in stellar kinematic groups in the young disk». In: *A&A* 567, A52, A52.
Kraicheva, Z. et al. (1980). «Catalogue of physical parameters of spectroscopic binary stars.» In: *Bulletin d'Information du Centre de Donnees Stellaires* 19, p. 71.
Kraus, A. L. et al. (2017). «The Greater Taurus–Auriga Ecosystem. I. There is a Distributed Older Population». In: *ApJ* 838.2, 150, p. 150.
Kroupa, P., C. A. Tout and G. Gilmore (1990). «The low-luminosity stellar mass function». In: *MNRAS* 244, pp. 76–85.
Kroupa, P. (2001). «On the variation of the initial mass function». In: *MNRAS* 322.2, pp. 231–246.
— (2002). «The Initial Mass Function of Stars: Evidence for Uniformity in Variable Systems». In: *Science* 295.5552, pp. 82–91.
Krumholz, M. R., C. F. McKee and R. I. Klein (2005). «The formation of stars by gravitational collapse rather than competitive accretion». In: *Nature* 438.7066, pp. 332–334.
Kuijken, K. et al. (2002). «OmegaCAM: the 16k×16k CCD camera for the VLT survey telescope». In: *The Messenger* 110, pp. 15–18.
Kumar, R. et al. (2019). «ArviZ a unified library for exploratory analysis of Bayesian models in Python». In: *The Journal of Open Source Software*.
Kumar, S. S. (1962). «Study of Degeneracy in Very Light Stars.» In: *AJ* 67, p. 579.

Küpper, A. H. W. et al. (2010). «Peculiarities in velocity dispersion and surface density profiles of star clusters». In: *MNRAS* 407, pp. 2241–2260.

Lada, C. J. (2006). «Stellar Multiplicity and the Initial Mass Function: Most Stars Are Single». In: *ApJ* 640, pp. L63–L66.

Lada, C. J. (1987). «Star formation: from OB associations to protostars.» In: *Star Forming Regions*. Ed. by M. Peimbert and J. Jugaku. Vol. 115. IAU Symposium, p. 1.

Lagrange, A. M. et al. (2010). «A Giant Planet Imaged in the Disk of the Young Star β Pictoris». In: *Science* 329.5987, p. 57.

Lagrange, A. M. et al. (2019). «Evidence for an additional planet in the β Pictoris system». In: *Nature Astronomy* 3, pp. 1135–1142.

Larson, R. B. (1969). «Numerical calculations of the dynamics of collapsing proto-star». In: *MNRAS* 145, p. 271.

Lawrence, A. et al. (2007). «The UKIRT Infrared Deep Sky Survey (UKIDSS)». In: *MNRAS* 379, pp. 1599–1617.

Le Fèvre, O. et al. (2003). «Commissioning and performances of the VLT-VIMOS instrument». In: *Instrument Design and Performance for Optical/Infrared Ground-based Telescopes*. Ed. by M. Iye and A. F. M. Moorwood. Vol. 4841. Society of Photo-Optical Instrumentation Engineers (SPIE) Conference Series, pp. 1670–1681.

Lee, S.-W. and H. Sung (1995). «The Luminosity Function and Initial Mass Function for the Pleiades Cluster». In: *Journal of Korean Astronomical Society* 28, pp. 45–59.

Lee, S.-W., H. Sung and D.-H. Cho (1997). «The Luminosity Function and Mass Function for the Praesepe and Hyades Clusters». In: *Journal of Korean Astronomical Society* 30, pp. 181–189.

Levato, H. and S. Malaroda (1977). «Spectroscopic study of two peculiar stars in IC 4665 : HD 161480 and HD 161733.» In: *PASP* 89, pp. 84–94.

Lillo-Box, J. et al. (2020). «CAFE$_2$: an upgrade to the CAFE high-resolution spectrograph. Commissioning results and new public pipeline». In: *MNRAS* 491.3, pp. 4496–4508.

Lindegren, L. et al. (2018a). «Gaia Data Release 2. The astrometric solution». In: *A&A* 616, A2, A2.

— (2018b). «Gaia Data Release 2. The astrometric solution». In: *A&A* 616, A2, A2.

Lodieu, N. (2013). «Astrometric and photometric initial mass functions from the UKIDSS Galactic Clusters Survey - IV. Upper Sco». In: *MNRAS* 431.4, pp. 3222–3235.

Lodieu, N. et al. (2007). «New brown dwarfs in Upper Sco using UKIDSS Galactic Cluster Survey science verification data». In: *MNRAS* 374.1, pp. 372–384.

Lodieu, N. et al. (2011). «The mass function of IC 4665 revisited by the UKIDSS Galactic Clusters Survey». In: *A&A* 532, A103, A103.

Lodieu, N. et al. (2018). «The optical + infrared L dwarf spectral sequence of young planetary-mass objects in the Upper Scorpius association». In: *MNRAS* 473.2, pp. 2020–2059.

Lomax, O., A. P. Whitworth and D. A. Hubber (2016). «Forming isolated brown dwarfs by turbulent fragmentation». In: *MNRAS* 458.2, pp. 1242–1252.

López-Santiago, J. et al. (2006). «The Nearest Young Moving Groups». In: *ApJ* 643.2, pp. 1160–1165.
Luhman, K. L. (2007). «The Stellar Population of the Chamaeleon I Star-forming Region». In: *ApJS* 173.1, pp. 104–136.
Luhman, K. L. et al. (2018). «New Young Stars and Brown Dwarfs in the Upper Scorpius Association». In: *AJ* 156.2, 76, p. 76.
Luri, X. et al. (2018). «Gaia Data Release 2. Using Gaia parallaxes». In: *A&A* 616, A9, A9.
Mac Low, M.-M. and R. S. Klessen (2004). «Control of star formation by supersonic turbulence». In: *Reviews of Modern Physics* 76.1, pp. 125–194.
Macdonald, J. and D. J. Mullan (2010). «Magneto-convection and Lithium Age Estimates of the β Pictoris Moving Group». In: *ApJ* 723.2, pp. 1599–1606.
Magnier, E. A. and J.-C. Cuillandre (2004). «The Elixir System: Data Characterization and Calibration at the Canada-France-Hawaii Telescope». In: *PASP* 116, pp. 449–464.
Makarov, V. V. (2007). «Unraveling the Origins of Nearby Young Stars». In: *ApJS* 169, pp. 105–119.
Malo, L. et al. (2013). «Bayesian Analysis to Identify New Star Candidates in Nearby Young Stellar Kinematic Groups». In: *ApJ* 762.2, 88, p. 88.
Malo, L. et al. (2014a). «BANYAN. III. Radial Velocity, Rotation, and X-Ray Emission of Low-mass Star Candidates in Nearby Young Kinematic Groups». In: *ApJ* 788.1, 81, p. 81.
Malo, L. et al. (2014b). «BANYAN. IV. Fundamental Parameters of Low-mass Star Candidates in Nearby Young Stellar Kinematic Groups—Isochronal Age Determination using Magnetic Evolutionary Models». In: *ApJ* 792.1, 37, p. 37.
Mamajek, E. E. and C. P. M. Bell (2014). «On the age of the β Pictoris moving group». In: *MNRAS* 445, pp. 2169–2180.
Manzi, S. et al. (2008). «Detection of the lithium depletion boundary in the young open cluster IC 4665». In: *A&A* 479, pp. 141–148.
Marigo, P. et al. (2017). «A New Generation of PARSEC-COLIBRI Stellar Isochrones Including the TP-AGB Phase». In: *ApJ* 835, 77, p. 77.
Marois, C. et al. (2008). «Direct Imaging of Multiple Planets Orbiting the Star HR 8799». In: *Science* 322.5906, p. 1348.
Mason, B. D. et al. (2001). «The 2001 US Naval Observatory Double Star CD-ROM. I. The Washington Double Star Catalog». In: *AJ* 122.6, pp. 3466–3471.
Mayor, M. et al. (2011). «The HARPS search for southern extra-solar planets XXXIV. Occurrence, mass distribution and orbital properties of super-Earths and Neptune-mass planets». In: *arXiv e-prints*, arXiv:1109.2497, arXiv:1109.2497.
McKee, C. F. and E. C. Ostriker (2007). «Theory of Star Formation». In: *ARA&A* 45.1, pp. 565–687.
McMillan, P. J. (2017). «The mass distribution and gravitational potential of the Milky Way». In: *MNRAS* 465.1, pp. 76–94.

Meng, H. Y. A. et al. (2017). «The First 40 Million Years of Circumstellar Disk Evolution: The Signature of Terrestrial Planet Formation». In: *ApJ* 836.1, 34, p. 34.

Mentuch, E. et al. (2008). «Lithium Depletion of Nearby Young Stellar Associations». In: *ApJ* 689.2, pp. 1127–1140.

Messina, S. et al. (2016). «The rotation-lithium depletion correlation in the β Pictoris association and the LDB age determination». In: *A&A* 596, A29, A29.

Messina, S. et al. (2017). «The β Pictoris association: Catalog of photometric rotational periods of low-mass members and candidate members». In: *A&A* 600, A83, A83.

Miller, G. E. and J. M. Scalo (1979). «The Initial Mass Function and Stellar Birthrate in the Solar Neighborhood». In: *ApJS* 41, p. 513.

Miret-Roig, N., N. Huélamo and H. Bouy (2020). «Searching for debris discs in the 30 Myr open cluster IC 4665». In: *A&A* 641, A156, A156.

Miret-Roig, N. et al. (2018). «Dynamical ages of the young local associations with Gaia». In: *A&A* 615, A51, A51.

Miret-Roig, N. et al. (2019). «IC 4665 DANCe. I. Members, empirical isochrones, magnitude distributions, present-day system mass function, and spatial distribution». In: *A&A* 631, A57, A57.

Miret-Roig, N. et al. (2020). «Dynamical traceback age of the β Pictoris moving group». In: *A&A* 642, A179, A179.

Miyazaki, S. et al. (2018). «Hyper Suprime-Cam: System design and verification of image quality». In: *PASJ* 70, S1, S1.

Miyazaki, S. et al. (2002). «Subaru Prime Focus Camera – Suprime-Cam». In: *PASJ* 54, pp. 833–853.

Molinari, S. et al. (2014). «The Milky Way as a Star Formation Engine». In: *Protostars and Planets VI*. Ed. by H. Beuther et al., p. 125.

Moór, A. et al. (2006). «Nearby Debris Disk Systems with High Fractional Luminosity Reconsidered». In: *ApJ* 644.1, pp. 525–542.

Morrell, N. and H. A. Abt (1991). «Reinvestigation of the Binary Frequency in the Open Cluster IC 4665». In: *ApJ* 378, p. 157.

Motte, F., P. Andre and R. Neri (1998). «The initial conditions of star formation in the rho Ophiuchi main cloud: wide-field millimeter continuum mapping». In: *A&A* 336, pp. 150–172.

Mužić, K. et al. (2012). «Substellar Objects in Nearby Young Clusters (SONYC). V. New Brown Dwarfs in ρ Ophiuchi». In: *ApJ* 744.2, 134, p. 134.

Naylor, T. et al. (2002). «Optimal photometry for colour-magnitude diagrams and its application to NGC 2547». In: *MNRAS* 335, pp. 291–310.

Offner, S. S. R. et al. (2014). «The Origin and Universality of the Stellar Initial Mass Function». In: *Protostars and Planets VI*.

Olivares, J. et al. (2018). «The seven sisters DANCe. III. Projected spatial distribution». In: *A&A* 612, A70, A70.

Olivares, J. et al. (2019). «Ruprecht 147 DANCe I. Members, empirical isochrone, luminosity and mass distributions». In: *arXiv e-prints*.

Olivares, J. et al. (2020). «Kalkayotl: A cluster distance inference code». In: *arXiv e-prints*, arXiv:2010.00272, arXiv:2010.00272.

Oliveira, J. M., R. D. Jeffries and J. T. van Loon (2009). «The low-mass initial mass function in the young cluster NGC6611». In: *MNRAS* 392.3, pp. 1034–1050.

Oppenheimer, B. R. et al. (1995). «Infrared Spectrum of the Cool Brown Dwarf Gl 229B». In: *Science* 270.5241, pp. 1478–1479.

Ortega, V. G. et al. (2002). «The Origin of the β Pictoris Moving Group». In: *ApJ* 575, pp. L75–L78.

— (2004). «New Aspects of the Formation of the β Pictoris Moving Group». In: *ApJ* 609, pp. 243–246.

Padoan, P. and Å. Nordlund (2002). «The Stellar Initial Mass Function from Turbulent Fragmentation». In: *ApJ* 576.2, pp. 870–879.

Padoan, P. et al. (2019). «The Origin of Massive Stars: The Inertial-Inflow Model». In: *arXiv e-prints*, arXiv:1911.04465, arXiv:1911.04465.

Paillassa, M., E. Bertin and H. Bouy (2020). «MAXIMASK and MAXITRACK: Two new tools for identifying contaminants in astronomical images using convolutional neural networks». In: *A&A* 634, A48, A48.

Parker, R. J. and S. P. Quanz (2012). «The effects of dynamical interactions on planets in young substructured star clusters». In: *MNRAS* 419.3, pp. 2448–2458.

Peña Ramírez, K. et al. (2012). «New Isolated Planetary-mass Objects and the Stellar and Substellar Mass Function of the σ Orionis Cluster». In: *ApJ* 754.1, 30, p. 30.

Pecaut, M. J. and E. E. Mamajek (2016). «The star formation history and accretion-disc fraction among the K-type members of the Scorpius-Centaurus OB association». In: *MNRAS* 461.1, pp. 794–815.

Pecaut, M. J., E. E. Mamajek and E. J. Bubar (2012). «A Revised Age for Upper Scorpius and the Star Formation History among the F-type Members of the Scorpius-Centaurus OB Association». In: *ApJ* 746.2, 154, p. 154.

Pédoussaut, A. and J. M. Carquillat (1973). «Spectroscopic binaries - 12th complementary catalogue». In: *A&AS* 10, p. 105.

Pedregosa, F. et al. (2011). «Scikit-learn: Machine Learning in Python». In: *Journal of Machine Learning Research* 12, pp. 2825–2830.

Penston, M. V. (1969). «Dynamics of self-gravitating gaseous spheres-III. Analytical results in the free-fall of isothermal cases». In: *MNRAS* 144, p. 425.

Pepe, F. et al. (2002). «The CORALIE survey for southern extra-solar planets VII. Two short-period Saturnian companions to <ASTROBJ>HD 108147</ASTROBJ> and <ASTROBJ>HD 168746</ASTROBJ>». In: *A&A* 388, pp. 632–638.

Perruchot, S. et al. (2008). «The SOPHIE spectrograph: design and technical key-points for high throughput and high stability». In: *Proc. SPIE*. Vol. 7014. Society of Photo-Optical Instrumentation Engineers (SPIE) Conference Series, 70140J.

Pichardo, B. et al. (2003). «Nonlinear Effects in Models of the Galaxy. I. Midplane Stellar Orbits in the Presence of Three-dimensional Spiral Arms». In: *ApJ* 582, pp. 230–245.

Pirard, J.-F. et al. (2004). «HAWK-I: A new wide-field 1- to 2.5-μm imager for the VLT». In: *Ground-based Instrumentation for Astronomy*. Ed. by A. F. M. Moorwood and M. Iye. Vol. 5492. Society of Photo-Optical Instrumentation Engineers (SPIE) Conference Series, pp. 1763–1772.

Plavchan, P. et al. (2009). «New Debris Disks Around Young, Low-Mass Stars Discovered with the Spitzer Space Telescope». In: *ApJ* 698.2, pp. 1068–1094.

Preibisch, T. and H. Zinnecker (1999). «The History of Low-Mass Star Formation in the Upper Scorpius OB Association». In: *AJ* 117.5, pp. 2381–2397.

Preibisch, T. et al. (2002). «Exploring the Full Stellar Population of the Upper Scorpius OB Association». In: *AJ* 124.1, pp. 404–416.

Prosser, C. F. and M. S. Giampapa (1994). «A Radial Velocity Survey of the Open Cluster IC 4665». In: *AJ* 108, p. 964.

Rahmer, G. et al. (2008). «The 12K×8K CCD mosaic camera for the Palomar Transient Factory». In: *Proc. SPIE*. Vol. 7014. Society of Photo-Optical Instrumentation Engineers (SPIE) Conference Series, 70144Y.

Raymond, S. N., P. J. Armitage and N. Gorelick (2010). «Planet-Planet Scattering in Planetesimal Disks. II. Predictions for Outer Extrasolar Planetary Systems». In: *ApJ* 711.2, pp. 772–795.

Rebolo, R., M. R. Zapatero Osorio and E. L. Martín (1995). «Discovery of a brown dwarf in the Pleiades star cluster». In: *Nature* 377.6545, pp. 129–131.

Rebull, L. M. et al. (2016). «Rotation in the Pleiades with K2. I. Data and First Results». In: *AJ* 152, 113, p. 113.

Rebull, L. M. et al. (2018). «Rotation of Low-mass Stars in Upper Scorpius and ρ Ophiuchus with K2». In: *AJ* 155, 196, p. 196.

Reipurth, B. and C. Clarke (2001). «The Formation of Brown Dwarfs as Ejected Stellar Embryos». In: *AJ* 122.1, pp. 432–439.

Rheault, J.-P. et al. (2014). «Spectrophotometric calibration of the Swope and duPont telescopes for the Carnegie supernova project 2». In: *Ground-based and Airborne Instrumentation for Astronomy V*. Vol. 9147. Proc. SPIE, p. 91475L.

Rhee, J. H. et al. (2007). «Characterization of Dusty Debris Disks: The IRAS and Hipparcos Catalogs». In: *ApJ* 660.2, pp. 1556–1571.

Riaz, B., J. E. Gizis and J. Harvin (2006). «Identification of New M Dwarfs in the Solar Neighborhood». In: *AJ* 132.2, pp. 866–872.

Riedel, A. R. et al. (2017a). «LACEwING: A New Moving Group Analysis Code». In: *AJ* 153, 95, p. 95.

Riedel, A. R. et al. (2017b). «Young Stars with SALT». In: *ApJ* 840.2, 87, p. 87.

Rieke, G. H. et al. (2005). «Decay of Planetary Debris Disks». In: *ApJ* 620.2, pp. 1010–1026.

Rizzuto, A. C. et al. (2016). «Dynamical Masses of Young Stars. I. Discordant Model Ages of Upper Scorpius». In: *ApJ* 817.2, 164, p. 164.

Rosen, A. L. et al. (2020). «Zooming in on Individual Star Formation: Low- and High-Mass Stars». In: *Space Sci. Rev.* 216.4, 62, p. 62.

Salpeter, E. E. (1955). «The Luminosity Function and Stellar Evolution.» In: *ApJ* 121, p. 161.

Samus', N. N. et al. (2017). «General catalogue of variable stars: Version GCVS 5.1». In: *Astronomy Reports* 61.1, pp. 80–88.

Sarro, L. M. et al. (2014). «Cluster membership probabilities from proper motions and multi-wavelength photometric catalogues. I. Method and application to the Pleiades cluster». In: *A&A* 563, A45, A45.

Schlieder, J. E., S. Lépine and M. Simon (2012). «Cool Young Stars in the Northern Hemisphere: β Pictoris and AB Doradus Moving Group Candidates». In: *AJ* 143.4, 80, p. 80.

Schneider, A. C. et al. (2019). «ACRONYM. III. Radial Velocities for 336 Candidate Young Low-mass Stars in the Solar Neighborhood, Including 77 Newly Confirmed Young Moving Group Members». In: *AJ* 157.6, 234, p. 234.

Scholz, A. et al. (2012a). «Substellar Objects in Nearby Young Clusters (SONYC). IV. A Census of Very Low Mass Objects in NGC 1333». In: *ApJ* 744, 6, p. 6.

Scholz, A. et al. (2012b). «Substellar Objects in Nearby Young Clusters (SONYC). VI. The Planetary-mass Domain of NGC 1333». In: *ApJ* 756.1, 24, p. 24.

Schönrich, R., J. Binney and W. Dehnen (2010). «Local kinematics and the local standard of rest». In: *MNRAS* 403, pp. 1829–1833.

Scott, D. W. (1992). *Multivariate Density Estimation. Theory, Practice, and Visualization*. Wiley.

Shkolnik, E. L. et al. (2012). «Identifying the Young Low-mass Stars within 25 pc. II. Distances, Kinematics, and Group Membership». In: *ApJ* 758.1, 56, p. 56.

Shkolnik, E. L. et al. (2017). «All-sky Co-moving Recovery Of Nearby Young Members (ACRONYM). II. The β Pictoris Moving Group». In: *AJ* 154.2, 69, p. 69.

Shu, F. H. (1977). «Self-similar collapse of isothermal spheres and star formation.» In: *ApJ* 214, pp. 488–497.

Siegler, N. et al. (2007). «Spitzer 24 μm Observations of Open Cluster IC 2391 and Debris Disk Evolution of FGK Stars». In: *ApJ* 654.1, pp. 580–594.

Silverman, B. W. (1986). *Density Estimation*. London: Chapman and Hall.

Slesnick, C. L., L. A. Hillenbrand and J. M. Carpenter (2008). «A Large-Area Search for Low-Mass Objects in Upper Scorpius. II. Age and Mass Distributions». In: *ApJ* 688.1, pp. 377–397.

Smith, R., R. D. Jeffries and J. M. Oliveira (2011). «Debris discs in the 27 Myr old open cluster IC 4665». In: *MNRAS* 411.4, pp. 2186–2198.

Song, I., B. Zuckerman and M. S. Bessell (2003). «New Members of the TW Hydrae Association, β Pictoris Moving Group, and Tucana/Horologium Association». In: *ApJ* 599.1, pp. 342–350.

Soubiran, C. et al. (2018). «Gaia Data Release 2. The catalogue of radial velocity standard stars». In: *A&A* 616, A7, A7.

Spiegel, D. S., A. Burrows and J. A. Milsom (2011). «The Deuterium-burning Mass Limit for Brown Dwarfs and Giant Planets». In: *ApJ* 727.1, 57, p. 57.

Stauffer, J. R. et al. (2010). «Debris Disks of Members of the Blanco 1 Open Cluster». In: *ApJ* 719.2, pp. 1859–1871.

Sung, H. and M. S. Bessell (2010). «The Initial Mass Function and Young Brown Dwarf Candidates in NGC 2264. IV. The Initial Mass Function and Star Formation History». In: *AJ* 140.6, pp. 2070–2085.

Sutherland, A. P. and D. C. Fabrycky (2016). «On the Fate of Unstable Circumbinary Planets: Tatooine's Close Encounters with a Death Star». In: *ApJ* 818.1, 6, p. 6.

Suzuki, D. et al. (2016). «The Exoplanet Mass-ratio Function from the MOA-II Survey: Discovery of a Break and Likely Peak at a Neptune Mass». In: *ApJ* 833.2, 145, p. 145.

Tange, O. (2011). «GNU Parallel - The Command-Line Power Tool». In: *;login: The USENIX Magazine* 36.1, pp. 42–47.

Tarter, J. C. (1975). «The Interaction of Gas and Galaxies Within Galaxy Clusters.» PhD thesis. California Univ., Berkeley.

Taylor, M. B. (2005). «TOPCAT & STIL: Starlink Table/VOTable Processing Software». In: *Astronomical Data Analysis Software and Systems XIV*. Ed. by P. Shopbell, M. Britton and R. Ebert. Vol. 347. Astronomical Society of the Pacific Conference Series, p. 29.

— (2006). «STILTS - A Package for Command-Line Processing of Tabular Data». In: *Astronomical Data Analysis Software and Systems XV*. Ed. by C. Gabriel et al. Vol. 351. Astronomical Society of the Pacific Conference Series, p. 666.

Thibault, S. et al. (2002). «Optical design of CPAPIR, a cryogenic IR camera for OMM». In: *International Optical Design Conference 2002*. Vol. 4832.

Thibault, S. et al. (2003). «Optical design of WIRCAM, the CFHT wide-field infrared camera». In: *Instrument Design and Performance for Optical/Infrared Ground-based Telescopes*. Ed. by M. Iye and A. F. M. Moorwood. Vol. 4841. Proc. SPIE, pp. 932–943.

Thies, I. and P. Kroupa (2007). «A Discontinuity in the Low-Mass Initial Mass Function». In: *ApJ* 671, pp. 767–780.

Thies, I. et al. (2015). «Characterizing the Brown Dwarf Formation Channels from the Initial Mass Function and Binary-star Dynamics». In: *ApJ* 800, 72, p. 72.

Torres, C. A. O. et al. (2006). «Search for associations containing young stars (SACY). I. Sample and searching method». In: *A&A* 460, pp. 695–708.

Torres, C. A. O. et al. (2008). «Young Nearby Loose Associations». In: *Handbook of Star Forming Regions, Volume II*. Ed. by B. Reipurth. Vol. 5, p. 757.

Ujjwal, K. et al. (2020). «Analysis of membership probability in nearby young moving groups with Gaia DR2». In: *arXiv e-prints*, arXiv:2002.04801, arXiv:2002.04801.

Valdes, F., R. Gruendl and DES Project (2014). «The DECam Community Pipeline». In: *Astronomical Data Analysis Software and Systems XXIII*. Ed. by N. Manset and P. Forshay. Vol. 485. Astronomical Society of the Pacific Conference Series, p. 379.

Vandame, B. (2002). «New algorithms and technologies for the un-supervised reduction of Optical/IR images». In: *Astronomical Data Analysis II*. Ed. by J.-L. Starck and F. D. Murtagh. Vol. 4847. Society of Photo-Optical Instrumentation Engineers (SPIE) Conference Series, pp. 123–134.

Veras, D. and S. N. Raymond (2012). «Planet-planet scattering alone cannot explain the free-floating planet population». In: *MNRAS* 421.1, pp. L117–L121.

White, R. J., J. M. Gabor and L. A. Hillenbrand (2007). «High-Dispersion Optical Spectra of Nearby Stars Younger Than the Sun». In: *AJ* 133.6, pp. 2524–2536.

Whitworth, A. P. and H. Zinnecker (2004). «The formation of free-floating brown dwarves and planetary-mass objects by photo-erosion of prestellar cores». In: *A&A* 427, pp. 299–306.

Whitworth, A. (2018). «Brown Dwarf Formation: Theory». In: *arXiv e-prints*, arXiv:1811.06833, arXiv:1811.06833.

Wielen, R., H. Jahreiß and R. Krüger (1983). «The Determination of the Luminosity Function of Nearby Stars». In: *IAU Colloq. 76: Nearby Stars and the Stellar Luminosity Function*. Ed. by A. G. D. Philip and A. R. Upgren, pp. 163–170.

Winston, E. et al. (2009). «A Spectroscopic Study of Young Stellar Objects in the Serpens Cloud Core and NGC 1333». In: *AJ* 137.6, pp. 4777–4794.

Winter, A. J. et al. (2020). «Stellar clustering shapes the architectures of planetary systems». In: *arXiv e-prints*, arXiv:2010.10531, arXiv:2010.10531.

Wright, E. L. et al. (2010). «The Wide-field Infrared Survey Explorer (WISE): Mission Description and Initial On-orbit Performance». In: *AJ* 140, pp. 1868–1881.

Wright, N. J. and E. E. Mamajek (2018). «The kinematics of the Scorpius-Centaurus OB association from Gaia DR1». In: *MNRAS* 476.1, pp. 381–398.

Zacharias, N. et al. (2000). «The First US Naval Observatory CCD Astrograph Catalog». In: *AJ* 120.4, pp. 2131–2147.

Zari, E. et al. (2018). «3D mapping of young stars in the solar neighbourhood with Gaia DR2». In: *A&A* 620, A172, A172.

Zinnecker, H. (1982). «Prediction of the protostellar mass spectrum in the Orion near-infrared cluster». In: *Annals of the New York Academy of Sciences* 395, pp. 226–235.

Zuckerman, B. et al. (2001). «The β Pictoris Moving Group». In: *ApJ* 562.1, pp. L87–L90.

Zuckerman, B. et al. (2011). «The Tucana/Horologium, Columba, AB Doradus, and Argus Associations: New Members and Dusty Debris Disks». In: *ApJ* 732.2, 61, p. 61.

de Wit, W. J. et al. (2006). «Exploring the lower mass function in the young open cluster IC 4665». In: *A&A* 448, pp. 189–202.

de Zeeuw, P. T. et al. (1999). «A HIPPARCOS Census of the Nearby OB Associations». In: *AJ* 117.1, pp. 354–399.

van der Bliek, N. S. et al. (2004). «ISPI: a wide-field NIR imager for the CTIO Blanco 4-m telescope». In: *Ground-based Instrumentation for Astronomy*. Ed. by A. F. M. Moorwood and M. Iye. Vol. 5492. Society of Photo-Optical Instrumentation Engineers (SPIE) Conference Series, pp. 1582–1589.